Identification, Characterization, and Mitigation of the Performance Limiting Processes in Battery Electrodes

Kevin W. Knehr

Submitted in partial fulfillment of the
requirements for the degree of
Doctor of Philosophy
in the Graduate School of Arts and Sciences

Columbia University in the City of New York

2016

ABSTRACT

Identification, Characterization, and Mitigation of the Performance Limiting Processes in Battery Electrodes

Kevin W. Knehr

Batteries are complex, multidisciplinary, electrochemical energy storage systems that are crucial for powering our society. During operation, all battery technologies suffer from voltage losses due to energetic penalties associated with the electrochemical processes (*i.e.,* ohmic resistance, kinetic barriers, and mass transport limitations). A majority of the voltage losses can be attributed to processes occurring on/in the battery electrodes, which are responsible for facilitating the electrochemical reactions. A major challenge in the battery field is developing strategies to mitigate these losses. To accomplish this, researchers must *i) identify* the processes limiting the performance of the electrode, *ii) characterize* the main, performance-limiting processes to understand the underlying mechanisms responsible for the poor performance, and *iii) mitigate* the voltage losses by developing strategies which target these underlying mechanisms. In this thesis, three studies are presented which highlight the role of electrochemical engineers in alleviating the performance limiting processes in battery electrodes. Each study is focused on a different step of the research approach (*i.e.,* identification, characterization, and mitigation) and analyzes an electrode from a different battery system.

The first part of the thesis is focused on identifying the processes limiting the capacity in nanocomposite lithium-magnetite electrodes. To accomplish this, the mass transport processes and phase changes occurring within magnetite electrodes during discharge and voltage recovery are investigated using a combined experimental and modeling approach. First, voltage recovery data are analyzed through a comparison of the mass transport time-constants associated with

different length-scales in the electrode. The long voltage recovery times are hypothesized to result from the relaxation of concentration profiles on the mesoscale, which consists of the agglomerate and crystallite length-scales. The hypothesis was tested through the development of a multi-scale mathematical model. Using the model, experimental discharge and voltage recovery data are compared to three sets of simulations, which incorporate crystal-only, agglomerate-only, or multi-scale transport effects. The results of the study indicate that, depending on the crystal size, the low utilization of the active material (*i.e.*, low capacity) is caused by transport limitations on the agglomerate and/or crystal length-scales. For electrodes composed of small crystals (6 and 8 nm diameters), it is concluded that the transport limitations in the agglomerate are primarily responsible for the long voltage recovery times and low utilization of the active material. In the electrodes composed of large crystals (32 nm diameter), the slow voltage recovery is attributed to transport limitations on both the agglomerate and crystal length-scales.

Next, the multi-scale model is further expanded to study the phase changes occurring in magnetite during lithiation and voltage recovery experiments. Phase changes are described using kinetic expressions based on the Avrami theory for nucleation and growth. Simulated results indicate that the slow, linear voltage change observed at long times during the voltage recovery experiments can be attributed to a slow phase change from α-$Li_xFe_3O_4$ to β-$Li_4Fe_3O_4$. In addition, simulations for the lithiation of 6 and 32 nm Fe_3O_4 suggest the rate of conversion from α-$Li_xFe_3O_4$ to γ-(4 Li_2O + 3 Fe) decreases with decreasing crystal size.

The next part of the thesis presents a study aimed at characterizing the formation of $PbSO_4$ films on Pb in H_2SO_4, which has been previously identified as a performance-limiting process in lead-acid batteries. Transmission X-ray microscopy (TXM) is utilized to monitor, in

real time, the initial formation, the resulting passivation, and the subsequent reduction of the $PbSO_4$ film. It is concluded with support from quartz-crystal-microbalance experiments that the initial formation of $PbSO_4$ crystals occurs as a result of acidic corrosion. Additionally, the film is shown to coalesce during the early stages of galvanostatic oxidation and to passivate as a result of morphological changes in the existing film. Finally, it is observed that the passivation process results in the formation of large $PbSO_4$ crystals with low area-to-volume ratios, which are difficult to reduce under both galvanostatic and potentiostatic conditions.

In a further extension of this study, TXM and scanning electron microscopy are combined to investigate the effects of sodium lignosulfonate on the $PbSO_4$ formation and the initial growth of $PbSO_4$ crystals. Sodium lignosulfonate is shown to retard, on average, the growth of the $PbSO_4$ crystals, yielding a film with smaller crystals and higher crystal densities. In addition, an analysis of the growth rates of individual, large crystals showed an initial rapid growth which declined as the $PbSO_4$ surface coverage increased. It was concluded that the increase in $PbSO_4$ provides additional sites for precipitation and reduces the precipitation rate on the existing crystals. Finally, the potential-time transient at the beginning of oxidation is suggested to result from the relaxation of a supersaturated solution and the development of a $PbSO_4$ film with increasing resistance.

The final part of the thesis presents a study aimed at mitigating the ohmic losses during pulse-power discharge of a battery by the adding a second electrochemically active material to the electrode. Porous electrode theory is used to conduct case studies for when the addition of a second active material can improve the pulse-power performance. Case studies are conducted for the positive electrode of a sodium metal-halide battery and the graphite negative electrode of a lithium-ion battery. The replacement of a fraction of the nickel chloride capacity with iron

chloride in a sodium metal-halide electrode and the replacement of a fraction of the graphite capacity with carbon black in a lithium-ion negative electrode were both predicted to increase the maximum pulse power by up to 40%. In general, whether or not a second electrochemically active material increases the pulse power depends on the relative importance of ohmic-to-charge transfer resistances within the porous structure, the capacity fraction of the second electrochemically active material, and the kinetic and thermodynamic parameters of the two active materials.

TABLE OF CONTENTS

LIST OF FIGURES

CHAPTER 1

CHAPTER 2

CHAPTER 3

CHAPTER 5

CHAPTER 7

LIST OF TABLES

CHAPTER 2

CHAPTER 3

CHAPTER 4

CHAPTER 7

ACKNOWLEDGEMENTS

First, I would like to thank my advisor, Alan C. West, for the endless guidance, direction, and opportunities he's given me over these past four years. Next, I would like to thank all of my collaborators at Brookhaven National Laboratory and Stony Brook University who have made my research possible: Professor Esther Takeuchi, Professor Kenneth Takeuchi, Professor Amy Marschilok, Dr. Jun Wang, Dr. Feng Wang, Dr. Wei Zhang, Dr. Karen Chen-Wiegart, Dr. Jiajun Wang, Dr. David Bock, Dr. Chris Pellicione, Christina Cama, Zhou Lin, and Chris Eng. I have learned so much from each of you about the diversity and depth of scientific research. I'd also like to thank Nick Brady, Christianna Lininger, and Constantine Spanos for their involvement in these projects. It has been a pleasure working with you three, and I truly hope our paths cross in the future. I also want to thank Ali Goksu and Jeremy Zee for their help. To my other lab mates, thank you for the constant support: (now Assistant Professor) Damla Eroglu, Dr. Saeed Rahimian, Dr. Feng Qiao, Dr. Derek Sun, Dr. Ruixing Zhu, Roel Mercado, Sebastian Russell, Anna Dorfi, Aditya Jayan, and Sarah Berlinger. I'd like to give a special thank you to Dr. Robert von Gutfeld. Your guidance and friendship during my time at Columbia have been a blessing.

Thank you to the entire chemical engineering community at Columbia for making my time here extremely enjoyable. In particular, thank you to Kathy Marte, Krystal Paulino, Michelle McCormack, Teresa Colaizzo, Andrew Strycharz, Ariel Sanchez and Mary Ko. Nothing would be accomplished without your tireless work. Thank you to my fellow TA Emily Hsu. To my fellow ChEGO board members, thank you for your friendship and support, especially for those who survived my rein of tyranny (I'm honestly surprised we're still friends): (now Assistant Professor) Joe Woo, Harun Ferit Ozbakir, Beyza Bulutoglu, Kristen Garcia, Thu Vi, Chris Hawxhurst, Ellie Buenning, Kolade Adebowale, Brian Tackett, and Jack Davis. I'd

also like to thank all past and current members of our community whom I'm proud to call my friends, especially: Dr. Zack Whiteman, Dr. Lizzy Mahoney, Dr. Yannick Kimmel, Dr. Marc Porosoff, Dr. Glen O'Neill, Hakhamanesh Mostafavi, Matt Conway, Maxim Stonor, Alison Fankhauser, and Weiming Wan.

Next, I'd like to thank my old lab at Drexel University for starting my research career off in the right direction. In particular, thank you to Professor E. Caglan Kumbur for your countless guidance and support. Thank you to my old lab mates and colleagues for your friendship and support: Dr. Christopher Dennison, Dr. Ertan Agar, Dr. Eric Wargo, Dr. Reyhan Taspinar, Gang Qui, and Arvind Kalidindi.

Lastly, I'd like to thank all of my friends and family who have kept me sane during my Ph.D. Thank you to the friends I met in New York: Steven Melanson, Dustin Brewer, Kevin Kleinguetl, Erin Jacklin, Matt Tibaldi, Jasmine Elsayed, Diana Oakes, Mike Lamprecht, Ryan Taylor, Genna McCabe, Jen Lande, Angel Chan, and Kirsten Kim. Thank you to the BMEs for helping me un-wind with your shenanigans, especially: Milos Spasic, Samuel Robinson, Emily Moore, Andrea Morrell, Matthew Downs, Eben Estell, and Jen Hoi. Thank you to the friends I met in Philadelphia and the MHFBBL for keeping me grounded: Alex Wands, Sean McDonald, Kevin Wiley, Gerry Wosewick, Vinny Greco, Craig Hollish, Michael Loftus, Michael Thorley, and Steve Squibb. Thank you to my high school friends, Mike Kraft and Rob Schultz, for your friendship over these years. Finally, I'd like to give a huge thank you to my family. To my siblings, Brian and Sarah (and Mitch), thank you for always being there for me. To my parents, George and Elaine, thank you most of all for nurturing and loving me into the person I have become. Last, but not least, thank you to Natalie Labrador for the countless love, support, and laughs you provide every day.

CHAPTER 1

INTRODUCTION

1.1. Batteries and Energy Storage

Batteries are arguably the most well-known electrochemical technologies used by our society. They are responsible for powering both high-end consumer electronics (*e.g.,* smart phones, laptop computers, tablets, and power tools) and low-end devices (*e.g.,* remote controls, calculators, and watches). In addition, larger battery systems are used as uninterruptible power supplies for emergency, no-fail applications and are prevalent in the transportation sector as starters for all-gasoline vehicles [1, 2]. As our society continues to grow and mature, a new generation of batteries is required to meet a new generation of energy storage challenges, especially those related to the looming global energy crisis. In recent years, "next-generation" batteries have shown significant potential as efficient, cost-effective energy storage devices for several important applications, including: storing energy from intermittent renewable sources (*i.e.*, wind and solar), powering electric and hybrid-electric vehicles, and providing back-up power for important infrastructure such as telecommunication equipment [3-5].

1.2. Battery Operation

A schematic of a generic battery cell is shown in Figure 1.1. A battery cell typically contains a positive and a negative electrode, which are immersed in a liquid electrolyte and are spatially divided by a separator. The electrodes are often metal or metal-composites which store and release energy through reactions with the electrolyte. The separator is a porous, electronic insulator and its role is to prevent electrical contact between the electrodes in the cell while simultaneously allowing for the transfer of ions between the electrodes. To form a battery cell,

these components are tightly sandwiched between two current collectors that provide electrical connection to an external circuit [6].

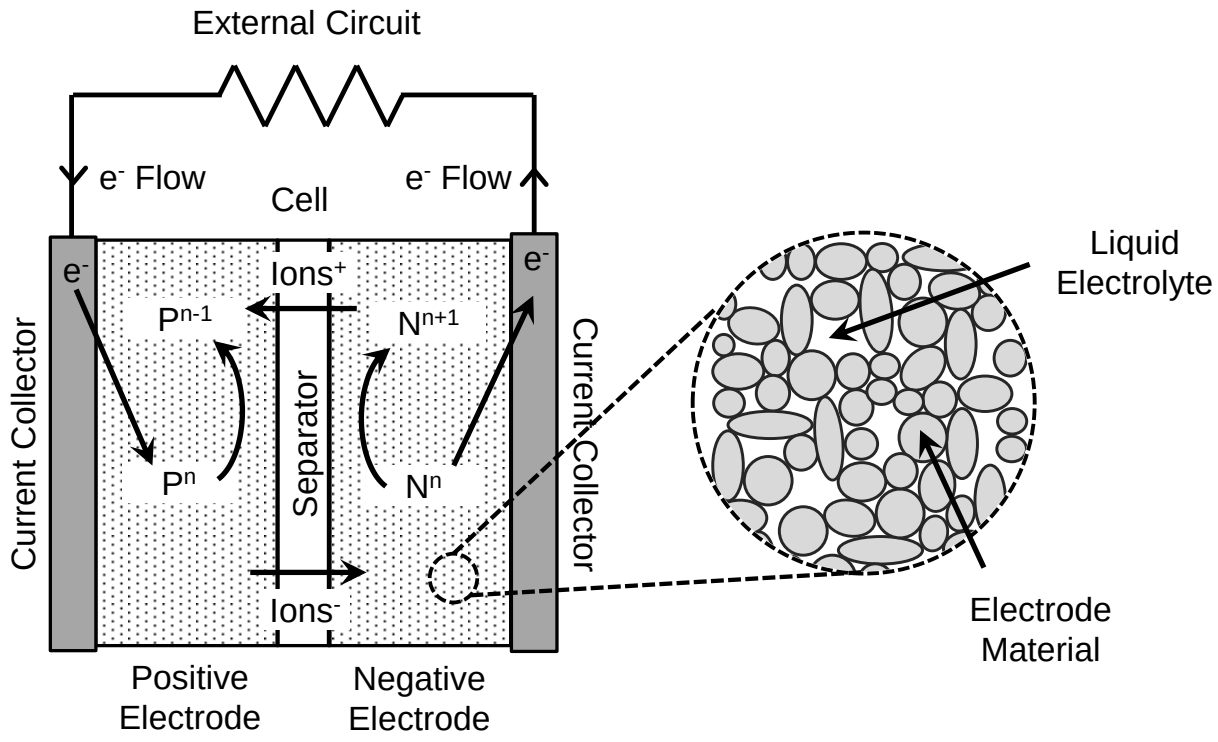

Figure 1.1. Operation of a battery cell during discharge

Figure 1.1 also depicts the discharge process for a generic battery cell, where it is assumed the positive electrode is composed of some metal, *P*, and the negative electrode of some metal, *N*. Upon discharge, an electrical connection is made between the current collectors, which results in spontaneous electrochemical reactions. The negative electrode acts as an anode and is oxidized, releasing an electron into the current collector. This electron flows through the external circuit to the positive electrode (cathode) where it is used to complete a reduction reaction. Useful work is obtained from the electrons flowing between the two electrodes across the external circuit. In addition to the electron flow, there is a continual exchange of ions between

the negative and positive electrode, which occurs through the liquid electrolyte and across the separator. The ions are necessary to maintain electro-neutrality in the cell and are often used to complete the electrochemical reactions.

During charging of a battery cell, an external power supply is used to apply work into the system, which causes all of the electrochemical processes in Figure 1.1 to progress in the reverse (non-spontaneous) direction. The work is applied in the form of excess voltage, which is used to overcome the energetic penalties associated with reversing the reactions.

1.3. Battery Performance

The power released by a battery cell is determined by the voltage between the electrodes and the current flowing through the external circuit, which is controlled by the rates of the electrochemical reactions. The power is calculated as follows:

$$P = I \times V \tag{1.1}$$

The total amount of energy released by a battery cell is determined by integrating the power over time:

$$E = \int_0^t I(t)V(t)dt \tag{1.2}$$

The integration is necessary because, depending on the way the battery is discharged (*e.g.*, constant load, constant current, or constant voltage), both the current and/or the voltage can fluctuate with time.

At rest (*i.e.*, no current flowing through the external circuit), the voltage of a battery cell corresponds to the difference between the chemical potentials of the positive and negative electrodes. This is often referred to as the open circuit potential. Upon discharge, the voltage of

the cell deviates from the open circuit potential due to losses associated with the electrochemical processes. Conceptually, this voltage can be represented as follows:

$$V_{discharge} = U - \eta_{ohm} - \eta_s - \eta_c \tag{1.3}$$

where U is the open circuit potential and η_{ohm} is the voltage loss due to ohmic resistances associated with the flow of electrons and ions. η_s is the voltage loss due to surface overpotentials associated with the reactions happening at the positive and negative electrodes. η_c is the concentration overpotential, which accounts for deviations from ideal behavior due to unfavorable distributions of reactants and products in the cell (*e.g.* failure of reactants to quickly diffuse to the reaction sites at the surface of the electrodes). During charging, the voltage in the cell can be represented in a manner similar to Eq. 1.3, but now the voltage losses are added to the open circuit potential:

$$V_{charge} = U + \eta_{ohm} + \eta_s + \eta_c \tag{1.4}$$

The extent of the voltage losses in Equations 1.3 and 1.4 is proportional to the current flowing through the cell. Higher currents correspond to higher voltage losses due to increases in the energetic penalties associated with maintaining high reaction rates and current flow. However, high current also corresponds to higher power (see Eq. 1.1). This indicates that maximizing the power of a battery cell during discharge is an optimization problem, where the current should be high enough to increase the power, but not so high that voltage losses become too great. A similar tradeoff is observed during charging, where using high currents is important for rapid charging of batteries.

1.4. Electrode Design

When developing a battery cell, the various components (*i.e.,* electrodes, electrolyte, separator, and current collectors) must be designed to achieve three main objectives: *i)* accomplish their designated roles during operation of the cell, *ii)* minimize voltage losses while completing their roles, and *iii)* meet design specifications associated with the battery's application (*e.g.*, cost, lifetime, safety, size and weight). Sometimes, these three objectives are interrelated, and satisfying one objective will satisfy all three. More often, designing and developing a component to meet one objective may negatively impact another, especially when attempting to meet multiple design specifications. Therefore, when developing the next generation of batteries, researchers must know how to tailor the components to achieve all three objectives as best as possible. To accomplish this, one must understand the tradeoffs and challenges associated with component development and design.

Proper design of the battery electrodes is crucial to optimizing battery performance due to their role in facilitating the electrochemical reactions. One of the major challenges when developing an electrode is guaranteeing full utilization of the material. For instance, in order for the electrode material to undergo an electrochemical reaction, the reaction sites must be accessible to both ions and electrons. Failure to accomplish this makes portions of the electrode material electrochemically inactive, which increases the size, weight, and cost of the battery. To facilitate ion transport, the electrodes must be designed with porous structures that allow for complete wetting of the electrode material by the liquid electrolyte. This is often obtained by fabricating the electrodes from small particles of material (mm to nm in size), which are compressed together to give the electrodes a structure resembling soil or sand [7, 8]. To facilitate electron transport, the electrode materials must be good electronic conductors. For some next-

generation electrodes, the materials which undergo the electrochemical reactions are actually poor electronic conductors [9, 10]. In these cases, the poor electronic conductivity is overcome by blending particles of the electrochemically active material with particles of a highly-conductive, electrochemically-inactive material. This blend of particles is then used to fabricate electrodes with the desired properties.

Another challenge when developing an electrode is reducing the surface overpotential associated with the electrochemical reactions. Reducing the surface overpotential decreases the voltage losses which increases the efficiency, power density, and energy density of the cell. All of these factors help to reduce the size, weight, and cost of the battery. The easiest way to reduce the surface overpotential is by developing electrochemically-active materials with inherently facile kinetics. However, some novel battery systems employ active materials with relatively poor kinetics because the materials satisfy other important specifications like low cost and light weight. To overcome the kinetics limitations, electrodes can be designed with high surface area. This is often done by reducing the particle size of the active material in the electrodes (often down to the nanoscale) [11, 12].

The development of materials with good inherent properties is another important part of electrode design. For instance, the electrochemical performance of a material and the amount of that material needed to meet design specifications (*i.e.* energy and power requirements) are inversely proportional, with better performance corresponding to less material. Good electronic conductivity and facile kinetics have already been identified as important properties for improving the size, weight, and cost of batteries. Further improvements can be obtained by developing negative and positive electrode materials which produce a large open circuit potential (*i.e.*, a large cell voltage) [13]. Materials should also be developed with large inherent capacities

(C cm^{-3} or C g^{-1}), which maximize the amount of charge stored per a given quantity of material. In addition, lifetime and safety are other important design specifications. These specifications can be obtained by developing electrode materials which are stable in the liquid electrolytes.

1.5. Optimizing Electrode Performance

No matter the material or the design, to some extent, all battery electrodes will suffer from the voltage losses described in Section 1.3. A major challenge in the battery field is developing strategies to mitigate these losses in both emerging and existing battery technologies. Accomplishing this requires a three step approach (see Figure 1.2). First, the main processes limiting the overall performance must be identified (*i.e.*, ionic transport, electronic transport, reaction kinetics, or inherent physical properties of the material). Second, the main performance-limiting processes must be characterized to understand the underlying mechanisms responsible for the poor performance. Finally, strategies must be developed which target the underlying mechanisms and mitigate the voltage losses. Due to the multidisciplinary nature of batteries, this three-step process is often accomplished collectively within the battery field using input from synthetic chemists, materials scientists, and electrochemical engineers (to name a few).

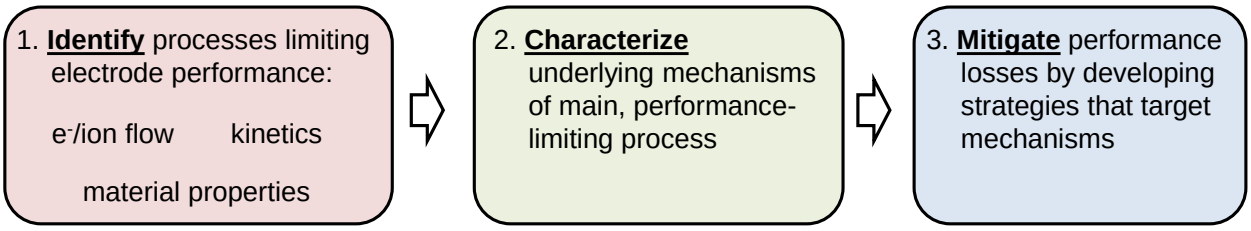

Figure 1.2. Research methodology used to optimize the performance of battery electrodes.

1.6. Thesis Overview

In this thesis, three studies are presented which highlight the role of electrochemical engineers in alleviating the performance limiting processes in battery electrodes. Each study is focused on a different step of the process outlined in Figure 1.2 (*i.e.*, identification, characterization, and mitigation) and analyzes an electrode from a different battery system. The remainder of this section provides a brief description of each study. Further details can be found in individual chapters, including more specific background information, experimental details, and model formulations.

1.6.1. Identification of the Processes Limiting Capacity in Lithium-Magnetite Electrodes

Lithium-ion batteries are by far the most widely used battery systems in our society. They are responsible for powering cells phones, laptops, cameras, tablets, electric vehicles and more. Part of the success of lithium-ion batteries can be attributed to their high efficiency and long cycle life. Both of these characteristics arise from the use of electrode materials which undergo electrochemical, intercalation reactions. Intercalation is the reversible insertion of a molecule into the crystalline lattice of a host material (see Figure 1.3). The process is highly efficient because it does not require breaking and reforming of the chemical bonds between the atoms of the host material. Instead, the intercalation process only causes the host material to expand and contract upon insertion and removal of the molecules. Intercalation reactions have relatively low kinetic overpotentials, which is one of the main reasons for the high efficiency of lithium ion batteries (>95% energy efficiency). In addition, the lack of bond breaking in the host material prevents rapid degradation, which gives the batteries a high cycle life (upwards of 10,000 cycles) [13, 14].

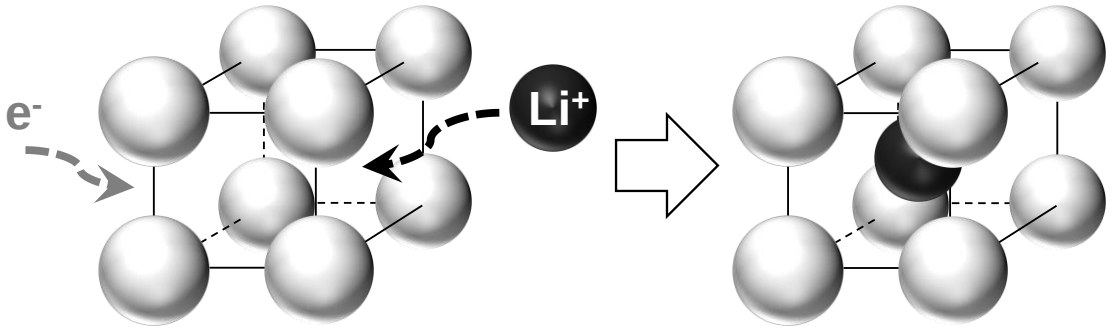

Figure 1.3. Schematic of the electrochemical intercalation of a lithium-ion into a host material

Both electrodes in a lithium-ion battery cell undergo intercalation reactions. The cell is charged and discharged by moving lithium from one electrode to the other. During charge/discharge cycling, lithium is continuously moving back and forth between the electrodes; hence, these batteries are commonly referred to as "rocking-chair" batteries. The reactions are given as:

$$\mathrm{Li^+ + e^- + \Gamma_N} \underset{\text{discharge}}{\overset{\text{charge}}{\rightleftharpoons}} \mathrm{Li\Gamma_N} \qquad \text{(Negative)} \qquad (1.5)$$

$$\mathrm{Li\Gamma_P} \underset{\text{discharge}}{\overset{\text{charge}}{\rightleftharpoons}} \mathrm{Li^+ + e^- + \Gamma_P} \qquad \text{(Positive)} \qquad (1.6)$$

where Γ and LiΓ refer to open and occupied insertion sites in the host material, respectively. The subscripts 'N' and 'P' denote the negative and positive electrodes, respectively.

A key to the success of lithium-ion batteries is the development of host materials that are lightweight, inexpensive, and have high intrinsic capacities (*i.e.*, dense quantities of insertion sites). Recently, considerable research efforts have focused on the advancement of magnetite (Fe_3O_4) as an electrode in lithium-ion batteries due to its high theoretical capacity (926 mAh g^{-1}),

low cost and safety (non-toxic) [15-20]. Despite these advantages, one of the major challenges limiting the advancement of magnetite electrodes is a considerable difference between the maximum, theoretical capacity and the observed, experimental capacity of the active material. One reason for the differences in capacity is the close-packed inverse spinel structure of Fe_3O_4, which restricts the transport of lithium in the material. The slow transport prevents lithium from penetrating deep within the host material, which prevents the full utilization of the electrode material. To address this issue, several authors have synthesized Fe_3O_4 nano-crystallites in attempts to minimize the path length for ion transport. Electrodes fabricated with nano-crystalline magnetite have shown significant improvement in capacity; however, the theoretical capacity has still proven difficult to obtain, especially during cycling [15, 16].

To address this issue, Chapters 2 to 4 of this thesis focus on identifying the processes limiting the capacity in nanocomposite lithium-magnetite electrodes. In Chapter 2, a combined experimental and modeling approach is used to identify which mass transport processes are limiting the performance of the electrodes: *i)* transport of lithium ions through the bulk electrolyte, *ii)* transport of lithium ions between agglomerated nano-crystals, and/or *iii)* transport of solid-state lithium within the crystals. Based on the results of the experimental study, a multi-scale mathematical model is developed and validated against electrodes comprised of small (6 nm) crystals. The model is able to simulate the performance of a battery electrode by coupling mass transport on the agglomerate and crystal length-scales with thermodynamic and kinetic expressions for the electrochemical reactions. In Chapter 3, the multi-scale mathematical model is further utilized to explore the mass transport limiting processes in electrodes comprised of 6, 8, and 32 nm crystals. In particular, the model is used to identify the impact of mass transport limitations in the agglomerate and crystal length-scales. Finally, in Chapter 4, the multi-scale

model is expanded to study the phase change occurring within magnetite during lithiation. Phase change is an unavoidable consequence of the large capacity of magnetite. At high levels of lithiation, the bonds between the atoms in the host material begin to break and rearrange into different structures. Understanding the impact of phase change on electrode performance is crucial to further advancement of Fe_3O_4 as a lithium-ion host material.

1.6.2. Characterization of Film Formation in Lead-Acid Batteries

Lead-acid batteries have been a major part of the economy for over 100 years. Recently, they have seen significant use in next-generation stand-alone and automotive applications due to their high energy efficiency (75 to 80%), low cost (200 to 400 $/kWh), and the existence of a strong manufacturing and recycling infrastructure [21, 22]. For example, recycling efforts are able to recover up to 96% of the Pb from spent batteries [23]. The lead-acid battery contains two lead-based electrodes separated by a liquid sulfuric acid (H_2SO_4) electrolyte. During cycling, the following reactions occur:

$$Pb + SO_4^- \underset{\text{charge}}{\overset{\text{discharge}}{\rightleftharpoons}} PbSO_4 + 2e^- \quad \text{(Negative)} \qquad (1)$$

$$PbO_2 + SO_4^{2-} + 4H^+ + 2e^- \underset{\text{charge}}{\overset{\text{discharge}}{\rightleftharpoons}} PbSO_4 + 2H_2O \quad \text{(Positive)} \qquad (2)$$

Both electrodes are coated by a lead sulfate ($PbSO_4$) film during discharge, which is dissolved during charge. The performance, capacity, and life-time of the battery is greatly affected by the formation, growth, and resulting structure of these salt films [24]. For instance, one of the major issues reducing the lifetime of lead-acid batteries in high-rate, partial state-of-charge applications (*i.e.*, electric vehicles) is the progressive sulfation of the negative electrode, whereby the $PbSO_4$

becomes irreversible and cannot be fully converted back into Pb after a sufficient charge. Over time, the unreacted $PbSO_4$ builds-up as a film on the Pb surface (see Figure 1.4), which blocks available reaction sites and increases the voltage losses due to kinetic and concentration overpotentials [25].

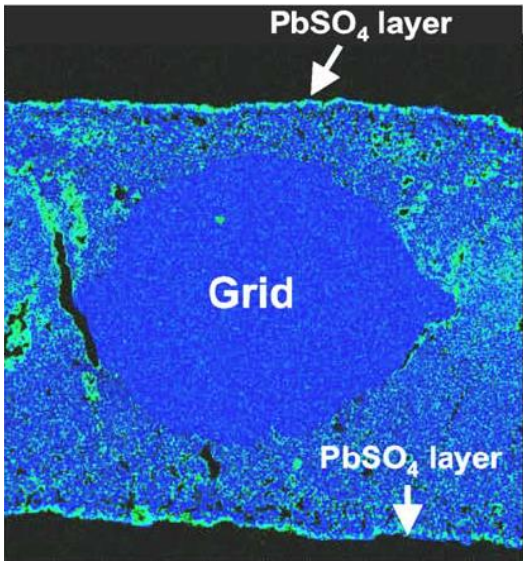

Figure 1.4. Presence of $PbSO_4$ salt film at failure of lead-acid battery [25].

Despite the importance of the $PbSO_4$ films on the performance of the electrode, there is a lack of understanding on the mechanisms of film formation and the resulting microstructure. To address this issue, Chapters 5 and 6 present a study aimed at characterizing the formation of $PbSO_4$ films on Pb using an advanced, in situ, synchrotron technique (*i.e.*, transmission X-ray microscopy). The technique is used to study, in real time, the formation and dissolution of $PbSO_4$ films on Pb under normal operating conditions. Chapter 5 gives an in-depth description of the experimental technique and provides results on the formation and dissolution of the film in H_2SO_4. Chapter 6 expands this work by studying how the film growth is impacted by the inclusion of a common chemical additive into the H_2SO_4 solution.

1.6.3. Mitigation of Ohmic Losses during Pulse Power Operation of Electrodes

The ability to deliver high power pulses at all depths of discharge is an important requirement of a battery, especially for transportation applications [5, 26]. Nevertheless, high power is often difficult to achieve at high depths of discharge (DoD) because of an increase in the ohmic resistance. The ohmic resistance increases due to the movement of the reaction fronts within the electrodes from more favorable (less resistive) to less favorable (more resistive) locations [27, 28]. For instance, this behavior has been documented in the positive electrode of sodium metal-halide batteries, where the low resistivity of the electrode (nickel and/or iron) and the higher resistivity of the liquid electrolyte (sodium tetrachloroaluminate) cause the reaction front to move from the separator to the current collector during discharge [29, 30]. At high DoD, the reaction front is far from the separator and the ionic path length is increased, which increases the ohmic resistance in the electrode.

One strategy for mitigating this resistance and improving the pulse-power performance is to add a second electrochemically active material to the electrode, which only reacts at high DoD. At low DoD, only the first active material reacts, and the reaction front associated with this material moves from the separator to the current collector while the second active material remains evenly distributed throughout the electrode. When the electrode is pulsed at high DoD, the high ohmic losses are avoided by reacting the second material close to the separator instead of the first material deep within the electrode.

This concept has already been used to improve the pulse-power performance of the positive electrode in sodium metal-halide batteries [30, 31]. However, the conclusions were based entirely off of data from commercial cells with no attempts to analyze this concept

quantitatively. Therefore, the objective of Chapter 7 is to explore conditions and designs when this concept is viable and if it may be applicable to other battery electrodes. To accomplish this, a generic model is developed based on porous electrode theory. The model is used to conduct two case studies on the positive electrode of a sodium metal-halide battery and the negative electrode of a lithium-ion battery. In both cases, the analysis demonstrates how the addition of a second electrochemically active material can mitigate ohmic losses in the battery and improve pulse-power at high DoD.

1.7. References

1. H. Ibrahim, A. Ilinca and J. Perron, *Renew. Sust. Energ. Rev.*, **12**, 1221 (2008).
2. K. C. Divya and J. Ostergaard, *Electr. Power Syst. Res.*, **79**, 511 (2009).
3. Z. G. Yang, J. L. Zhang, M. C. W. Kintner-Meyer, X. C. Lu, D. W. Choi, J. P. Lemmon and J. Liu, *Chem. Rev.*, **111**, 3577 (2011).
4. *Electricity Energy Storage Technology Options: A White Paper Primer on Applications, Costs, and Benefits*, EPRI, Palo Alto, CA, 1020676 (2010).
5. *U.S. Department of Energy Vehicle Technologies Program: Battery Test Manual for Electric Vehicles*, United States Department of Energy, Office of Energy Efficiency and Renewable Energy, Vehicle Technologies Office, INL/EXT-15-34184 (2015).
6. D. Linden and T. B. Reddy, *Handbook of batteries*, McGraw-Hill, New York (2002).
7. C. Delacourt, P. Poizot, S. Levasseur and C. Masquelier, *Electrochem. Solid-State Lett.*, **9**, A352 (2006).
8. M. Wagemaker, W. J. H. Borghols and F. M. Mulder, *J. Am. Chem. Soc.*, **129**, 4323 (2007).
9. M. S. Whittingham, *Proc. IEEE*, **100**, 1518 (2012).
10. C. H. Dustmann, *J. Power Sources*, **127**, 85 (2004).
11. P. G. Bruce, B. Scrosati and J. M. Tarascon, *Angew. Chem. Int. Edit.*, **47**, 2930 (2008).
12. A. S. Aricò, P. Bruce, B. Scrosati, J.-M. Tarascon and W. van Schalkwijk, *Nat. Mater.*, **4**, 366 (2005).
13. H. S. Chen, T. N. Cong, W. Yang, C. Q. Tan, Y. L. Li and Y. L. Ding, *Prog. Nat. Sci.*, **19**, 291 (2009).
14. M. S. Whittingham, *Chem Rev*, **104**, 4271 (2004).
15. S. L. Zhu, A. C. Marschilok, E. S. Takeuchi, G. T. Yee, G. B. Wang and K. J. Takeuchi, *J. Electrochem. Soc.*, **157**, A1158 (2010).
16. S. L. Zhu, A. C. Marschilok, E. S. Takeuchi and K. J. Takeuchi, *Electrochem. Solid-State Lett.*, **12**, A91 (2009).
17. M. C. Menard, K. J. Takeuchi, A. C. Marschilok and E. S. Takeuchi, *Phys. Chem. Chem. Phys.*, **15**, 18539 (2013).

18. M. C. Menard, A. C. Marschilok, K. J. Takeuchi and E. S. Takeuchi, *Electrochim. Acta*, **94**, 320 (2013).
19. S. Komaba, T. Mikumo, N. Yabuuchi, A. Ogata, H. Yoshida and Y. Yamada, *J. Electrochem. Soc.*, **157**, A60 (2010).
20. S. Komaba, T. Mikumo and A. Ogata, *Electrochem. Commun.*, **10**, 1276 (2008).
21. A. J. Salkind, A. G. Cannone and F. A. Trumbure, in *Handbook of Batteries*, 3rd ed., D. Linden and T. B. Reddy, Editors, p. 23.1, McGraw-Hill, New York (2002).
22. K. Bradbury, L. Pratson and D. Patino-Echeverri, *Appl Energ*, **114**, 512 (2014).
23. P. T. Moseley and D. A. J. Rand, in *Valve-Regulated Lead-Acid Batteries*, D. A. J. Rand, P. T. Moseley, J. Garche and C. D. Parker, Editors, p. 1, Elsevier B. V., The Netherlands (2004).
24. P. Ruetschi, *J Power Sources*, **127**, 33 (2004).
25. L. T. Lam, N. P. Haigh, C. G. Phyland and A. J. Urban, *J Power Sources*, **133**, 126 (2004).
26. *Battery Requirements for Plug-in Hybrid Electric Vehicles - Analysis and Rationale*, National Renewable Energy Laboratory, NREL/CP-540-42240 (2009).
27. M. Doyle, J. Newman, A. S. Gozdz, C. N. Schmutz and J. M. Tarascon, *J. Electrochem. Soc.*, **143**, 1890 (1996).
28. M. Doyle, T. F. Fuller and J. Newman, *J. Electrochem. Soc.*, **140**, 1526 (1993).
29. J. Rijssenbeek, Y. Gao, Z. Zhong, M. Croft, N. Jisrawi, A. Ignatov and T. Tsakalakos, *J. Power Sources*, **196**, 2332 (2011).
30. J. L. Sudworth, *J. Power Sources*, **100**, 149 (2001).
31. R. C. Galloway and S. Haslam, *J. Power Sources*, **80**, 164 (1999).

CHAPTER 2

MESOSCALE TRANSPORT IN MAGNETITE ELECTRODES FOR LITHIUM-ION BATTERIES: ANALYSIS OF VOLTAGE RELAXATION TIMES AND MODEL FORMULATION

This chapter provides the groundwork for the next three chapters, whose aim is to identify the performance limiting processes in lithium-magnetite electrodes. In this chapter, the mass transport processes occurring within magnetite electrodes during lithiation and voltage recovery are investigated using a combined experimental and modeling approach. Voltage recovery data are analyzed through a comparison of the mass transport time-constants associated with different length-scales within the electrode. Based on this analysis, a multi-scale mathematical model is developed, which incorporates an agglomerate and a crystallite length-scale. In Chapter 3, the multi-scale model is used to determine, which length-scale, agglomerate or crystallite, is responsible for the low utilization of the active material. In Chapter 4, the model is further expanded to analyze the phase changes occurring within the electrodes during lithiation and voltage recovery experiments.

2.1. Introduction

In recent years, magnetite (Fe_3O_4) has shown promise as a lithium-ion electrode material due to its low cost, safety (non-toxic), and high theoretical capacity (926 mAh/g). The high theoretical capacity results from the close-packing, inverse spinel structure of the material. One problem of this material is that the close-packing structure also hinders rapid ion transfer, which causes the experimental capacity to deviate significantly from the theoretical value. To address

this issue, several authors have synthesized Fe_3O_4 nano-crystallites in attempts to minimize the path length for ion transport [1-6]. The smaller path length increases the capacity at higher discharge currents by increasing the utilization of the active material. For example, Zhu et. al. have previously reported that magnetite electrodes with crystallite sizes of 6-10 nm exhibit a 30% increase in delivered capacity [2-3].

In addition to the size of the Fe_3O_4 crystallites, the size of agglomerates of the active material can have a large effect on electrochemical behavior [7-8]. The influence of agglomerates makes it difficult to directly interpret the impact of crystallite size using electrochemical data. One approach to understand the coupled behavior of agglomerates and crystals is through the development of a mathematical model that can predict the electrochemical performance while simultaneously allowing for the decoupling of the two length-scales (agglomerate and crystal). To date, the development of such a model has been challenging due to a lack of understanding of the mesoscale (atoms to μm) transport processes occurring within battery electrodes.

In this study, the electrochemical behavior of Fe_3O_4 is investigated using a combined experimental and analytical approach. In particular, the voltage recovery of the material is used to analyze the mass transport occurring within the electrode on the mesoscale. The results of this analysis are used to develop a multi-scale mathematical model, which incorporates the agglomerate and crystal length-scales and can predict the performance of the Fe_3O_4 electrodes during discharge and voltage recovery.

2.2. Experimental

2.2.1. Experimental Set-up

All experimental work in this chapter was conducted by collaborators at Stony Brook University and Brookhaven National Laboratory. Nanocrystalline magnetite (6 and 8 nm), Fe_3O_4, was synthesized using a co-precipitation approach, utilizing aqueous solutions of iron (III) chloride hexahydrate, iron (II) chloride hexahydrate, and base according to a previously reported method [2, 3]. Larger sized nanocrystalline magnetite, ~32 nm, was purchased from Alfa Aesar. X-ray diffraction data was collected using a Rigaku Smart Lab diffractometer with Cu Kα radiation. The crystallite sizes of the Fe_3O_4 powders were calculated by applying the Scherrer equation to the FWHM of the (311) peak. An instrumental broadening correction was applied using a LaB_6 standard.

Electrodes were prepared using magnetite, carbon, and polyvinylidene fluoride binder coated onto an aluminum foil substrate. Electrochemical tests were performed using two electrode coin-type experimental cells with lithium metal anodes and 1M $LiPF_6$ in dimethyl carbonate:ethylene carbonate electrolyte. The electrodes were comprised by weight of 90% Fe_3O_4, 5% acetylene carbon black, and 5% PVDF. Discharge was conducted with no preconditioning under a C/200 rate to 0.5, 1.0, 1.5, 2.0 and 2.5 electron equivalents per Fe_3O_4 and then allowed to rest under open circuit conditions for up to 30 days. A total of 15 coin-cells were used, one for each depth of discharge and each crystal size (6, 8, and 32 nm). Good agreement was observed between the discharge curves for cells comprised of the same crystal size. The cells had a thickness of 51±4 μm and an active mass loading of 4.2±0.3 mg cm^{-2}. All electrochemical testing was conducted at 30°C.

Cross sectional TEM images of the Fe_3O_4 electrodes were acquired by embedding the samples in an epoxy resin. A Reichert-Jung UltracutE ultramicrotome was used to slice 80 nm sections of the embedded electrodes for TEM analysis. Sections were viewed with a FEI Tecnai12 BioTwinG^2 transmission electron microscope. Digital images were acquired with an AMT XR-60 CCD Digital Camera system. The public domain Java image processing program Image J was used to determine the size and agglomerate distributions from the TEM cross sectional images [9].

2.2.2. Experimental Results and Discussion

2.2.2.1. Discharge and Relaxation

Figure 2.1a shows the results of the discharge and voltage recovery experiments for the 6, 8 and 32 nm diameter crystals. Each crystal size consists of 5 overlaid curves, one for each depth of discharge. The vertical lines correspond to the recovery portions of the experiments. In this work, the maximum values of the vertical lines represent the equilibrium potential at each depth of discharge. For the three crystal sizes, there is good agreement between the maximum values of the vertical lines. This suggests the equilibrium potential at each depth of discharge is a material property that is independent of crystal size. Therefore, the variations in the discharge curves of the different crystal sizes are not due to thermodynamic differences. The variations likely result from transport (mass and charge) and kinetic effects.

In Figure 2.1b, the voltage recovery portions of the 6 nm experiments are shown. For all five depths of discharge, the voltage starts to approach a steady value between 200 and 700 hours after the current is interrupted. These long recovery times could be associated with a slow phase transition occurring within the material. However, this is unlikely because the phase transition of

magnetite from an inverse cubic spinel ($Li_xFe_3O_4$) to a rock-salt like phase ($LiFeO_2$) does not occur until between x = 2.8 and x = 4.0 (for x in $Li_xFe_3O_4$) [1]. Instead, these long times are likely caused by the slow relaxation of concentration profiles to a uniform value. This assumption provides the basis for determining mass transport parameters in solids (i.e., diffusion coefficients) using the galvanostatic intermittent titration technique (GITT) [10, 11].

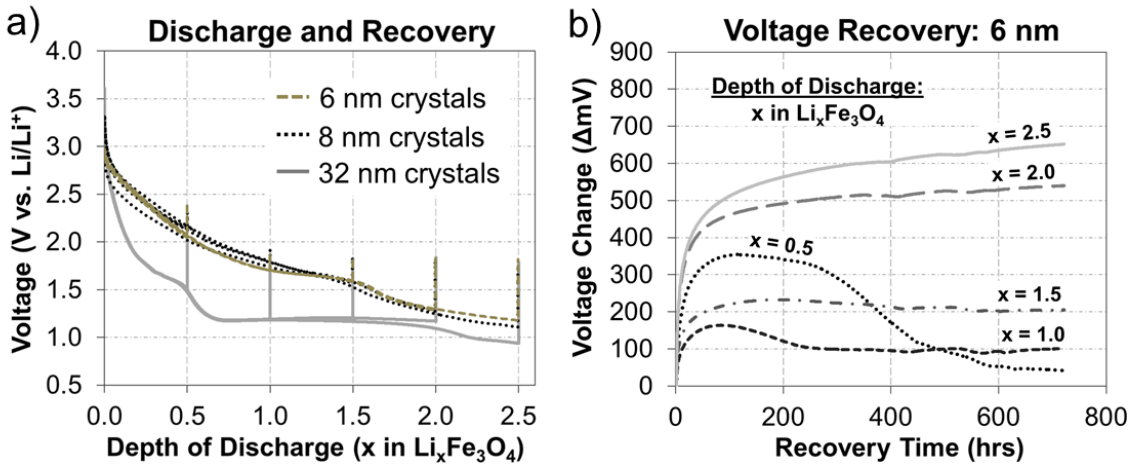

Figure 2.1. a) Discharge and voltage recovery data for Fe_3O_4 electrodes used in voltage recovery experiments. Each crystal size consists of 5 overlaid curves. b) Voltage recovery experiments for crystals with an average diameter of 6 nm.

Accurately determining mass transport parameters from voltage recovery data using a technique like GITT requires an understanding of the structure of the electrode material. For instance, Fig. 2.2 shows TEM micrographs of a magnetite electrode, where the dark contrast is magnetite and the light contrast is carbon black and polymer binder. The micrographs show the existence of large agglomerates (on the order of 5 μm in diameter) formed by groups of 32 nm crystals. The presence of these agglomerates suggests that mass transport within the system may

occur across three length-scales: the bulk electrode, the agglomerate, and the crystal scales. An understanding of the time constants associated with concentration relaxation on each length-scale is required to identify which feature(s) of the electrode are responsible for the long voltage recovery times.

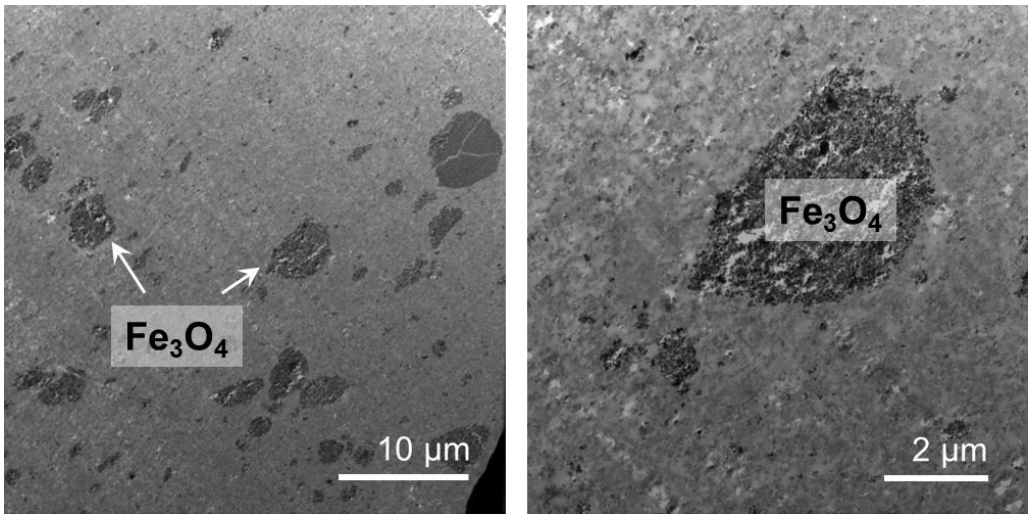

Figure 2.2. Transmission electron micrographs of the cross-section of a magnetite electrode composed of Fe_3O_4 (dark contrast), carbon, and PVDF binder. Fe_3O_4 nano-crystals have an average diameter of 32 nm.

2.2.2.2. Time Constant Analysis

A comparison of the concentration relaxation times associated with each length-scale can be accomplished using the mass transport time-constant, τ, which characterizes the time required for the concentration in the system to relax after a step change in concentration at one boundary. This time-constant is defined as follows:

$$\tau = \frac{\ell^2}{D} \tag{2.1}$$

where ℓ is the characteristic length and D is the mass transfer diffusion coefficient. The values of these parameters for typical lithium-ion electrode materials are given in Table 2.1. For the magnetite material used in this work, the bulk electrode has a thickness of ~50 μm, which (using the diffusion coefficients in Table 2.1) corresponds to a time-constant between 2.5 and 25 seconds. This time constant is too small to explain the voltage recovery times observed in Figure 2.1b and suggests that mass transport on the agglomerate and/or crystal scales are dominant.

Table 2.1. Sizes and diffusion coefficients for typical lithium-ion electrode materials.

	Characteristic Length	**Diffusion Coefficient (cm^2 s^{-1})**
Bulk Electrode (thickness)	10 μm – 1 cm	10^{-5} to 10^{-6} (12)
Agglomerate (radius)	100 nm – 10 μm	–
Nano-Crystal (radius)	1 nm – 100 nm	10^{-8} to 10^{-18} (12)

To determine which length scale (agglomerate or crystal) is dominant, a direct comparison of their time constants was conducted. The results of this comparison are provided in Figure 2.3, which shows how the ratio between the time constants varies due to changes in the ratios of the characteristic lengths and diffusion coefficients. In the figure, the subscript x refers to the crystal length scale. The shaded areas were calculated using the values given in Table 2.1. For these calculations, it was assumed the diffusion coefficient of the agglomerate spans both the crystal and bulk values. The shaded areas are sectioned to indicate when the mass transport on the agglomerate, crystal, or both length scales are expected to control the recovery time. The dashed box corresponds to the time-constant ratios expected from the magnetite electrodes used in the present experiments. The ratios of the radii were determined from TEM images, with the radii of the agglomerates ranging from 500 nm to 15 μm and the radii of the crystals ranging

from 3 to 16 nm. Due to a lack of experimental data available in the literature for the diffusion of Li^+ in magnetite crystals and agglomerates, the diffusion coefficients were estimated from Eq. 2.1 using τ = 400 hrs (from Fig. 2.1b) and the radii from the TEM images as the characteristic lengths. The resulting diffusion coefficients ranged from 10^{-12} to 10^{-15} cm^2 s^{-1} for the agglomerates and 10^{-17} to 10^{-20} cm^2 s^{-1} for the crystals. Both of these ranges were concluded to be physically reasonable for the magnetite material. The location of the dashed box in Fig. 2.3 indicates that the mass transport within the agglomerate and/or crystal length-scales may be responsible for the long voltage relaxation times.

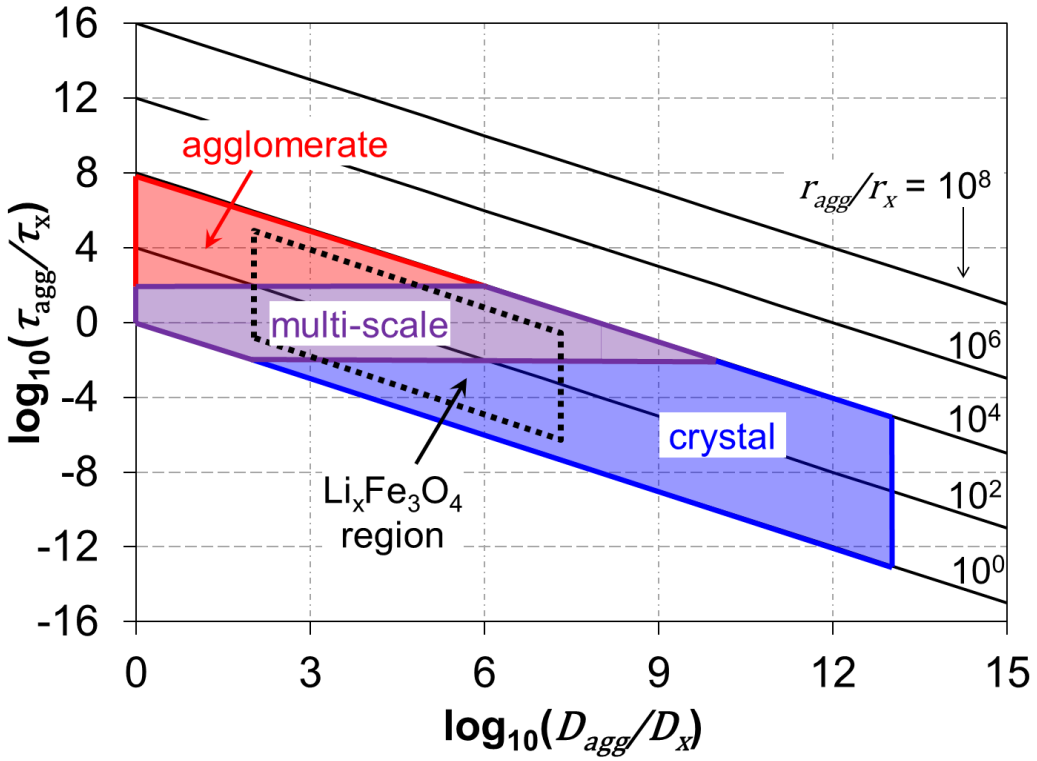

Figure 2.3. Comparison of the mass transport time-constants for the agglomerate and crystal length-scales. The shaded areas were calculated from the values given in Table 2.1. It is assumed the diffusion coefficient of the agglomerate spans both the crystal and bulk values. The three colored areas correspond to regions where mass transport during relaxation is dominated by one,

the other, or both length-scales. The dashed box corresponds to the time-constant ratios expected from the Fe_3O_4 electrodes used in the present experiments.

2.3. Modeling

2.3.1. Model Development

The results of the time-constant analysis in Section 2.2.2.2 suggest that the voltage recovery behavior of the magnetite electrodes may result from mass transport effects on both the agglomerate and crystal length-scales. To further explore this, a multi-scale model has been developed, which consists of the agglomerate and crystal length-scales (Fig. 2.4). The model is constructed based on the following assumptions:

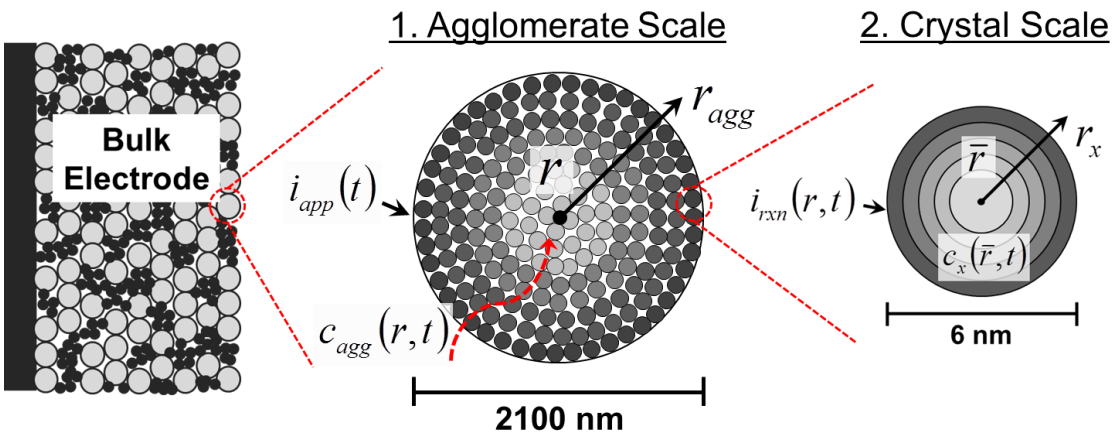

Figure 2.4. Schematic of the agglomerate and crystal length-scales in the model.

1. The system is considered isothermal.
2. The mass and charge transfer properties (i.e., conductivity and diffusion coefficients) are assumed to be isotropic.

3. The impact of intermolecular interactions on species transport is neglected (*i.e.*, dilute solution).
4. Variations in concentration and potential within the bulk electrode are considered negligible.
5. The agglomerates and crystals are assumed to be spherical and have a constant volume.
6. Variations in concentration and potential within the agglomerate and crystal are assumed to occur only in the radial directions.
7. The polarization associated with the lithium-metal negative electrode is considered negligible.

2.3.1.1. Agglomerate Scale Governing Equations

In the agglomerate, the conservation of mass for lithium is defined using the following equation:

$$\varepsilon \frac{\partial c_{agg}}{\partial t} = \varepsilon D_{agg} \frac{\partial^2 c_{agg}}{\partial r^2} + \frac{2\varepsilon D_{agg}}{r} \frac{\partial c_{agg}}{\partial r} + \frac{a i_{rxn}}{F} \tag{2.2}$$

where c_{agg} is the concentration of lithium between the crystals in the agglomerate, D_{agg} is the Li^+ diffusion coefficient within the agglomerate, ε is the porosity, a is the specific surface area, F is Faraday's constant, and i_{rxn} is the local reaction current density. Eq. 2.2 is derived assuming that there is no convection within the pores of the agglomerate and that migration due to spatial variations in electrolyte potential is negligible. The local reaction current density is determined assuming an intercalation reaction of the following form:

$$Li^+ + \Gamma + e^- \leftrightarrow Li\Gamma \tag{2.3}$$

where Γ and $Li\Gamma$ are unoccupied and occupied interstitial sites in the crystal lattice, respectively. From this description, the reaction rate is derived, resulting in the following kinetic expression:

$$i_{rxn} = i_0\left[\exp\left(\frac{\alpha_a F(\varphi_1 - U)}{R_G T}\right) - \exp\left(\frac{-\alpha_c F(\varphi_1 - U)}{R_G T}\right)\right] \tag{2.4}$$

$$i_0 = F k_{rxn} c_{agg}^{\alpha_a} c_x^{\alpha_c} \left(c_{x,\max} - c_x\right)^{\alpha_a} \tag{2.5}$$

In Eq. 2.4, F is Faraday's constant, R_G is the ideal gas constant, T is the temperature and α_a and α_c are the anodic and cathodic charge transfer coefficients, respectively. i_0 is the exchange current density, φ_1 is the potential in the solid phase, and U is the equilibrium potential. The potential in the liquid is used as a point of reference and has been arbitrarily set to zero for convenience. In Eq. 2.5, k_{rxn} is the reaction rate constant, c_x is the concentration of intercalated lithium at the surface of the crystal (LiΓ in Eq. 2.3), and $c_{x,\max}$ is the maximum concentration of lithium within the crystal (i.e., the concentration of Li in $Li_8Fe_3O_4$).

The potential in the solid is assumed to obey Ohm's law, and a conservation of charge relationship gives:

$$a i_{rxn} = (1-\varepsilon)\sigma \nabla^2 \varphi_1 \tag{2.6}$$

where σ is the electronic conductivity of magnetite.

2.3.1.2. Crystal Scale Governing Equations

Within each crystal, the lithium is assumed to diffuse between the interstitial sites of the crystal lattice. The concentration of lithium in the crystal, c_x, is determined from the following mass balance:

$$\frac{\partial c_x}{\partial t} = D_x \frac{\partial^2 c_x}{\partial \bar{r}^2} + \frac{2D_x}{\bar{r}} \frac{\partial c_x}{\partial \bar{r}} \tag{2.7}$$

2.3.1.3. Boundary and Initial Conditions.

For the lithium concentration on the agglomerate scale, the concentration at the agglomerate surface is equal to the bulk electrolyte concentration, and there is zero flux at the center of the agglomerate:

$$c_{agg}\Big|_{r=r_{agg}} = c_0 \tag{2.8}$$

$$\left.\frac{\partial c_{agg}}{\partial r}\right|_{r=0} = 0 \tag{2.9}$$

For the potential, the gradient at the center of the agglomerate is also zero.

$$\left.\frac{\partial \varphi_1}{\partial r}\right|_{r=0} = 0 \tag{2.10}$$

At the surface of the agglomerate, the potential gradient is set by the applied current:

$$-\sigma \left.\frac{\partial \varphi_1}{\partial r}\right|_{r=r_{agg}} = \frac{-i_{app}\rho_{Fe_3O_4} r_{agg}}{3} \tag{2.11}$$

where i_{app} is the applied current (mA g^{-1}), and $\rho_{Fe_3O_4}$ is the density of magnetite.

In each crystal, the flux at the surface is defined by the local reaction current and the flux at the center is zero:

$$-D_x \left.\frac{\partial c_x}{\partial \bar{r}}\right|_{\bar{r}=r_x} = \frac{i_{rxn}(r)}{nF} \tag{2.12}$$

$$\left.\frac{\partial c_x}{\partial \bar{r}}\right|_{\bar{r}=0} = 0 \tag{2.13}$$

In Eq. 2.12, i_{rxn} is evaluated with respect to the crystal's position in the agglomerate scale. At the beginning of the simulation, all three variables are set to initial values, as follows:

$$c_{agg}\Big|_{t=0} = c_0; \quad \varphi_1\Big|_{t=0} = \varphi_{1,0}; \quad c_x\Big|_{t=0} = c_{x,0} \tag{2.14}$$

2.3.1.4. Equilibrium Potential, Parameters, and Constants

The expression for the equilibrium potential as a function of lithium concentration is derived using the approach from Karthikeyan *et al*. [13]. The expression is developed using the Redlich-Kister thermodynamic equation to define the excess Gibbs free energy. The excess Gibbs free energy is used to calculate the activity corrections for the chemical potentials of the species in Eq. 2.3, which results in the following expression for the equilibrium potential:

$$U = U_{ref} + \frac{R_G T}{F} \ln\left[\left(\frac{c_{agg}}{c_0}\right)\left(\frac{(1-\theta)}{\theta}\right)\right] + \sum_{k=0}^{N} A_k \left[(2\theta-1)^{k+1} - \frac{2\theta k(1-\theta)}{(2\theta-1)^{1-k}}\right];\ \theta = \frac{c_x}{c_{x,\max}} \qquad (2.15)$$

The parameters in Eq. 2.15 (U_{ref} and A_k) are obtained by fitting the equation to experimental data using a generalized reduced gradient algorithm. The values for the parameters are given in Table 2.2 and the resulting fit is shown in Figure 2.5. For the fit, the experimental data up to x = 4 (for x in $Li_xFe_3O_4$) were obtained from the maximum voltage during the voltage recovery experiments for the 6 and 8 nm crystals. The data between x = 4 and x = 8 were linearly extrapolated. The voltage at x = 8 was approximated using the final voltage of a 0.16 mA g^{-1} discharge out to 8 electron equivalents [1].

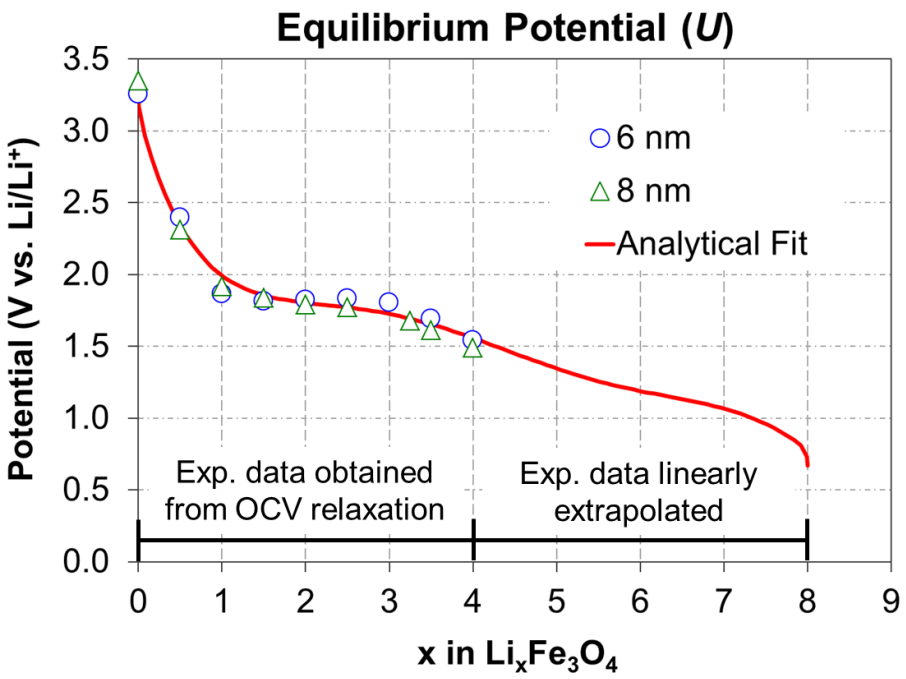

Figure 2.5. Fit of analytical expression for the equilibrium potential to experimental data using the Redlich-Kister expansion for the activity coefficients.

Table 2.2. Parameters determined for the Redlich-Kister expansion.

Parameter	Value
N	7
U_{ref}	1.5617
A_0	-6.5811×10^{-1}
A_1	6.5863×10^{-3}
A_2	1.2249×10^{-1}
A_3	2.7651×10^{-1}
A_4	-5.1470×10^{-1}
A_5	-1.2049×10^{-4}
A_6	-4.3649×10^{-8}
A_7	1.1099×10^{-1}

The results of the voltage recovery experiment were also used to obtain an order of magnitude estimate for k_{rxn} in Eq. 2.5. Figure 2.6a shows the instantaneous jump in voltage 10 ms after the current was interrupted during the recovery experiments for the 6, 8, and 32 nm

crystals. These potential jumps are the sum of the activation and ohmic overpotentials in the electrode. Assuming linear kinetics, the potential jumps can be expressed as:

$$\eta_{tot} = \frac{\hat{i}_{rxn} R_G T}{i_0 F\left(\alpha_a + \alpha_c\right)} + \eta_{ohm} \tag{2.16}$$

where η is the overpotential and $\hat{i}_{rxn}$ is the estimated reaction rate, which can be calculated for each data point in Fig. 2.6a assuming every crystal is electrochemically active and the reaction is uniform. This results in the following equation:

$$\hat{i}_{rxn} = \frac{i_{app} \rho_{Fe_3O_4} r_x}{3} \tag{2.17}$$

Figure 2.6b plots $\hat{i}_{rxn}$ vs. η_{tot}. The slope of a linear fit though the data yields a numerical expression for the exchange current density. Using Eq. 2.5 and providing an order of magnitude estimate of 10^{-4} mol cm^{-3} for the concentration terms, the reaction rate constant can be approximated using the following equation:

$$k_{rxn} = \frac{slope^{-1} R_G T}{F^2 10^{-4}} \tag{2.18}$$

The value of k_{rxn} and all other constants used to simulate the 6 nm electrodes in Section 2.3.2, except the specific surface area (a), are given in Tables 2.3 and 2.4. The specific surface area is determined by assuming the spherical crystals are close-packed ($\varepsilon = 0.26$) and all the crystal surface area is electrochemically active. These assumptions yield the following equation:

$$a = \frac{3\left(1-\varepsilon\right)}{r_x} \tag{2.19}$$

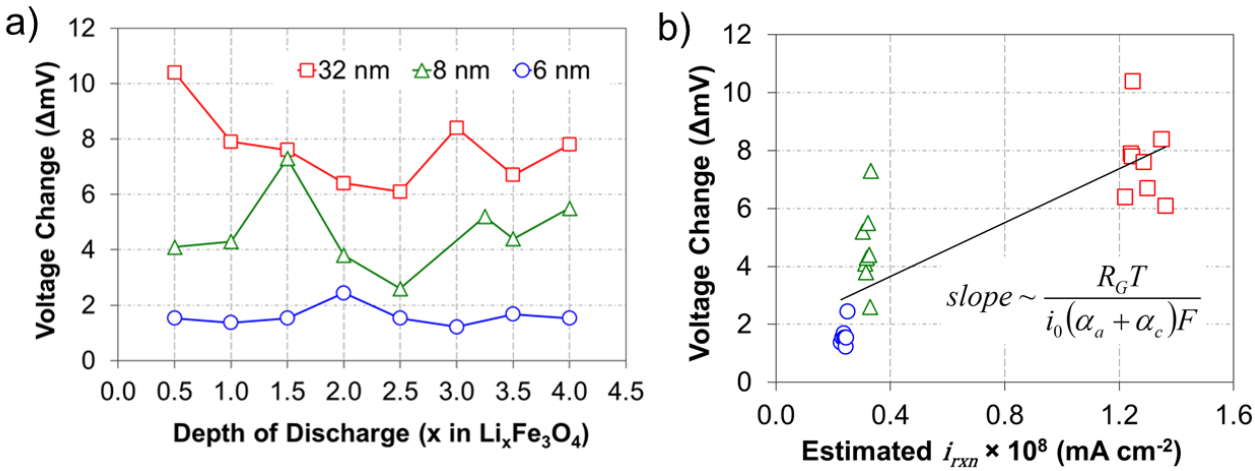

Figure 2.6. a) Instantaneous voltage change at the start of the recovery experiments caused by the interruption of the current (Δt = 10 ms). b) Psuedo-polarization curve obtained from current interrupt data. Reaction current was estimated using Eq. 2.16.

Table 2.3. Values and description of physical parameters

Symbol	Description	Value
$c_{x,\max}$	Maximum Li^+ concentration in Fe_3O_4 (mol cm^{-3})	1.788×10^{-1}
D_{agg}	Diffusion coefficient in the agglomerate ($cm^2\ s^{-1}$)[a]	2.25×10^{-13}
D_x	Diffusion coefficient in the crystal ($cm^2\ s^{-1}$)[a]	2.0×10^{-18}
k_{rxn}	Reaction rate constant ($mol^{-1/2}\ cm^{-1/2}\ s^{-1}$)[b]	5.62×10^{-9}
r_x	Radius of crystal (nm)[b]	3.0
r_{agg}	Radius of agglomerate – average from TEM (μm)[b]	1.05
α_a	Anodic charge transfer coefficient[c]	0.5
α_c	Cathodic charge transfer coefficient[c]	0.5
ε	Agglomerate porosity[c]	0.26
$\rho_{Fe_3O_4}$	Density of magnetite (g cm^{-3})	5.175
σ	Conductivity of magnetite (S cm^{-1}) (15)	4.269×10^{-2}

[a]Fit to experimental data
[b]Experimentally determined
[c]Estimated

Table 2.4. Values and description of constants and initial conditions

Symbol	Description	Value
c_0	Bulk Li^+ concentration in the electrolyte (mol cm^{-3})	10^{-3}
$c_{x,0}$	Initial lithium concentration in the crystal (mol cm^{-3})	10^{-5}
F	Faraday's constant (C mol^{-1})	96,485
i_{app}	Applied current (mA g^{-1})	4.40 to 4.84
R_G	Ideal gas constant (J mol^{-1} K^{-1})	8.314
T	Temperature (K)	303
$\varphi_{1,0}$	Initial potential of the electrode (V)	3.3

2.3.1.5. Numerical Methods

The governing equations were discretized using the forward-time, central-space finite difference method. For each time step, first the agglomerate scale was discretized, and the resulting block, tri-diagonal matrix was solved in Fortran 95 using the BAND(J) algorithm (14). Next, the resulting concentration and potential profiles were used to re-calculate the reaction current density. Finally, at every node in the agglomerate, the concentration profile within the crystal was determined using the updated reaction current as a boundary condition. Each discretized governing equation for each crystal was subsequently solved using the BAND(J) algorithm. Mesh sizes of 51 points were used for both the agglomerate and crystal scales. The time step was 0.5 seconds. Computer experiments were performed for the mesh sizes and time step in order to guarantee convergence.

2.3.2. Comparison with Experiments

The multi-scale model was validated against the discharge and voltage recovery data for the 6 nm experiments (Figure 2.7). For the discharge and recovery curves in Fig. 2.7a, a good agreement is shown between the simulated results and experimental data. Both sets of data in this

figure consist of 5 overlaid curves, one for each depth of discharge. Slight variations between the discharge curves of individual simulations occur because different applied current densities were used to match the experimental conditions. Good agreement is also observed for the voltage recovery data in Fig. 2.7b. The simulation is able to capture both the initial rise and the plateau voltage observed in the experiments. The results of these two plots suggest that the discharge and recovery behavior for the given experiments can be explained using the multi-scale model.

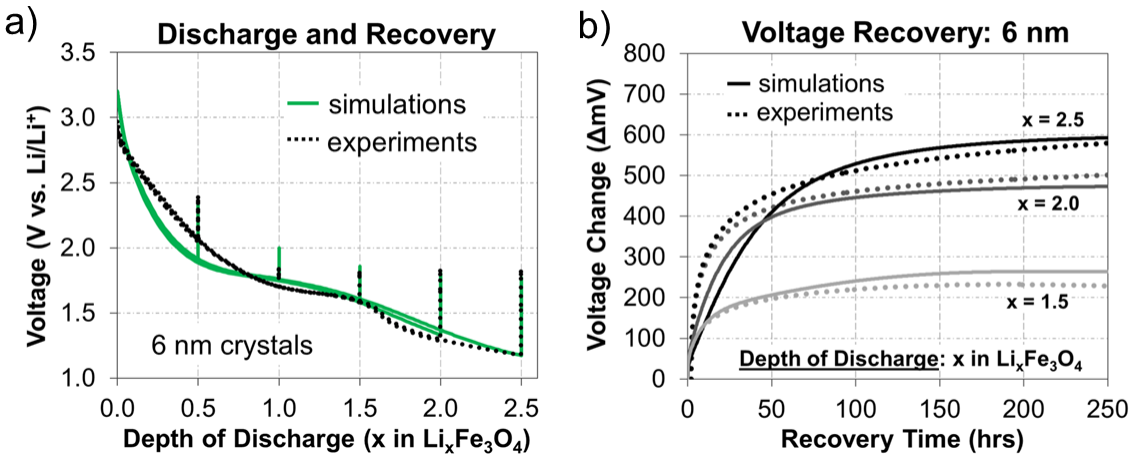

Figure 2.7. Comparison of multi-scale model simulations to experimental data: a) discharge and voltage recovery and b) voltage recovery for crystals with an average diameter of 6 nm.

2.4. Summary

The comparison of mass transport time-constants was shown to be a useful tool in determining which transport processes within an electrode contribute to the voltage recovery. The long voltage recovery times observed for magnetite electrodes were attributed to the slow relaxation of lithium concentration profiles on the agglomerate and crystal length-scales. This conclusion was verified through the development of a multi-scale model, which showed good agreement with experimental data.

2.5. References

1. M. C. Menard, K. J. Takeuchi, A. C. Marschilok, and E. S. Takeuchi, *Phys. Chem. Chem. Phys.*, **15**, 18539 (2013).
2. S. Zhu, A. C. Marschilok, E. S. Takeuchi, and K. J. Takeuchi, *Electrochem. Solid-State Lett.*, **12**, A91 (2009)
3. S. Zhu, A. C. Marschilok, E. S. Takeuchi, G. T. Yee, G. Wang, and K. J. Takeuchi, *J. Electrochem. Soc.*, **157,** A1158 (2010).
4. Z. Cui, L. Jiang, W. Song, and Y. Guo, *Chem. Mat.*, **21**, 1162 (2009).
5. S. Komaba, T. Mikumo, and A. Ogata, *Electrochem. Commun.*, **10**, 1276 (2008)
6. S. Komaba, T. Mikumo, N. Yabuuchi, A. Ogata, H. Yoshida, and Y. Yamada, *J. Electrochem. Soc*, **157**, A60 (2010).
7. O. V. Kharissova, B. I. Kharisov, V. M. Jimenez-Perez, B. M. Flores, and U. O. Mendez, *Rsc. Advances*, **3**, 22648 (2013).
8. D. C. Bock, K. C. Kirshenbaum, J. Wang, W. Zhange, F. Wang, J. Wang, A. C. Marschilok, K. J. Takeuchi, and E. S. Takeuchi, *ACS Appl. Mater. Interfaces*, **7**, 13457 (2015).
9. C. A. Schneider, W. S. Rasband, and K. W. Eliceiri, *Nat. Methods*, **9**, 671 (2012).
10. J. Cho, H. Jung, Y. Park, G. Kim, and H. S. Lim, *J. Electrochem. Soc.*, **147** 15 (2000).
11. P. P. Prosini, M. Lisi, D. Zane, and M. Pasquali, *Solid State Ionics*, **148**, 45 (2002).
12. M. Park, X. Zhang, M. Chung, G. B. Less, and A. M. Sastry, *J. Power Sources*, **195**, 7904 (2010).
13. D. K. Karthikeyan, G. Sikha, and R. E. White, *J. Power Sources.*, **185**, 1398 (2008).
14. J. Newman and K. E. Thomas-Alyea, *Electrochemical Systems*, p. 611, Wiley Interscience, Hoboken, New Jersey (2004).
15. P. Brahma, S. Dutta, D. Dutta, S. Banerjee, A. Ghosh, and D. Chakravorty, *J. Magn. Magn. Mater.*, **321** 1045 (2009).

CHAPTER 3

MODELING THE MESOSCALE TRANSPORT OF LITHIUM-MAGNETITE ELECTRODES USING INSIGHT FROM DISCHARGE AND VOLTAGE RECOVERY EXPERIMENTS

In this chapter, the multi-scale mathematical model developed in Chapter 2 is used to investigate the electrochemical performance of lithium-magnetite electrochemical cells. Experimental discharge and voltage recovery data are compared to three sets of simulations, which incorporate crystal-only, agglomerate-only, or multi-scale transport effects. Conclusions are drawn about the transport limitations on the agglomerate and crystal length-scales. In addition, a further extension of the multi-scale model is proposed which accounts for the impact of agglomerate size distributions on electrochemical performance.

3.1. Introduction

Large increases in the use of distributed and intermittent energy sources (*i.e.*, wind and solar) have increased the need for cost effective, reliable, and efficient energy storage technologies [1]. To address these needs, significant research efforts have focused on the development of next generation materials for secondary batteries, which can provide inexpensive and long lasting energy storage solutions [2-4]. In particular, considerable work has focused on the advancement of magnetite (Fe_3O_4) as an electrode in lithium-ion batteries due to its high theoretical capacity (926 mAh g^{-1}), low cost and safety (non-toxic) [5-14]. Despite these advantages, one of the major challenges limiting the advancement of magnetite electrodes is a considerable difference between the maximum, theoretical capacity and the observed, experimental capacity of the active material. This difference increases the anticipated cost of

magnetite batteries because it requires the electrodes to be overdesigned with excess amounts of active material.

The difference between the theoretical and experimental capacity is related to the close-packed inverse spinel structure of Fe_3O_4, which restricts the transport of lithium in the material. To address this issue, several authors have synthesized Fe_3O_4 nano-crystallites in attempts to minimize the path length for ion transport [9-14]. The smaller path length increases the utilization of the active material by making it possible for ions to penetrate to the center of the crystals, especially at high rates of discharge. Electrodes fabricated with nano-crystalline magnetite have shown significant improvement in capacity; however, the theoretical capacity has still proven difficult to obtain [11]. Further improvements in capacity may require a more detailed understanding of the ancillary effects associated with fabricating an electrode from nano-crystalline active materials. For instance, due to the materials synthesis and electrode fabrication processes, Fe_3O_4 nanocrystals tend to form micron-sized agglomerates [15]. These agglomerates could decrease the utilization of the active material by hindering ion transport towards the crystals at the center of the agglomerate.

At present, it has been difficult to directly quantify the impact of agglomerates on electrochemical performance due to the complex structure of the battery electrodes. With the addition of agglomerates, there are three length-scales within the electrode that can impact the overall battery performance: the bulk electrode (macro-scale), the agglomerates (mesoscale), and the crystals (nanoscale). An understanding of the processes, especially ion transport, occurring on all three length-scales is needed to further optimize the nanocomposite magnetite electrodes.

One way to help clarify which physical processes on which length-scales influence the battery performance is through the development of a mathematical model with predictive

capabilities. A variety of modeling efforts exist in the literature for a variety of lithium ion batteries and electrodes [16-29]; however, to the best of the authors' knowledge, there have been no attempts to simulate the performance of a Fe_3O_4 electrode. In addition, most of the current models only account for the physical processes in the bulk electrode and the solid crystal because the investigated electrode materials tended to have larger crystal sizes (>50 nm in diameter) which do not readily form agglomerates. One exception is the work of Dargaville and Farrell, which simulated the performance of a lithium iron phosphate battery and included an agglomerate length-scale [19]. In that work, the authors used insight from the experimental literature to assume the $FePO_4$ crystals formed porous agglomerates [30, 31]. They concluded from simulations that the agglomerates only impacted the electrochemical performance at high rates of discharge. In contrast, transmission electron microscope images of Fe_3O_4 electrodes indicate that the nanocrystals, which typically have diameters of 8 to 32 nm, form tightly packed agglomerates with small void spaces [15]. These observations suggest that the Fe_3O_4 agglomerates could have a more significant impact on the electrochemical performance of the electrode.

This chapter seeks to investigate the performance-limiting processes of a magnetite electrode using a mathematical model that was developed with insight from experimental discharge and voltage recovery data. Recent voltage recovery experiments performed by Zhu *et. al.* have shown that electrodes fabricated with nano-crystalline magnetite take over 100 hours to reach an equilibrium voltage in response to current interruption [11]. In Chapter 4, it was suggested that these long voltage recovery times were caused by the relaxation of concentration distributions within the agglomerate and/or crystal length-scales of the electrode. To further investigate this behavior, a multi-scale mathematical model was proposed, which was validated

against discharge and recovery data from electrodes comprised of 6 nm crystals. In the present work, a more in depth study is conducted using the multi-scale model. The performance-limiting processes within the agglomerate and crystal length-scales of a Li/Fe_3O_4 electrode are simulated and compared to experimental discharge and voltage recovery data for electrodes composed of 6, 8, and 32 nm nanocrystals. Results provide information on how the ion transport on each length-scale impacts the electrochemical performance. In addition, an extension to the model is proposed which accounts for the influence of distributions in agglomerate size.

3.2. Method of Approach

3.2.1. Experimental

All experimental work in this chapter was conducted by collaborators at Stony Brook University and Brookhaven National Laboratory. Nanocrystalline magnetite (6 and 8 nm), Fe_3O_4, was synthesized using the co-precipitation approach described in Chapter 2. Larger sized nanocrystalline magnetite, ~32 nm, was purchased from Alfa Aesar. Electrodes were prepared using the same method described in Chapter 2. Lithiation was conducted with no preconditioning under a C/200 rate to 0.5, 1.0, 1.5, 2.0 and 2.5 electron equivalents per Fe_3O_4 and then allowed to rest under open circuit conditions for up to 30 days. A total of 15 coin-cells were used, one for each depth of discharge and each crystal size (6, 8, and 32 nm).

3.2.2. Modeling

Simulations were conducted using the multi-scale model developed in Chapter 2. In this chapter, simplifications to the multi-scale model were made in order to develop crystal-only and agglomerate-only models (Figure 3.1). Results from all three models were compared to experimental data in order to understand which length-scales were responsible for the observed

trends in electrochemical performance. The crystal-only model was developed by assuming a fast diffusion coefficient of lithium on the agglomerate scale (10^{-6} cm^2 s^{-1}), which, under the current experimental conditions, yielded negligible variations in lithium-ion concentration throughout the agglomerate. Likewise, the agglomerate-only model was developed by assuming a fast diffusion coefficient for lithium on the crystal scale (10^{-12} cm^2 s^{-1}).

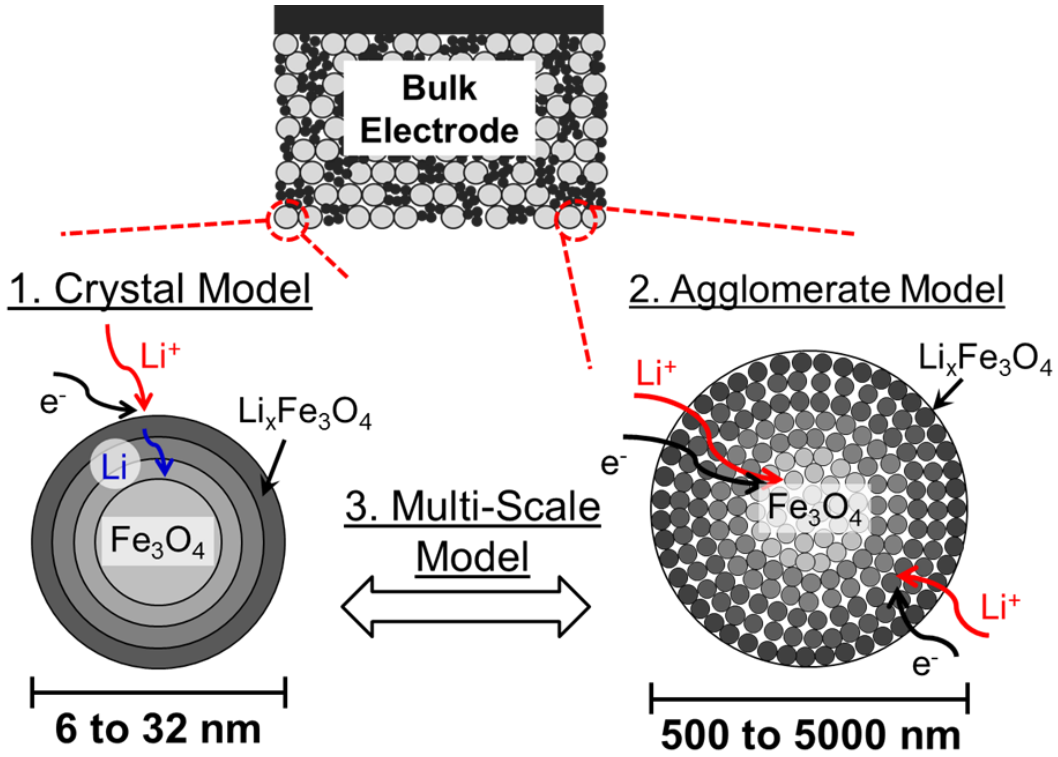

Figure 3.1. Schematic of the transport processes occurring on the crystal and agglomerate length scales, which provide the foundation for the crystal-only, agglomerate-only, and multi-scale models.

3.3. Results and Discussion

3.3.1. Voltage Recovery Experiments

Figures 3.2a and 3.2b show the voltage recovery data for experiments conducted with electrodes comprised of crystals with diameters of 8 and 32 nm, respectively. Data for 6 nm

diameter crystals can be found in Chapter 2. For each set of data, the cells were discharged at C/200 to 0.5, 1.0, 1.5, 2.0 and 2.5 electron equivalents per Fe_3O_4 prior to the observed voltage recovery. During voltage recovery of electrodes with 8 nm crystals, the voltage of electrodes that were discharged to low electron equivalents (0.5, 1.0, and 1.5) goes through a maximum before falling to an equilibrium value. A similar behavior is observed for electrodes with 6 nm crystals that were discharged to low electron equivalents in Chapter 2. For all other sizes and levels of discharge, the maximum voltage occurs at the end of the recovery experiment.

Recovery times greater than 200 hours are observed for all five depths of discharge and all crystal sizes. As discussed in Chapter 2, these long times are likely caused by the slow relaxation of concentration profiles on the agglomerate and/or crystal length scales to a uniform value. The long voltage recovery times indicate large non-uniformities in the lithium concentration within the electrode at the end of discharge. This suggests a poor utilization of the active material, where only a fraction of the material participates in the reaction.

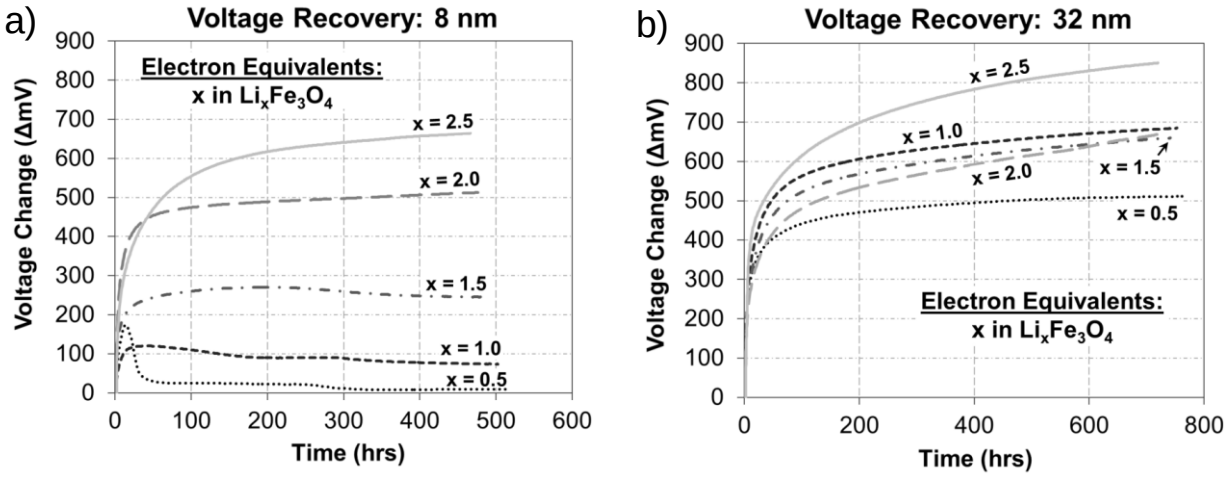

Figure 3.2. Voltage recovery data for Fe_3O_4 electrodes comprised of crystals with an average diameter of a) 8 nm and b) 32 nm.

3.3.2. Comparison of Models to Experimental Data

To further explore whether mass transport effects on the agglomerate and/or crystal length-scales are responsible for the long voltage recovery times, simulations from three different models (*i.e.*, crystal-only, agglomerate-only, and multi-scale) were compared to experimental data. To accomplish this, the mass transport diffusion coefficients were first obtained by fitting each model to the 6 nm experiments. The resulting values were kept constant for the 8 and 32 nm simulations in order to gauge how each model predicted the observed trends in experimental data. For the agglomerate-only and multi-scale models, the agglomerate radius (r_{agg}) was 1.05 μm, which was obtained by taking the average of all agglomerate sizes from transmission electron micrographs of the cross-section of two electrodes fabricated with 8 and 32 nm crystals, respectively. This value was used for all simulations, unless specified otherwise.

To the best of the authors' knowledge, there are no reported values of lithium-ion diffusion coefficients in magnetite crystals (or agglomerates of crystals) reported in the literature. Therefore, the mass transport diffusion coefficients for each model were determined by fitting the simulated voltage recovery times to experimental data. The diffusion coefficients were selected to give the best agreement over the entire range of simulations (*i.e.*, for discharges to 0.5, 1.0, 1.5, 2.0, and 2.5 electron equivalents per Fe_3O_4). For the fitting procedure, the recovery time was defined as the time it takes the voltage to reach 90% of its maximum value. As an example, the results of the fitting procedure for the agglomerate model are shown in Figure 3.3. The figure compares the experimental recovery time to simulations using the best fit diffusion coefficient (D_{agg}), 0.5 × D_{agg}, 2 × D_{agg}, and 10 × D_{agg}. The results indicate that fitting the simulations to the recovery time can provide a reasonable estimate for the diffusion coefficient, at least within an order of magnitude. The simulations using 0.5 × D_{agg} could not be completed

past 2.05 electron equivalents due to mass transport limitations (*i.e.*, onset of a mass-transfer limited current was predicted).

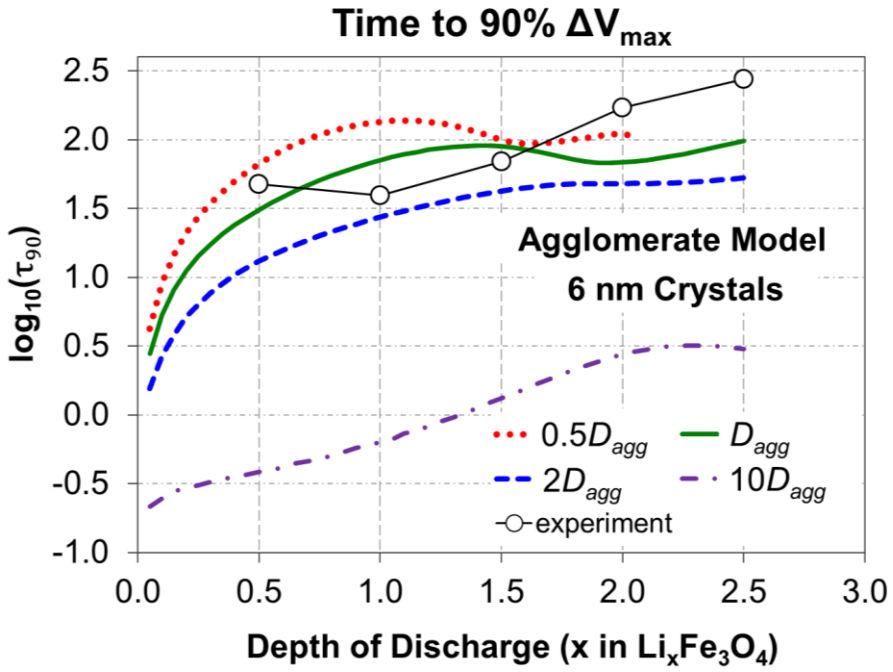

Figure 3.3. Comparison of experimental recovery time to agglomerate models with different Li^+ diffusion coefficients. Best fit diffusion coefficient was used for all agglomerate model simulations.

Table 3.1 contains the diffusion coefficients obtained for each model using the fitting procedure. For the multi-scale model, the diffusion coefficient in the agglomerate (D_{agg}) was set equal to D_{agg} from the agglomerate-only model. The diffusion coefficient in the crystal (D_x) was determined by selecting the lowest possible value that did not have an impact on the simulated discharge or voltage recovery. Obtaining the diffusion coefficient in this manner yielded the best agreement for the multi-scale model with the discharge and voltage recovery data, including trends in electrochemical performance with changes in crystal size.

Table 3.1. Diffusion coefficients used to fit models to experimental voltage recovery for electrodes with 6 nm crystals

Model	Diffusion Coefficient ($cm^2 s^{-1}$)	
	Agglomerate (D_{agg})	Crystal (D_x)
Crystal	–	3.0×10^{-20}
Agglomerate	2.3×10^{-13}	–
Multi-scale	2.3×10^{-13}	2.0×10^{-18}

Note that the agglomerate diffusion coefficient used in the simulations is within the range of experimentally reported values for the solid-state lithium diffusion coefficient in commercial lithium-ion materials (10^{-8} to 10^{-18} cm^2 s^{-1}) [32]. This value is much lower than the agglomerate diffusion coefficient (~10^{-6} cm^2 s^{-1}) used by other authors to simulate lithium transport through loosely-packed agglomerates of $FePO_4$ [19]. The low diffusion coefficient likely results from the tight packing of the nano-crystals within the Fe_3O_4 agglomerates, which has been observed using transmission electron microscopy [15]. Furthermore, assuming the crystals are close-packed, the maximum and minimum size of the void spaces for ion transport in the agglomerate can be determined from the size of the octahedral and trigonal void spaces, respectively. Figure 3.4 shows how the size of the crystals impacts the size of the void spaces in the agglomerate. The upper and lower bounds of the highlighted region were determined from a geometric analysis of the void spaces. The size of the void space is determined from the diameter of the largest sphere capable of fitting in the void (see equations in Figure 3.4). For the magnetite experiments, the

maximum crystal radius was 16 nm, which suggests that the largest void spaces range from ~5 to 13 nm. In this range, it is likely that ion-surface (as opposed to ion-ion or ion-solvent) interactions dictate the rate of mass transport through the agglomerate. Therefore, diffusion coefficients in the agglomerate are expected to be significantly lower than those obtained by using porosity/tortuosity corrections, which inherently assume ion-solvent interactions dominate.

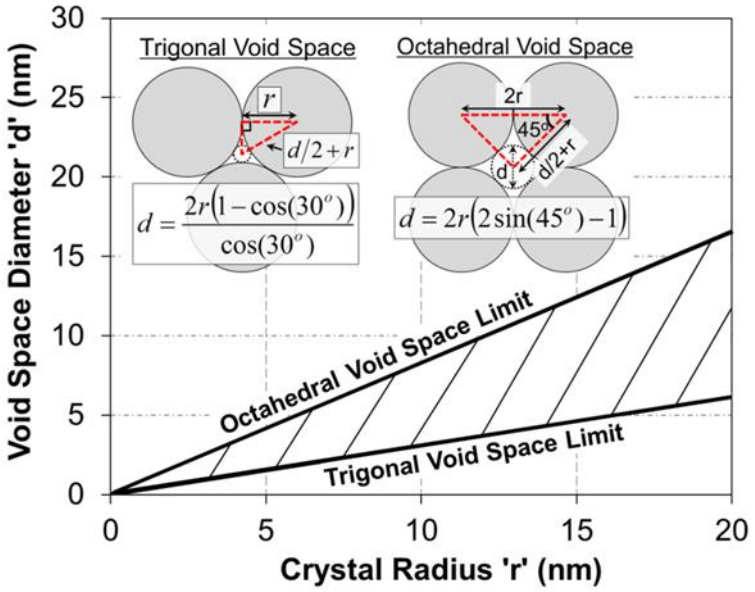

Figure 3.4. Range of void space sizes expected for an agglomerate of close-packed nano-crystals. Size of the void space is determined from the diameter of the largest sphere capable of fitting in the void. Octahedral and trigonal packed spheres provide the upper and lower bounds of the agglomerate void space, respectively.

In addition, the agglomerate diffusion coefficient is five orders of magnitude higher than the solid-state lithium diffusion coefficient used in the simulations. Similar differences in diffusion coefficients are observed for metals, where diffusion within the grain-boundaries and

on the surfaces is typically several (four to six) orders of magnitude faster than solid-state diffusion through the bulk material [33-35]. This suggests that the mechanism responsible for diffusion through the agglomerate may be similar to the mechanisms associated with grain boundary and surface diffusion. Additionally, this trend agrees with the observations of Wang et. al., who tracked lithium transport and conversion in FeF_2 nanoparticles using *in-situ* transmission electron microscopy and concluded that diffusion along the surface of the nanoparticles was much quicker than the diffusion in the bulk material [36].

Figure 3.5 shows the maximum voltage change during the voltage recovery (ΔV_{max}) for all three experiments (6, 8, and 32 nm crystals) and all three models (crystal-only, agglomerate-only, and multi-scale). For each set of experimental data, there were slight variations in the applied current density due to variations in the active mass. The current densities for the 6, 8 and 32 nm datasets were 4.6±0.1, 4.6±0.1, and 4.6±0.2 mA g^{-1} (mean ± standard deviation), respectively. To account for these variations, three simulations were conducted for each crystal size. In the figure, each simulation curve was obtained using the average current density with the error bars corresponding to the ΔV_{max} obtained from simulations using the maximum and minimum current densities.

According to the experimental data, there is almost no difference in ΔV_{max} for the 6 and 8 nm crystals and a significant increase in ΔV_{max} for the 32 nm crystals. The results of Figure 3.5 indicate that only the multi-scale model is able to predict these trends (Fig. 3.5c). For instance, the crystal-only model (Fig. 3.5a) over-predicts the change in ΔV_{max} due to changes in crystal size. It also cannot simulate discharges past an average of 0.4 electron equivalents per Fe_3O_4 for the 32 nm crystals because, at this point, the model predicts that the surface of the crystal will be

fully lithiated (8 electron equivalents). In addition, the agglomerate-only model (Fig. 3.5b) significantly under-predicts the increase in ΔV_{max} for the 32 nm crystals.

A similar behavior is observed for the predicted discharge curves. Figure 3.6 shows the discharge curves for all three experiments and all three models. The discharges were conducted to a cut-off voltage of 1.5 V with current densities of 4.4, 4.7, and 4.5 mA g^{-1} for the 6, 8, and 32 nm cases (simulations and experiments), respectively. Figure 3.6a shows that the crystal-only model over-predicts the changes in discharge time due to changes in crystal size. It also predicts a change in the discharge time between the 6 and 8 nm data which is not observed experimentally. Figure 3.6b shows that the agglomerate-only model does not predict the observed decrease in discharge time for the 32 nm crystals. In fact, all three simulations for the agglomerate model produce the same result. Only the multi-scale model (Fig. 3.6c) is able to predict the similar discharge time for the 6 and 8 nm crystals and the decrease in discharge time for the 32 nm crystals.

The results of the comparison of the models suggest that the long voltage recovery times of the Fe_3O_4 electrodes are caused by the relaxation of concentration distributions on both the agglomerate and crystal length-scales. These concentration distributions arise from mass transport limitations within the electrode. For the electrodes comprised of 6 and 8 nm crystals, recovery is caused by concentration relaxation on the agglomerate scale. This explains why there is no variation in the discharge or recovery behavior between the two crystal sizes. For the electrodes composed of 32 nm crystals, recovery is caused by concentration relaxation on both the agglomerate and crystal scales. The crystal-scale becomes a factor when going from 8 to 32 nm crystals because, according to Eq. 2.1 (see Chapter 2), this corresponds to a 16-fold increase in the mass-transport time constant.

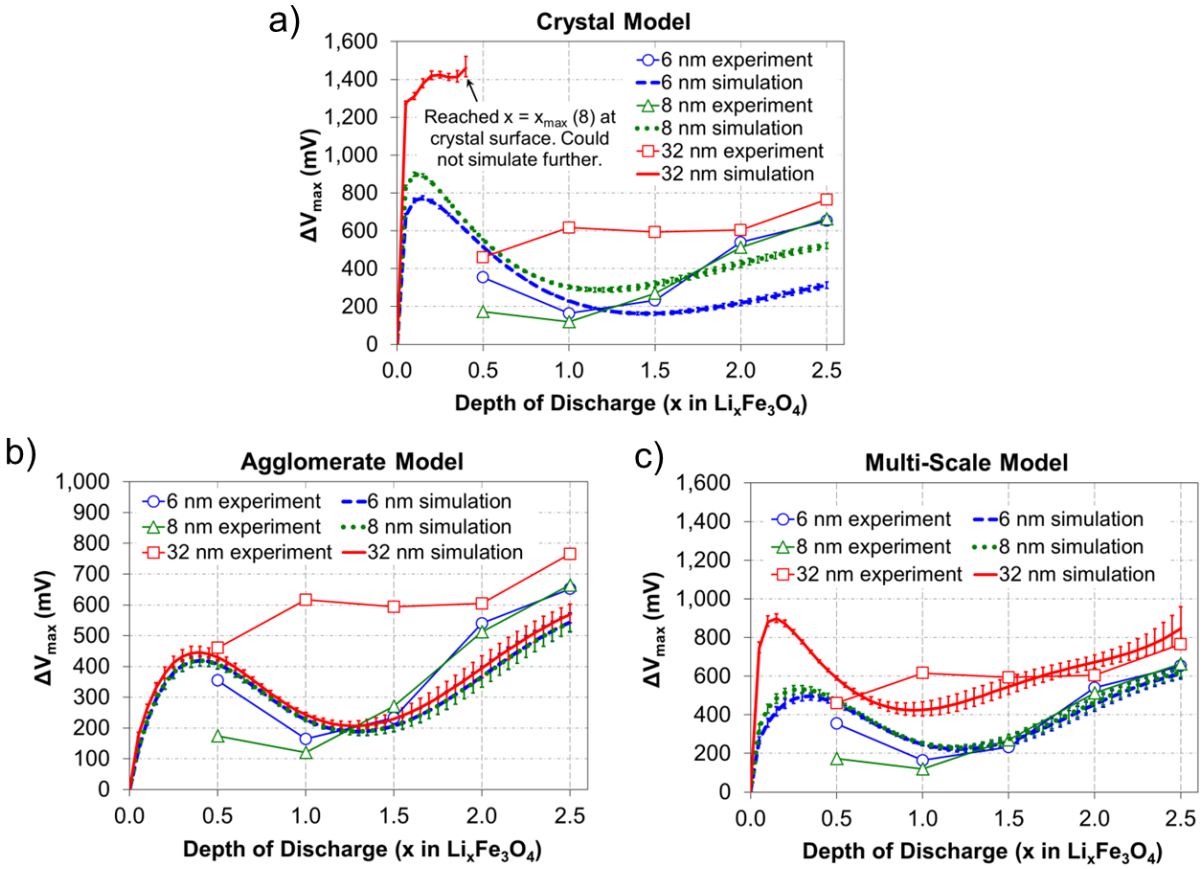

Figure 3.5. Maximum voltage during voltage recovery. Comparison of a) crystal-only, b) agglomerate-only, and c) multi-scale models to experimental data. Multiple simulations were conducted for each crystal size to account for slight variations in the experimental current density. The maximum and minimum ΔV_{max} are displayed as error bars. Current densities: 6 nm (4.4 to 4.8 mA g^{-1}), 8 nm (4.4 to 4.8 mA g^{-1}), 32 nm (4.5 to 4.9 mA g^{-1}).

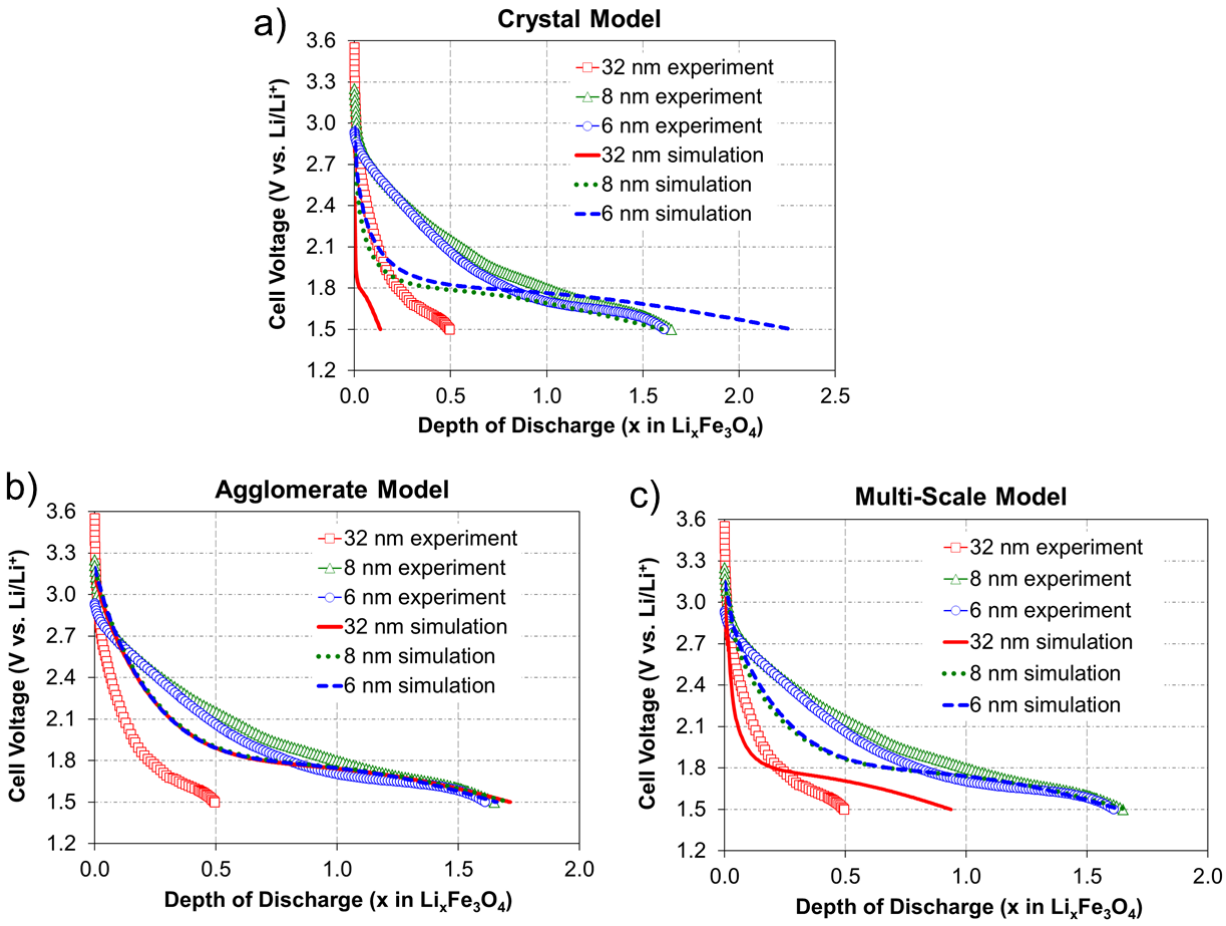

Figure 3.6. Comparison of the discharges to a cutoff voltage of 1.5 V for the a) crystal-only, b) agglomerate-only, and c) multi-scale models. Current densities are 4.4, 4.7, and 4.5 mA g^{-1} for the 6, 8, and 32 nm cases (simulations and experiments), respectively. All electrodes were 50 µm thick with an active mass loading of 4.4 mg cm^{-2} (6 nm), 4.0 mg cm^{-2} (8 nm), and 4.6 mg cm^{-2} (32 nm).

3.3.3. Multi-Scale Model Results

In the previous section, it was concluded that the multi-scale model provides the best agreement with the Fe_3O_4 voltage recovery experiments. This section provides a more thorough analysis of the multi-scale simulation results. Figure 3.7 compares the voltage recovery after

discharges to 1.5, 2.0, and 2.5 electron equivalents per Fe_3O_4 for the 8 and 32 nm data. Good agreement is observed between the experimental and simulated results for the 8 nm data. For the 32 nm data, fairly good agreement is observed for the final voltage, but there are discrepancies between the recovery times to reach the final voltage. The origin of this discrepancy can be identified through an analysis of the predicted concentration distributions.

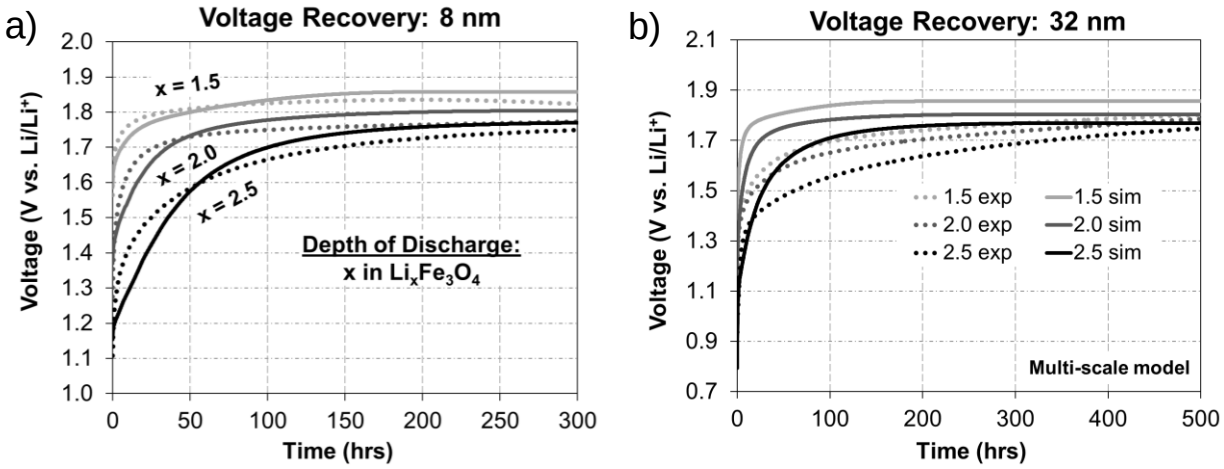

Figure 3.7. Comparison of experimental voltage recovery to the multi-scale model for electrodes composed of a) 8 and b) 32 nm magnetite crystals.

For instance, Figures 3.8 and 3.9 contain predicted concentration distributions within the electrodes composed of 8 and 32 nm crystals during voltage recovery after discharge to 1.5 electron equivalents. Figure 3.8 shows the predicted distributions of the average solid-state lithium concentration within the agglomerate, and Figure 3.9 shows the predicted distributions of the solid-state lithium within the crystal at the agglomerate surface. In the figures, c_{agg} is the concentration of lithium-ions in the agglomerate, c_0 is the bulk concentration of lithium-ions in the electrolyte, and c_x is the concentration of intercalated lithium in each crystal. r and $\bar{r}$ are the radial positions within the agglomerate and crystal, respectively, and r_{agg} and r_x are the radii of

the agglomerate and crystal, respectively. In Fig. 3.8, there is little difference between the 8 and 32 nm simulations. Both show an equilibration of the solid-state lithium concentration in the agglomerate within 200 hours. Because the model assumes there is no direct crystal to crystal exchange of solid-state lithium, the predicted equilibration is caused by lithium transport within the void spaces of the agglomerate. Near the surface of the agglomerate, the solid-state lithium is oxidized to produce mobile lithium-ions, which diffuse to the center of the agglomerate and subsequently reduce back into solid-state lithium. The rate of reduction towards the center is controlled by the mass transport of lithium through the crystal. This is shown by the inset in Fig. 3.8a, which provides the simulated relaxation profiles of the mobile ions in the agglomerate. A similar result is observed for the 32 nm simulations.

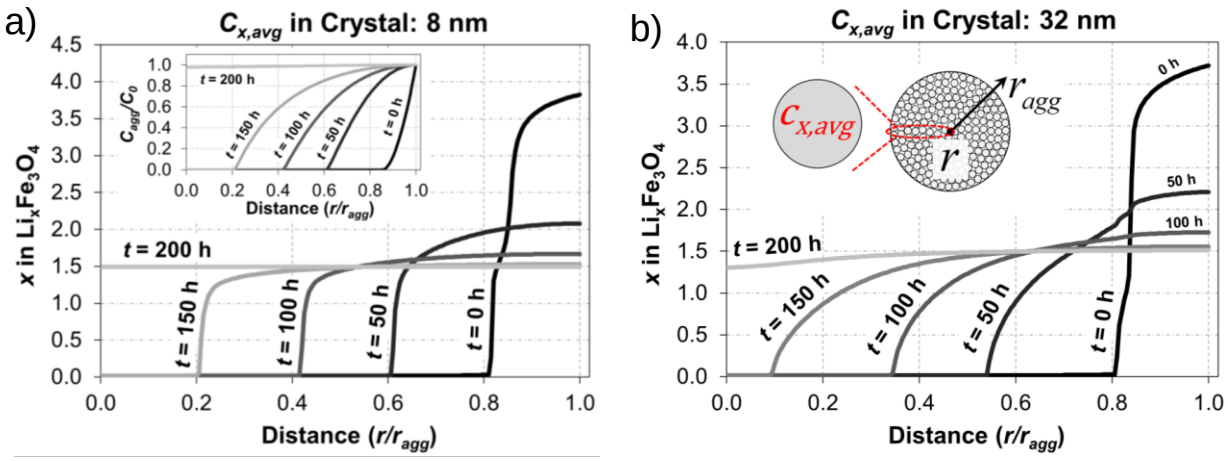

Figure 3.8. Distribution of the average intercalated lithium in each crystal (i.e., $c_{x,avg}$) throughout the agglomerate during voltage recovery after discharge to 1.5 electron equivalents per mole Fe_3O_4. Plots are for simulations of electrodes with a) 8 and b) 32 nm crystals. Inset in a) shows the distribution of lithium-ions in the agglomerate (i.e., c_{agg}) during the same recovery. Similar predictions of c_{agg} are observed for the simulations with 32 nm crystals. Symbols: r is the radial

position within the agglomerate, r_{agg} is the radius of the agglomerate (1.05 μm), and c_0 is the concentration of lithium-ions in the bulk electrolyte (1 M).

In addition, the agglomerate distributions provide information about the utilization of the active mass. For both simulations, at the end of discharge/start of recovery (t = 0), the reaction was only able to penetrate ~20% of the crystal radius. Using this value, the percent volume of the agglomerate which participated in the reaction, v_{active}, can be calculated using the following:

$$v_{active} = \frac{r_{agg}^3 - \left(r_{agg} - \Delta r\right)^3}{r_{agg}^3} \tag{3.1}$$

where r_{agg} is the radius of the agglomerate (1.05 μm for these simulations) and Δr is the penetration depth of the reaction into the agglomerate (0.21 μm). The results of this calculation indicate that only 48.8% of the active material in the agglomerate was utilized during discharge.

In contrast to the agglomerate-scale distributions, there are strong differences between the distributions of solid-state lithium within the crystal at the surface of the agglomerate. For the 8 nm simulations (Fig. 3.9a), there is little spatial variation within the crystal, which indicates that mass transport within the crystal has a negligible impact on the voltage recovery. The decreases in concentration over time are due to the relaxation behavior on the agglomerate scale. For the 32 nm data (Fig. 3.9b), large variations within the concentration of the solid-state lithium are observed. At the start of relaxation, the concentration at the surface of the crystal is over 3× higher than the concentration at the center. These distributions reinforce the conclusion that crystal-scale effects only impact the voltage recovery for experiments with the large, 32 nm crystals and not those conducted with the 6 or 8 nm crystals. It also suggests that the discrepancy

between the simulations and experiments at 32 nm (Fig. 3.7b) is because other phenomena such as phase change within the crystal may contribute to the large recovery times.

In addition to phase change, other factors may explain the discrepancy in the voltage recovery times for the cases with the 32 nm crystals. In the following two paragraphs, three such factors are discussed which were investigated by making adjustments to the multi-scale model. For brevity (and because none of the factors showed significant improvements in the predicted results), no simulated data are shown. First, a decrease in the agglomerate scale diffusion coefficient due to variations in the geometry and packing of the nano-crystals may partially explain the discrepancy in voltage recovery times. To test this hypothesis, simulations were conducted with a decreased agglomerate scale diffusion coefficient (2X lower or 1.15×10^{-13} cm^2 s^{-1}). Slight improvements were observed in the agreement between the rise time of the simulations and experiments. However, significant discrepancies between the maximum voltage changes during recovery (ΔV_{max}) were observed. In an attempt to get better agreement with ΔV_{max}, the diffusion coefficient in the crystal scale (D_x) was also adjusted for the 32 nm simulations. However, even over a wide range of D_x (1.0×10^{-15} to 1.0×10^{-18} cm^2 s^{-1}), good agreement between the experiments and simulations for both the voltage recovery time and ΔV_{max} could not be obtained. Based on these findings, we concluded that a decrease in the agglomerate scale diffusion coefficient is not likely to be the sole reason for the discrepancies in rise time.

In addition, we tested the hypothesis that the presence of electrochemically inactive crystals could explain the discrepancy in the voltage recovery time. Simulations were conducted assuming 60% and 85% of the crystals were electrochemically active. Both sets of simulations yielded negligible improvements in the agreement between the rise time and negatively impacted

the agreement with ΔV_{max}. Therefore, we also concluded that inactive crystals would not likely explain the discrepancy. Finally, we investigated the use of concentrated solution theory to describe the mass transport within the crystal, whereby the differences in chemical potential provide the driving force for mass transport. To accomplish this, the governing equation for mass conservation within the crystal (see Eq. 2.7 in Chapter 2) was reformulated as shown in [24-27]. A new solid-state diffusion coefficient was obtained by fitting the reformulated set of equations to experimental data using the procedure outlined earlier in the text. Slight variations in the predicted performance were observed with concentrated solution theory; however, the agreement with experimental data was not improved.

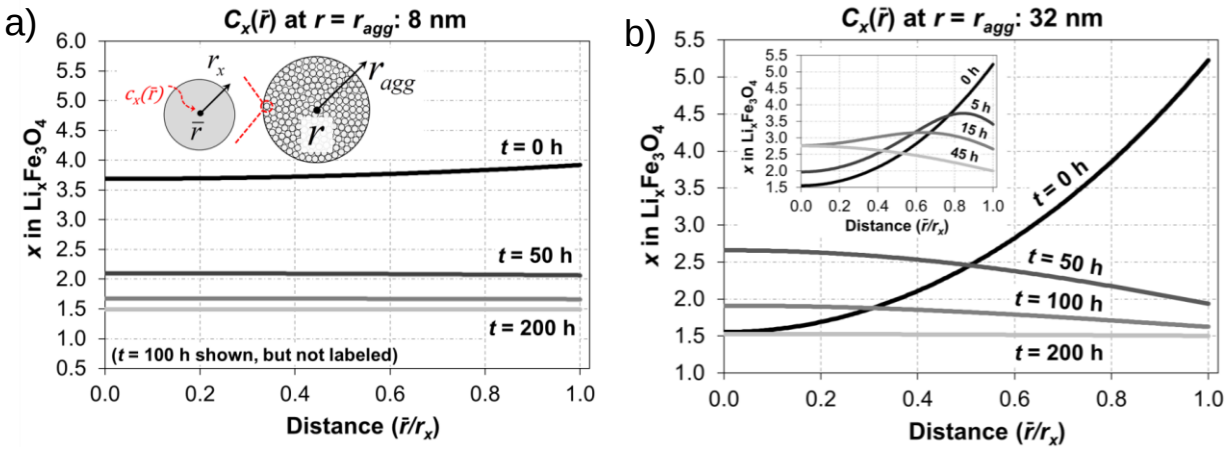

Figure 3.9. Distribution of lithium in the crystal (i.e., $c_x(\bar{r})$) located at the surface of the agglomerate during voltage recovery after discharge to 1.5 electron equivalents per mole Fe_3O_4. Plots are for simulations of electrodes with a) 8 and b) 32 nm crystals. Inset in b) shows profiles at early times for simulations with 32 nm crystals. Symbols: r and $\bar{r}$ are the radial positions within the agglomerate and crystal, respectively, and r_{agg} and r_x are the radii of the agglomerate (1.05 µm) and crystal, respectively.

3.3.4. Impact of Agglomerate Distributions

The analysis of the voltage recovery data using the multi-scale model indicated that the formation of agglomerates impacts the electrochemical performance of the magnetite electrodes. These simulations were conducted using a single, average agglomerate size; however, electrodes typically contain a range of agglomerate sizes [15]. To study the impact of agglomerate size distributions on the predicted performance, the multi-scale model was adjusted to include a representative distribution of agglomerate sizes.

Figure 3.10 shows the experimental distribution of agglomerates composed of 8 nm crystals obtained from transmission electron micrographs of the cross-section of a fully-fabricated battery electrode. A similar distribution for agglomerates composed of 32 nm crystals was also observed [15]. Both distributions were obtained using the experimental approach described in Chapter 2. Along with the experimental data, Figure 3.10 includes the representative distribution of agglomerates used in the simulation. The sizes (*i.e.,* diameters) and number fractions (*i.e.,* frequencies) were selected to best match the experimental data. These values were incorporated into a multi-agglomerate model, which is capable of simultaneously solving for the coupled concentration and potential distributions in all three representative agglomerate sizes. The full mathematical formulation of the multi-agglomerate model is available in Section 3.5.

In order to understand the impact of the agglomerate distribution, two case studies were conducted, which compared the simulated results from a multi-agglomerate and a single-agglomerate model. For the single-agglomerate model, the agglomerate diameter was set equal to the average agglomerate size reported earlier in the manuscript (2.1 μm). In the first study, separate diffusion coefficients were obtained for the single-agglomerate and multi-agglomerate simulations by fitting both of the models to experimental data for a discharge at 4.7 mA g^{-1} to a

cut-off of 1.5 V. The results of this study are shown in Fig 3.11a. To get good agreement for both models, the multi-agglomerate diffusion coefficient ($D_{m\text{-}agg}$) is ~2× higher than the single-agglomerate diffusion coefficient ($D_{s\text{-}agg}$). This indicates that, for the magnetite electrodes, a failure to incorporate the agglomerate distribution in the multi-scale model impacts the fitted agglomerate diffusion coefficient by a factor of ~2.

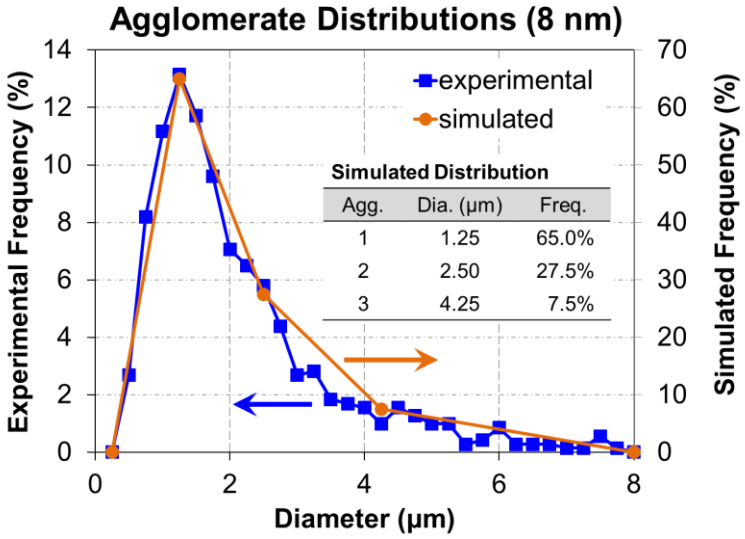

Figure 3.10. Experimental and simulated agglomerate distributions for electrodes comprised of 8 nm crystals. A similar distribution was observed for electrodes with 32 nm crystals [15].

In the second study, the diffusion coefficient in the agglomerate (D_{agg}) was obtained by fitting the multi-agglomerate model to experimental data. This value was then used in the single-agglomerate simulation. Figure 3.11b shows the results of this study. For the single-agglomerate simulation, a ~50% increase in capacity is observed when compared to the experimental and multi-agglomerate simulation results. The increase in capacity can be explained by an increase in the utilization of the active mass. For instance, Figure 3.12 shows the predicted concentration distributions of solid-state lithium in the agglomerate for the single-agglomerate and multi-

agglomerate models during the simulations in Fig. 3.11b. For all four agglomerates (one from the single-agglomerate model and three from the multi-agglomerate model), the simulated distributions indicate that the reactions only occur near the surface of the agglomerate. This is due to mass transport limitations of lithium ions through the agglomerate.

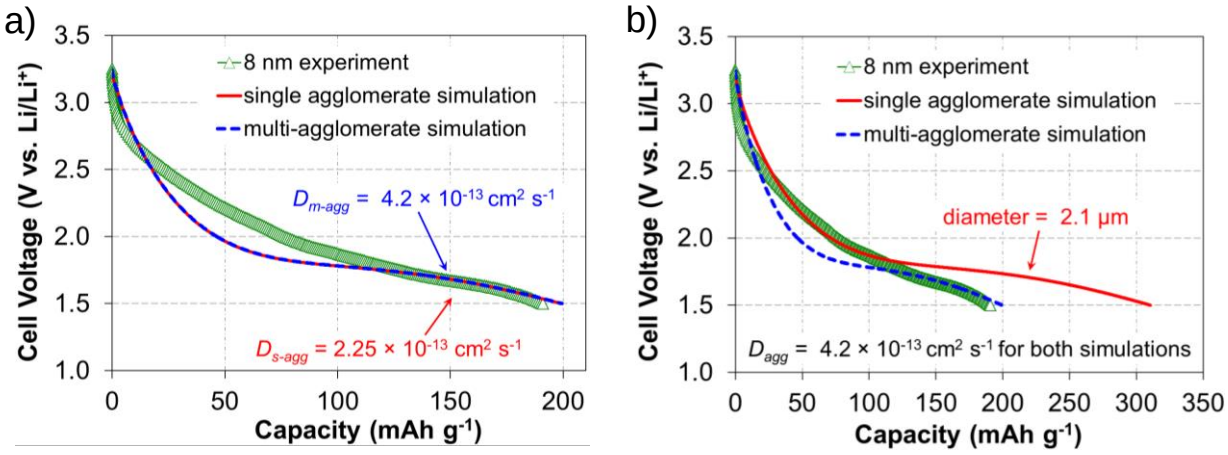

Figure 3.11. Comparison of simulations conducted using a single, average agglomerate size (single agglomerate) or a representative distribution of three agglomerates (multi-agglomerate). a) Diffusion coefficient is adjusted for both simulations to fit data. b) Simulations are conducted with the same diffusion coefficient. The electrode in the experiment was 50 µm thick with an active mass loading of 4.0 mg cm^{-2} and was discharged at 4.7 mA g^{-1} to a cutoff voltage of 1.5 V.

In Figure 3.12, the percent volume of each agglomerate which participates in the reaction, v_{active}, was calculated using Eq. 3.1. For the single agglomerate model, v_{active} is representative of the total active mass utilization in the electrode. For the multi-agglomerate model, the total utilization can be determined using the following equation.

$$\nu_{active,tot} = \frac{\sum_k \nu_{active,k} f_k r_{agg,k}^3}{\sum_k f_k r_{agg,k}^3} \tag{3.2}$$

where f_k is the number fraction of agglomerates with radius k. Evaluation of Eq. 3.2 results in a total active mass utilization of 47.3% for the multi-agglomerate simulation. The utilization predicted in the single-agglomerate model (71.9%) represents a 52% increase in the total utilization when compared to the multi-scale model. This accounts for the ~50% increase in capacity predicted in Fig. 3.11b. The low utilization predicted by the multi-agglomerate model results from the low utilization of the large agglomerates in the distribution. Although the largest agglomerates have a number fraction of less than 10% (f_3 = 7.5%), they account for over 50% of the active mass. Therefore, even a few large agglomerates in the electrode can negatively impact the capacity of the battery.

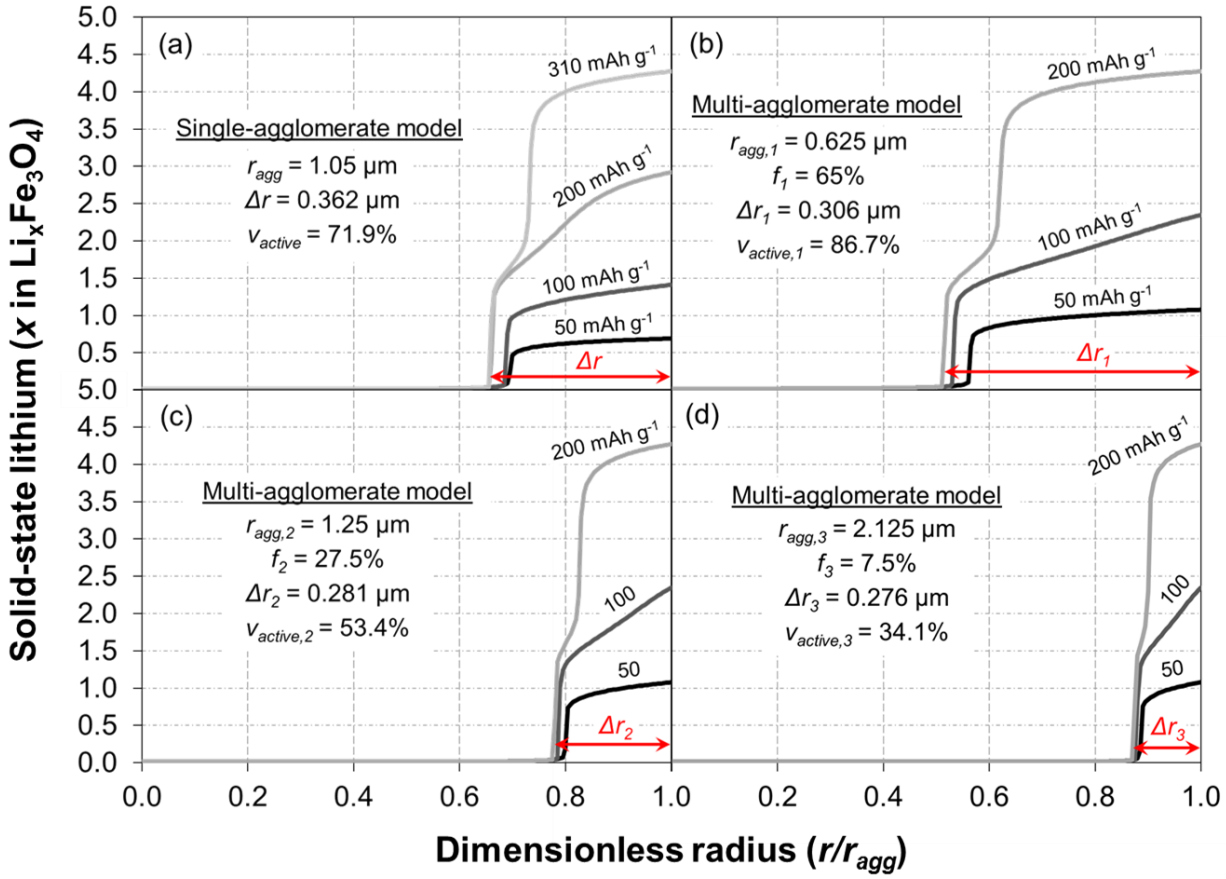

Figure 3.12. Simulated distributions of the solid-state lithium (c_x) throughout the agglomerates during discharge of the a) single-agglomerate and b-d) multi-agglomerate simulations. Capacities are in reference to Figure 3.11b.

3.4. Summary

We report here an analysis of the ion transport limitations occurring within a lithium-magnetite electrochemical cell using a combined experimental and theoretical approach. A multi-scale mathematical model, which accounted for mass transport in the agglomerate and crystal length-scales, was used to analyze experimental discharge and voltage recovery data. It was concluded that the long voltage recovery times of the magnetite electrodes were caused by the relaxation of concentration distributions, which developed as a result of mass transport

limitations within the electrode. For electrodes comprised of 6 and 8 nm crystals, the mass transport limitations were shown to mostly occur within the agglomerate length-scale. For electrodes composed of 32 nm crystals, mass transport limitations were shown to occur in both the agglomerate and crystal length-scales. Therefore, the observed decrease in the discharge capacity between 8 and 32 nm was attributed to the addition of crystal-scale transport limitations.

In addition, the impact of a representative agglomerate size distribution on simulation results was studied using an expanded version of the multi-scale model. Inclusion of a representative agglomerate distribution indicated that variations in agglomerate size could impact the values of the fitted diffusion coefficients by a factor of ~2. The inclusion of a small number fraction of large agglomerates was shown to significantly decrease the predicted capacity, which indicates a possible direction for improving magnetite electrode performance.

3.5. Appendix A: Multi-Agglomerate Model

The multi-agglomerate model was developed using the same assumptions and governing equations reported in Chapter 2. The agglomerate size distribution was simulated using three representative agglomerate sizes. The lithium concentrations ($c_{agg,k}$ and $c_{x,k}$) and voltage ($\varphi_{1,k}$) distributions in the three agglomerates were solved for simultaneously by defining the variables using dimensionless groups and applying coupled boundary conditions between the agglomerates. To accomplish this, the following dimensionless groups were employed:

$$\tilde{i}_{rxn,k} = \frac{a r_{agg,k}^2}{D_{agg} c_0 F} i_{rxn,k} \qquad \tilde{c}_{agg,k} = \frac{c_{agg,k}}{c_0} \qquad \tilde{c}_{x,k} = \frac{c_{x,k}}{c_{x,\max}} \qquad \tilde{\varphi}_{1,k} = \frac{F}{R_G T} \varphi_{1,k}$$

$$\tilde{r} = \frac{r_k}{r_{agg,k}} \qquad \tilde{t}_k = \frac{D_{agg}}{r_{agg,k}^2} t \qquad \tilde{U}_k = \frac{F}{R_G T} U_k \qquad (3.3)$$

where the subscript *k*, denotes the 1st, 2nd, or 3rd agglomerate size in the representative distribution. The reaction rate, $i_{rxn,k}$, is defined using the Butler-Volmer equation:

$$i_{rxn,k} = \tilde{i}_{0,k}\left[\exp\left(\alpha_a\left(\tilde{\varphi}_{1,k} - \tilde{U}_k\right)\right) - \exp\left(-\alpha_c\left(\tilde{\varphi}_{1,k} - \tilde{U}_k\right)\right)\right] \tag{3.4}$$

$$\tilde{i}_{0,k} = Fk_{rxn}\left(c_0\right)^{\alpha_a}\left(c_{x,\max}\right)^{\alpha_a+\alpha_c}\left(\tilde{c}_{agg,k}\right)^{\alpha_a}\left(\tilde{c}_{x,k}\right)^{\alpha_c}\left(1-\tilde{c}_{x,k}\right)^{\alpha_a} \tag{3.5}$$

The equilibrium potential, U_k, is obtained by fitting a thermodynamic description of the system to experimental voltage recovery data. Definitions for all other variables can be found in Section 3.6.

The dimensionless groups in Eq. 3.3 are used to transform the original governing equations into dimensionless equations, resulting in the following expressions for mass and charge conservation in each agglomerate, *k*:

Mass in agglomerates:
$$\varepsilon\frac{\partial\tilde{c}_{agg,k}}{\partial\tilde{t}_k} = \varepsilon\frac{\partial^2\tilde{c}_{agg,k}}{\partial\tilde{r}^2} + \frac{2\varepsilon}{\tilde{r}}\frac{\partial\tilde{c}_{agg,k}}{\partial\tilde{r}} + \tilde{i}_{rxn,k} \tag{3.6}$$

Charge in agglomerates:
$$\frac{\beta}{(1-\varepsilon)}\tilde{i}_{rxn,k} = \frac{\partial^2\tilde{\varphi}_{1,k}}{\partial\tilde{r}^2} + \frac{2}{\tilde{r}}\frac{\partial\tilde{\varphi}_{1,k}}{\partial\tilde{r}}, \qquad \beta = \frac{D_{agg}c_0F^2}{\sigma R_G T} \tag{3.7}$$

The multi-agglomerate simulations were only conducted for the experiments with 8 nm crystals. Therefore, to decrease the solving time, it was assumed that the concentration of solid-state lithium in each crystal increased uniformly (*i.e*, no spatial variations of lithium within the crystals). The validity of this assumption is demonstrated by the predicted concentration distributions in Fig. 3.8a. This assumption makes it possible to solve for the solid-state concentration without solving for the mass transport in the crystal. Instead, the conservation of mass for the solid-state lithium was determined using the following equation:

$$(1-\varepsilon)\frac{\partial c_{x,k}}{\partial t} = -\frac{a i_{rxn,k}}{F} \tag{3.8}$$

The dimensionless form of Eq. 3.8 is written as follows:

Mass in crystals: $$(1-\varepsilon)\frac{\partial \tilde{c}_{x,k}}{\partial \tilde{t}_k} = -\frac{c_0}{c_{x,\max}}\tilde{i}_{rxn,k} \tag{3.9}$$

The solution of these equations (Eqs. 3.4-3.7 and 3.9) was obtained using the following boundary conditions:

Mass in agglomerates: $$\left.\frac{\partial \tilde{c}_{agg,k}}{\partial \tilde{r}}\right|_{\tilde{r}=0} = 0 \qquad \tilde{c}_{agg,k}\big|_{\tilde{r}=1} = 1 \tag{3.10}$$

Mass in crystals: $$\left.\frac{\partial \tilde{c}_{x,k}}{\partial \tilde{r}}\right|_{\tilde{r}=0} = 0 \tag{3.11}$$

Charge in agglomerates: $$\left.\frac{\partial \tilde{\varphi}_{1,k}}{\partial \tilde{r}}\right|_{\tilde{r}=0} = 0 \qquad \tilde{\varphi}_{1,1}\big|_{\tilde{r}=1} = \tilde{\varphi}_{1,2}\big|_{\tilde{r}=1} = \tilde{\varphi}_{1,3}\big|_{\tilde{r}=1} \tag{3.12}$$

In Eq. 3.12, the potentials of all three agglomerates are set equal because it is assumed there are no spatial variations of potential within the bulk electrode. This assumption is valid for the small applied current (C/200) and thin electrodes (50 μm thick) used in the present experiments. The final conservation of charge boundary condition is obtained by setting the sum of the electronic current at the surface of all the agglomerates equal to the applied current.

$$\frac{\sigma R_G T}{F}\sum_k f_k r_{agg,k}\left.\frac{\partial \tilde{\varphi}_{1,k}}{\partial \tilde{r}}\right|_{\tilde{r}=1} = \frac{i_{app}\rho_{Fe_3O_4}}{3}\sum_k f_k r_{agg,k}^3 \tag{3.13}$$

where f_k is the number fraction of agglomerates of size k in the electrode and both sides of Eq. 3.13 have units of amps.

Note that the value of the dimensionless distance, $\tilde{r}$ (Eq. 3.3), does not depend on the agglomerate size *k*. Because of this, it is possible to simultaneously solve the domain equations in all three agglomerate sizes using the same finite-difference grid. To accomplish this, the finite-difference method is used to discretize all nine governing equations in dimensionless space and dimensionless time (Eqs. 3.6, 3.7 and 3.9 for all three agglomerate sizes). At each time step in real time, *t*, the resulting block, tri-diagonal matrix containing all nine independent, dimensionless variables is solved using the BAND(J) algorithm [37].

3.6. List of Symbols

a	specific surface area ($cm^2\ cm^{-3}$)
c_{agg}	lithium concentration in the agglomerate ($mol\ cm^{-3}$)
c_0	bulk concentration in the electrolyte ($mol\ cm^{-3}$)
c_x	solid-state lithium concentration ($mol\ cm^{-3}$)
$c_{x,\max}$	maximum solid-state lithium concentration ($mol\ cm^{-3}$)
D_{agg}	diffusion coefficient in the agglomerate ($cm^2\ s^{-1}$)
D_x	diffusion coefficient in the crystal ($cm^{-2}\ s^{-1}$)
f	number fraction of agglomerates
F	Faraday's constant (96,485 $C\ mol^{-1}$)
i_{app}	applied current ($A\ g^{-1}$)
i_0	exchange current density ($A\ cm^{-2}$)
i_{rxn}	reaction rate ($A\ cm^{-2}$)
k_{rxn}	reaction rate constant ($mol^{-1/2}\ cm^{-1/2}\ s^{-1}$)

r	radial position in the agglomerate (cm)
r_{agg}	agglomerate radius (cm)
$\bar{r}$	radial position in the crystal (cm)
r_x	crystal radius (cm)
R_G	ideal gas constant (8.314 J mol^{-1} K^{-1})
t	time (s)
T	temperature (K)
U	equilibrium potential (V)

Greek

α_a, α_c	anodic and cathodic charge transfer coefficients
ε	porosity
φ_1	potential in the solid (V)
$\rho_{Fe_3O_4}$	density of magnetite (g cm^{-3})
σ	conductivity of magnetite (S cm^{-1})

Subscript

agg	denotes agglomerate
k	denotes agglomerate size
x	denotes crystal

3.7. References

1. *Electricity Energy Storage Technology Options: A White Paper Primer on Applications, Costs, and Benefits*, EPRI, Palo Alto, CA, 1020676 (2010).
2. Z. G. Yang, J. L. Zhang, M. C. W. Kintner-Meyer, X. C. Lu, D. W. Choi, J. P. Lemmon and J. Liu, *Chem. Rev.*, **111**, 3577 (2011).
3. M. S. Whittingham, *Proc. IEEE*, **100**, 1518 (2012).

4. K. C. Divya and J. Ostergaard, *Electr. Power Syst. Res.*, **79**, 511 (2009).
5. S. Mitra, P. Poizot, A. Finke and J. M. Tarascon, *Adv. Funct. Mater.*, **16**, 2281 (2006).
6. S. K. V. Sivakumar, C. A. Ross, Y. Shao-Horn, *ECS Trans.*, **2**, 1 (2007).
7. Z. M. Cui, L. Y. Hang, W. G. Song and Y. G. Guo, *Chem. Mater.*, **21**, 1162 (2009).
8. G. H. Qin, Z. W. Fang and C. Y. Wang, *Dalton Trans.*, **44**, 5735 (2015).
9. S. Komaba, T. Mikumo and A. Ogata, *Electrochem. Commun.*, **10**, 1276 (2008).
10. S. Komaba, T. Mikumo, N. Yabuuchi, A. Ogata, H. Yoshida and Y. Yamada, *J. Electrochem. Soc.*, **157**, A60 (2010).
11. S. L. Zhu, A. C. Marschilok, E. S. Takeuchi, G. T. Yee, G. B. Wang and K. J. Takeuchi, *J. Electrochem. Soc.*, **157**, A1158 (2010).
12. S. L. Zhu, A. C. Marschilok, E. S. Takeuchi and K. J. Takeuchi, *Electrochem. Solid-State Lett.*, **12**, A91 (2009).
13. M. C. Menard, A. C. Marschilok, K. J. Takeuchi and E. S. Takeuchi, *Electrochim. Acta*, **94**, 320 (2013).
14. M. C. Menard, K. J. Takeuchi, A. C. Marschilok and E. S. Takeuchi, *Phys. Chem. Chem. Phys.*, **15**, 18539 (2013).
15. D. C. Bock, K. C. Kirshenbaum, J. Wang, W. Zhang, F. Wang, J. Wang, A. C. Marschilok, K. J. Takeuchi and E. S. Takeuchi, *ACS Appl. Mater. Interfaces*, **7**, 13457 (2015).
16. G. K. Singh, G. Ceder and M. Z. Bazant, *Electrochim. Acta*, **53**, 7599 (2008).
17. T. R. Ferguson and M. Z. Bazant, *J. Electrochem. Soc.*, **159**, A1967 (2012).
18. V. Srinivasan and J. Newman, *J. Electrochem. Soc.*, **151**, A1517 (2004).
19. S. Dargaville and T. W. Farrell, *J. Electrochem. Soc.*, **157**, A830 (2010).
20. M. Doyle, T. F. Fuller and J. Newman, *J. Electrochem. Soc.*, **140**, 1526 (1993).
21. M. Safari and C. Delacourt, *J. Electrochem. Soc.*, **158**, A63 (2011).
22. C. W. Wang and A. M. Sastry, *J. Electrochem. Soc.*, **154**, A1035 (2007).
23. A. Gupta, J. H. Seo, X. C. Zhang, W. B. Du, A. M. Sastry and W. Shyy, *J. Electrochem. Soc.*, **158**, A487 (2011).
24. M. Farkhondeh and C. Delacourt, *J. Electrochem. Soc.*, **159**, A177 (2012).
25. M. W. Verbrugge and B. J. Koch, *J. Electrochem. Soc.*, **143**, 600 (1996).
26. D. K. Karthikeyan, G. Sikha and R. E. White, *J. Power Sources*, **185**, 1398 (2008).
27. M. W. Verbrugge, D. R. Baker, X. C. Xiao, Q. L. Zhang and Y. T. Cheng, *J. Phys. Chem. C*, **119**, 5341 (2015).
28. K. West, T. Jacobsen and S. Atlung, *J. Electrochem. Soc.*, **129**, 1480 (1982).
29. C. S. Wang, U. S. Kasavajjula and P. E. Arce, *J. Phys. Chem. C*, **111**, 16656 (2007).
30. M. Maccario, L. Croguennec, F. Weill, F. Le Cras and C. Delmas, *Solid State Ionics*, **179**, 2383 (2008).
31. S.-T. Myung, S. Komaba, N. Hirosaki, H. Yashiro and N. Kumagai, *Electrochim. Acta*, **49**, 4213 (2004).
32. M. Park, X. Zhang, M. Chung, G. B. Less and A. M. Sastry, *J. Power Sources*, **195**, 7904 (2010).
33. J. C. Fisher, *J. Appl. Phys.*, **22**, 74 (1951).
34. J. Horváth, R. Birringer and H. Gleiter, *Solid State Commun.*, **62**, 319 (1987).
35. Y. Mishin and C. Herzig, *Mater. Sci. Eng., A*, **260**, 55 (1999).
36. F. Wang, H. C. Yu, M. H. Chen, L. J. Wu, N. Pereira, K. Thornton, A. Van der Ven, Y. M. Zhu, G. G. Amatucci and J. Graetz, *Nat. Commun.*, **3** (2012).

37. J. Newman and K. E. Thomas-Alyea, *Electrochemical Systems*, Wiley Interscience, Hoboken, New Jersey (2004).

CHAPTER 4

MULTI-SCALE SIMULATIONS OF LITHIUM-MAGNETITE ELECTRODES INCORPORATING PHASE CHANGE

In this chapter, the phase changes occurring in magnetite (Fe_3O_4) during lithiation and voltage recovery experiments are modeled using a multi-scale model whose groundwork was presented in Chapter 2. Phase changes are described using kinetic expressions based on the Avrami theory for nucleation and growth. Simulated results provide information on the rate and onset of phase formation in magnetite during lithiation and voltage recovery experiments.

4.1. Introduction

Two major factors limiting the widespread use of electric vehicles are the size and cost of the lithium-ion batteries used in the power system. To address these issues, next-generation batteries must contain active materials with high specific energy (Wh L^{-1} or Wh g^{-1}), which can meet the required design specifications with smaller quantities of material. Currently, the specific energies of commercially available lithium-ion battery electrodes are limited by relatively low theoretical capacities – 140 to 200 mAh g^{-1} and ~370 mAh g^{-1} for positive and negative electrode materials, respectively [1, 2]. These materials have low capacities because they can only accept ~1 mole of lithium per mole of host material (*e.g.*, C_6, CoO_2, and $FePO_4$). In an effort to expand the capacity of battery electrodes, new compounds are being investigated which undergo multiple electron transfers (MET) and can accommodate multiple moles of lithium per mole of host material. These compounds include metal oxides, fluorides, oxyfluorides, nitrides, and sulfides [3-9]. Unlike commercial lithium-ion electrode materials, which store and release energy through a (de)intercalation reaction, the MET compounds can undergo conversion reactions,

which result in the structural rearrangement and phase change of the host material. The kinetics of formation and reversibility of these phase changes are important factors dictating the applicability of these new materials.

Among the new set of compounds, magnetite (Fe_3O_4) is of particular interest due to its low cost, safety, and high theoretical capacity (926 mAh g^{-1}), which is associated with its ability to accommodate 8 moles of lithium per mole of Fe_3O_4 [10-15]. During lithiation, magnetite first undergoes an intercalation process which results in the structural rearrangement of the material from an inverse spinel to a rock-salt-like structure [16-20]. Upon further lithiation, magnetite undergoes a conversion process to Li_2O and Fe metal [21-24]. Until recently, the performance of magnetite was limited by slow solid-state transport of lithium ions through the close-packed structure of the material. However, nanosizing has been utilized to shorten the path length for lithium ion diffusion, which has improved the rate capability and increased the utilization of the active material [13-15, 25-27]. Further improvements in rate capability and utilization have been obtained using alternative electrode synthesis methods that reduce agglomeration of the nanocrystals [28, 29]. Despite these improvements, it is still difficult to obtain the theoretical capacity of Fe_3O_4, especially during cycling. Recently, investigations of the (de)lithiation process using synchrotron X-ray and transmission electron microscopy techniques have suggested that the poor capacity is caused by an inability to fully convert from Li_2O and Fe metal into the inverse-spinel phase (Fe_3O_4) during delithiation [21, 24]. This suggests that further improvements in performance may result from a better understanding of the kinetics of structural rearrangement and phase change within the material.

This work seeks to complement recent experimental investigations by modeling the phase changes occurring within magnetite during lithiation and voltage recovery. In the battery field,

modeling of phase change has been done in other materials (*e.g.* $FePO_4$ and FeF_2) using phase-field theory, which implements the Cahn-Hilliard equation to describe the concentration distribution of Li^+ within a crystal [30-34]. Phase-field modeling is capable of simulating phase-separation of materials into regions of high- and low-levels of lithiation by calculating the distribution of Li^+ which minimizes the free energy of the crystal. The concentration distributions agree well with experimental observations; however, the results are highly dependent on the use of a representation of the free energy of the system (often arising from regular solution theory and developed based on experimental observations), which often results in poor agreement between simulations and electrochemical performance data [33-37]. Other attempts to simulate the electrochemical performance of a material which undergoes phase change have utilized a "shrinking-core" model, which tracks the boundary separating the high- and low-lithium phases as it progresses from the surface of a crystal to the center during lithiation [38-40]. These models agree well with electrochemical data; however, they often only simulate the battery during lithiation of the electrode because modeling the subsequent delithiation is difficult due to the existence of multiple moving boundaries. In addition, shrinking-core models assume that both phases (high- and low- lithium) are already present at the start of the simulation. Therefore, they do not provide kinetic descriptions of the initial formation of the highly concentrated phase.

In this chapter, we seek to simulate the phase changes within magnetite during lithiation by incorporating the kinetics of nucleation and growth of new phases into the multi-scale model previously developed in Chapter 2. In Chapter 3, a version of the model without phase change was able to capture the electrochemical performance of an electrode at low levels of lithiation, where Fe_3O_4 undergoes an intercalation process. To expand our understanding to higher levels of lithiation, the formation of new phases are incorporated into the model using kinetic expressions

inspired by the Avrami theory for nucleation and growth [41-43]. Herein, simulations with phase change are used to explain the behavior of electrodes with "small" (~6 nm) and "large" (32 nm) crystals during lithiation and voltage recovery experiments.

4.2. Experimental

All experimental work in this chapter was conducted by collaborators at Stony Brook University and Brookhaven National Laboratory. The materials synthesis and electrode fabrication follow the same approach outlined in Chapters 2 and 3. In this study, for electrodes comprised of 6 and 32 nm crystals, lithiation was conducted under a C/200 rate to 0.5, 1.0, 1.5, 2.0, 2.5, 3.0, 3.5 and 4.0 electron equivalents per Fe_3O_4 and then allowed to rest under open circuit conditions for up to 30 days. For electrodes comprised of 8 nm crystals, similar experiments were conducted to 0.5, 1.0, 1.5, 2.0, 2.5, 3.25, 3.5, 4.0, 4.5, 5.0, 6.0, 7.0, and 8.0 electron equivalents per Fe_3O_4.

4.3. Kinetics of Phase Change

This section describes the generic approach used to model the rearrangement of a material from "*a*" to "*b*," where *a* and *b* are unique phases of the same host material. Both *a* and *b* contain the same number of host atoms (*e.g.,* for a host material of Fe_3O_4 both phases contain 3 Fe and 4 O), but they differ in the arrangement of those atoms and in the concentration of solid-state lithium within the phases, designated as c_a and c_b. At equilibrium, both phases have the same chemical potential and well-defined concentrations of solid-state lithium, whereby $c_a^* < c_b^*$ with the * denoting equilibrium values (see Figure 4.1). Because both phases are at the same chemical potential, a plateau is observed in the equilibrium voltage, whereby the host material has the same equilibrium voltage at all solid-state lithium concentrations between c_a^* and c_b^*

[39]. In this region between c_a^* and c_b^*, the equilibrium structure of the host material corresponds to a fraction of phase *a* at concentration c_a^* and a fraction of phase *b* at concentration c_b^*. Under equilibrium conditions, the fractions of *a* and *b* can be determined from a mass balance. Under non-equilibrium conditions, such as the discharge of an electrode, the formation of phase *b* must be described by a kinetic process. If the formation of phase *b* is instantaneous, the kinetic process can be described by the following equation:

$$\mathrm{Li_a\Gamma_a} + (\mathrm{b}-\mathrm{a})\mathrm{Li^+} + (\mathrm{b}-\mathrm{a})\mathrm{e^-} \rightarrow \mathrm{Li_b\Gamma_b} \tag{4.1}$$

where $\mathrm{Li_a\Gamma_a}$ and $\mathrm{Li_b\Gamma_b}$ are the equilibrium phases of *a* and *b*, respectively, and Γ_a and Γ_b represent the arrangement of the atoms in the host material in phases *a* and *b*, respectively. During lithiation of a material with instantaneous formation of phase *b*, the voltage is practically constant between c_a^* and c_b^* because Eq. 4.1 does not depend on the total solid-state lithium concentration.

In actuality, instantaneous formation of phase *b* is only an ideal case that does not apply to all systems or at every operating condition. Therefore, a kinetic description is needed for the non-instantaneous formation of phase *b* (from *a*). In this work, the driving force for formation of *b* is an increase in c_a above a saturation value, $c_{a,sat}$, which is equal to the equilibrium concentration in *a* (c_a^*), for this case. This hypothesis suggests that, although phase *a* has a well-defined equilibrium concentration, it is able to exist in a supersaturated state with a concentration of solid-state lithium greater than the equilibrium concentration (see Figure 4.1). Assuming that only the *a* phase is electrochemically active, the formation of *b* can be described by the following two step process, whereby lithium is first inserted into *a* and then the host material rearranges into the equilibrium phases:

$$\mathrm{Li_a\Gamma_a + xLi^+ + xe^- \xrightarrow{\text{lithiation}} Li_{a+x}\Gamma_a} \tag{4.2}$$

$$\mathrm{Li_{a+x}\Gamma_a \xrightarrow{\text{phase change}} yLi_a\Gamma_a + (1-y)Li_b\Gamma_b}, \text{ where } y = \frac{a+x-b}{a-b} \tag{4.3}$$

During lithiation of a material with non-instantaneous formation of phase *b*, the voltage does not remain constant between c_a^* and c_b^*. The voltage depends on the degree of supersaturation of phase *a*, which can continuously change during lithiation and depends on the relative rates of the two steps.

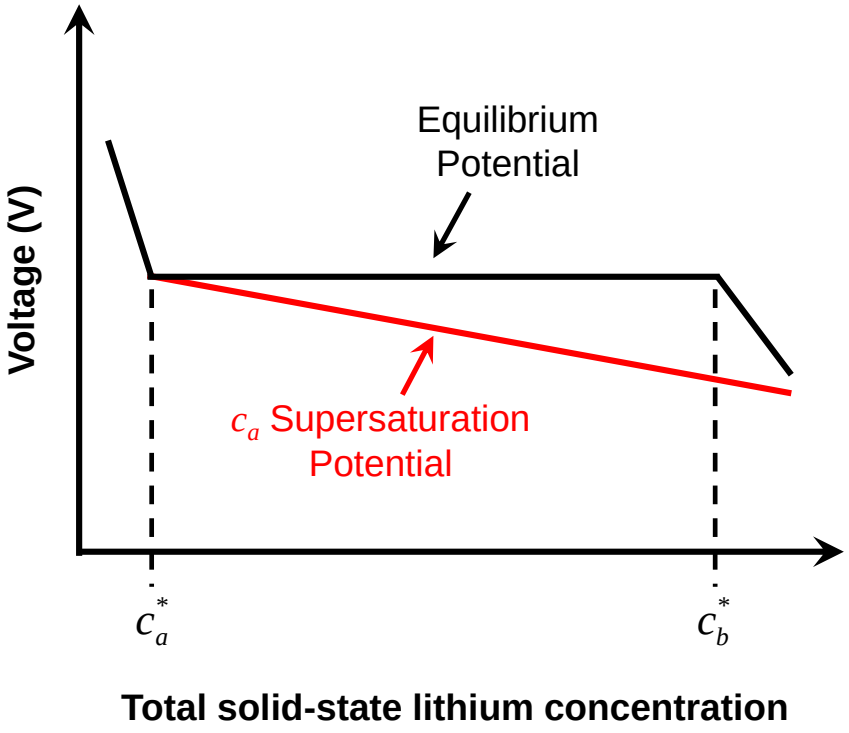

Figure 4.1. Schematic of the equilibrium potential and supersaturation potential during phase change of a host material from phase *a* (at a solid-state lithium concentration of c_a) to phase *b* (at a solid-state lithium concentration of c_b^*).

In this work, the kinetic description for the formation of *b* from *a* in Eq. 4.3 is given as follows:

$$\frac{\partial \theta_b}{\partial t} = k_b \left(c_a - c_{a,sat}\right)\theta_b^{2/3}\left(1-\theta_b\right)$$
$$k_b = k_{b,1}\left(1+k_{b,2}c_a\right) \tag{4.4}$$

where θ corresponds to the volume fraction of a given structure. The 2/3 dependence on θ_b results from the assumptions that new structures of phase *b* nucleate as spheres and grow in three dimensions [41]. The term (1-θ_b) causes a reduction in the rate of formation as the volume fraction of *a* approaches zero [42]. The rate constant for formation k_b is assumed to depend linearly on c_a.

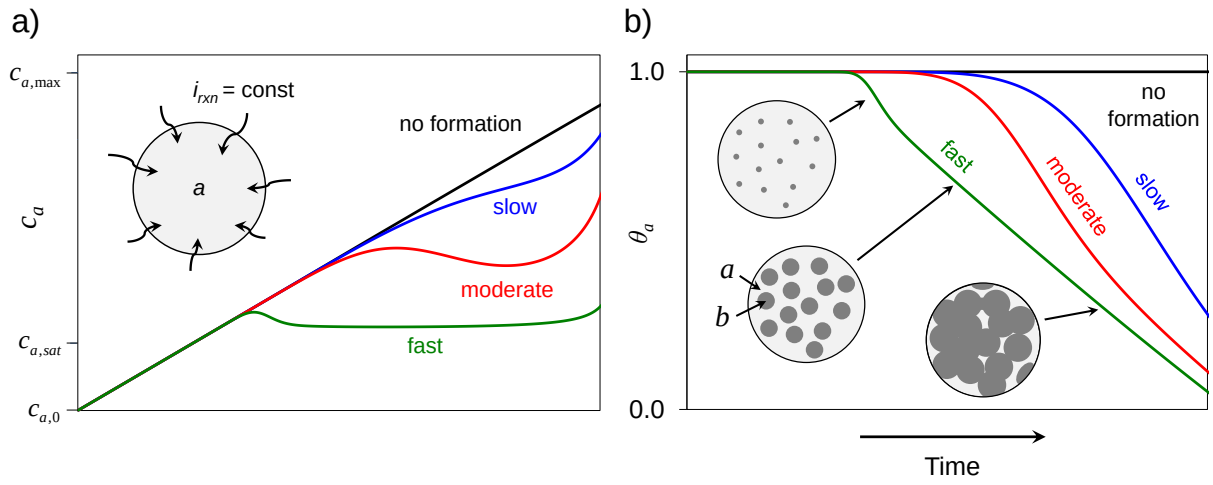

Figure 4.2. Generic results for a particle undergoing phase change from phase *a* to *b*. a) Concentration of solid-state lithium in phase *a* (c_a) and b) volume fraction of phase *a* (θ_a) during uniform lithiation of a particle at a constant reaction rate. Diagrams show how c_a and θ_a are impacted by the slow, moderate, and fast formation of phase *b* (from *a*) as described in Eq. 4.1.

Figure 4.2 provides a pictorial representation of the process described by Eq. 4.4 for a slow, moderate, and fast rate of θ_b formation. The pictorial representation was developed assuming that a single crystal of host material comprised of only phase *a* and at an initial solid-state lithium concentration, $c_{a,0}$, is lithiated uniformly at a constant reaction rate. At the start of lithiation ($c_a < c_{a,sat}$), only θ_a is present, and c_a increases linearly with time as a result of the constant reaction rate. As the concentration in *a* exceeds the critical saturation concentration ($c_{a,sat}$), phase *b* starts to form, which decreases the volume fraction of *a* (θ_a) in the crystal. In addition, the formation of phase *b* impacts c_a due to the rearrangement of solid-state lithium within the particle. The value of c_a can be determined through a mass balance on the total amount of solid-state lithium in the particle, as follows:

$$\frac{\partial(\theta_a c_a)}{\partial t} + \frac{\partial(\theta_b c_b)}{\partial t} = \frac{3 i_{rxn}}{r_x n F} \tag{4.5}$$

where r_x is the radius of the crystal, and it is assumed only the *a*-phase is electrochemically active. Assuming a negligible difference between the size of the unit cells of phases *a* and *b* and a constant value of $c_b = c_b^*$, which corresponds to the concentration at equilibrium, Eq. 4.5 can be simplified to:

$$(1-\theta_b)\frac{\partial c_a}{\partial t} = (c_a - c_b^*)\frac{\partial \theta_b}{\partial t} + \frac{3 i_{rxn}}{r_x n F} \tag{4.6}$$

The values of c_a during a slow, moderate, and fast rate of θ_b formation are also shown in Figure 4.2a. If no θ_b is formed, c_a increases linearly with time. If θ_b is formed, the rate of change of c_a decreases because $c_a < c_b^*$, which indicates that the formation of θ_b corresponds to a "repackaging" of the solid-state lithium in the particle into a more concentrated structure. Because only the *a*-phase is assumed to be electrochemically active, the variations in c_a for the

different rates of formation result in variations in the voltage profile observed during discharge. Therefore, accurate modeling of this process requires determination of $c_{a,sat}$, c_b^*, a description of the supersaturation potential for c_a, and the rate constants $k_{b,1}$ and $k_{b,2}$.

4.4. Results and Discussion

4.4.1 Determination of α, β, and γ Phases

Figure 4.3 shows the results of the voltage recovery experiments, whereby electrodes comprised of 6, 8, and 32 nm Fe_3O_4 crystals were lithiated to a set concentration of lithium (x in $Li_xFe_3O_4$) and then allowed to rest under open circuit conditions for up to 30 days. The figure plots the maximum voltage for each electrode during the 30 day rest period. According to this plot, there are two plateaus in the equilibrium potential of Fe_3O_4. The first plateau starts at $x \sim 1$, and the second starts at $x \sim 6$. The existence of two plateaus indicates that there are two regions where Fe_3O_4 undergoes an electrochemical reaction involving two solid phases. This suggests that Fe_3O_4 can exist in three unique arrangements, referred to herein as α, β, and γ.

The first voltage plateau at $x = 1$ corresponds to an equilibrium between the α- and β-phases. According to the schematic in Figure 4.1, the existence of the plateau from $x = 1$ to $x = 3$ suggests that, at equilibrium, the α phase has a solid state lithium concentration of $x = 1$ (α-$LiFe_3O_4$) and the β phase has a concentration of $x = 3$. However, this result is only valid under the assumption that the voltage recovery experiments have reached equilibrium potentials after 30 days. For experiments lithiated to $x < 3.0$, the electrodes are close to equilibrium after 30 days and the voltage in Figure 4.3 roughly corresponds to the equilibrium potential (see Chapters 2 and 3). For experiments lithiated to $x > 3.0$, the voltage of the electrodes is still changing significantly at 30 days. For instance, the inset in Figure 4.3 shows that the voltages of electrodes discharged to 4 moles of Li^+ per mole of Fe_3O_4 are still rapidly changing at 30 days. In addition,

structural characterization suggests the existence of a rock-salt phase at a concentration of $x = 4$, which has a structure resembling Li_2O and FeO closely packed on an O-anion framework [21]. Therefore, in this work, the β phase is assumed to have an equilibrium structure of the form β-$Li_4Fe_3O_4$, and the first voltage plateau is assumed to extend to $x = 4$. Based on this assumption, the reaction for the *instantaneous* formation of the β phase is given as follows:

$$\underbrace{LiFe_3O_4}_{\alpha} + 3Li^+ + 3e^- \rightarrow \underbrace{Li_4Fe_3O_4}_{\beta} \tag{4.7}$$

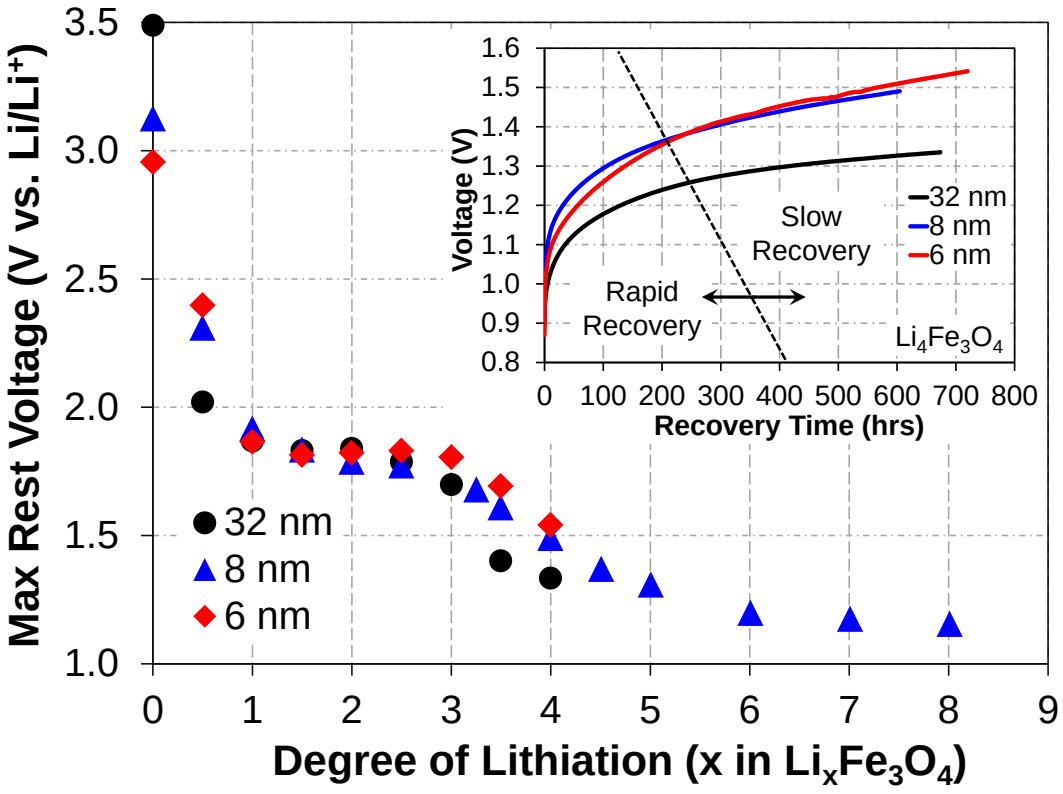

Figure 4.3. Maximum voltage during recovery at open circuit for up to 30 days after lithiation to a set amount of x in $Li_xFe_3O_4$. Inset: Experimental data for voltage recovery after lithiation to $x = 4$ for x in $Li_xFe_3O_4$. Voltage recovery data sectioned into an initial, rapid recovery attributed to the relaxation of concentration distributions on the agglomerate and crystal length-scales and a later, slow recovery attributed to the formation of the β phase from the α phase.

For the second plateau, it extends out to x = 8 and is believed to be associated with the conversion reaction that forms Li_2O and metallic Fe [21]. In this work, these conversion products are represented as the γ phase, which is assumed to have a solid-state lithium concentration of x = 8 lithium per Fe_3O_4. The *instantaneous* formation of γ can be expressed by the following equation:

$$Li_yFe_3O_4 + (8-y)Li^+ + (8-y)e^- \rightarrow \underbrace{4Li_2O + 3Fe}_{\gamma} \tag{4.8}$$

where the solid-state concentration at the onset of the plateau is defined by the variable y. The solid-state concentration at the onset is unknown because the voltage recovery experiments are still changing at 30 days. Its value is obtained below by fitting simulations with γ formation to experimental results (see Section 4.4.3.2).

Evidence of these phases during lithiation of electrodes containing 8 and 32 nm Fe_3O_4 crystals at a C/200 rate is shown in Figure 4.4. The degree of lithiation (*i.e.*, lithiated capacity) is defined as the average moles of lithium inserted into one mole of Fe_3O_4 electrode material. For both curves, the plateaus at ~1.5 V and ~1.2 V correspond to β and γ formation, respectively. Note that these "plateaus" do not maintain a constant voltage during lithiation, which suggests that the formations of β and γ are *non-instantaneous*. The third plateau at ~0.8 V can be attributed to continual lithiation accompanied by electrolyte reduction [44]. To avoid uncertainty associated with the electrolyte reduction, the analysis of phase change is restricted to lithiation above 1.0 V. Differences in the degree of lithiation at which these three plateaus are observed can be attributed to lithium transport resistances that result in higher local solid-state concentrations within the electrodes containing 32 nm crystals [24]. For instance, the inset in the figure plots the experimental voltage versus the maximum solid-state lithium concentration predicted by the multi-scale model given in Section 4.4.3. The data was obtained by cross-

referencing the experimental voltage at a given degree of lithiation to the predicted maximum solid-state concentration at that same degree of lithiation. The results indicate that the voltage plateaus for the 8 and 32 nm crystals correspond to the same maximum solid-state concentration in the electrode.

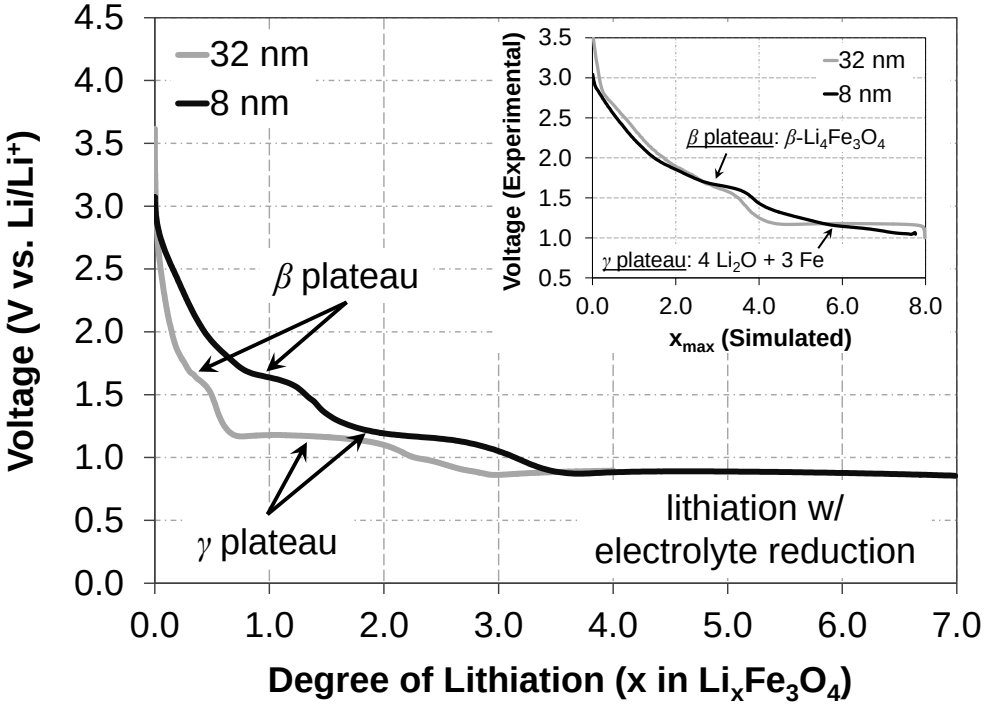

Figure 4.4. Lithiation of pristine electrodes comprised of 8 and 32 nm crystals at a C/200 rate. Inset: Plot of experimental voltage vs. maximum solid-state concentration predicted by model during lithiation (see Section 4.4.3 for model details).

4.4.2 Phase Change from α-$Li_xFe_3O_4$ to β-$Li_4Fe_3O_4$

4.4.2.1 Formulation with β-$Li_4Fe_3O_4$ Phase

The phase change from α-$Li_xFe_3O_4$ to β-$Li_4Fe_3O_4$ is simulated by incorporating the kinetic description in Eq. 4.1 into the multi-scale model developed in Chapter 2. A comparison of the governing equations and boundary conditions with and without phase change is provided

in Tables 4.1 and 4.2. The two formulations are identical in the agglomerate length-scale. Differences in the formulations arise in the treatment of mass transport and phase formation on the crystal length-scale. In the phase change model, the β phase is assumed to undergo a non-instantaneous formation according to the following process:

$$\underbrace{\mathrm{LiFe_3O_4}}_{\alpha} + \mathrm{xLi^+} + \mathrm{xe^-} \rightleftharpoons \underbrace{\mathrm{Li_{1+x}Fe_3O_4}}_{\alpha} \tag{4.9}$$

$$\underbrace{\mathrm{Li_{1+x}Fe_3O_4}}_{\alpha} \rightleftharpoons \mathrm{y}\underbrace{\mathrm{LiFe_3O_4}}_{\alpha} + (1-y)\underbrace{\mathrm{Li_4Fe_3O_4}}_{\beta}, \text{ where } y = 1 - \frac{x}{3} \tag{4.10}$$

Equations 4.9 and 4.10 are formulated to show that phase change only occurs when $x > 1$ in the α phase. To determine the volume fraction of the β phase, the kinetic description in Eq. 4.4 can be rewritten as follows:

$$\begin{aligned} \frac{\partial \theta_\beta}{\partial t} &= k_\beta \left(c_\alpha - c_{\alpha,sat}^\beta\right) \theta_\beta^{2/3} \left(1 - \theta_\beta\right) \\ k_\beta &= k_{\beta,1}\left(1 + k_{\beta,2} c_\alpha\right) \end{aligned} \tag{4.11}$$

where $c_{\alpha,sat}^\beta$ is the saturation concentration in α at which β starts to form. The volume fraction of α phase is calculated from a conservation of mass assuming negligible variations in the size of the unit cells of the two phases:

$$\theta_\alpha + \theta_\beta = 1 \tag{4.12}$$

To calculate the distribution of solid-state lithium in the crystal, it is assumed that lithium can only move through the α phase. A mass balance on the total lithium in the α phase yields the following:

$$\left(1 - \theta_\beta\right)\frac{\partial c_\alpha}{\partial t} = \nabla \cdot \left(D_{x,eff} \nabla c_\alpha\right) + \left(c_\alpha - c_\beta\right)\frac{\partial \theta_\beta}{\partial t} \tag{4.13}$$

which is formulated based on the same assumption used to develop Eq. 4.6 – *i.e.*, that the lithium concentration in the newly formed β phase is constant. The effective diffusion coefficient, $D_{x,eff,}$ in Eq. 4.13 is defined as:

$$D_{x,eff} = \theta_{\alpha} D_{x,\alpha} \tag{4.14}$$

The total concentration of solid-state lithium, c_x, at a given location in a crystal can be calculated from:

$$c_x = c_{\alpha}\theta_{\alpha} + c_{\beta}\theta_{\beta} \tag{15}$$

In addition, this formulation assumes only the α phase is electrochemically active. To account for this assumption, slight variations were made to the kinetic expressions and the boundary conditions at the crystal surface, which are provided in Tables 4.1 and 4.2.

The last difference between the models with and without phase change is the expression used to model the open circuit potential of the system. According to the schematic in Figure 4.1, the open circuit potential during discharge of a system with phase change depends on the degree of supersaturation of the α phase. Therefore, an expression is needed for the open circuit potential as a function of the concentration of solid-state lithium in the α phase, c_{α}. This expression is obtained by fitting a thermodynamic equation to a set of experimental data obtained from the voltage recovery experiments. The procedure for the fitting is provided in Section 4.6. The experimental data are obtained by exploiting the fact that the voltage recovery curves (see inset in Figure 4.3 for example) have two characteristic regions. During the first ~200 hours, there is a voltage recovery that can be attributed to the relaxation of concentration profiles in the agglomerate and crystal length-scales (see Chapter 3). Afterwards, there is a slower, seemingly linear recovery at long times that can be attributed to phase change. Assuming that the concentration distributions relax more quickly than the phase transformation, at the start of the

linear region of the recovery curve, Fe_3O_4 mostly exists in the α phase. Therefore, at this point, $c_\alpha \sim c_x$. The open circuit potential in the α phase at each degree of lithiation can then be approximated using the voltage at this point.

Table 4.1. Comparison of governing equations used in models with and without phase change.

	w/o β Formation (Ch. 2)	**w/ β Formation**
Mass (agg.)	$\varepsilon \frac{\partial c_{agg}}{\partial t} = \varepsilon D_{agg} \nabla^2 c_{agg} + \frac{a i_{rxn}}{F}$	No change
Mass (crystal)	$\frac{\partial c_x}{\partial t} = D_x \nabla^2 c_x$	$\left(1-\theta_\beta\right)\frac{\partial c_\alpha}{\partial t} = \nabla \cdot \left(D_{x,eff} \nabla c_\alpha\right) + \left(c_\alpha - c_\beta\right)\frac{\partial \theta_\beta}{\partial t}$
	-	$c_x = c_\alpha \theta_\alpha + c_\beta \theta_\beta$
Phase	-	$\frac{\partial \theta_\beta}{\partial t} = k_\beta \left(c_\alpha - c_{\alpha,sat}^{\beta}\right)\theta_\beta^{2/3}\left(1-\theta_\beta\right)$
Charge	$a i_{rxn} = \left(1-\varepsilon\right)\sigma \nabla^2 \varphi_1$	No change
Reaction	$i_{rxn} = i_0\left[\exp\left(\frac{\alpha_a F\left(\varphi_1 - U\right)}{R_G T}\right) - \exp\left(\frac{-\alpha_c F\left(\varphi_1 - U\right)}{R_G T}\right)\right]$	No change
	$i_0 = F k_{rxn} c_{agg}^{\alpha_a} c_x^{\alpha_c}\left(c_{x,\max} - c_x\right)^{\alpha_a}$	$i_0 = F k_{rxn} c_{agg}^{\alpha_a} c_\alpha^{\alpha_c}\left(c_{\alpha,\max} - c_\alpha\right)^{\alpha_a}$

Table 4.2. Comparison of boundary conditions used in models with and without phase change. r and $\bar{r}$ refer to units of distance in the agglomerate and crystal length-scales, respectively. r_{agg} and r_x are the radii of the agglomerate and crystals, respectively.

	w/o β Formation (Ch. 2)	**w/ β Formation**
Mass (agg.)	$\frac{\partial c_{agg}}{\partial r} = 0$ at $r = 0$	No change
	$c_{agg} = c_0$ at $r = r_{agg}$	
Mass (crystal)	$\frac{\partial c_x}{\partial \bar{r}} = 0$ at $\bar{r} = 0$	$\frac{\partial c_\alpha}{\partial \bar{r}} = 0$ at $\bar{r} = 0$
	$-D_x \frac{\partial c_x}{\partial \bar{r}} = \frac{i_{rxn}(r)}{nF}$ at $\bar{r} = r_x$	$-D_{x,eff} \frac{\partial c_\alpha}{\partial \bar{r}} = \frac{\theta_\alpha i_{rxn}(r)}{nF}$ at $\bar{r} = r_x$
Charge	$\frac{\partial \varphi_1}{\partial r} = 0$ at $r = 0$	No change
	$\frac{\partial \varphi_1}{\partial r} = \frac{i_{app}\rho_{Fe_3O_4} r_{agg}}{3\sigma}$ at $r = r_{agg}$	

The parameters used to model the phase change and mass transport are provided in Table 4.3 along with the mass transport parameters used in the model without phase change. Values for all other parameters remain unchanged from Chapter 2. $c^{\beta}_{\alpha,sat}$, c_β, and $c_{\alpha,max}$ in Table 4.3 correspond to x = 1, x = 4, and x = 8 for x in $Li_xFe_3O_4$, respectively. This assumes that the α-$Li_xFe_3O_4$ phase can accept the theoretical maximum of 8 moles of lithium per mole of Fe_3O_4, which is not unlikely due to the existence of 64 open tetrahedral sites per unit cell of Fe_3O_4 [45]. Note the good agreement between the mass transport diffusion coefficients for both models. This agreement indicates that the addition of β formation does not change earlier conclusions that a

large portion of the voltage recovery results from the relaxation of concentration distributions in the agglomerate and crystal length scales (see Chapter 3).

Table 4.3. Parameters used in multi-scale simulations with and without phase change from α-$Li_xFe_3O_4$ to β-$Li_4Fe_3O_4$.

Symbol	Description	Value	
		w/o β (Ch. 2)	w/ β
D_{agg}	Diffusion in agglomerate ($cm^2\ s^{-1}$)[a]	2.3×10^{-13}	2.6×10^{-13}
D_x or $D_{x,\alpha}$	Diffusion in crystal ($cm^2\ s^{-1}$)[a]	2.0×10^{-18}	1.25×10^{-18}
$c_{x,max}$ or $c_{\alpha,max}$	Max concentration in crystal (mol cm^{-3})[b]	1.79×10^{-1}	1.79×10^{-1}
$k_{\beta,1}$	β phase rate constant 1 ($cm^3\ mol^{-1}\ s^{-1}$) [a]	-	1.0×10^{-5}
$k_{\beta,2}$	β phase rate constant 2 ($cm^3\ mol^{-1}$)[a]	-	60
$c_{\alpha,sat}^{\beta}$	Saturation concentration of α (mol cm^{-3})[b]	-	2.24×10^{-2}
c_β	Concentration in β (mol cm^{-3})[b]	-	8.94×10^{-2}

[a]fit to experimental data

[b]obtained from analysis of voltage recovery

4.4.2.2 Validation with Voltage Recovery Experiments

Figure 4.5 compares experimental data for voltage recovery experiments of electrodes comprised of 6 nm crystals to results for simulations with and without phase change. All simulations were conducted using the model formulation described herein. Simulations without phase formation were conducted by setting the rate constant $k_{\beta,1}$ equal to zero. Comparisons are shown for electrodes that were lithiated to an average concentration of x = 2.0 and 2.5 in $Li_xFe_3O_4$. At both degrees of lithiation, simulations with phase change show better agreement with experimental data. Both simulations (with and without phase change) capture the initial behavior during the first ~200 hours of the voltage recovery, which is attributed to the relaxation of concentration distributions within the agglomerate and crystal length-scales. However, only the model with phase change is able to capture the gradual rise in voltage at later times, which is

attributed to the rearrangement of the supersaturated α-$Li_xFe_3O_4$ phase into the lower energy, equilibrium phases of α-$LiFe_3O_4$ and β-$Li_4Fe_3O_4$. Similar results were obtained for electrodes comprised of 8 nm crystals. An analysis of the voltage recovery behavior of the electrodes comprised of 32 nm Fe_3O_4 was not conducted due to the early onset of γ-(4 Li_2O + 3 Fe) phase formation during the lithiation process.

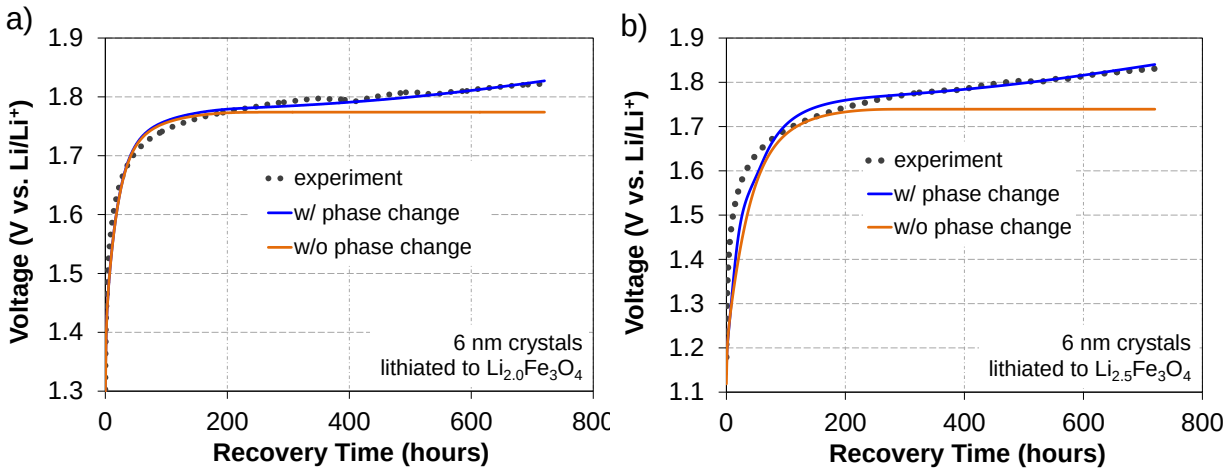

Figure 4.5. Comparison of experimental voltage recovery data to simulated results from models with and without phase change from α to β. Data is shown for recovery after lithiation to average concentrations of a) x = 2 and b) x = 2.5 in $Li_xFe_3O_4$ at a C/200 rate.

In addition to the examples at x = 2.0 and 2.5 in Figure 4.5, Figures 4.6 and 4.7 demonstrate how the model with β-$Li_4Fe_3O_4$ phase formation improves agreement with the voltage recovery experiments from x = 0.5 to 3.0. Figures 4.6 and 4.7 compare experimental data to simulated results for two parameters used to describe the voltage recovery: the rise time and the maximum change in voltage. The rise time is defined as the time it takes the voltage to reach 90% of its maximum value during recovery. Qualitatively similar results were observed for all definitions of the rise time between 85% and 95% of the maximum voltage. In Figure 4.6,

simulations with and without phase change show good agreement at low degrees of lithiation (x < 2.0) where the amount of β formation is expected to be low because the level of supersaturation in the α phase is low. At higher degrees of lithiation, where the level of supersaturation in the α phase is high, only the simulations with β formation are able to capture the experimental trends in rise time. Similarly, for the maximum change in voltage during recovery (Figure 4.7), both simulations show good agreement at low degrees of lithiation, but only the model with phase change is able to capture the performance at higher degrees of lithiation. For instance, the simulations without phase change under predict the voltage change for all recoveries where x > 1.5.

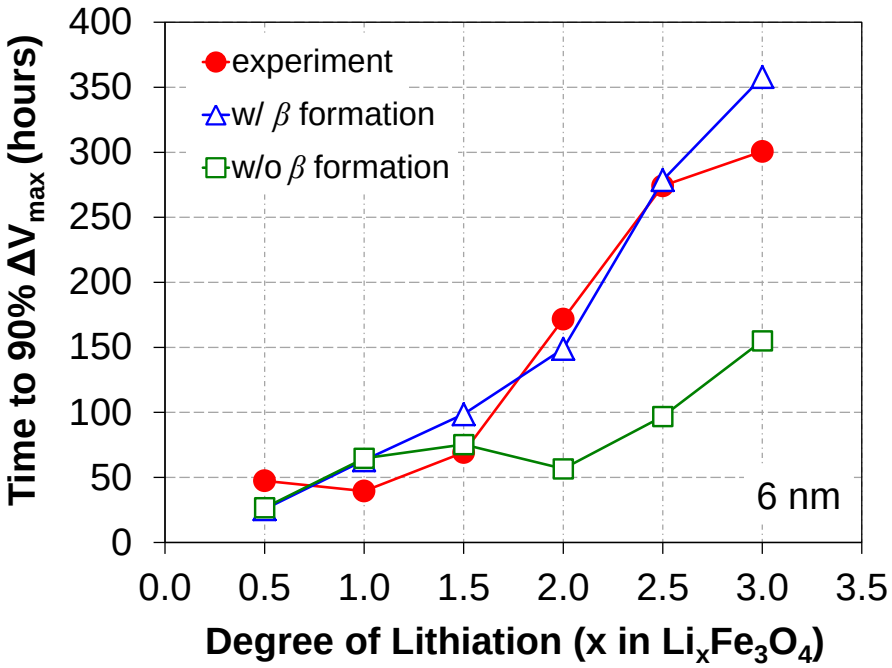

Figure 4.6. Rise time during voltage recovery, which is defined as the time required to reach 90% of the maximum voltage.

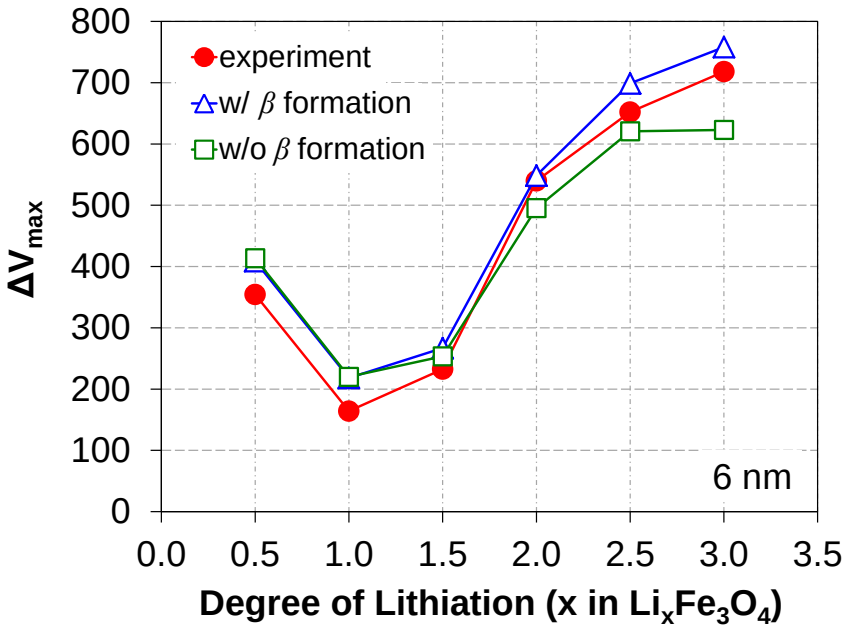

Figure 4.7. Maximum change in voltage during voltage recovery.

4.4.2.3 Distributions during Voltage Recovery

This section provides a more detailed description of the voltage recovery process by analyzing the predicted distributions of solid-state lithium (c_x, c_α) and volume fraction of α-$Li_xFe_3O_4$ (θ_α) within the agglomerate. These distributions are shown in Figure 4.8 for the simulation of an agglomerate comprised of 6 nm crystals that was lithiated to an average concentration of x = 2.5 in $Li_xFe_3O_4$. The times correspond to the start of the recovery process. All of the variables (c_x, c_α, and θ_α) correspond to the average value within a crystal at a given location in the agglomerate. r and r_{agg} refer to the distance from the center of the agglomerate and the agglomerate radius, respectively. Figure 4.8a shows the distribution of the volume fraction of α phase. The simulations indicate that, at the start of the recovery, Fe_3O_4 is almost entirely in the α phase even though the concentration of solid-state lithium (Figure 4.8b) is well above the saturation value (x = 1). This occurs because of the slow kinetics of β phase formation, which produced <1% of β phase during the 63-hour lithiation process. During the first 90 hours

of the recovery, the α phase starts to transform into β phase near the outside of the agglomerate (Fig. 4.8a) while the solid-state concentration in the α phase begins to redistribute towards a uniform concentration (Fig. 4.8b). The redistribution in the α phase is controlled by mass transport of lithium ions through the pores of the agglomerate (see Chapter 3). The majority of the β phase is formed near the edge of the agglomerate because, initially, the α phase is at a higher supersaturated concentration at that location. The higher concentration arises because mass transport resistances restrict the lithiation reaction towards the outside of the agglomerate during discharge.

Between 180 and 360 hours, the concentration in the α phase completely relaxes to a uniform value. This corresponds to the end of the initial region of the voltage recovery described by the inset in Figure 4.3. After this time, the concentration continues to change, which is caused by the formation of β phase. The concentration decreases as β phase is formed because the solid-state concentration in the β phase is higher ($x = 4$) than the concentration in the α phase (see Eq. 4.13). This period corresponds to the slow, linear portion of the recovery (see Figure 4.5b). At the end of the 30 day recovery (720 hours), the model predicts 43% of Fe_3O_4 is in the β phase. Note that because of the uneven distribution of β within the agglomerate, at the end of recovery, the concentration of total solid-state lithium (c_x) is higher at the edge of the agglomerate (see inset in Figure 4.8b).

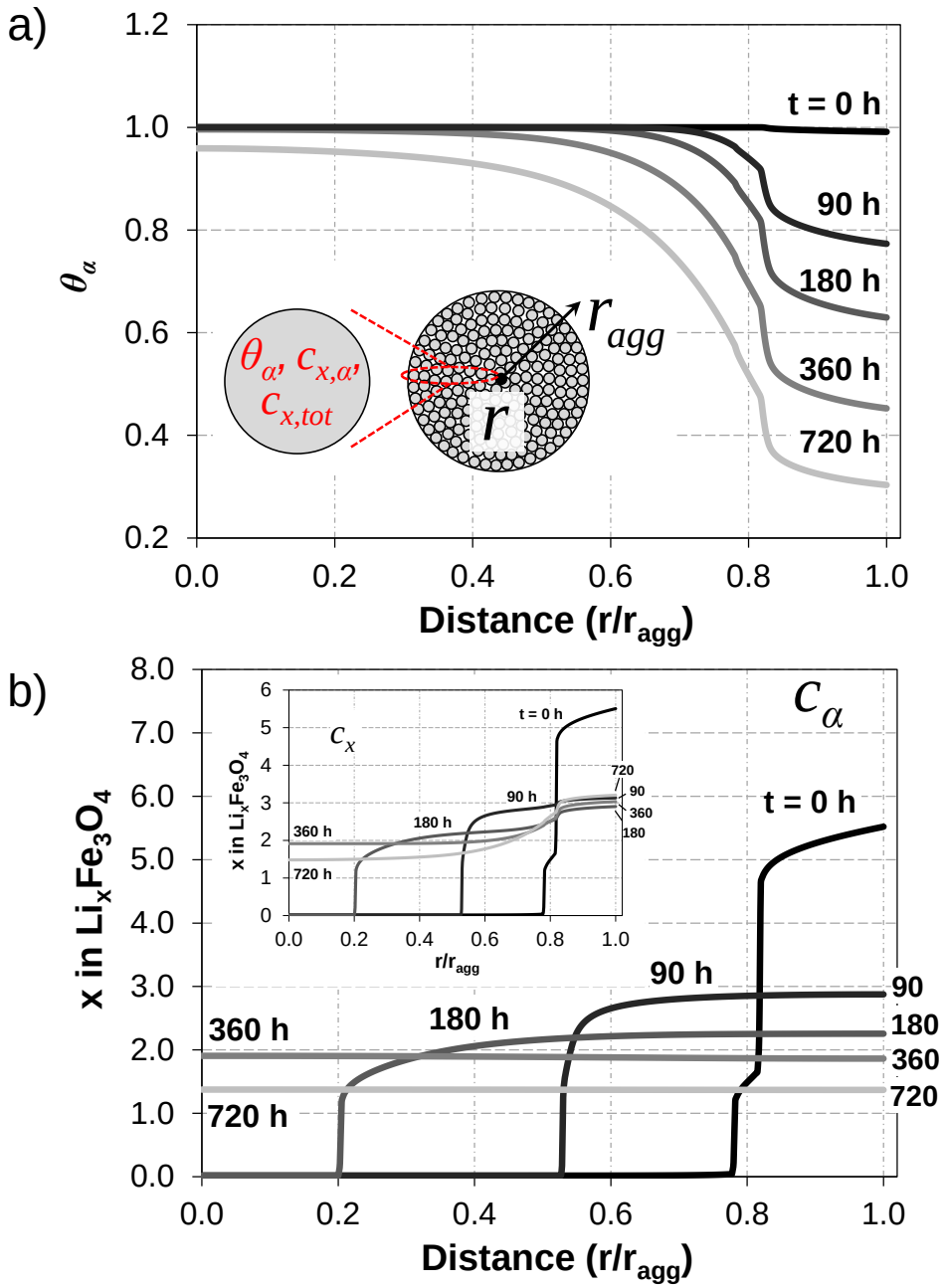

Figure 4.8. Distributions of a) θ_α and b) c_α within agglomerate during recovery of an agglomerate comprised of 6 nm crystals after a lithiation to an average concentration of x = 2.5 in $Li_xFe_3O_4$. Times are reported with respect to the start of recovery. Inset in b): Distribution of the total solid-state lithium concentration in both the α and β phases.

4.4.3 Conversion from α-$Li_xFe_3O_4$ to γ-(4Li_2O+3Fe)

According to the previous section, the rate of β formation is slow with almost no β forming during the lithiation of the electrode. Due to the absence of β phase, it is unlikely that the γ "phase" (which is comprised of Li_2O + Fe metal) forms from β-$Li_4Fe_3O_4$. Instead, we hypothesize that the γ phase forms directly from α-$Li_xFe_3O_4$. Therefore, in order to explain the behavior of Fe_3O_4 electrodes during lithiation to 1.0 V, a version of the multi-scale model was formulated, which incorporated the phase change from of α to γ (without any β phase).

4.4.3.1 Formulation with γ-(4 Li_2O + 3 Fe)

In this formulation, the γ-(4 Li_2O + 3 Fe) is assumed to undergo a non-instantaneous formation from the α phase according to the following process:

$$\underbrace{Li_4Fe_3O_4}_{\alpha} + xLi^+ + xe^- \rightleftharpoons \underbrace{Li_{4+x}Fe_3O_4}_{\alpha} \tag{4.16}$$

$$\underbrace{Li_{4+x}Fe_3O_4}_{\alpha} \rightleftharpoons y\underbrace{Li_4Fe_3O_4}_{\alpha} + (1-y)\underbrace{(4Li_2O + 3Fe)}_{\gamma}, \text{ where } y = 1 - \frac{x}{4} \tag{4.17}$$

Equations 4.16 and 4.17 are formulated to show that γ formation only occurs when $x > 4$ in the α phase. This value of x was determined by fitting the model to experimental data (see Figure 4.9 and related discussion). The governing equations and boundary conditions for the model with γ are almost identical to the equations for β phase formation (see Tables 4.1 and 4.2). Changes are only made to the values of the constants used to solve for the mass transport in the crystal and the phase change. These equations are rewritten for the model with γ formation as follows:

$$(1-\theta_\gamma)\frac{\partial c_\alpha}{\partial t} = \nabla \cdot (D_{x,eff}\nabla c_\alpha) + (c_\alpha - c_\gamma)\frac{\partial \theta_\gamma}{\partial t} \tag{4.18}$$

$$c_x = c_\alpha \theta_\alpha + c_\gamma \theta_\gamma \tag{4.19}$$

$$\frac{\partial \theta_\gamma}{\partial t} = k_\gamma \left(c_\alpha - c_{\alpha,sat}^{\gamma} \right) \theta_\gamma^{2/3} \left(1 - \theta_\gamma \right) \tag{4.20}$$

The major difference between the models is the definition of the effective diffusion coefficient. Recent investigations using in situ TEM have revealed that, even after a shell of γ "phase" (Li_2O + Fe metal) forms around a nanocrystal of Fe_3O_4, the inside of the crystal continues to lithiate [23]. This suggests that lithium ions are able to diffuse through γ-(4 Li_2O + 3 Fe). One possible mechanism of diffusion is between the grain boundaries of the nanosized structures of Li_2O and Fe metal [46]. To account for this additional pathway for lithium transport, the effective diffusion coefficient is defined as:

$$D_{x,eff} = \theta_\alpha D_{x,\alpha} \left(1 - \frac{c_\alpha}{c_{\alpha,\max}} \right) + \theta_\gamma D_{x,\gamma} \tag{4.21}$$

$$\text{where, } \theta_\alpha + \theta_\gamma = 1 \tag{4.22}$$

Equation 4.21 was developed assuming there are two pathways which solid-state lithium (c_α) can transport through the crystal: *i)* diffusion through the α phase and *ii)* diffusion through the nanograins of the γ structure. The equation was formulated using an equivalent circuit model with both pathways existing in parallel. In addition, the effective diffusion coefficient ($D_{x,eff}$) includes a relation of ($1 - c_\alpha/c_{\alpha,max}$) within the α phase. This relation has been previously used in battery simulations to account for a decrease in the diffusivity at higher concentrations of solid-state lithium, which results from a decline in the number of lattice sites available for diffusion [32, 47].

4.4.3.2 Model Parameterization and Analysis

The mass transport and phase-change parameters for the simulations with γ formation are provided in Table 4.4. The values of all other parameters and constants are unchanged from the previously developed model (see Chapter 2). The diffusion coefficient in γ ($D_{x,\gamma}$) was selected to approximate "infinitely" fast diffusion when compared to diffusion in the α phase. The supersaturation value at which γ forms from the α phase ($c^{\gamma}_{\alpha,sat}$) was determined by fitting simulations to experimental data for lithiation of 32 nm Fe_3O_4 at C/200. The results of the fitting are shown in Figure 4.9. Best agreement was obtained for a solid-state lithium concentration of x = 4, for x in $Li_xFe_3O_4$.

Table 4.4. Parameters used in multi-scale simulations with phase change from α-$Li_xFe_3O_4$ to γ-(4 Li_2O + 3 Fe).

Symbol	Description	Value
D_{agg}	Diffusion in agglomerate ($cm^2\ s^{-1}$)[a]	2.6×10^{-13}
$D_{x,\alpha}$	Diffusion in α phase ($cm^2\ s^{-1}$)[a]	1.25×10^{-18}
$D_{x,\gamma}$	Diffusion in γ phase ($cm^2\ s^{-1}$)[a]	5.0×10^{-17}
$c_{\alpha,max}$	Max concentration in crystal (mol cm^{-3})[b]	1.79×10^{-1}
k_γ (6 nm)	γ phase rate constant ($cm^3\ mol^{-1}\ s^{-1}$) [a]	0.8×10^{-3}
k_γ (32 nm)	γ phase rate constant ($cm^3\ mol^{-1}\ s^{-1}$)[a]	2.5×10^{-3}
$c^{\gamma}_{\alpha,sat}$	Saturation concentration of α (mol cm^{-3})[a]	8.94×10^{-2}
c_γ	Concentration in γ (mol cm^{-3})[b]	1.79×10^{-1}

[a]fit to experimental data
[b]obtained from analysis of voltage recovery

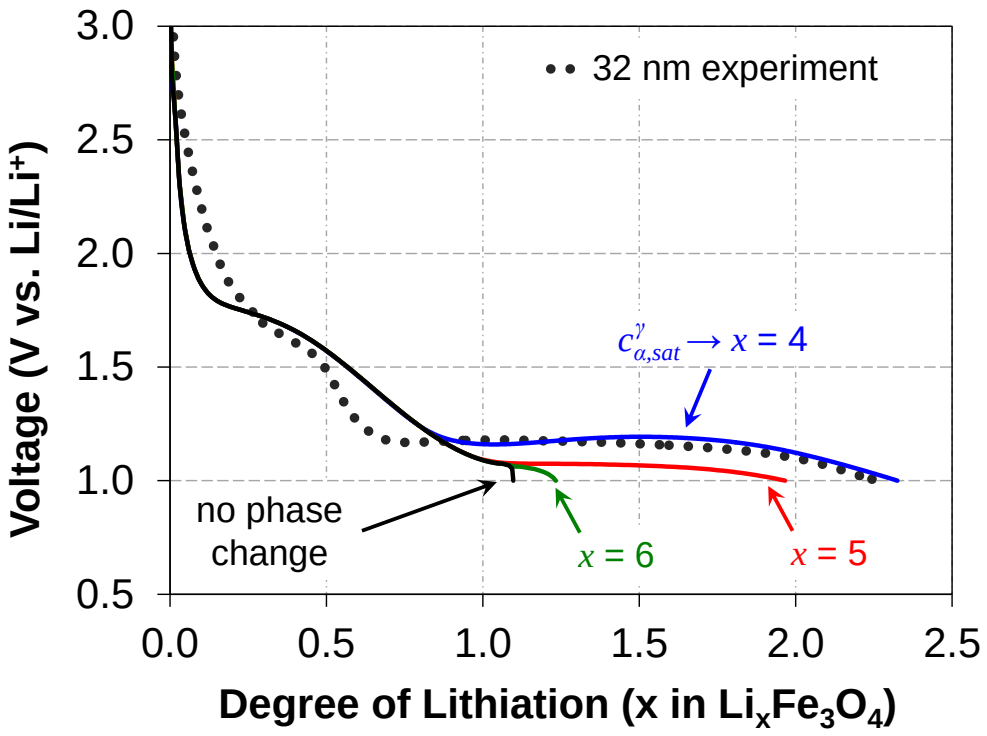

Figure 4.9. Comparison of experimental data to multi-scale simulations with different values for the saturation concentration at which γ starts to form from α. All other parameters remain unchanged from Table 4.4. Experiments and simulations were conducted at a C/200 rate for electrodes comprised of 32 nm crystals.

Figure 4.10 shows how the inclusion of the $(1 - c_\alpha/c_{\alpha,max})$ relation in the definition of the effective diffusion coefficient (Eq. 4.21) improves the simulated results. The figure compares simulations to experimental data for lithiation of 32 nm Fe_3O_4 at C/200. Both simulations were run using the γ-model with the same parameters, constants, and governing equations. The only difference between the simulations is whether or not the $(1 - c_\alpha/c_{\alpha,max})$ relation is included in the definition of the effective diffusion coefficient (Eq. 4.21). According to Figure 4.10, the simulation with the $(1 - c_\alpha/c_{\alpha,max})$ relation shows much better agreement with experimental data, especially during lithiation up to $x = 1$. Without this term, the model under predicts the decrease

in voltage at the onset of lithiation. This suggests that the initial decrease in voltage before the phase-change plateau is accelerated by an increase in the mass transport resistances of solid-state lithium within the crystal. Note that slight deviations still exist between the experiments and the model with the $(1 - c_\alpha/c_{\alpha,max})$ relation. These deviations likely result from an oversimplification of the relationship between solid-state concentration and diffusivity. For instance, studies have shown that the solid-state diffusion coefficient of lithium in graphite can be expressed by a series of exponential relations, which depend on the solid-state lithium concentration [48].

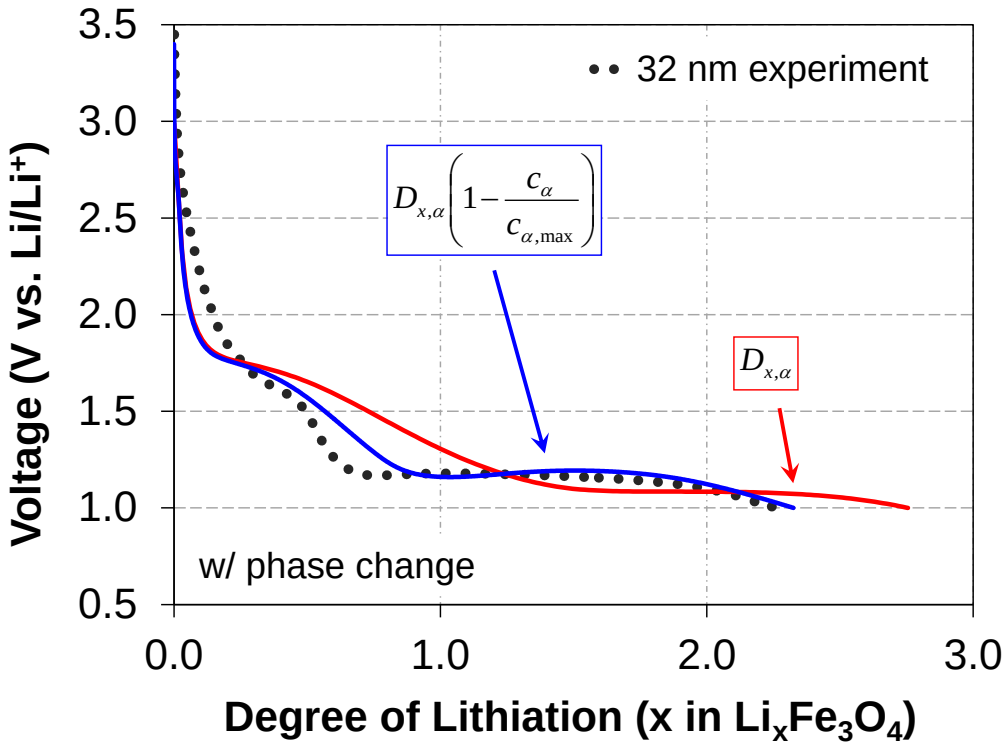

Figure 4.10. Comparison of experimental data to multi-scale simulations with and without the $(1 - c_\alpha/c_{\alpha,max})$ relation in the definition of the effective solid-state diffusion coefficient (Eq. 4.12). All other parameters remain unchanged from Table 4.4. Experiments and simulations were conducted at a C/200 rate for electrodes comprised of 32 nm crystals.

4.4.3.3 Lithiation of 6 and 32 nm Fe_3O_4

Comparisons of simulations to experiments during the lithiation of 6 and 32 nm Fe_3O_4 at C/200 is shown in Figure 4.11. Three simulations were conducted for each crystal size: *i)* no γ formation, *ii)* γ formation with the rate constant fit to the 6 nm experiments (k_γ = 0.8 × 10^{-3} cm^3 mol^{-1} s^{-1}), and *iii)* γ formation with the rate constant fit to the 32 nm experiments (k_γ = 2.5 × 10^{-3} cm^3 mol^{-1} s^{-1}). The results indicate that the rate constant associated with γ formation decreases as the size of the Fe_3O_4 crystal decreases. Therefore, the rate of γ formation is predicted to decrease as the size of the crystal decreases. This trend is in agreement with other nanoscale lithiation materials. For instance, decreasing the crystal size in the nanoscale regime of both $FePO_4$ and TiO_2 has been shown to suppress phase separation [49, 50]. It has been suggested that phase separation is suppressed because the surface strain between the two phases becomes energetically too costly for the smaller crystals [49].

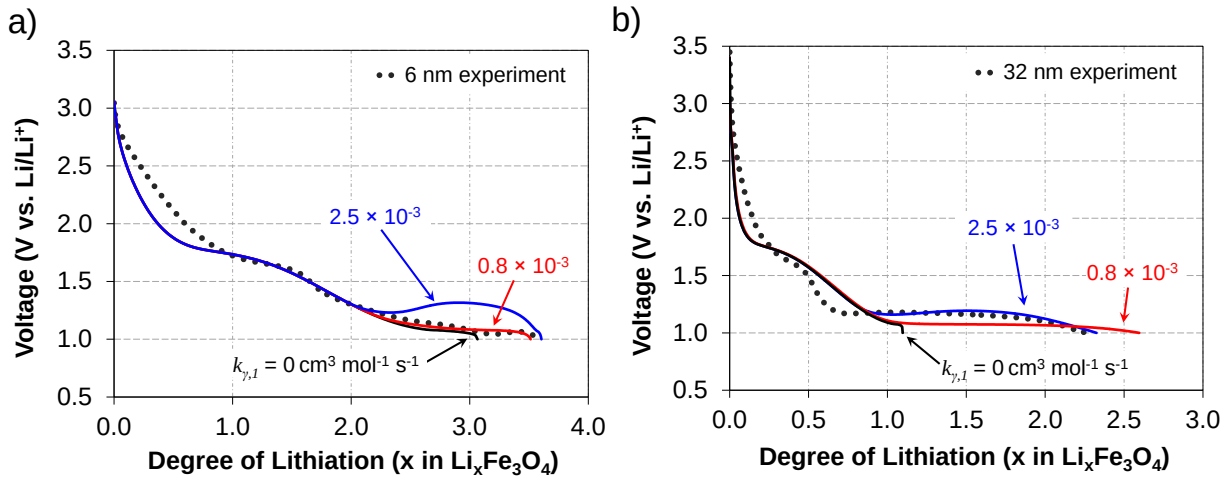

Figure 4.11. Voltage profiles during lithiation of electrodes containing a) 6 and b) 32 nm Fe_3O_4 crystals at a C/200 rate. Simulations are shown on each figure for different rate constants for the formation of the γ structure.

In addition to impacting the rate constant associated with formation of γ, the size of the crystal impacts the onset of the conversion process, where the onset is measured in reference to the total number of coulombs passed into the electrode. The onset of γ formation occurs earlier in the electrodes with larger crystals because of an increase in the solid-state transport limitations. For example, Figure 4.12 shows predicted profiles of the volume fraction of the α phase in the crystal at the edge of the agglomerate. Simulations were conducted using the best fit values for k_γ (*i.e.*, 0.8×10^{-3} and 2.5×10^{-3} for 6 and 32 nm crystals, respectively). The crystal at the edge of the agglomerate was chosen because it has the highest degree of lithiation in the agglomerate, which results in the maximum amount of phase change. In the figure, r_x and $\bar{r}$ are the radius of the crystal and the distance from the center of the crystal, respectively. The x_{avg} label corresponds to the degree of lithiation (*i.e.,* lithiated capacity) and is defined as the average moles of lithium inserted into one mole of Fe_3O_4 electrode material. The profiles for the electrodes with 6 nm crystals (Figure 4.12a) indicate that the conversion from α to γ starts at $x_{avg} \sim 2.75$. Once initiated, the conversion occurs relatively uniformly within the crystal due to small mass transport limitations (see Chapter 3). In contrast, the profiles for the 32 nm crystals (Figure 4.12b) indicate that conversion from α to γ starts at $x_{avg} \sim 1.0$. The early onset of γ formation arises because of large transport limitations within the 32 nm crystals. The large transport limitations result in concentration gradients with higher solid-state lithium concentrations near the edge of the crystal, which drive γ formation (see Chapter 3). The presence of concentration gradients also explains the non-uniformity in the distribution of θ_α within the crystal. For instance, when the cutoff voltage of 1.0 V is reached, phase formation has only occurred in the outermost 20% of the crystal radius because the innermost region was at a solid-state lithium concentration below the supersaturated concentration, $c^{\gamma}_{\alpha,sat}$.

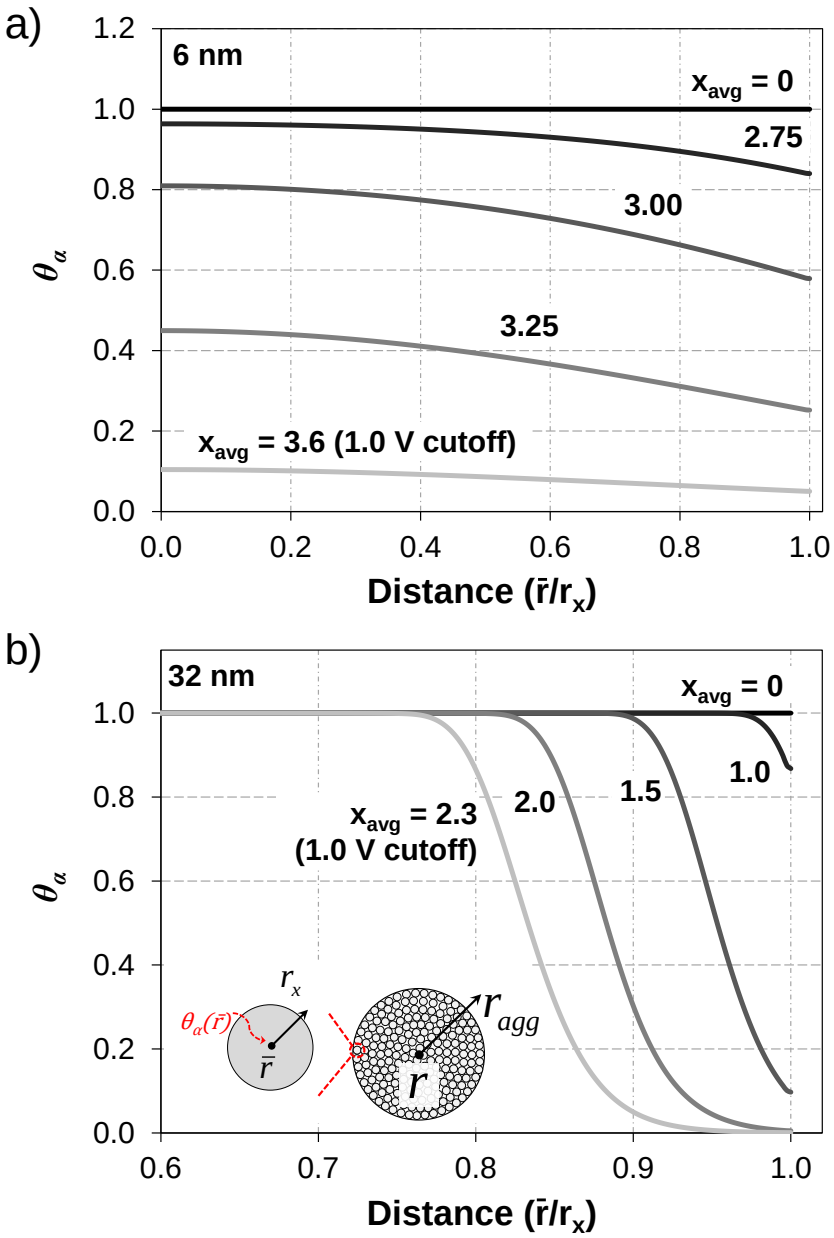

Figure 4.12**.** Predicted distributions of the volume fraction of α phase in the crystal at the outermost edge of the agglomerate. Distributions were obtained from simulations with a) 6 and b) 32 nm Fe_3O_4 crystals. Simulations were conducted using the best fit values for k_γ (*i.e.*, 0.8 × 10^{-3} and 2.5 × 10^{-3} for 6 and 32 nm crystals, respectively). x_{avg} label corresponds to the degree of lithiation in Figure 11, where x refers to the average moles of lithium inserted into one mole of Fe_3O_4 electrode material.

Simulations of the lithiation to 1.0 V were also conducted using a model which incorporated phase formation from α to β and α to γ. The model was formulated with the same kinetic descriptions of phase formation defined in Equations 4.11 and 4.20. No changes were made to the values of parameters and constants given in Tables 4.3 and 4.4. The objective was to test the assumption that there is negligible β formation during lithiation, and, therefore, γ must be directly formed from the α phase. The resulting simulations predict negligible formation of β phase during the lithiation of the 6 and 32 nm crystals to the 1.0 V cutoff voltage. For instance, when the cutoff voltage is reached, the maximum volume fraction of β phase (*i.e.*, the value of θ_β at the edge of the crystal at the edge of the agglomerate) for electrodes comprised of 6 and 32 nm crystals is 6% and 0.4%, respectively. These small fractions of β phase produced negligible variations in the voltage profile. Therefore (and for brevity), no simulation data are shown.

4.5. Summary

In this work, a combined experimental and theoretical approach is used to describe the phase changes occurring within magnetite (Fe_3O_4) during lithiation and voltage recovery. Data from voltage recovery experiments of 6, 8, and 32 nm Fe_3O_4 was utilized to identify the existence of three distinct materials, defined as: α-$Li_xFe_3O_4$, β-$Li_4Fe_3O_4$, and γ-(4 Li_2O + 3 Fe). The formation of the β and γ materials was incorporated into a multi-scale model, which accounted for mass transport in the agglomerate and crystal length scales. The kinetics of the phase formations were described by an expression derived from Avrami theory for nucleation and growth. It was concluded that the potential change observed at the start of the voltage recovery experiments is caused by the relaxation of concentration distributions in the agglomerate and crystal, while the slow, linear voltage change observed at long times is caused by a slow phase change from α-$Li_xFe_3O_4$ to β-$Li_4Fe_3O_4$. In addition, it was concluded that

negligible amounts of β phase formed during lithiation of Fe_3O_4 to a 1.0 V cutoff due to the slow kinetics of phase change. Furthermore, simulations of the lithiation process indicate that the voltage plateau at ~1.2 V can be attributed to the formation of γ-(4 Li_2O + 3 Fe) from α-$Li_xFe_3O_4$. These simulations also indicated that the rate of γ formation is suppressed as the size of the nanocrystalline Fe_3O_4 is decreased, which is in agreement with previous studies on other nanocrystalline, lithium host materials.

4.6. Appendix A: Open Circuit Potential for α-$Li_xFe_3O_4$ Phase

An equation for the open circuit potential of the α-$Li_xFe_3O_4$ phase as a function of the degree of supersaturation was obtained by fitting a thermodynamic expression derived from Karthikeyan *et al*. to experimental voltage recovery data [51]. The equation was derived based on the Redlich-Kister expression for the excess Gibbs free energy. It includes a Nernstian dependence on both the concentration of lithium ions in the agglomerate and the concentration of solid-state lithium in the α phase, with an activity correction for non-idealities in the α phase. It is defined as follows:

$$U = U_{ref} + \frac{R_G T}{F} \ln\left[\left(\frac{c_{agg}}{c_0}\right)\left(\frac{(1-x_\alpha)}{x_\alpha}\right)\right] + \sum_{k=0}^{N} A_k \left[(2x_\alpha - 1)^{k+1} - \frac{2x_\alpha k(1-x_\alpha)}{(2x_\alpha - 1)^{1-k}}\right];\ x_\alpha = \frac{c_\alpha}{c_{\alpha,\max}} \qquad (4.23)$$

The experimental data for the supersaturated α phase was approximated using the points on the voltage recovery curves where the recovery transitions from the initial region, where the voltage change is rapid, to the later region, where the voltage change is slow and seemingly linear (see inset in Figure 4.3). This point was assumed to represent the portion of the recovery experiment where the concentration distributions have completely relaxed, but there is still minimal phase formation. Under these assumptions, the degree of lithiation and voltage at this point correspond to the degree of supersaturation of the α phase and the open circuit potential at

that degree of supersaturation, respectively. Further discussion on these assumptions is provided in Section 4.4.2.1. The point where the voltage recovery curve transitions into the linear region is determined mathematically based on the change in voltage (dV/dt) of the recovery experiments. The time at which this occurs is defined as the first point during the voltage recovery experiment where dV/dt is less than twice dV/dt at the end of the recovery experiments (first time when $dV/dt < 2(dV/dt)_{end}$).

The maximum voltage during recovery and the supersaturated voltage defined using the above criteria are provided in Figure 4.13 Both sets of data represent the average obtained from the experiments conducted with 6, 8, and 32 nm Fe_3O_4 crystals. The error bars represent the maximum and minimum deviation from the average. Also included in the figure are the values predicted by the equation for the open circuit potential, which was determined by fitting Eq. 4.23 to the data for the supersaturated α phase. The values of the constants in the fit are provided in Table 4.5.

Table 4.5. Parameters determined for the equation of the open circuit potential of the α phase derived from the Redlich-Kister expansion.

Parameter	Value
N	7
U_{ref}	1.518
A_0	-0.6472
A_1	0.1283
A_2	0.3218
A_3	0.1577
A_4	-0.6670
A_5	0.3445
A_6	0.1228
A_7	-0.1405

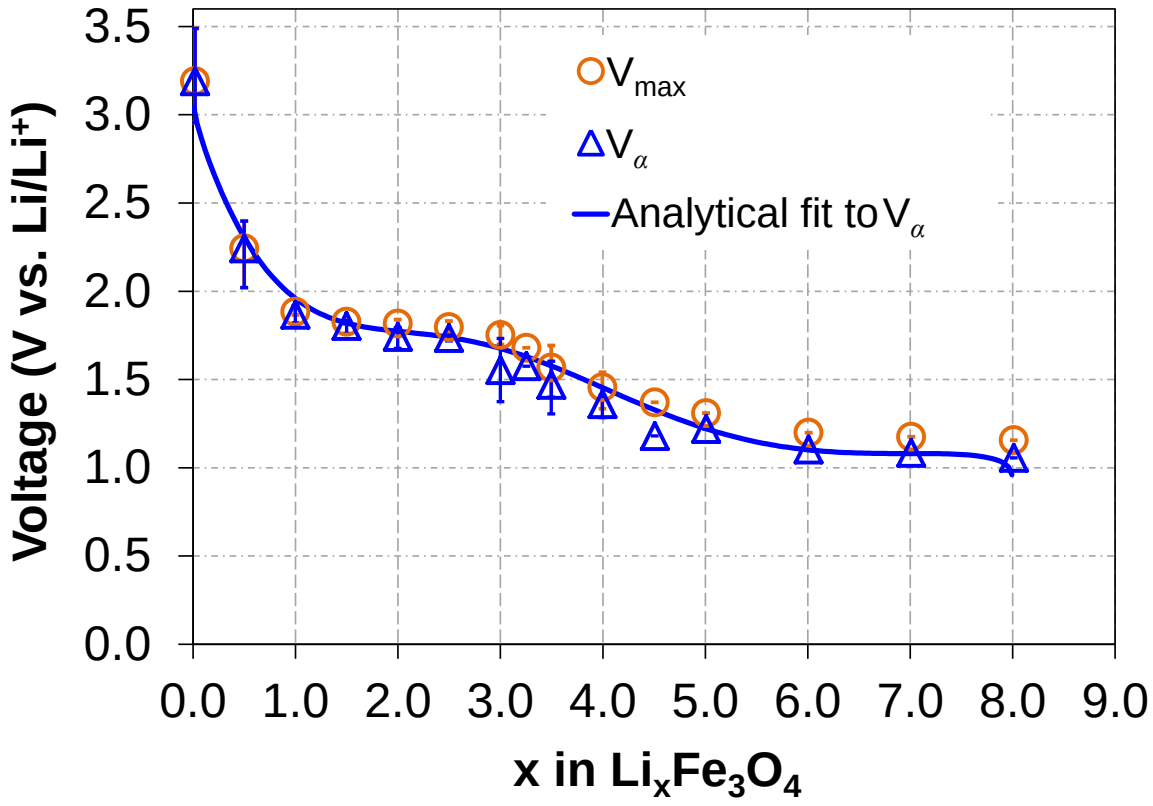

Figure 4.13**.** Maximum voltage (V_{max}) and voltage used to determine the open circuit potential of the supersaturated α phase (V_{α}). All voltage obtained from recovery experiments. Data points represent the average value of the 6, 8,and 32 nm experiments and the error bars represent the maximum and minimum deviation from average.

4.7. List of Symbols

a	specific surface area ($cm^2\ cm^{-3}$)
c_{agg}	lithium concentration in the agglomerate (mol cm^{-3})
$c_{\alpha,sat}^{\beta}$	concentration at which β begins to form from α (mol cm^{-3})
$c_{\alpha,sat}^{\gamma}$	concentration at which γ begins to form from α (mol cm^{-3})
c_0	bulk concentration in the electrolyte (mol cm^{-3})

c_x total solid-state lithium concentration (mol cm^{-3})

$c_{\alpha,\max}$ maximum solid-state lithium concentration in α phase (mol cm^{-3})

D_{agg} diffusion coefficient in the agglomerate (cm^2 s^{-1})

D_x diffusion coefficient in crystal (cm^2 s^{-1})

f number fraction of agglomerates

F Faraday's constant (96,485 C mol^{-1})

i_{app} applied current (A g^{-1})

i_{rxn} reaction rate (A cm^{-2})

k_β, k_γ rate constant for phase formation (cm^{-3} mol^{-1} or cm^{-3} mol^{-1} s^{-1})

k_{rxn} reaction rate constant ($mol^{-1/2}$ $cm^{-1/2}$ s^{-1})

r radial position in the agglomerate (cm)

r_{agg} agglomerate radius (cm)

R_G ideal gas constant (8.314 J mol^{-1} K^{-1})

t time (s)

T temperature (K)

U equilibrium potential (V)

Greek

α_a, α_c anodic and cathodic charge transfer coefficients

ε porosity

φ_1 potential in the solid (V)

$\rho_{Fe_3O_4}$ density of magnetite (g cm^{-3})

σ conductivity of magnetite (S cm^{-1})

θ volume fraction of phase

Subscript

agg denotes agglomerate

α denotes alpha phase ($Li_xFe_3O_4$)

β denotes beta phase ($Li_4Fe_3O_4$)

γ denotes gamma phase (4 Li_2O + 3 Fe)

x denotes crystal

4.8. References

1. M. S. Whittingham, *Proc. IEEE*, **100**, 1518 (2012).
2. B. L. Ellis, K. T. Lee and L. F. Nazar, *Chem. Mater.*, **22**, 691 (2010).
3. G. G. Amatucci and N. Pereira, *J. Fluorine Chem.*, **128**, 243 (2007).
4. R. Malini, U. Uma, T. Sheela, M. Ganesan and N. G. Renganathan, *Ionics*, **15**, 301 (2009).
5. P. Poizot, S. Laruelle, S. Grugeon, L. Dupont and J. M. Tarascon, *Nature*, **407**, 496 (2000).
6. S. Kim, N. Pereira, N. A. Chernova, F. Omenya, P. Gao, M. S. Whittingham, G. G. Amatucci, D. Su and F. Wang, *Acs Nano*, **9**, 10076 (2015).
7. L. Li, R. Jacobs, P. Gao, L. Gan, F. Wang, D. Morgan and S. Jin, *J. Am. Chem. Soc.*, **138**, 2838 (2016).
8. D. C. Bock, K. C. Kirshenbaum, J. Wang, W. Zhang, F. Wang, J. Wang, A. C. Marschilok, K. J. Takeuchi and E. S. Takeuchi, *ACS Appl. Mater. Interfaces*, **7**, 13457 (2015).
9. A. Abraham, L. M. Housel, C. N. Lininger, D. C. Bock, J. Jou, F. Wang, A. C. West, A. C. Marschilok, K. J. Takeuchi and E. S. Takeuchi, *ACS Cent. Sci.*, **2**, 380 (2016).
10. S. Mitra, P. Poizot, A. Finke and J. M. Tarascon, *Adv. Funct. Mater.*, **16**, 2281 (2006).
11. S. K. V. Sivakumar, C. A. Ross, Y. Shao-Horn, *ECS Trans.*, **2**, 1 (2007).
12. Z. M. Cui, L. Y. Hang, W. G. Song and Y. G. Guo, *Chem. Mater.*, **21**, 1162 (2009).
13. S. Komaba, T. Mikumo, N. Yabuuchi, A. Ogata, H. Yoshida and Y. Yamada, *J. Electrochem. Soc.*, **157**, A60 (2010).
14. S. L. Zhu, A. C. Marschilok, E. S. Takeuchi and K. J. Takeuchi, *Electrochem. Solid-State Lett.*, **12**, A91 (2009).
15. S. L. Zhu, A. C. Marschilok, E. S. Takeuchi, G. T. Yee, G. B. Wang and K. J. Takeuchi, *J. Electrochem. Soc.*, **157**, A1158 (2010).
16. M. M. Thackeray, W. I. F. David and J. B. Goodenough, *Mater. Res. Bull.*, **17**, 785 (1982).

17. M. Thackeray, L. De Picciotto, A. De Kock, P. Johnson, V. Nicholas and K. Adendorff, *J. Power Sources*, **21**, 1 (1987).
18. J. Fontcuberta, J. Rodriguez, M. Pernet, G. Longworth and J. B. Goodenough, *J. Appl. Phys.*, **59**, 1918 (1986).
19. M. S. Islam and C. R. A. Catlow, *J. Solid State Chem.*, **77**, 180 (1988).
20. T. Yamada, K. Morita, K. Kume, H. Yoshikawa and K. Awaga, *J. Mater. Chem. C*, **2**, 5183 (2014).
21. W. Zhang, D. C. Bock, C. J. Pelliccione, Y. Li, L. Wu, Y. Zhu, A. C. Marschilok, E. S. Takeuchi, K. J. Takeuchi and F. Wang, *Adv. Energy Mater.*, **6**, 1502471 (2016).
22. M. C. Menard, K. J. Takeuchi, A. C. Marschilok and E. S. Takeuchi, *Phys. Chem. Chem. Phys.*, **15**, 18539 (2013).
23. K. He, S. Zhang, J. Li, X. Yu, Q. Meng, Y. Zhu, E. Hu, K. Sun, H. Yun, X.-Q. Yang, Y. Zhu, H. Gan, Y. Mo, E. A. Stach, C. B. Murray and D. Su, *Nat. Commun.*, **7**, 11441 (2016).
24. C. J. Pelliccione, D. C. Bock, W. Zhang, K. W. Knehr, A. C. West, F. Wang, Y. Li, E. S. Takeuchi, A. C. Marschilok and K. J. Takeuchi, *in review* (2016).
25. H. Duan, J. Gnanaraj and J. Liang, *J. Power Sources*, **196**, 4779 (2011).
26. Q. Q. Xiong, J. P. Tu, Y. Lu, J. Chen, Y. X. Yu, Y. Q. Qiao, X. L. Wang and C. D. Gu, *J. Phys. Chem. C*, **116**, 6495 (2012).
27. M. C. Menard, A. C. Marschilok, K. J. Takeuchi and E. S. Takeuchi, *Electrochim. Acta*, **94**, 320 (2013).
28. D. C. Bock, C. J. Pelliccione, W. Zhang, J. Wang, K. W. Knehr, J. Wang, F. Wang, A. C. West, A. C. Marschilok, K. J. Takeuchi and E. S. Takeuchi, *ACS App. Mater. Interfaces* (2016).
29. Y. H. Kwon, M. M. Huie, D. Choi, M. Chang, A. C. Marschilok, K. J. Takeuchi, E. S. Takeuchi and E. Reichmanis, *ACS App. Mater. Interfaces*, **8**, 3452 (2016).
30. B. C. Han, A. Van der Ven, D. Morgan and G. Ceder, *Electrochim. Acta*, **49**, 4691 (2004).
31. G. K. Singh, G. Ceder and M. Z. Bazant, *Electrochim. Acta*, **53**, 7599 (2008).
32. T. R. Ferguson and M. Z. Bazant, *J. Electrochem. Soc.*, **159**, A1967 (2012).
33. S. Dargaville and T. W. Farrell, *Electrochim. Acta*, **94**, 143 (2013).
34. H. C. Yu, F. Wang, G. G. Amatucci and K. Thornton, *J. Phase Equilib. Diff.*, **37**, 86 (2016).
35. G. Chen, X. Song and T. J. Richardson, *Electrochem. Solid-State Lett.*, **9**, A295 (2006).
36. L. Laffont, C. Delacourt, P. Gibot, M. Y. Wu, P. Kooyman, C. Masquelier and J. M. Tarascon, *Chem. Mater.*, **18**, 5520 (2006).
37. R. Amin, P. Balaya and J. Maier, *Electrochem. Solid-State Lett.*, **10**, A13 (2007).
38. V. R. Subramanian, H. J. Ploehn and R. E. White, *J. Electrochem. Soc.*, **147**, 2868 (2000).
39. V. Srinivasan and J. Newman, *J. Electrochem. Soc.*, **151**, A1517 (2004).
40. Y. Zhu and C. Wang, *J. Phys. Chem. C*, **114**, 2830 (2010).
41. M. Avrami, *J. Chem. Phys.*, **7**, 1103 (1939).
42. M. Avrami, *J. Chem. Phys.*, **8**, 212 (1940).
43. M. Avrami, *J. Chem. Phys.*, **9**, 177 (1941).
44. X. Zhang, R. Kostecki, T. J. Richardson, J. K. Pugh and P. N. Ross, *J. Electrochem. Soc.*, **148**, A1341 (2001).

45. M. E. Fleet, *J. Solid State Chem.*, **62**, 75 (1986).
46. M. Park, X. Zhang, M. Chung, G. B. Less and A. M. Sastry, *J. Power Sources*, **195**, 7904 (2010).
47. E. B. Nauman and D. Q. He, *Chem. Eng. Sci.*, **56**, 1999 (2001).
48. D. R. Baker and M. W. Verbrugge, *J. Electrochem. Soc.*, **159**, A1341 (2012).
49. M. Wagemaker, W. J. H. Borghols and F. M. Mulder, *J. Am. Chem. Soc.*, **129**, 4323 (2007).
50. N. Meethong, H.-Y. S. Huang, W. C. Carter and Y.-M. Chiang, *Electrochem. Solid-State Lett.*, **10**, A134 (2007).
51. D. K. Karthikeyan, G. Sikha and R. E. White, *J. Power Sources*, **185**, 1398 (2008).

CHAPTER 5

IN SITU TRANSMISSION X-RAY MICROSCOPY OF THE LEAD SULFATE FILM FORMATION ON LEAD IN SULFURIC ACID

Chapters 5 and 6 present the utilization of transmission X-ray microscopy to monitor, in real time, the behavior of the $PbSO_4$ film that is formed on Pb in H_2SO_4. Images collected from the synchrotron x-rays are coupled with voltammetric data to characterize the initial formation, the resulting passivation, and the subsequent reduction of the film. This chapter gives an in-depth description of the experimental technique and provides results on the formation and dissolution of the film in H_2SO_4. Chapter 6 expands this work by studying how the film growth is impacted by the inclusion of a common chemical additive into the H_2SO_4 solution.

5.1. Introduction

Lead-acid batteries have been a major part of the economy for over 100 years [1]. Recently, they have seen significant use in next-generation energy storage applications (*e.g.*, renewable energy storage, smart-grid buffering, and transportation) due to their high energy efficiency (up to 80%), low capital cost, and the existence of a strong manufacturing, distribution, and recycling infrastructure [2]. During discharge of a lead-acid battery, Pb is transformed into $PbSO_4$ at the surface of the negative electrode through the following reaction with H_2SO_4:

$$Pb + HSO_4^- \xrightarrow{\text{discharge}} PbSO_4 + H^+ + 2e^- \quad (5.1)$$

As a result of the reaction, the Pb electrode is coated by a $PbSO_4$ film, which is reduced during charge. The performance and life-time of lead-acid batteries is greatly affected by the formation,

growth, and resulting morphology of the $PbSO_4$ film [3]. For instance, one of the major factors limiting the lifetime of lead-acid batteries in high-rate, partial state-of-charge applications (*i.e.*, electric and hybrid-electric vehicles) is the progressive sulfation of the negative electrode, whereby the $PbSO_4$ film becomes irreversible and cannot be fully converted back into Pb after a sufficient charge [4, 5].

In the past 40 years, there has been a considerable effort focused on the formation of the $PbSO_4$ film; however, there is still no general consensus on the exact mechanisms of nucleation and growth. For instance, both the Lakeman and Harrison groups studied the mechanisms of $PbSO_4$ formation and suggested a dissolution-precipitation mechanism at low overpotentials with solid-state nucleation-and-growth occurring at high overpotentials [6-11]. Later work by Hall and Wright, which was further developed by Varela *et al*., suggested that both mechanisms (dissolution-precipitation and solid-state nucleation-and-growth) occur simultaneously in a complex manner which results in a bi-layered salt film with different properties for each layer. They suggested that passivation resulted from large crystals forming on top of a porous film as a result of a dissolution-precipitation mechanism [12-14]. More recently, Yamaguchi *et al.* have concluded that only a single layer of $PbSO_4$ forms as a result of a dissolution-precipitation mechanism and that sulfation may result from the chemical re-crystallization of electrochemically formed $PbSO_4$ [15].

Most of the early studies on $PbSO_4$ formation relied on the interpretation of voltammetric data to indirectly understand the formation processes on Pb. Potentiostatic pulses and voltammetric sweeps were applied to the electrode, while the resulting current responses were measured and analyzed. Later, attempts were made to provide visual evidence by combining the same voltammetric techniques with atomic force microscopy (AFM). The AFM studies were

able to obtain valuable information on the effects of operating conditions (*e.g.*, open circuit standing time and cyclic voltammetry sweep rate) and the impact of electrolyte additives on the size and growth rates of the $PbSO_4$ crystals [15-20]. Further advancement of this *in situ* work would require a new technique that overcomes the small viewing window (25 to 100 μm^2) and slow acquisition time (52 sec per image) associated with AFM. A larger viewing window and a faster acquisition rate would make it possible to capture inhomogeneities in crystal formation and to better quantify growth. In addition, these experiments could be further improved through the use of constant current (galvanostatic) operating conditions. Electrochemical testing of full scale battery systems is typically done using constant current cycling at variable C-rates [21-23]. Therefore, a fundamental understanding of $PbSO_4$ growth under these conditions could yield valuable information which can be directly related to lead-acid battery performance. In particular, this understanding could help to further identify methods for significantly reducing irreversible or hard sulfation.

This work seeks to elucidate the mechanisms of $PbSO_4$ film formation on Pb in H_2SO_4 using *in situ* transmission x-ray microscopy (TXM). TXM is a newly developed imaging technique with a large field of view (1600 μm^2), which is capable of producing x-ray micrographs at fast acquisition rates (up to one second time intervals) and with sub-40 nm resolutions. The formation, growth, and reduction of $PbSO_4$ on Pb in H_2SO_4 are monitored, in real time, under potentiostatic and galvanostatic operating conditions. In addition, quartz-crystal-microbalance experiments are conducted to support the voltammetric and visual data collected from the TXM. In the following sections, the *in situ* set-up is presented along with an investigation of the initial growth, passivation, and reduction of the $PbSO_4$ film.

5.2. Experimental Procedure

5.2.1. Cell Design

The visualization of the growth and reduction of $PbSO_4$ on Pb with synchrotron x-rays was made possible with the use of an in-house designed, *in situ*, micro-electrochemical cell. The design of the cell is shown in Figure 5.1. The Pb electrode was formed by sputter coating a 20-nm thick strip of Au/Pd on top of a translucent PET film (Fig. 5.1, part *iv*). Next, a 0.5-μm thick layer of Pb was electroplated on the Au/Pd strip using a Pb-plating bath continuously stirred at 200 rpm and consisting of 375 g/L lead fluoborate, 22.5 g/L fluoboric acid, 30 g/L boric acid, and 5.3 g/L peptone [24]. The plating was conducted at a constant current density of -18 mA cm^{-2} in a two-electrode system. A solid Pb sheet with a surface area that is 10× greater than the cathode area served as the counter electrode. After plating, the PET film was rinsed with de-ionized water, dried with compressed air, and immediately assembled into the *in situ* cell.

In the cell, the electrochemically active area (0.18 cm^2) was defined using a silicon gasket (Fig. 5.1, part *iii*), which was sandwiched between two PET films (Fig. 5.1, parts *ii* and *iv*). The gasket was 127 μm thick (before compression) and, along with defining the active area, also provided a channel for the H_2SO_4. The electrical connection was made to the Pb electrode by a 38-μm thick copper strip that was placed in between the gasket and the Pb (Fig. 5.2c). The whole cell was held in place by two polycarbonate braces, which were bolted together. Each brace contained a hollow window to provide a path for the synchrotron x-rays, which were only transmitted through the PET films, H_2SO_4, and Pb. One of the braces and the PET film without the Pb also contained inlet/outlet holes for the electrolyte (Fig. 5.1, parts *i* and *ii*). The polycarbonate brace (Fig. 5.1, part *i*) was fitted with landings for connection to tubing.

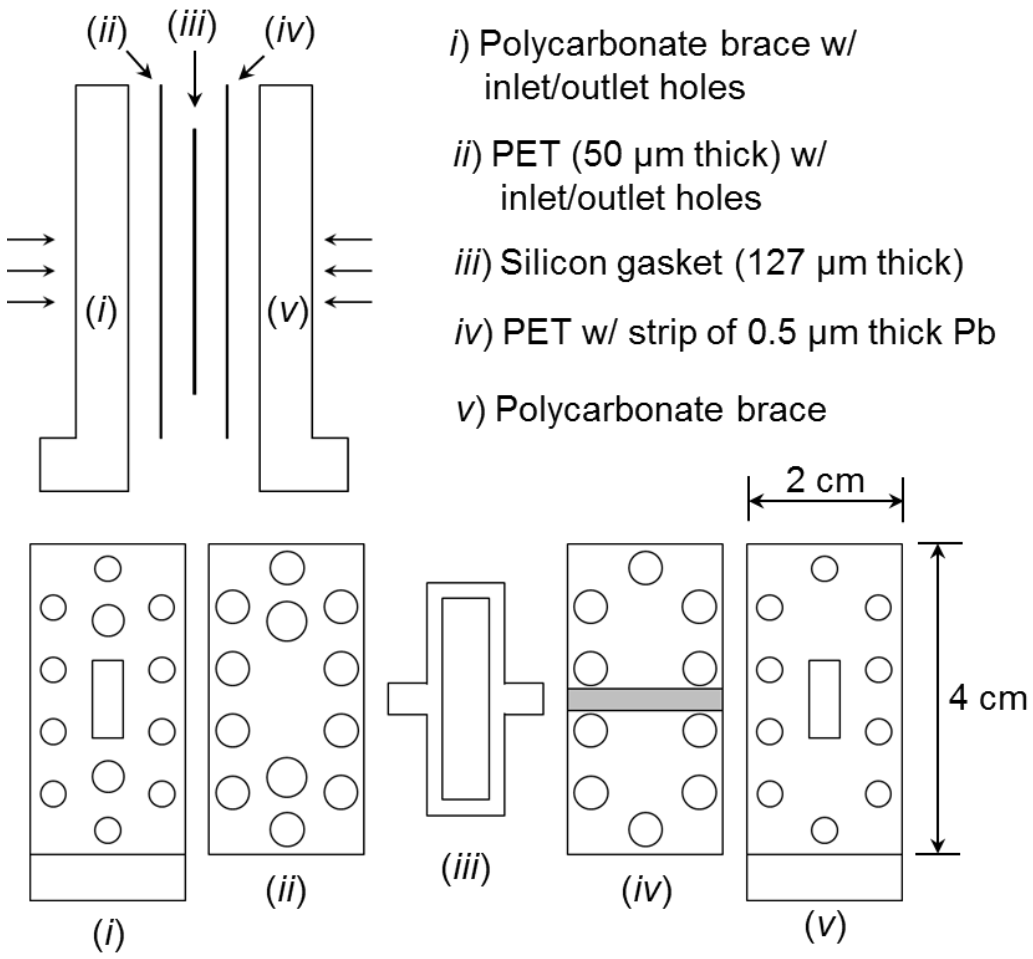

Figure 5.1. Design of *in situ*, micro-electrochemical cell used to monitor $PbSO_4$ growth on Pb using synchrotron X-rays.

5.2.2. TXM Set-up and Procedure

During the experiment, the *in situ* cell was positioned in the transmission x-ray microscope with the x-ray beam penetrating through the Pb in a direction normal to the surface (Fig. 5.2a). Using flow tubes, the top of the *in situ* cell was connected to an external cell, which was placed outside of the beam flight-path. A $Hg|Hg_2SO_4$ reference electrode in 4.6 M H_2SO_4 and a platinum counter electrode were placed inside the external cell (Fig. 5.2b). A syringe was

connected to the bottom of the *in situ* cell and used to fill the entire system with H_2SO_4. The experiment was conducted with 4.6 M H_2SO_4, which was deaerated for 3 hours with argon gas.

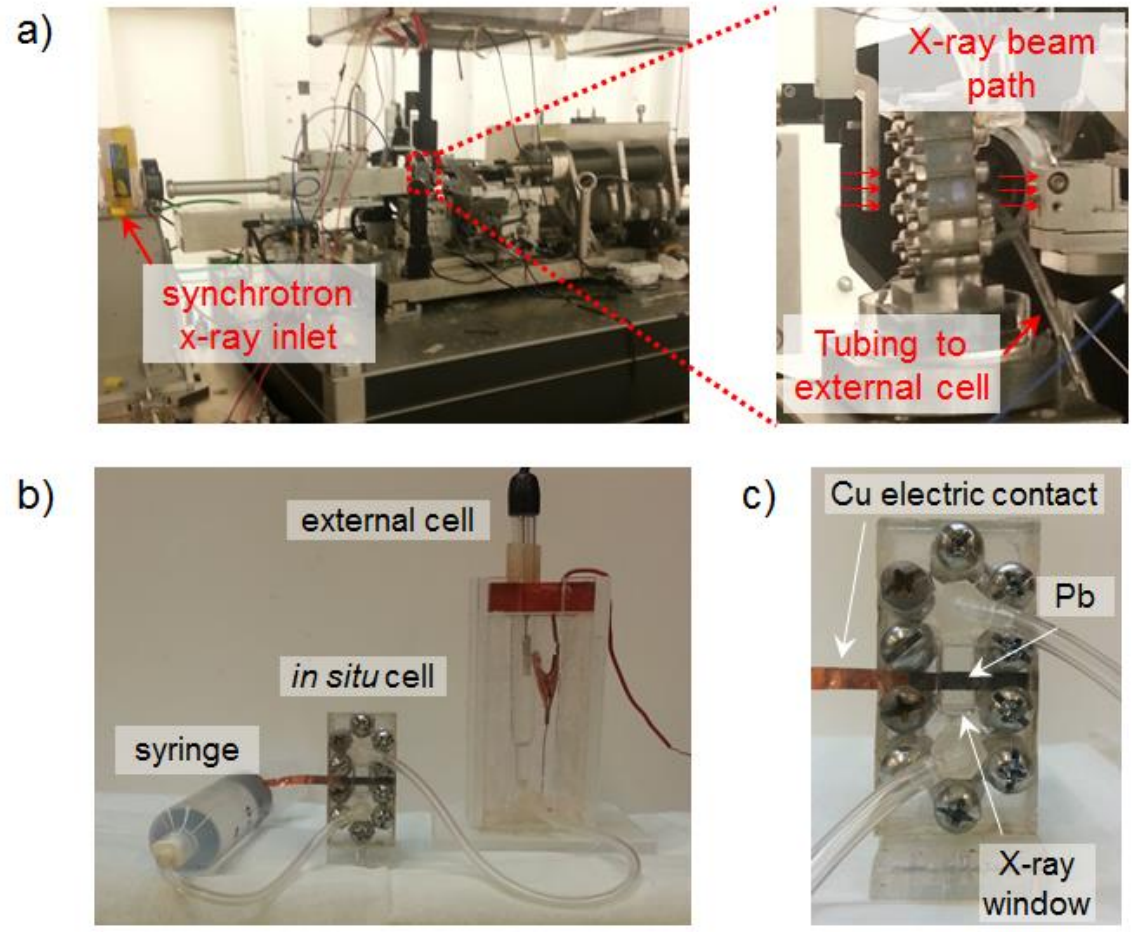

Figure 5.2. Experimental set-up for the in situ, electrochemical experiments. a) Placement of the in situ, micro-electrochemical cell in the TXM at Brookhaven National Laboratory. b) Image of the experimental system (i.e., syringe, in situ cell, and external cell) outside of the TXM. c) Close-up image of the in situ cell.

The electrochemical growth and reduction of the film was controlled using a BioLogic VMP3 potentiostat, which was connected to all three electrodes – the lead electrode in the *in situ*

cell and the reference and counter electrodes in the external cell. Prior to the experiment, galvanostatic electrochemical impedance spectroscopy (EIS) was conducted with a bias current equal to 0 μA, a frequency range from 10 kHz to 100 mHz, and an amplitude of ±10 μA cm^{-2}. The inherent ohmic resistance of the setup (3466 Ω) was determined from the high frequency intercept on the real axis of the Nyquist plot [25]. This value was used to correct for ohmic drop between the reference and Pb electrodes (*i.e.*, iR compensation) during the galvanostatic experiments. The full experimental procedure (without the EIS) is described in Figure 5.3, which includes the current and voltage of the system. All times in the remaining figures throughout the paper are reported in reference to Figure 5.3. To start the experiment, the Pb was first held at constant voltages of -1.1 V and -1.2 V for 30 minutes (regions 'a' and 'b') in order to reduce any $PbSO_4$ that formed on the Pb while sitting in H_2SO_4. Next, the working electrode was held at the open-circuit voltage (OCV) for 2 minutes (region 'c'), followed by a galvanostatic oxidation (region 'd') at 50 μA cm^{-2} with a cut-off voltage of -0.87 V (-0.84 V before correcting for ohmic drop). During the oxidation, $PbSO_4$ was formed on Pb. After reaching the cut-off voltage, the Pb was held at OCV for 2 minutes (region 'e') and then galvanostatically reduced (region 'f') at -50 μA cm^{-2} with a cut-off voltage of -1.17 V (-1.2 V before correcting for ohmic drop). Finally, a potentiostatic reduction was performed for 30 minutes at -1.1 V (region 'g') in an attempt to reduce all the remaining $PbSO_4$ back to Pb.

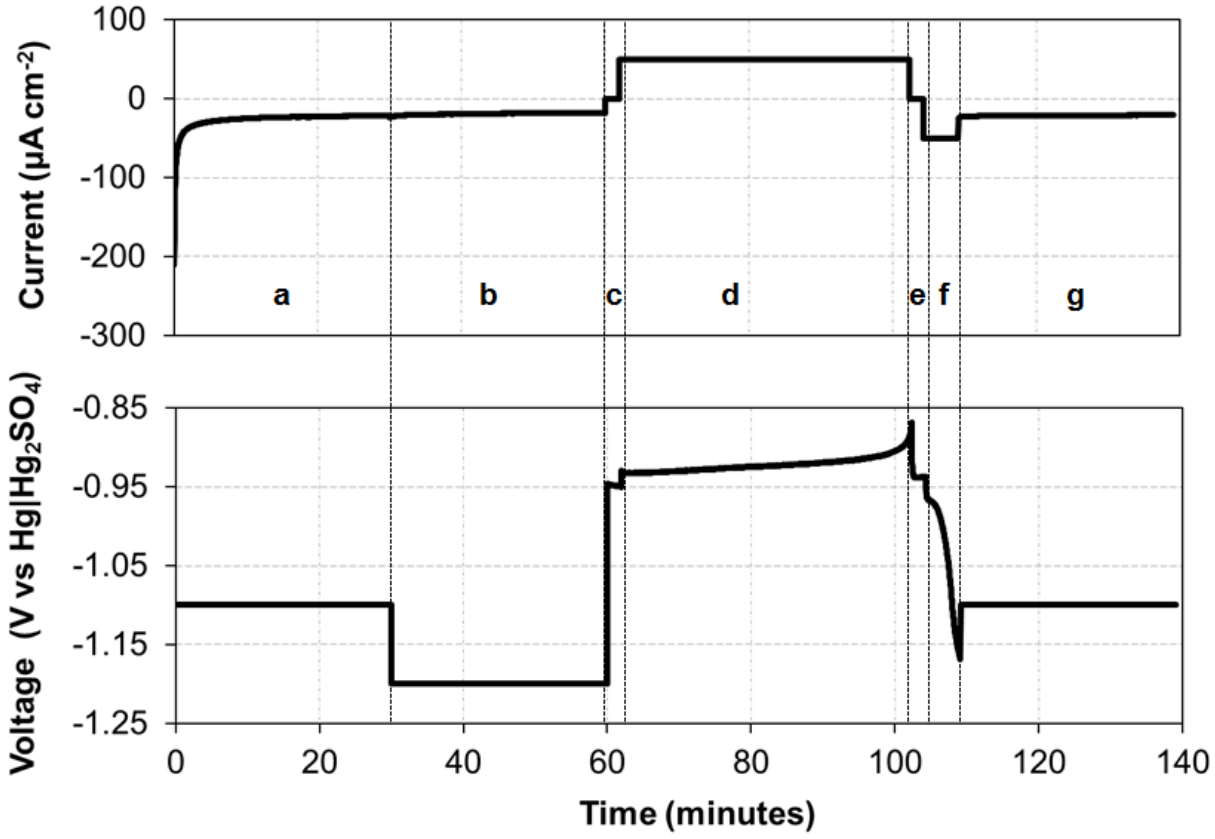

Figure 5.3. Voltage and current data during *in situ* experiment. Description of regions: (a) -1.1 V for 30 minutes; (b) -1.2 V for 30 min.; (c) OCV for 2 min.; (d) oxidation at 50 μA cm^{-2} with a cut off voltage of -0.87 V; (e) OCV for 2 min.; (f) reduction at -50 μA cm^{-2} with a cut off voltage of -1.17 V; (g) -1.1 V for 30 minutes.

5.2.3. Transmission X-ray Microscopy

The *in situ* transmission x-ray microscopy (TXM) was done at the X8C beamline of the National Synchrotron Light Source at Brookhaven National Laboratory. TXM is a non-destructive, nanoscale resolution, highly penetrative hard x-ray imaging technique in which the sample environment can be easily controlled via the development and implementation of *in situ* environmental apparatuses [26]. *In situ* imaging was done at an X-ray energy of 8 keV with a

large 40 × 40 μm (1600 μm^2) field of view and an exposure time of 20 seconds for each image. The moderate exposure time made it possible to generate a clear image by binning a 2 × 2 pixel region using the 2k × 2k CCD camera, resulting in a pixel size of 39 nm. At the start of the *in situ* experiment, five background images were collected of the lead sample and used for pixel-by-pixel normalization. Figure 5.4a shows an example of a TXM image after normalization. The image was taken during the galvanostatic oxidation at t = 62 minutes.

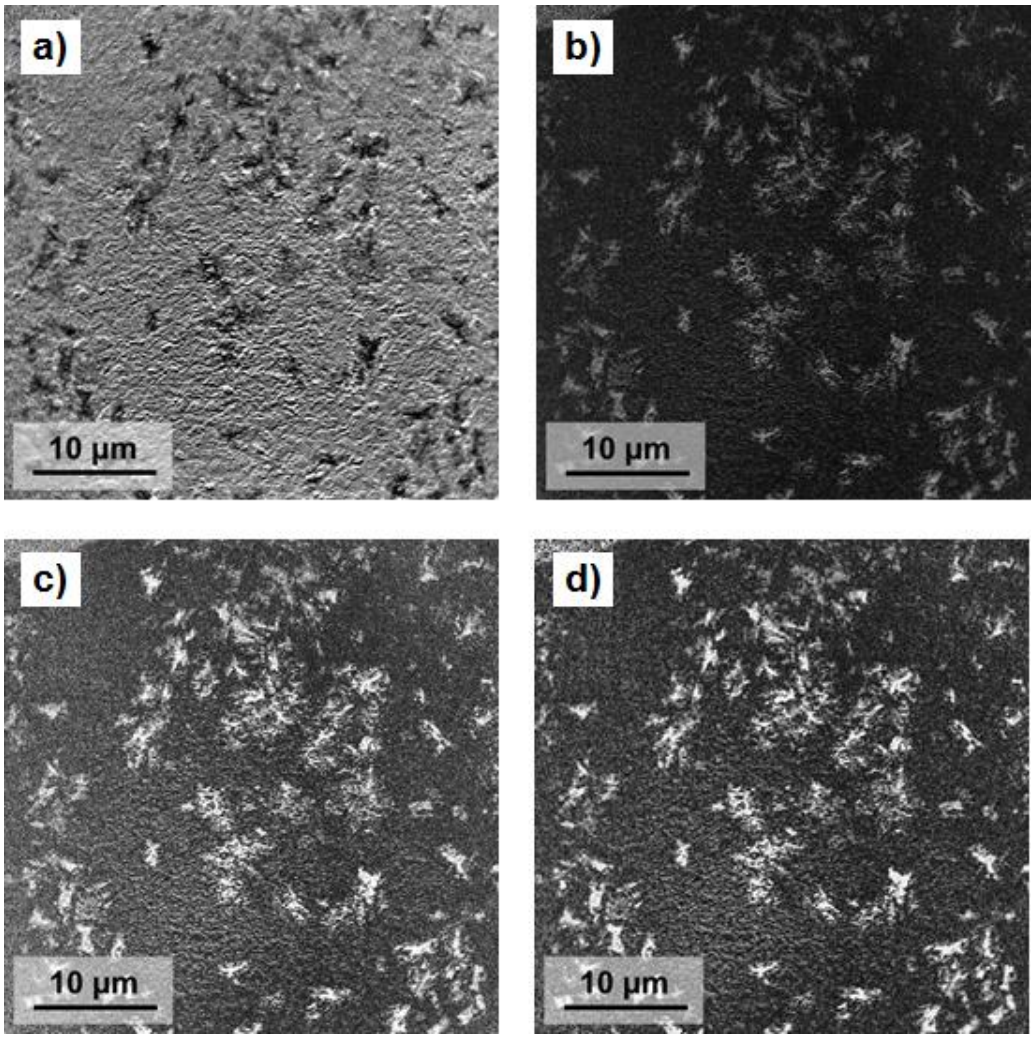

Figure 5.4. Processing of image taken at t = 62 min.: (a) original image, (b) difference with Pb background (*i.e.*, image taken at t = 60 min.), (c) contrast correction, (d) pixel outlier removal.

Additional refinement of the *in situ* images was done using ImageJ software in order to better visualize the nucleation and growth processes of the $PbSO_4$ film [27]. In light of this additional processing, TXM images which were only altered through normalization with the Pb background are considered un-processed. Figure 5.4 shows the three-step refinement process for a single TXM image. In the first step, an image calculator is used to take the pixel-by-pixel difference of the 8-bit grayscale values of two images: the image in question (Fig. 5.4a) and an un-processed image of pure Pb taken during OCV at t = 60 minutes into the experiment. The difference operator removes background features and enhances the $PbSO_4$ crystals, as shown in Figure 5.4b. For the next step, a contrast adjustment is performed on the image by setting the maximum 8-bit gray scale value to 100 and adjusting the respective pixel lookup tables (Fig. 5.4c). Finally, a pixel outlier removal operation is performed for both dark and bright outliers, which uses a pixel radius of two and an 8-bit grayscale threshold of 50 [28]. The final, processed image after all three steps is shown in Figure 5.4d.

5.2.4. Quartz Crystal Microbalance

The quartz-crystal-microbalance (QCM) experiment was conducted using a PLO-10i phase lock oscillator (Maxtex, Inc.) equipped with a Teflon crystal holder (model no. CHC-100). The experiment employed a 5 MHz AT-cut, polished quartz crystal, and the resonance frequency from the crystal was monitored using a Hewlet-Packard 53131A frequency counter [29]. The initial electrode was comprised of a platinum coating on top of a titanium seed layer. In order to obtain a Pb electrode, a 10-μm thick layer of Pb was electrodeposited on top of the platinum electrode using the plating procedure previously described in Section 5.2.1. The constant current plating was controlled using a μAutolabIII potentiostat (Metrohm USA, Inc.), and the electrode

was contained in the Teflon holder. After plating, the quartz crystal was removed from the Teflon holder, rinsed with deionized water, and dried with nitrogen gas. The quartz crystal was then placed back in the holder and submersed in 100 mL of 4.6 M H_2SO_4 for the QCM experiment. The H_2SO_4 was purged with argon gas for 3 hours prior to the experiment. Along with the Pb coated quartz crystal, the QCM set-up included a $Hg|Hg_2SO_4$ reference electrode in 4.6 M sulfuric acid to monitor the voltage and a platinum counter electrode.

5.3. Results and Discussion

5.3.1. TXM Results

5.3.1.1. Potentiostatic Reductions

Figure 5.5 shows the results of the potentiostatic reductions at -1.1 V and -1.2 V, which were performed at the beginning of the TXM experiment (Fig. 5.3, regions 'a' and 'b'). Each numbered point on the voltage curve corresponds to the time the respective image was taken. The objective of these procedures was to remove any $PbSO_4$ film that had grown on the Pb surface during the five-minute period between filling the *in situ*, micro-electrochemical cell with H_2SO_4 and the start of the experiment. Image 1, in Figure 5.5, shows the presence of a surface film at the start of the experiment. A similar film was observed by Yamaguchi *et al.* for a Pb electrode immersed in 0.05 M H_2SO_4 for 20 minutes using AFM [20]. There are two possible mechanisms for the formation of the initial $PbSO_4$ film. First, dissolved oxygen present in the electrolyte could form $PbSO_4$ through the following reaction [3, 30]:

$$Pb + \frac{1}{2}O_2 + H_2SO_4 \rightarrow PbSO_4 + H_2O, \quad \Delta G^0 = -306.5 \text{ kJ mol}^{-1} \tag{5.2}$$

Due to the fast kinetics of the electrochemical reduction of oxygen on the Pb electrode, the reaction in Eq. 5.2 is diffusion-limited, *i.e.* the reaction rate is controlled by the mass transfer of

oxygen to the Pb surface [31]. Therefore, any oxygen present near the electrode will readily cause the formation of $PbSO_4$. Despite the fast kinetics of the oxygen reaction, this mechanism is unlikely since the electrolyte in the current study was deaerated with argon before the experiment. Therefore, the film was most likely formed as a result of acid corrosion via the following reaction [3, 30]:

$$Pb + H_2SO_4 \rightarrow PbSO_4 + H_2, \quad \Delta G^0 = -69.3 \text{ kJ mol}^{-1} \tag{5.3}$$

According to the potential *vs*. pH (Pourbaix) diagram for the Pb/H_2SO_4 system, the corrosion reaction in Eq. 5.3 is thermodynamically unavoidable at the low pH of the 4.6 M H_2SO_4 [1].

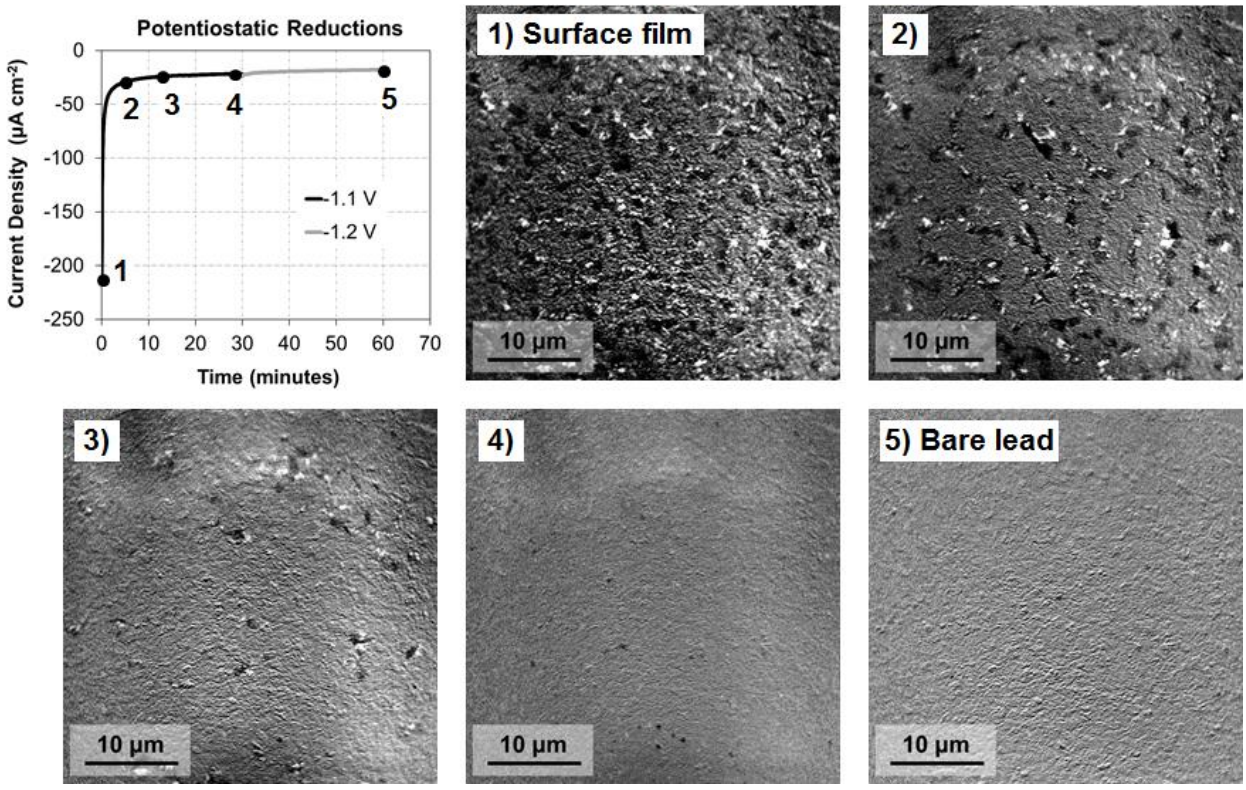

Figure 5.5. Current response of potentiostatic reductions (regions 'a' and 'b' in Fig. 5.3) and corresponding, un-processed TXM images.

Despite the initial presence of the film, images 2-5 in Figure 5.5 clearly depict that the constant potential procedures succeed in reducing the film to bare Pb. The majority of the surface film is reduced during the first 12 minutes at -1.1 V (Fig. 5.5, image 3), and all but a few crystals remain after 30 minutes (Fig. 5.5, image 4). Although most of the $PbSO_4$ is consumed within 30 minutes, there is still a constant cathodic current, which can be attributed to hydrogen evolution on the surface of the Pb. At t = 60 minutes into the experiment (Fig. 5.5, image 5), no surface film is present, providing a clean Pb sample as a starting point for the remainder of the TXM experiment.

5.3.1.2. OCV and Galvanostatic Oxidation

In order to investigate the nucleation and growth of the $PbSO_4$ film, after the potentiostatic reduction step, the Pb electrode was held at OCV for two minutes and then oxidized at a constant current density of 50 μA cm^{-2}. The voltage response and resulting TXM images of the OCV and initial oxidation can be found in Figure 5.6. The numbered regions on the voltage *vs*. time graph indicate the exposure time for each image. From image 2 of the figure, it appears that the nucleation of $PbSO_4$ crystals starts before the oxidation current is applied, indicating that the initial formation of $PbSO_4$ is due to an electrochemical corrosion reaction. The previously described acidic corrosion of Pb (Eq. 5.3) is most likely responsible for the initial nucleation. Image 2 also indicates that the onset of the corrosion reaction is rapid, with crystals up to 1 μm in diameter visible 1.5 minutes into the open-circuit voltage measurement. For a lead-acid battery at OCV, this rapid corrosion will occur on the negative electrode and has been shown to decrease the capacity of the electrode at rates of up to 0.5% per day [32].

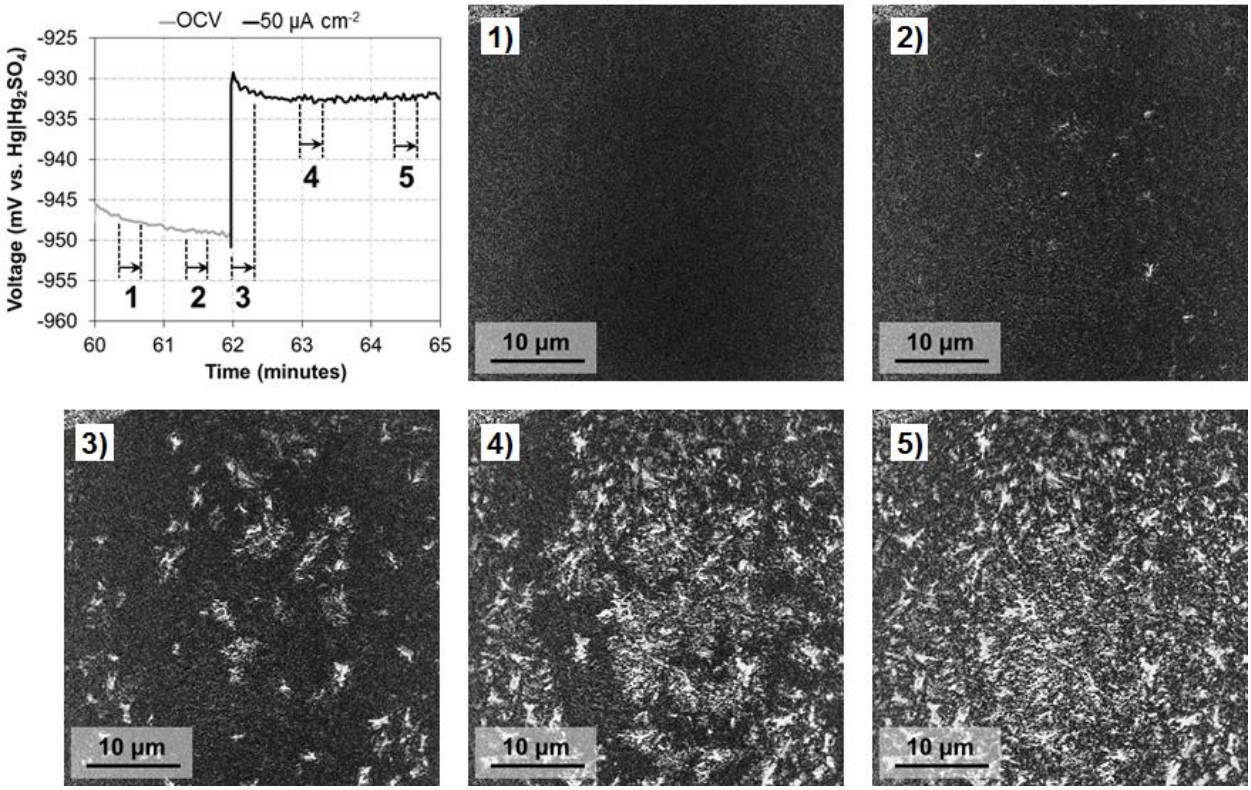

Figure 5.6. Voltage response of open-circuit voltage and initial stage of galvanostatic oxidation (regions 'c' and 'd' in Fig. 5.3, respectively) and corresponding TXM images.

Figure 5.6 also makes it possible to monitor the growth of the film. After the nucleation process, the film continues to grow, coating the Pb surface as it spreads out from the initial nucleation sites. In addition to the spreading of the film, a comparison of images 2 and 3 indicates an increase in the total number of $PbSO_4$ crystals during growth. This suggests that $PbSO_4$ crystals are constantly formed during the growth process, which would correspond to progressive nucleation. It is important to note that an increase in total crystals was observed for all images between t = 61.5 to 63 minutes. Therefore, the increase in crystals between images 2 and 3 was not a result of the application of an oxidation current, but a demonstration of the consistent formation of nuclei. This fact is clearly shown in Figure 5.7, where the crystal

densities from several TXM images are plotted as a function of time. These observations of a progressive nucleation are in contradiction with the findings of several authors who have interpreted chronoamperometry and concluded that the film forms as a result of an instantaneous nucleation process [11-13]. This discrepancy may be due to the fact that the previous nucleation and growth studies are typically reported for high anodic overpotentials (> 50 mV) where solid-state reactions are assumed to dominate. The present oxidation occurs at low anodic overpotentials (< 20 mV) where a dissolution-precipitation mechanism is thought to occur [7]. These conclusions suggest that the progressive nucleation of $PbSO_4$ observed in Figs. 5.6 and 5.7 results from a dissolution-precipitation mechanism.

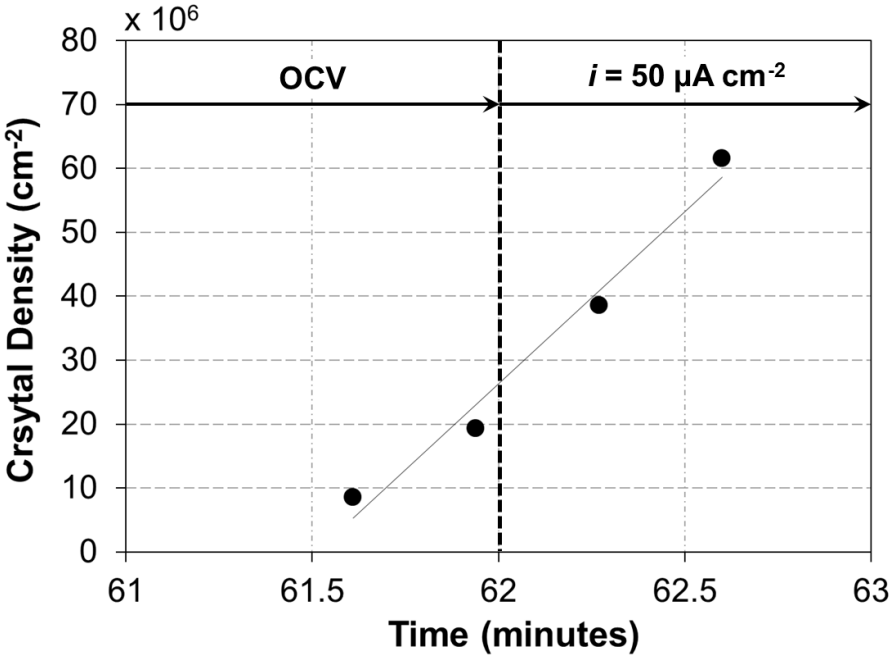

Figure 5.7. Lead sulfate crystal density at end of OCV and start of galvanostatic oxidation (regions 'c' and 'd' in Fig. 5.3, respectively). $R^2 = 0.98$.

At t = 64.5 minutes (Fig. 5.6, image 5), the film is fully coalesced, and the Pb electrode is completely covered by $PbSO_4$. This occurs three minutes after the first $PbSO_4$ crystal is observed (Fig. 5.6, image 2), and indicates that the Pb electrode is fully covered during the early stages of the oxidation experiment. Figure 5.8 shows the voltage response of the complete oxidation and the resulting TXM images. As a point of reference, image 1 in Figure 5.8 and image 3 in Figure 5.6 are the same image. In this experiment, the passivation of the electrode, as indicated by the rapid increase in anodic voltage, occurs at t = 102 minutes. A cut-off voltage of -0.87 V was used to indicate the end of $PbSO_4$ oxidation and to prevent the formation of PbO compounds at higher anodic potentials [33]. Since the $PbSO_4$ film fully covers the Pb electrode several minutes into the process, the majority of the galvanostatic oxidation (97.5% of the total time) corresponds to the growth of a pre-existing, fully coalesced film (Fig. 5.8, images 2 to 5). The passivation (image 5) can, therefore, be attributed to morphological changes in the $PbSO_4$ film which impede the oxidation process. Earlier authors have suggested that passivation is caused by a thickening or reduction in porosity of the film, which restricts the mass transport of ions (Pb^{2+} or SO_4^{2-}) to the reaction sites at or near the Pb surface [34, 35]. The TXM images in the present study support this conclusion.

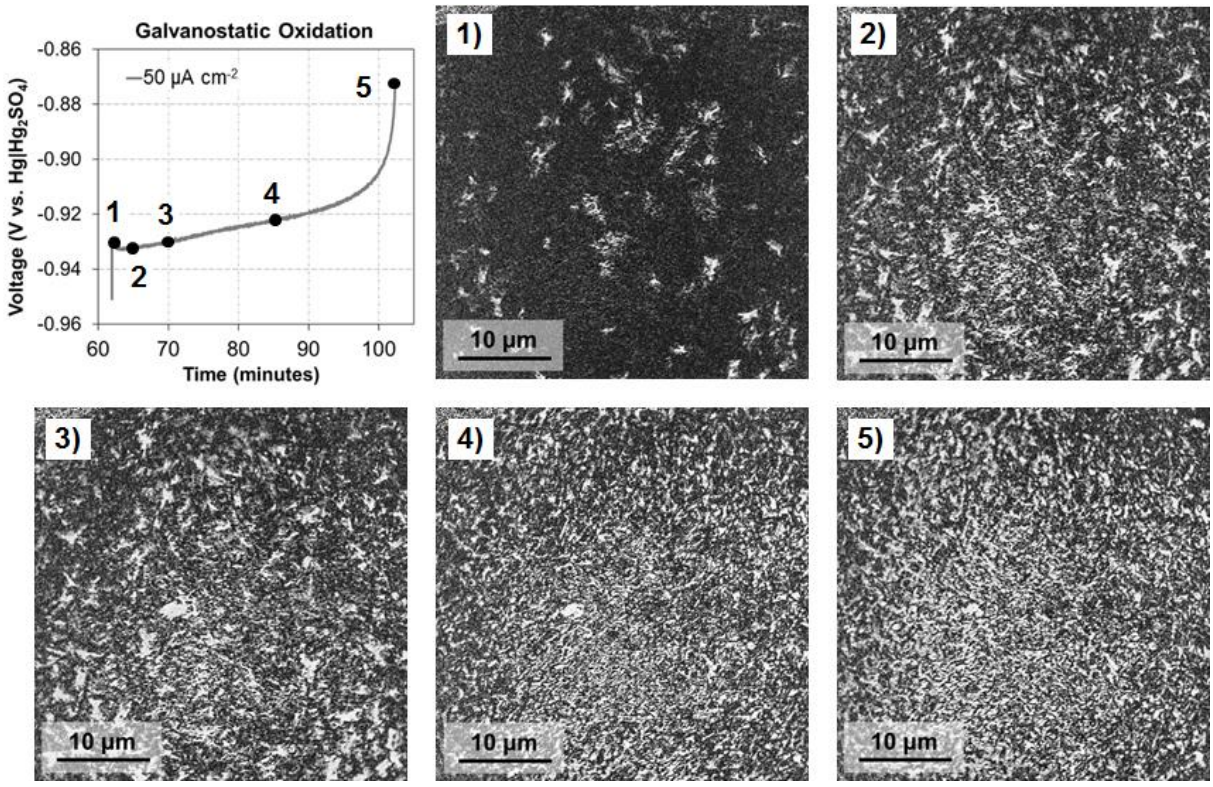

Figure 5.8. Voltage response of galvanostatic oxidation (region 'd' in Fig. 5.3) and corresponding TXM images.

5.3.1.3. Reduction of the $PbSO_4$ Film

After the completion of the galvanostatic oxidation, a galvanostatic reduction (Fig. 5.3, region 'f') was conducted at -50 µA cm^{-2} in an attempt to reduce the passivating $PbSO_4$ film back to Pb. A cut-off voltage of -1.17 V was used to indicate the end of $PbSO_4$ reduction and to prevent excess gassing of hydrogen at the electrode. The voltage curve in Fig. 5.3 shows that the reduction of $PbSO_4$ back to Pb is a rather inefficient reaction, with the reduction reaching the cut-off voltage in less than five minutes. The low efficiency can be attributed to the high applied current density, which caused the cut-off voltage to be reached before all the $PbSO_4$ was reduced. Ekdunge *et al.* have shown that the diffusion and/or dissolution of Pb^{2+} ions are the rate-determining steps during the reduction of the $PbSO_4$ electrode [36]. It is possible that the applied

current quickly exceeded the rates of these processes, causing a rapid increase in the overpotential in order to generate current via hydrogen evolution. A more complete reduction would be expected at lower current densities. By comparing the times of the galvanostatic reduction and oxidation procedures, it is reasonable to assume that up to 88% of the $PbSO_4$ formed on the electrode surface during the galvanostatic oxidation remains at the end of the galvanostatic reduction. In an attempt to further reduce this excess film, a potentiostatic reduction of -1.1 V was applied to the Pb electrode immediately after the galvanostatic reduction (Fig. 5.3, region 'g').

Figure 5.9 shows the current response of the -1.1 V potentiostatic reduction and the subsequent TXM images taken at the beginning and end of the technique. These images were only altered through normalization with the Pb background and were not processed with the ImageJ software. Image 1 shows the existence of well-defined $PbSO_4$ crystals up to 4 μm in diameter, which remained on the Pb surface at the end of the galvanostatic experiments. At the end of the potentiostatic reduction, these crystals appear to have shrunken in size but still remain on the surface (image 2). These images can be compared to those obtained during the potentiostatic reductions at the beginning of the experiment (Fig. 5.5). The $PbSO_4$ crystals formed during the TXM experiment persist longer than those formed at open-circuit voltage. This is most likely due to the fact that the $PbSO_4$ crystals in Fig. 5.9 are much larger than those in Fig. 5.5, and therefore, they have a lower area-to-volume ratio. The lower surface area impedes the dissolution of the $PbSO_4$, which is the first step in the reduction of the film [36]. Although the same potential of -1.1 V is applied to the electrode at the start (Fig. 5.3, region 'a') and end of the experiment (Fig. 5.3, region 'g'), the current obtained from the electrode differs due to changes in $PbSO_4$ crystal morphology. Similar results have been observed by Kanamura

and Takehara, who were able to model the effects of crystal size on the reduction current obtained from cyclic voltammograms [37].

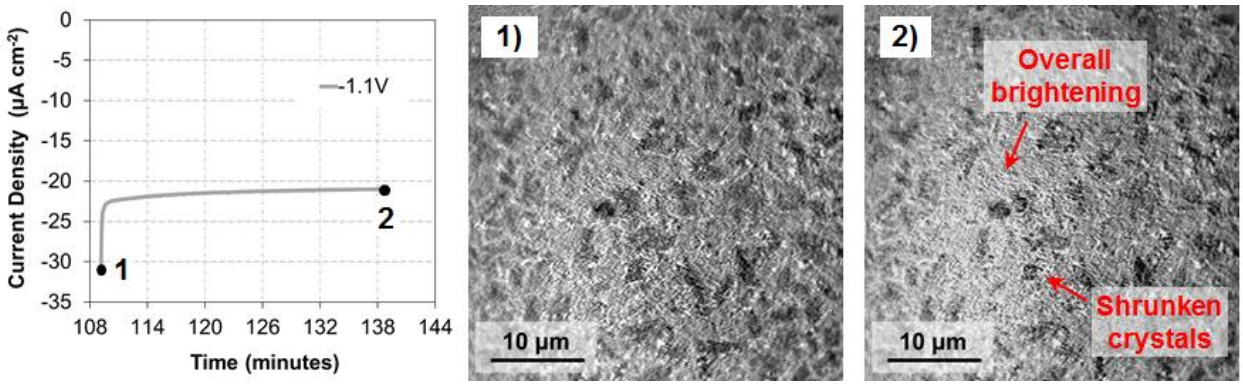

Figure 5.9. Current response of potentiostatic reduction performed after galvanostatic experiments (region 'g' in Fig. 5.3) and un-processed, TXM images before and after technique.

In addition, image 2 (Fig. 5.9) shows that the spaces between the large crystals appear to have brightened during the potentiostatic reduction, which corresponds to an increase in x-ray transmission through the sample. The increase in transmission can be attributed to the reduction of the $PbSO_4$ film. The brightened area in image 2 is most likely the bare, Pb electrode which is exposed as a result of the $PbSO_4$ reduction. Because no distinct crystals are observed in this region in image 1, the film between the large crystals most likely consists of smaller crystals whose morphology is indistinguishable using the TXM. This suggests that, while it was difficult for the large crystals to reduce, smaller $PbSO_4$ crystallites were reduced [5, 38]. The existence of large and small crystals can be associated with the progressive nucleation of $PbSO_4$ observed in Figures 5.6 and 5.7. The constant formation of new nuclei results in crystals of different sizes. An easily reduced $PbSO_4$ film would be preferred in order to maximize the efficiency and to maintain the capacity of a lead-acid battery.

5.3.2. Quartz Crystal Microbalance

In order to support the claims made in Sections 5.3.1.1 and 5.3.1.2 of a high acidic corrosion rate for Pb in H_2SO_4, quartz crystal microbalance (QCM) experiments were performed. A QCM is able to detect small changes in mass on top of a quartz crystal by measuring the associated change in resonant frequency of the crystal. Sauerbrey was the first to recognize that the change in frequency of a quartz crystal can be directly related to the added mass through the following equation [39]:

$$\Delta f = -C_f \times \Delta m \tag{5.4}$$

where Δf is the change in frequency, Δm is the change in mass per unit area, and C_f is a sensitivity factor, which is a fundamental property of the quartz crystal. It is defined as follows:

$$C_f = \frac{\alpha 2 f_0^2}{\sqrt{\rho_q \mu_q}} \tag{5.5}$$

where f_0 is the resonant frequency of the unloaded crystal, ρ_q is the density of quartz, μ_q is the elastic shear modulus of quartz, and α is a dimensionless instrument constant [29]. For the current set-up, $C_f = 0.0566$ Hz cm^2 ng^{-1}.

In these experiments, a quartz crystal plated with a 10-μm thick film of Pb was placed in 4.6 M H_2SO_4, and the change in mass per unit area was monitored over time. A Hg|Hg_2SO_4 reference electrode was used to monitor the open circuit voltage, and it was confirmed that the electrode was near the reversible Pb/$PbSO_4$ potential. Figure 5.10a shows the recorded mass change per unit area over a 30 minute period. Also included in the figure is the mass change per unit area detected by Taguchi *et al.* for a Pb electrode in 4.5 M H_2SO_4 using the same technique [40]. Good agreement is observed between the two experiments. Both show a sharp initial rise

in mass, which reaches a steady state ~10 minutes into the experiment. In order to compare the rate of corrosion with the oxidation rate used in the experiment, the mass change per unit area was converted into a corrosion current (i_{corr} [=] μA cm^{-2}). To accomplish this, the relative quantity of charge stored in the growing $PbSO_4$ film was determined from the change in measured mass per unit area using the following equation:

$$Q = \frac{nF\Delta m}{MW_{SO_4^{2-}}} \tag{5.6}$$

where F is Faraday's constant, n is the number of e$^-$ passed per mole of SO_4^{2-} reacting, $MW_{SO_4^{2-}}$ is the molecular weight of SO_4^{2-}, and Q has units of C cm^{-2}. This equation assumes that all the $PbSO_4$ products remained on the surface, which is a reasonable assumption due to the low solubility of $PbSO_4$ in H_2SO_4 [41].

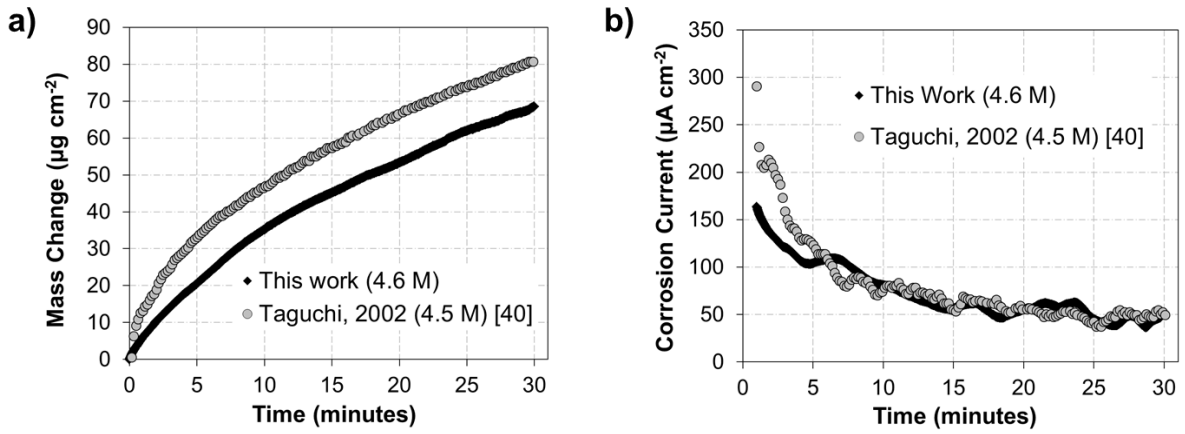

Figure 5.10. a) Mass change of Pb in H_2SO_4 determined using a quartz-crystal-microbalance. b) Corrosion rate calculated from slope of QCM results shown in (a).

Once the change in the quantity of charge (Q) was determined using Eq. 5.6, i_{corr} was calculated from the first order derivative of the quantity of charge with respect to time:

$$i_{corr} = \frac{dQ}{dt} \tag{5.7}$$

Figure 5.10b depicts the change in i_{corr} over the 30 minute experiment. After a high initial value, i_{corr} appears to settle at a value equivalent to 50 μA cm^{-2}. This is the same value used for the galvanostatic oxidation and reduction experiments performed in the TXM. It indicates that the acidic corrosion of Pb in H_2SO_4 is quite fast and is responsible for the nucleation of $PbSO_4$ crystals observed during the open-circuit voltage measurements.

5.4. Summary

This chapter presents an investigation of the surface behavior of the $Pb/PbSO_4$ electrode in a lead-acid battery. *In situ* transmission x-ray microscopy was used to monitor, in real time, the formation, growth, and reduction of $PbSO_4$ on Pb in H_2SO_4 under potentiostatic and galvanostatic operating conditions. The resulting TXM images were used to show that the initial nucleation of $PbSO_4$ crystals occurred while the Pb electrode was held at an open-circuit voltage. Using a quartz-crystal microbalance, it was shown that this behavior could be attributed to the acidic corrosion of Pb in H_2SO_4.

During the early stages of film formation, TXM images depicted a progressive nucleation of $PbSO_4$ crystals, which were concluded to form through a dissolution-precipitation mechanism. The data also showed that the $PbSO_4$ film was fully coalesced across the surface of the Pb electrode during the early stages of the galvanostatic oxidation. Therefore, it was concluded that the passivation of the electrode was due to morphological changes in the existing $PbSO_4$ film, which impeded the mass transport of reactants. In addition, the passivating film was shown to be

stable and difficult to reduce. This behavior was attributed to the formation of a significant number of large crystals with low area-to-volume ratios, which hindered the dissolution of $PbSO_4$.

5.5. References

1. P. Ruetschi, **2**, 3 (1977).
2. K. Peters, in *Valve-Regulated Lead-Acid Batteries*, D. A. J. Rand, P. T. Moseley, J. Garche and C. D. Parker, Editors, p. 135, Elsevier, The Netherlands (2004).
3. D. Pavlov, in *Lead-Acid Batteries Science and Technology: A Handbook of Lead-Acid Battery Technology and Its Influence on the Product*, p. 29, Elsevier Science Ltd., Amsterdam (2011).
4. P. Ruetschi, *J. Power Sources*, **127**, 33 (2004).
5. D. U. Sauer, in *Encyclopedia of Electrochemical Power Sources*, J. Garche, Editor, p. 805, Elsevier, Amsterdam (2009).
6. G. Archdale and J. A. Harrison, *J. Electroanal. Chem.*, **34**, 21 (1972).
7. G. Archdale and J. A. Harrison, *J. Electroanal. Chem.*, **39**, 357 (1972).
8. A. N. Fleming and J. A. Harrison, *Electrochim. Acta*, **21**, 905 (1976).
9. N. A. Hampson and J. B. Lakeman, *Surf. Technol.*, **9**, 97 (1979).
10. N. A. Hampson and J. B. Lakeman, *J. Power Sources*, **4**, 21 (1979).
11. N. A. Hampson and J. B. Lakeman, *J. Electroanal. Chem.*, **107**, 177 (1980).
12. S. B. Hall and G. A. Wright, *Corros. Sci.*, **31**, 709 (1990).
13. F. E. Varela, M. E. Vela, J. R. Vilche and A. J. Arvia, *Electrochim. Acta*, **38**, 1513 (1993).
14. F. E. Varela, J. R. Vilche and A. J. Arvia, *Electrochim. Acta*, **39**, 401 (1994).
15. Y. Yamaguchi, M. Shiota, Y. Nakayama, N. Hirai and S. Hara, *J. Power Sources*, **93**, 104 (2001).
16. I. Ban, Y. Yamaguchi, Y. Nakayama, N. Hirai and S. Hara, *J. Power Sources*, **107**, 167 (2002).
17. N. Hirai, S. Kubo and K. Magara, *J. Power Sources*, **191**, 97 (2009).
18. H. Vermesan, N. Hirai, M. Shiota and T. Tanaka, *J. Power Sources*, **133**, 52 (2004).
19. Y. Yamaguchi, M. Shiota, M. Hosokawa, Y. Nakayama, N. Hirai and S. Hara, *J. Power Sources*, **102**, 155 (2001).
20. Y. Yamaguchi, M. Shiota, Y. Nakayama, N. Hirai and S. Hara, *J. Power Sources*, **85**, 22 (2000).
21. B. O. Myrvold and D. Pavlov, *J. Power Sources*, **85**, 92 (2000).
22. D. Pavlov, B. O. Myrvold, T. Rogachev and M. Matrakova, *J Power Sources*, **85**, 79 (2000).
23. D. P. Boden, J. Arias and F. A. Fleming, *J Power Sources*, **95**, 277 (2001).
24. S. Hirsch and C. Rosenstein, **100, Supplement 1**, 291 (2002).
25. J. R. Macdonald and W. B. Johnson, in *Impedance Spectroscopy Theory, Experiment, and Applications*, 2nd ed., E. Barsoukov and J. R. Macdonald, Editors, p. 1, Wiley-Interscience, Hoboken, N.J. (2005).

26. J. Wang, Y. C. K. Chen, Q. X. Yuan, A. Tkachuk, C. Erdonmez, B. Hornberger and M. Feser, *Appl Phys Lett*, **100**, 143107 (2012).
27. C. A. Schneider, W. S. Rasband and K. W. Eliceiri, *Nat. Methods*, **9**, 671 (2012).
28. T. Ferreira and W. S. Rasband, *ImageJ User Guide - IJ 1.46*, imagej.nih.gov/ij/docs/guide/ (2010-2012).
29. J. J. Kelly, K. M. A. Rahman, C. J. Durning and A. C. West, *J Electrochem Soc*, **145**, 492 (1998).
30. P. Ruetschi and R. T. Angstadt, *J. Electrochem Soc*, **105**, 555 (1958).
31. L. M. Baugh, K. L. Bladen and F. L. Tye, *J. Electroanal. Chem.*, **145**, 355 (1983).
32. A. J. Salkind, A. G. Cannone and F. A. Trumbure, in *Handbook of Batteries*, 3rd ed., D. Linden and T. B. Reddy, Editors, p. 23.1, McGraw-Hill, New York (2002).
33. D. Pavlov, *Electrochim. Acta*, **13**, 2051 (1968).
34. P. Ruetschi and R. T. Angstadt, *J. Electrochem. Soc.*, **111**, 1323 (1964).
35. D. Pavlov and R. Popova, *Electrochim. Acta*, **15**, 1483 (1970).
36. P. Ekdunge, K. V. Rybalka and D. Simonsson, *Electrochim. Acta*, **32**, 659 (1987).
37. K. Kanamura and Z. Takehara, *J. Electrochem. Soc.*, **139**, 345 (1992).
38. Y. L. Guo, M. D. Wu and S. N. Hua, *J. Power Sources*, **64**, 65 (1997).
39. G. Sauerbrey, **155**, 206 (1959).
40. M. Taguchi and H. Sugita, *J. Power Sources*, **109**, 294 (2002).
41. D. N. Craig and G. W. Vinal, *J. Res. Nat. Bur. Stand.*, **22**, 55 (1939).

CHAPTER 6

TXM STUDY OF THE GALVANOSTATIC GROWTH OF LEAD SULFATE ON LEAD: IMPACT OF LIGNOSULFONATE

In this chapter, the galvanostatic growth of $PbSO_4$ on Pb in H_2SO_4 was studied using scanning electron microscopy and *in situ* transmission X-ray microscopy (TXM). Images from the TXM are used to investigate the effects of sodium lignosulfonate on the $PbSO_4$ formation and the initial growth of the $PbSO_4$ crystals.

6.1. Introduction

One of the major factors limiting the widespread use of lead-acid batteries for smart-grid applications (*e.g.,* load-leveling, distribution deferral, and renewable energy storage) is a relatively short cycle life when compared to other electrochemical energy storage technologies [1]. The short cycle life can be attributed to a variety of aging processes, including: anodic corrosion, positive active mass degradation, active mass sintering, and the irreversible formation of $PbSO_4$ on the surface of the electrodes (*i.e.,* sulfation) [2]. The prevalence of each aging mechanism on the various components in the battery strongly depends on the operating conditions and design of the system. For one of the components, the negative electrode, one of the major life limiting factors is sulfation, which occurs when the $PbSO_4$ film becomes irreversible and cannot be fully converted back into Pb after a sufficient charge [3].

For over 70 years, attempts have been made to increase the lifetime of the battery by including chemical additives in the active mass of the negative electrode [4]. Out of all the additives, wood-derived lignosulfonates (*i.e.,* lignin) have been the most extensively studied and

thorough overviews of the progress on this topic can be found in [5-7]. In recent years, further attempts to increase the lifetime have led to the development of novel chemical additives which are tailored to the specific applications of the battery. For batteries used in high-rate partial-state-of-charge applications, additions of polyaspartic acid, synthetic additive blends, and high amounts of carbon black have been shown to reduce sulfation and improve battery life [8-16]. While the results of these studies are impactful, the advances in performance typically result from trial and error testing of full-size batteries. In order to further identify methods for reducing sulfation, it would be beneficial to obtain a more fundamental understanding of the mechanisms of crystal formation, and how additives affect this process.

One promising method for researching the mechanisms of crystal formation is the use of imaging techniques to obtain *in situ* observations of the growth processes. Recently, several authors have utilized atomic force microscopy (AFM) to study the effects of operating conditions (*e.g.*, open circuit standing time and cyclic voltammetry sweep rate) and the impact of electrolyte additives on the morphology and growth rates of the $PbSO_4$ crystals [17-23]. In these studies, the growth and reduction of $PbSO_4$ was controlled using potentiostatic and voltammetric techniques, while the $PbSO_4$ crystals were simultaneously visualized using AFM. Further advancement of this work would require the use of a new technique which can overcome the relatively long acquisition time (52 seconds per image) associated with the AFM. In addition, it may be beneficial to utilize constant current (galvanostatic) operating conditions, which are typically used during the testing of full-scale batteries [10-12]. Galvanostatic operating conditions would make it easier to directly relate the observations and conclusions from the microscopic, *in situ* work with the full-scale, macroscopic battery performance.

In the previous chapter, transmission X-ray microscopy (TXM), an imaging technique with a fast acquisition time (up to one second per image), was used to study the initial growth, passivation, and reduction of the $PbSO_4$ film on Pb in H_2SO_4. The present chapter seeks to expand this work by investigating the galvanostatic growth of $PbSO_4$ in the presence of sodium lignosulfonate, an organic macromolecule which is the precursor to many commercial chemical additives (*e.g.* Vanisperse A and Vanillex N). In addition, this work seeks to further understand the mechanisms of $PbSO_4$ formation through an analysis of the growth of individual crystals, including an examination of the initial, galvanostatic potential-time transient. To accomplish this, both TXM and scanning electron microscopy (SEM) are employed.

6.2. Experimental Procedure

6.2.1. TXM Experiments

The transmission X-ray microscopy (TXM) experiments were conducted using the same experimental set-up and procedure outlined in Chapter 5. To study the impact of additives on the mechanisms of $PbSO_4$ growth, two separate experiments were conducted: one with and one without 26 ppm sodium lignosulfonate (*i.e.* lignin) added to the electrolyte. During each experiment, an electroplated Pb working electrode was assembled into an in-house designed, *in situ*, micro-electrochemical cell. The cell was placed in the transmission X-ray microscope with the X-ray beam penetrating through the Pb in a direction normal to the surface. An external half-cell compartment containing a $Hg|Hg_2SO_4$ reference electrode and a Pt counter electrode was placed outside the beam flight-path. The two compartments were connected via a tube, and the whole set-up was filled with 4.6 M H_2SO_4 (with and without lignin), which was deaerated for 3 hours with argon gas.

For both experiments, the electrochemical growth and reduction of the films were controlled using a BioLogic VMP3 potentiostat, which was connected to all three electrodes. Prior to each experiment, the ohmic resistance of the setup was determined using galvanostatic electrochemical impedance spectroscopy (EIS). This value was used to correct for ohmic drop between the reference and Pb electrodes (*i.e.*, iR compensation) during the galvanostatic experiments. After the EIS, the Pb electrode was held at constant voltages of -1.1 V and -1.2 V for 30 minutes in order to reduce any $PbSO_4$ that formed on the Pb while sitting in H_2SO_4. Next, the working electrode was held at the open-circuit voltage (OCV) for 2 minutes, followed by a galvanostatic oxidation at 50 $\mu A\ cm^{-2}$ with a cut-off voltage of -0.84 V (before correcting for ohmic drop).

The *in situ* transmission X-ray microscopy (TXM) was done at the X8C beamline of the National Synchrotron Light Source at Brookhaven National Laboratory. Imaging was performed at a X-ray energy of 8 keV with a 40×40 μm (1600 μm^2) field of view and an exposure time of 20 seconds for each image. The moderate exposure time made it possible to generate a clear image by binning a 2×2 pixel region using the $2k \times 2k$ CCD camera, resulting in a pixel size of 39 nm [24]. Images collected from both TXM experiments were processed using a pixel-by-pixel normalization with five background images taken from the corresponding Pb sample. In addition, all images in this work underwent further refinement using ImageJ software in order to better visualize the nucleation and growth of the $PbSO_4$ films. A more detailed description of the image refinement procedure can be found in Chapter 5, Section 5.2.

6.2.2. Experiments for SEM Images

Additional electrochemical experiments with and without 26 ppm lignin in the electrolyte were performed in order to support the TXM results. Pb electrodes were formed by electroplating a 10-μm thick layer of lead unto a 38-μm thick copper substrate using the same plating procedure outlined in Chapter 5. Prior to plating, the substrate was rinsed with isopropyl alcohol and de-ionized water. After plating, the electrode was rinsed with de-ionized water and dried with argon gas. The electrochemically active area of the Pb (~0.1 cm^2) was defined by melting paraffin wax onto the sample. The exact active area for each sample was obtained by analyzing an image of the electrode using the area selection tools available in the ImageJ software [25]. The electrochemical experiments were conducted using a three-electrode system with a $Hg|Hg_2SO_4$ reference electrode and a Pt counter electrode. All three electrodes were placed in a beaker containing 70 mL of 4.6 M H_2SO_4 (with and without 26 ppm lignin), which was deaerated for 3 hours with argon gas. The entire beaker was blanketed with argon gas for 15 minutes and then sealed with paraffin wax for the entirety of the experiment.

The electrochemical experiments were controlled using a μAutolabIII potentiostat (Metrohm USA, Inc.). The Pb electrode was first held at a constant voltage of -1.1 V for 30 minutes in an attempt to reduce any $PbSO_4$ that formed on the Pb while sitting in H_2SO_4. Next, the working electrode was held at the open-circuit voltage for 2 minutes, followed by a galvanostatic oxidation at 50 μA cm^{-2}. The end of the oxidation was either specified by a given amount of time (*e.g.,* 1 minute) or by allowing the electrode to passivate using a cutoff voltage of -0.85 V. Immediately after the oxidation, the sample was removed from the acid, rinsed with de-ionized water, and dried with argon gas. Scanning electron microscope (SEM) images were

taken of the sample surface using a Hitachi 4700 microscope. A minimum of three regions was imaged for each sample.

6.3. Results and Discussion

6.3.1. Comparison of TXM and SEM Images

In order to aid in the interpretation of the results from the TXM experiments, the images obtained from the TXM were compared to SEM images taken from separate experiments. Figures 6.1 and 6.2 show a comparison of TXM and SEM images of the $PbSO_4$ films grown with and without lignin in the electrolyte, respectively. Included in both figures are images taken 3 minutes after the start of the OCV procedure (images a1 and b1) and at passivation of the electrode (images a2 and b2). Good agreement is observed between the SEM and TXM images, especially for the images taken 3 minutes after the start of OCV (images a1 and b1) and for the experiments conducted with 26 ppm lignin in the electrolyte (Figure 6.2). In Fig. 6.2, both the TXM and SEM images at passivation (Fig. 6.2, images a2 and b2) depict a film containing a few, large crystals dispersed among many, smaller, $PbSO_4$ crystallites. In contrast, the SEM image taken at passivation from the experiment without lignin in the electrolyte (Fig. 6.1, image b2) shows a film containing many, large, overlapping crystals. It appears that these overlapping crystals were difficult to deconvolute using transmission X-rays (Fig. 6.1, image a2), resulting in an image without clearly defined crystallites.

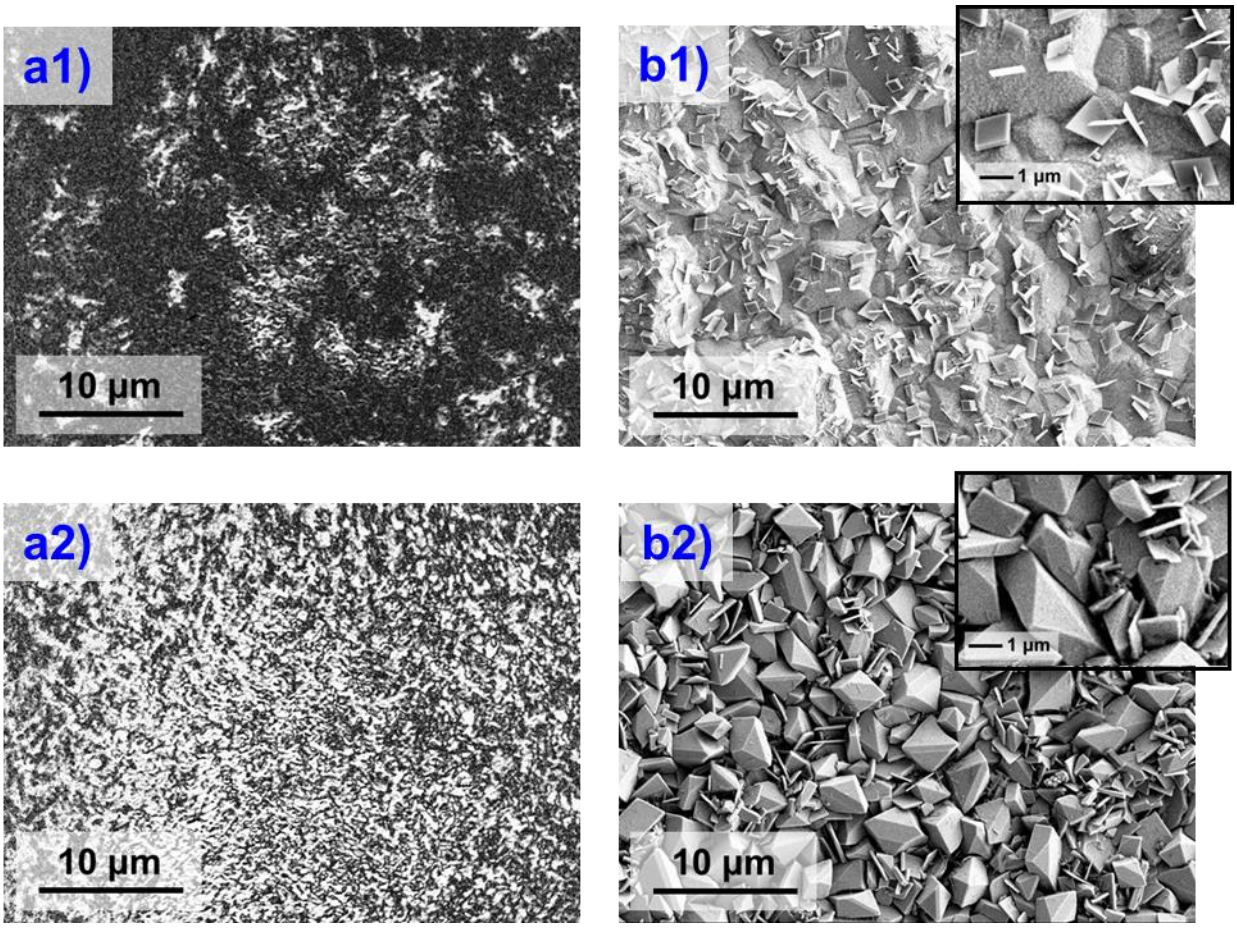

Figure 6.1. a) TXM and b) SEM images taken during oxidation of Pb at 50 µA cm^{-2} in 4.6 M H_2SO_4: 1) 3 minutes after the start of OCV (see Fig. 6.3); 2) passivation with $PbSO_4$.

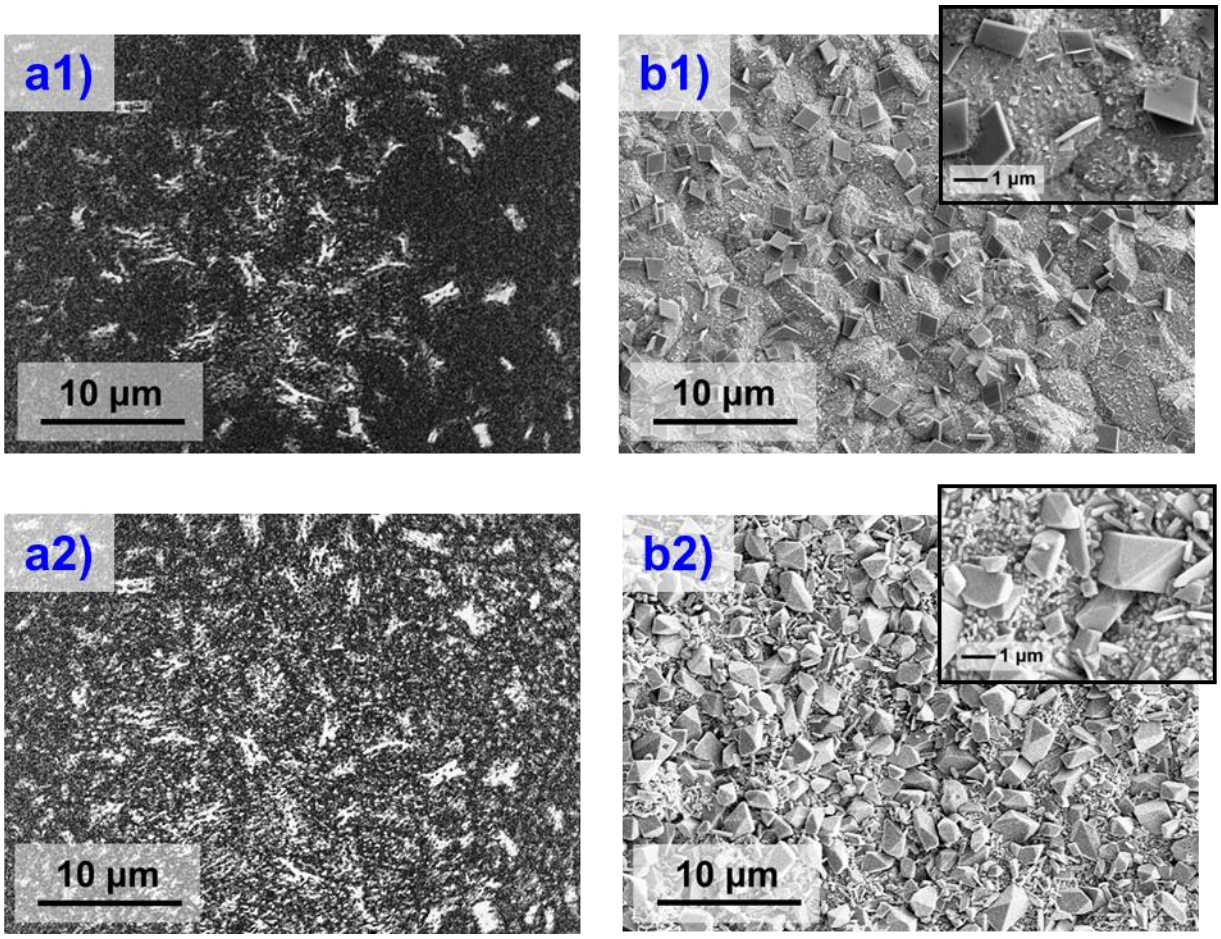

Figure 6.2. a) TXM and b) SEM images taken during oxidation of Pb at 50 µA cm^{-2} in 4.6 M H_2SO_4 with 26 ppm sodium lignosulfonate: 1) 3 minutes after the start of OCV (see Fig. 6.3); 2) passivation with $PbSO_4$.

6.3.2. Impact of Lignin on $PbSO_4$ Morphology and Growth

6.3.2.1. Oxidation until Passivation

The voltage responses of the open circuit voltage (OCV) and galvanostatic oxidation steps of the TXM experiments conducted with and without 26 ppm lignin are shown in Figure 6.3. All times in the remaining figures throughout the paper are reported in reference to this figure. The results show that addition of lignin to the electrolyte decreased the time to

passivation in the experiment by ~15%; whereby passivation is indicated by the sudden increase in voltage. The decrease in passivation time caused by lignin can be attributed to the morphological differences in the $PbSO_4$ films. When comparing the two films at passivation, the SEM images (images b2 in Figures 6.1 and 6.2) indicate that the film formed with lignin in the electrolyte contains higher amounts of small crystals. High amounts of small crystals result in a more densely packed morphology when the film is relatively thin. The thin, dense film blocks the diffusion of reactants, passivating the electrode with minimal $PbSO_4$. A similar observation was made by Hampson and Lakeman, who conducted potentiostatic oxidations on Pb at various potentials and recorded the charge required for passivation [26]. They also concluded that films with a higher crystal density and a smaller average crystal size resulted in a quicker passivation and a smaller capacity.

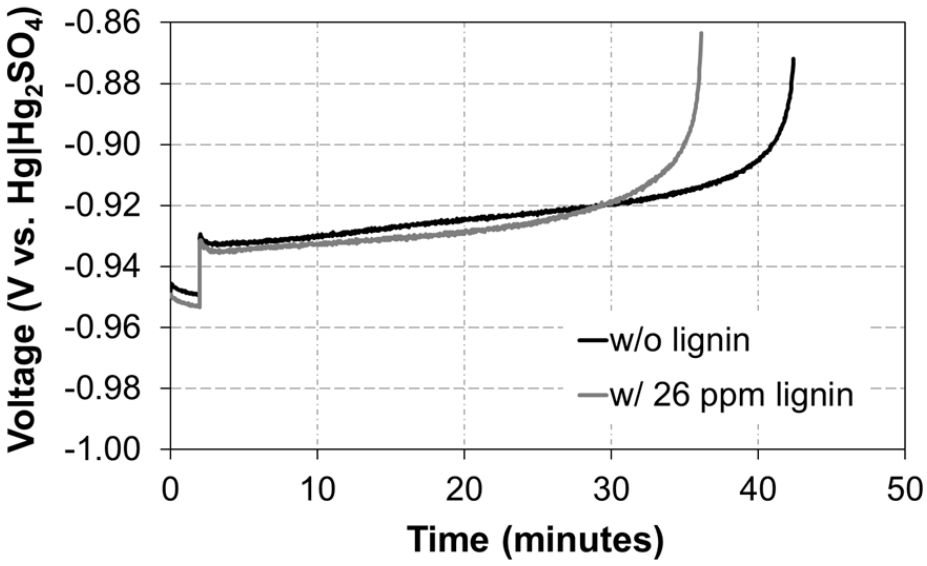

Figure 6.3. Voltage response of TXM experiments without and with 26 ppm sodium lignosulfonate added to the electrolyte. For both, Pb electrode was held at open-circuit voltage for 2 minutes, followed by a galvanostatic oxidation at 50 μA cm^{-2} (-0.87 V cutoff).

The observed decrease in passivation time contradicts the fact that lignin is known to increase the capacity of the negative electrode in a lead acid battery [4-6, 12, 27-31]. Currently, two main mechanisms have been proposed to explain why lignin increases the capacity, neither of which is expected to be a major factor in this study. First, lignin is known to increase the capacity during the forming of the electrode by producing a high porosity, high surface area structure, which improves utilization of the active mass [4, 12, 30, 31]. In the present study, these beneficial effects are not expected to occur because electroplated Pb was used, which did not undergo an electrode formation process. In the second mechanism, lignin in the electrolyte adsorbs onto the Pb surface, which causes the $PbSO_4$ to precipitate on top of the lignin instead of directly onto the Pb. This results in the formation of a more porous $PbSO_4$ film, which improves the capacity by leaving the active Pb available for further Pb^{2+} dissolution [5, 6, 27-29]. Before lignin can adsorb onto the Pb surface, it must first complex with Pb^{2+} ions in the solution to make an insoluble molecule [32]. In the present study, the potentiostatic reductions performed at the beginning of the experiment reduced any free Pb^{2+} ions. Therefore, the lignin was unable to complex and adsorb onto the Pb at the onset of the experiment. Without an initial layer of adsorbed lignin on the Pb surface, the beneficial effects on the $PbSO_4$ film are reduced and no increase in capacity is observed.

6.3.2.2. Crystal Size Distributions

In order to determine the mechanism by which lignin changes the morphology of the $PbSO_4$ film and decreases the capacity in this study, distributions of the crystal sizes at various times during the TXM experiments were obtained by analyzing the TXM images with ImageJ software. The size of each crystal was calculated by determining the maximum length of a

straight line which could be drawn from one end of the crystal to another. The measurement represents the diameter for non-spherical particles.

Figures 6.4 and 6.5 show the crystal size distributions obtained from the TXM and SEM experiments without and with lignin in the electrolyte, respectively. In addition, the mean, median, and mode of the distributions obtained from the TXM experiments are shown in Figure 6.6. For each histogram bar in Figures 6.4 and 6.5, the crystal size on the horizontal axis corresponds to the center of the bin. The distributions of the crystals from the TXM experiments (Figures 6.4a and 6.5a) were normalized based on the total amount of crystals at t = 160 seconds. After this time, distributions were unattainable due to overlapping of crystals in the films, which obscured determination of individual sizes (image a1 of Figures 6.1 and 6.2). Each SEM crystal distribution (Figures 6.4b and 6.5b) was obtained from three separate images of the same sample and was normalized with respect to the total number of crystals used in the study. An example image for each experiment is shown in image b1 of Figures 6.1 and 6.2. The TXM data show good agreement with the distributions obtained from the SEM images.

The mechanism of action of the lignin can be revealed from an analysis of the crystal distributions. For instance, Figures 6.4a and 6.6a show that the number and average size of the crystals increases during the early growth of the film without lignin. This behavior corresponds to a progressive nucleation and growth mechanism, where new crystals are continually forming, and pre-existing crystals are continually growing. In contrast, Figures 6.5a and 6.6b show that in the presence of lignin the number of crystals increases while the size distribution remains relatively the same. This trajectory in morphology indicates that lignin retards the growth of the crystals. Myrvold has shown that lignin will quickly adsorb onto $PbSO_4$, and it appears that this adsorption prevents the growth of the crystals [32]. Assuming the crystals grow due to

precipitation of Pb(II) species from the electrolyte, the adsorbed lignin most likely prevents the growth by physically blocking the precipitation sites on the crystals [33].

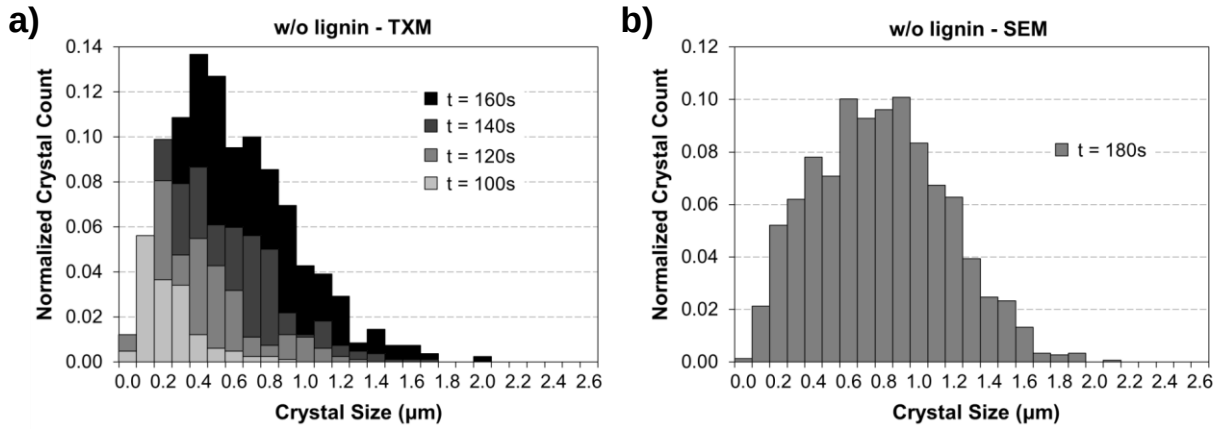

Figure 6.4. Distribution of crystal sizes for $PbSO_4$ grown on Pb in 4.6 M H_2SO_4: a) TXM experiment, b) separate experiment on electroplated Pb. Time in figures is in reference to the start of OCV (Fig. 6.3).

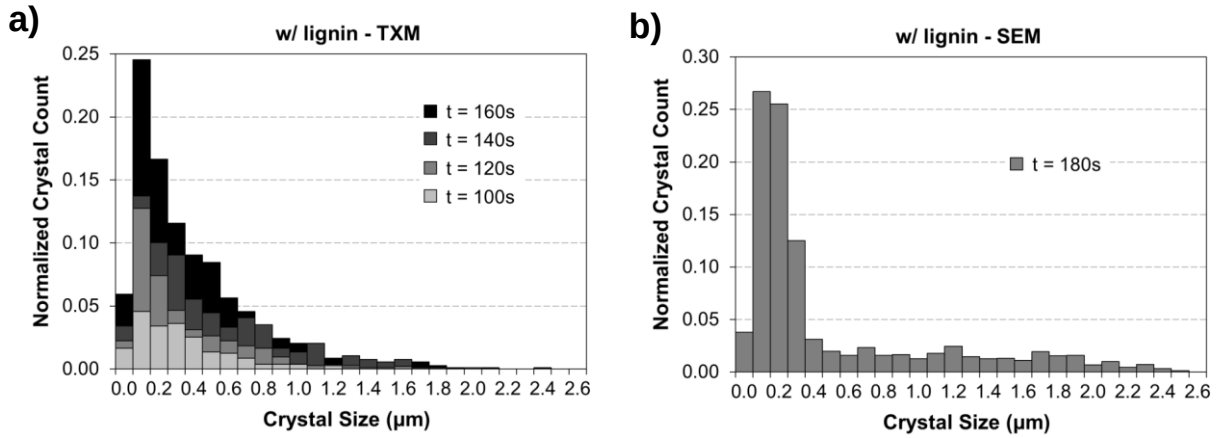

Figure 6.5. Distribution of crystal sizes for $PbSO_4$ grown on Pb in 4.6 M H_2SO_4 with 26 ppm sodium lignosulfonate: a) TXM experiment, b) separate experiment on electroplated Pb. Time in figures is in reference to the start of OCV (Fig. 6.3).

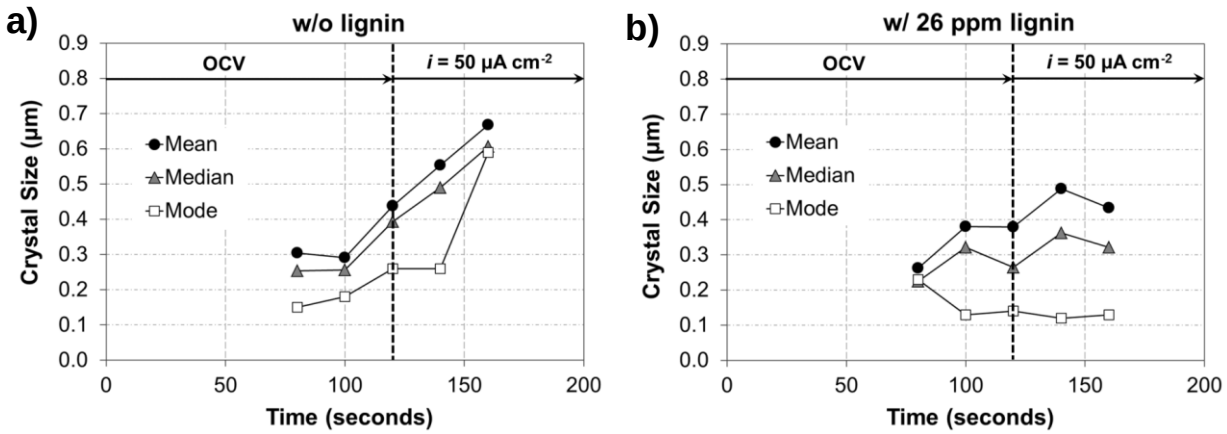

Figure 6.6. Mean, median, and mode of the crystal sizes obtained from the TXM experiments a) without and b) with 26 ppm sodium lignosulfonate in the electrolyte.

6.3.2.3. Crystal Density and Surface Coverage

Because lignin impedes the growth of the existing $PbSO_4$, it is anticipated that the number of crystals will increase in the presence of lignin in order to provide enough precipitation sites for the Pb(II) species. This hypothesis is verified in Figure 6.7, which shows $PbSO_4$ crystal densities for the images obtained from the TXM and SEM experiments. Each crystal density was determined by manually counting the number of crystals using ImageJ software and dividing that number by the area of the image. Similar to the crystal size distributions in Figures 6.4 and 6.5, the crystal densities for TXM images after t = 160 seconds were unattainable due to the overlapping of crystals and the coalescing of the films (images a1 of Figures 6.1 and 6.2). The data points for the SEM experiments were determined from the averages of three separate images of the same sample. The error bars represent the maximum and minimum values obtained from the sample. An example image for each SEM experiment is shown in image b1 of Figures 6.1 and 6.2.

In Fig. 6.7a, the experiments without lignin show good agreement between the TXM and SEM data. Extrapolation of the TXM data to t = 180 seconds results in a crystal density of ~80 × 10^6 cm^{-2}, which is only 1.1 times higher than the average crystal density reported for the SEM experiments (~70 × 10^6 cm^{-2}). For the experiments with lignin, there is less of an agreement between the TXM and SEM data. Extrapolation of the TXM data results in a crystal density of ~90 × 10^6 cm^{-2}, which is 1.3 times smaller than the average crystal density obtained from the SEM images (~120 × 10^6 cm^{-2}). Despite this discrepancy, the TXM extrapolation for the experiment with lignin still resides within the error bars of the SEM data.

Figure 6.7b shows the crystal densities for the TXM experiments. The results further confirm that lignin increases the crystal density. In addition, Fig. 6.7b shows that the rate of crystal nucleation approximately doubles in both experiments when the oxidation current is applied. The increase in crystal nucleation rate can be attributed to an increase in the oxidation rate, which increases *i)* the supersaturation concentration of Pb^{2+} in the electrolyte and *ii)* the overpotential. Both of these factors decrease the critical nucleus size, which increases the rate of nucleation [34].

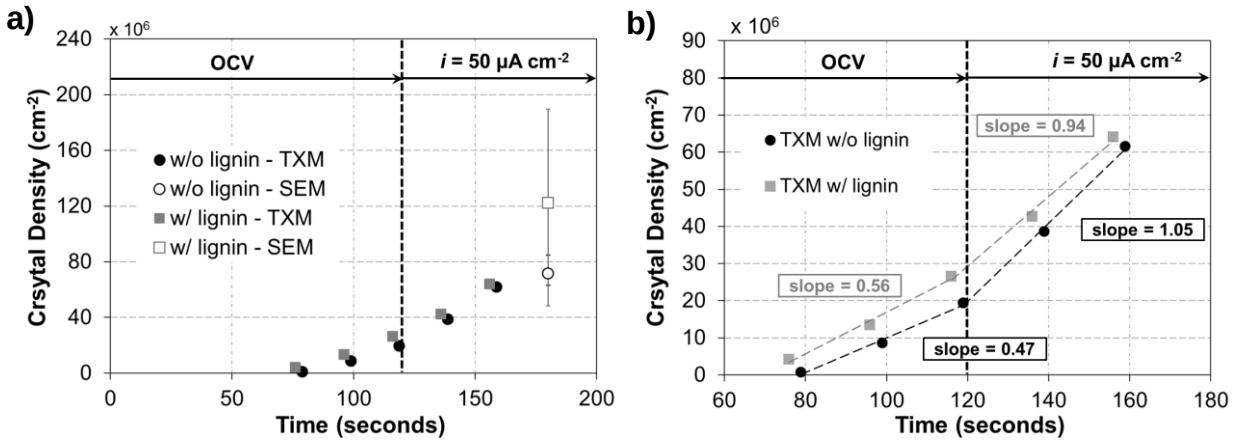

Figure 6.7. $PbSO_4$ crystal density on Pb in 4.6 M H_2SO_4 without and with 26 ppm sodium lignosulfonate. a) Comparison of SEM and TXM data. Error bars on SEM data indicate

maximum and minimum values observed from multiple images of the same sample. b) Close-up of TXM data. Slopes of fits have units [$\times 10^6$ cm^{-2} s^{-1}].

The supersaturation can increase when the current is applied because the oxidation rate exceeds that at OCV. For this system, the oxidation of Pb at OCV is balanced by the following proton reduction reaction:

$$2H^+ + 2e^- \rightarrow H_2, \qquad E^0 = -0.587 \text{ V vs. } Hg|Hg_2SO_4 \tag{6.1}$$

When the current is applied, the proton reduction rate decreases due to the increase in the electrode potential. The change in the proton reduction rate can be determined by performing a Taylor series expansion of the Tafel equation. This results in the following:

$$\Delta i = \frac{|i_{corr}|\alpha_c F}{RT}\Delta\phi \tag{6.2}$$

where α_c is the cathodic charge transfer coefficient (α_c = 0.5), R is the ideal gas constant, T is the temperature, F is Faraday's constant, and Δf is the change in potential applied to the electrode. Δf is ~18 mV at the beginning of oxidation (Figures 6.3 and 6.11). i_{corr} is the steady state corrosion rate, which for this system is 50 μA cm^{-2}. According to Eq. 6.2, Δi is equal to +17 μA cm^{-2} at the beginning of oxidation, indicating that the reduction rate changes from -50 μA cm^{-2} at OCV to -33 μA cm^{-2} when the current is applied. Therefore, in order for the applied current to reach 50 μA cm^{-2}, the actual oxidation rate can be estimated to be ~83 μA cm^{-2}, which is ~1.7 times higher than expected from the applied current.

To further understand the mechanism of growth of the $PbSO_4$ crystals, the surface coverage vs. time and overpotential vs. surface coverage are plotted in Figure 6.8. Fig. 6.8a

indicates that the electrode is fully covered with $PbSO_4$ within the first 3 to 5 minutes of oxidation. The remainder of the oxidation corresponds to a thickening of the film, see Chapter 5. In addition, both experiments (without and with lignin) have similar trends in overpotential (Fig. 6.8b), suggesting a similar mechanism of growth. The higher overpotential observed for the experiment with lignin can be attributed to the retardation in growth of the crystals. The trends in overpotential resemble the analytical expressions derived by Hills *et. al.* for the two dimensional growth of cylindrical crystals under galvanostatic conditions [35]. However, a rigorous analysis of the data to distinguish between instantaneous and progressive nucleation was not possible due to the scatter of the TXM results.

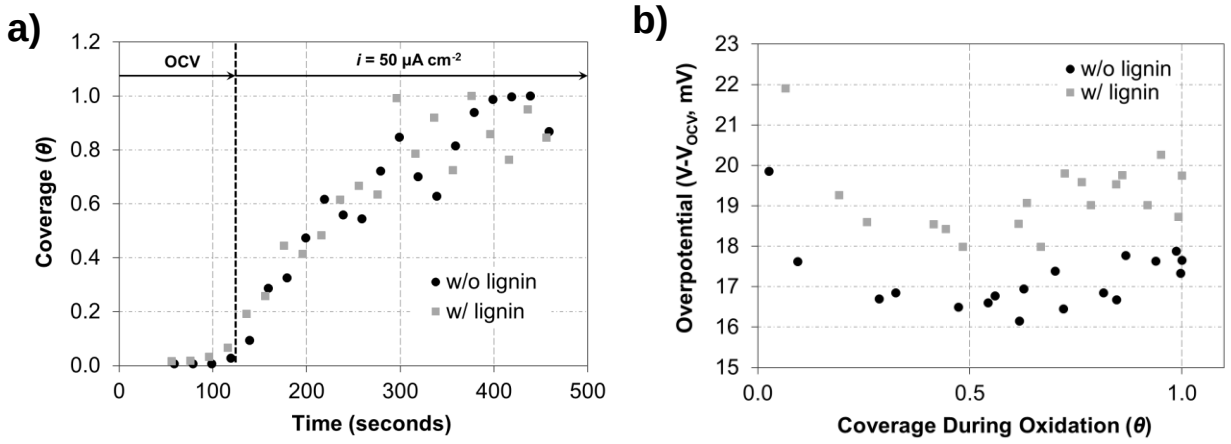

Figure 6.8. a) Surface coverage of $PbSO_4$ vs. time during the OCV and galvanostatic experiments. b) Overpotential vs. surface coverage during the oxidation experiment.

6.3.3. Growth of Individual Crystals

In Section 6.3.2.2, trends in crystal size obtained from the TXM images illustrated how lignin impacted the morphology of the $PbSO_4$. Although useful, the analysis cannot be applied to individual particles because size distributions (*i.e.*, mean, median, and mode) are heavily influenced by the continued nucleation of new crystals. In this section, we use TXM to track the

evolution of individual $PbSO_4$ crystals. A select group of crystals from the experiments without and with lignin were identified whose growth evolution was visualized by the TXM. Due to the need to easily visualize the crystals, the selected crystals tended to be the largest in the films. They are highlighted in images b1 and b2 of Figure 6.9.

In Figure 6.9, graphs a1 and a2 track the increase in area of the crystals (*i.e.,* the projections on the substrate) during the early stages of growth. For each crystal, the two-dimensional projections could not be tracked past t = 340 seconds due to crystal overlap and coalescence of the films. The crystals with and without lignin appear to have a similar growth pattern. Both sets of crystals appear to grow in two stages. In the first stage, the crystal area increases rapidly during the initial 50 to 150 seconds of growth. After this period, the growth rates appear to slow, signifying the second stage. This trend is most noticeable for crystals a, c, and d in the experiment without lignin and for crystals 1, 3, and 6 in the experiment with lignin. Note that the transition between the rapid and slow stages of growth occurs between t = 140 seconds and t = 180 seconds for these crystals. This is close to the time (t = 180 seconds) when the crystal sizes and crystal densities could no longer be determined in Figures 6.4a, 6.5a, and 6.7 due to coalescence of the film. It suggests that the decrease in growth rate from the first to the second stage may be attributed to an increase in the surface coverage of the $PbSO_4$. An increase in $PbSO_4$ increases the available precipitation sites and causes overlap between the diffusion zones of individual crystals. Both of these factors limit the amount of precipitation on the existing crystals [36].

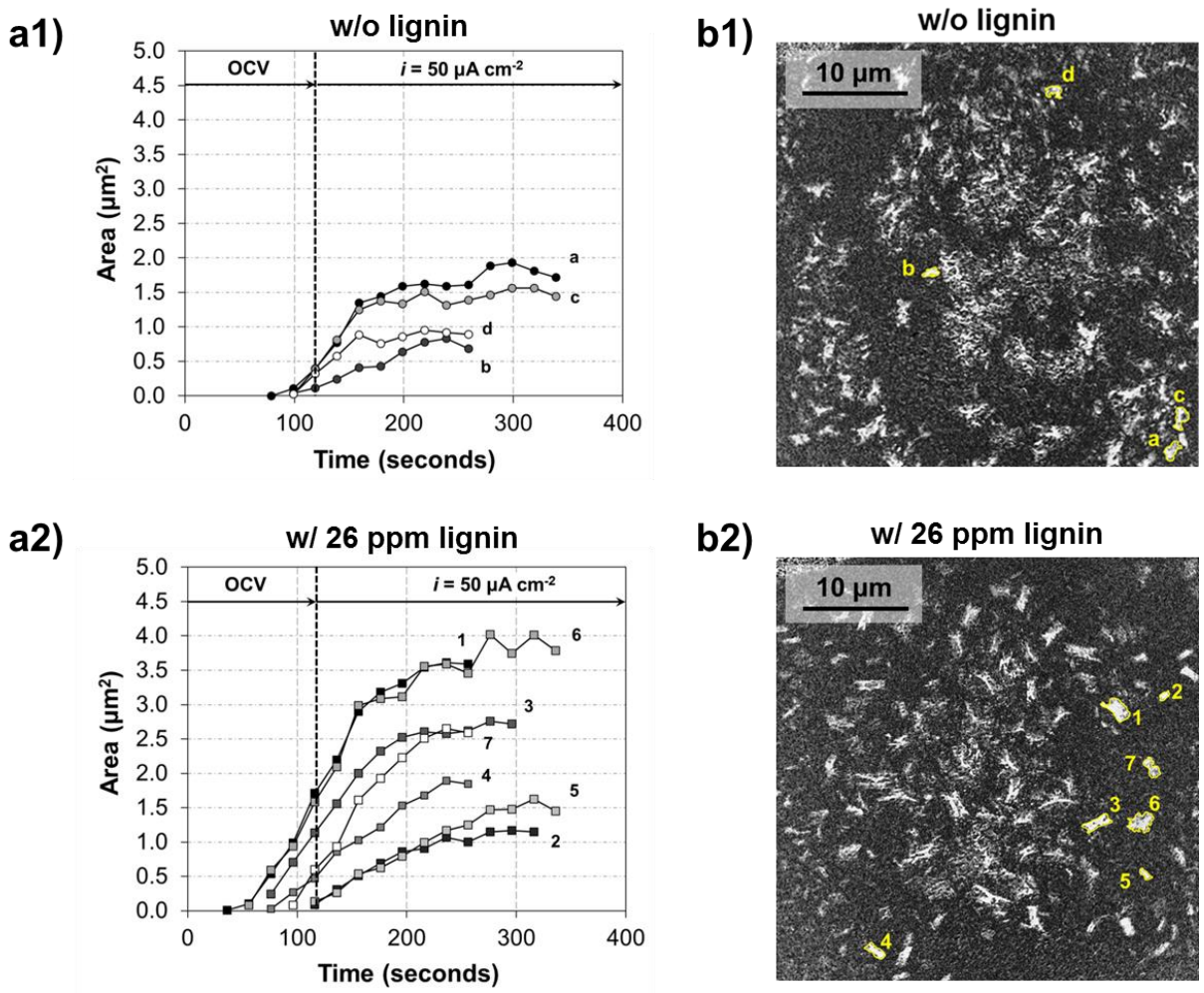

Figure 6.9. a) Initial increase in the projected area for a select group of crystals. b) TXM image of crystals used in study at t = 180 seconds. Results are from experiments 1) without and 2) with 26 ppm sodium lignosulfonate in the electrolyte.

To highlight the two observed stages of growth, Figure 6.10 shows magnified TXM images of crystals 3 and 6 in image b2 of Fig. 6.9. In order to aid in the interpretation of this figure, these crystals can be compared to the crystals in the SEM image shown in the magnified portion of image b1 in Fig. 6.2. The crystal on the right in Fig. 6.10 (crystal 6) resembles a thin, flat crystal that appears to be growing in a planar direction along the surface of the Pb electrode.

Meanwhile, the crystal on the left (crystal 3) more closely resembles a thin crystal growing in both the normal and planar directions.

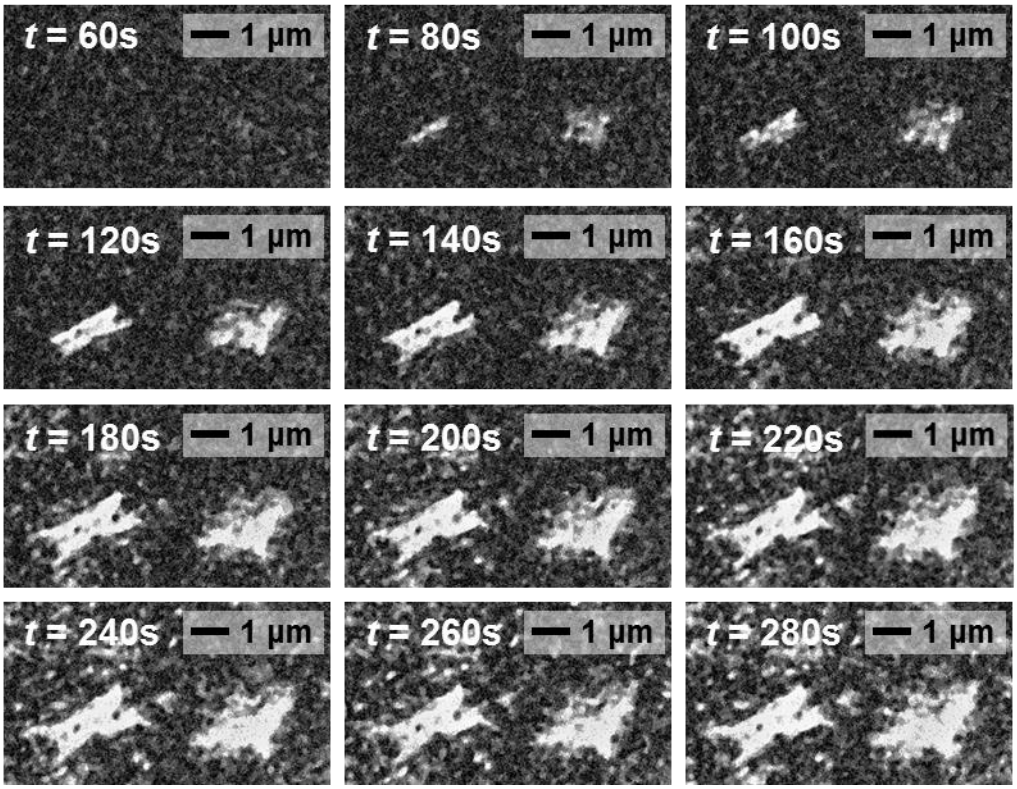

Figure 6.10. TXM images of crystals 3 and 6 (Fig. 6.8, image b2) grown at 50 µA cm^{-2}. Times are in reference to the start of OCV (Fig. 6.3).

Referring back to Fig. 6.10, during the first stage of growth (up to t = ~160 seconds), the two white $PbSO_4$ crystals appear to grow rapidly on the predominantly black Pb background. Based on the SEM comparison, the crystals are thin and flat. For the crystals to have this structure, their growth is likely two-dimensional. After t = ~160 seconds, additional small, white, $PbSO_4$ crystals become visible, especially around the crystal on the left (crystal 3). These times correspond well to the slowing of the growth rates observed in Fig. 6.9, further suggesting that the slowdown in growth during the second stage is due to the presence of other crystals on the

surface. Although crystal growth slows in the planar direction during the second stage, the SEM images in Fig. 6.2 suggest that crystal growth increases in the normal direction. For instance, a comparison of SEM images b1 and b2 in Fig. 6.2 shows that the large crystals at passivation (image b2) contain a more three-dimensional, pyramidal structure than the large crystals at the beginning of oxidation (image b1). In order for the large crystals in image b2 to have grown from large crystals similar to those in image b1, their growth in the normal direction would have to be greater-than-or-equal to their growth in the other two dimensions.

To further investigate the growth processes of the crystals, the projected area of each crystal was plotted versus time on a logarithmic plot. These graphs are shown in Figure 6.11. For both experiments (without and with lignin), no clear power-law dependence ($A \propto t^n$) is observed. This suggests that the growth mechanism is complex and cannot be explained by a simple diffusion-limited or kinetics-limited growth model.

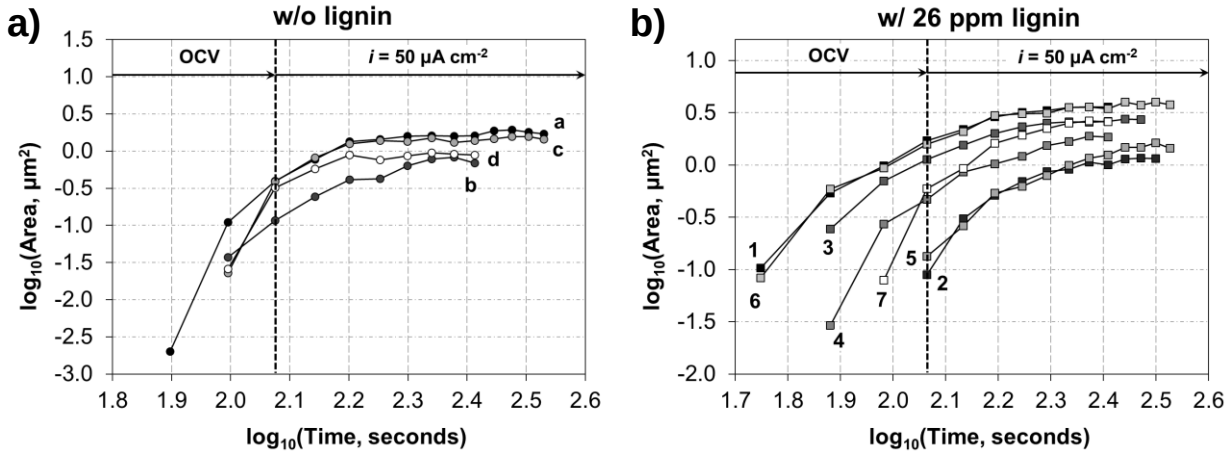

Figure 6.11. Logarithmic plots of crystal area vs. time for the projections of individual crystals in experiments a) without and b) with 26 ppm sodium lignosulfonate in the electrolyte.

6.3.4. Explanation for the Voltage Dip

An analysis of the early formation of $PbSO_4$ on Pb in H_2SO_4 may also provide insight into the potential-time transient behavior at the beginning of oxidation. Specifically, the anodic overpotential initially decreases, goes through a minimum, and then begins to increase [37]. In a lead acid battery, a similar behavior, termed the *coup de fouet*, is observed at the beginning of discharge, but it is attributed to the positive electrode, where PbO_2 is reduced to $PbSO_4$ [38]. Similar phenomena occur at the negative electrode, where Pb is oxidized to $PbSO_4$, but it is of smaller magnitude.

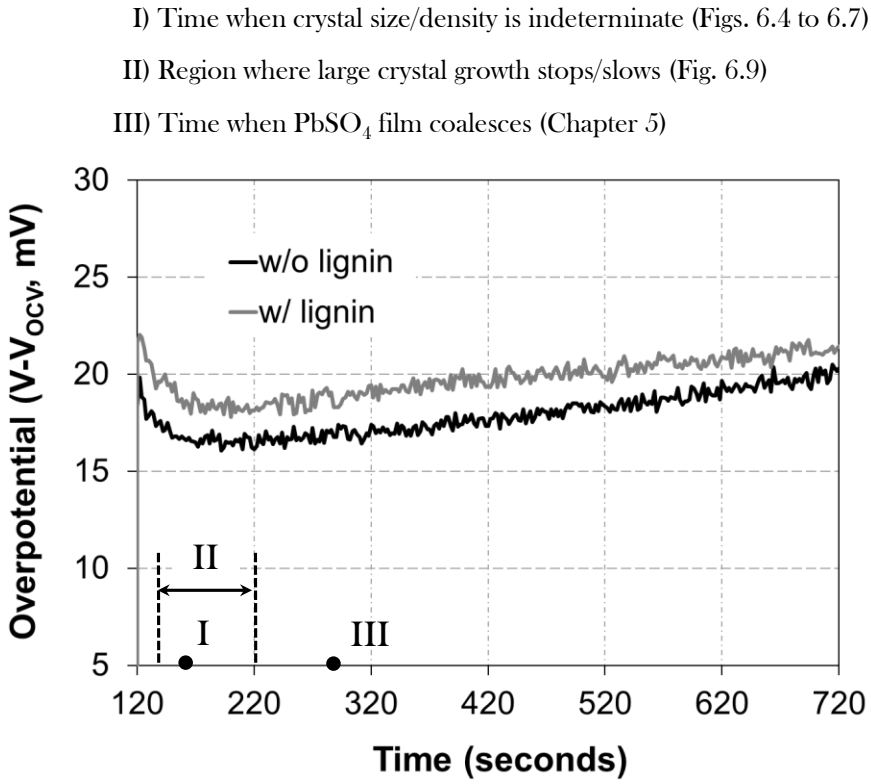

Figure 6.12. Initial voltage response of galvanostatic oxidation at 50 μA cm^{-2} in TXM set-up for experiment without and with 26 ppm sodium lignosulfonate in the electrolyte. I, II, and III mark the occurrence of specific events during the film growth.

The transient at the start of oxidation in the TXM experiments is shown in Figure 6.12. The initial increase in overpotential likely corresponds to an increase in *i)* the double layer capacitance of the electrode and *ii)* the supersaturation of the solution with Pb^{2+} ions. The supersaturation provides a driving force for crystallization and may be written as a concentration overpotential (η_c) [33]:

$$\eta_c = \frac{RT}{2F} \ln\left(\frac{c_{Pb^{2+}}}{c^e_{Pb^{2+}}} \right) \tag{6.3}$$

where $c_{Pb^{2+}}$ is the Pb^{2+} concentration in the solution, and $c^e_{Pb^{2+}}$ is the saturated Pb^{2+} concentration at equilibrium. Based on this equation, the decrease in overpotential from the initial spike to the plateau voltage is due to a relaxation in $c_{Pb^{2+}}$ back to the equilibrium value. The relaxation in $c_{Pb^{2+}}$ can be related to the increase in the surface coverage of $PbSO_4$ on the electrode (Fig. 6.8). For instance, the increase in surface coverage increases the number of available sites for precipitation of Pb^{2+} species. This increases the precipitation rate of Pb^{2+}, which causes $c_{Pb^{2+}}$ (and η_c) to decrease. This analysis implies that the rate of Pb^{2+} dissolution, which is equal to the applied current, may not equal the rate of $PbSO_4$ precipitation. This agrees with the explanation provided by Bernardi for the *coup de fouet* at the positive electrode [39].

In addition to the relaxation of the supersaturated concentration, the plateau voltage may correspond to the coalescence of the $PbSO_4$ film. For instance, Figure 6.12 highlights the occurrence of three specific events during the formation of the film. All three events occur close to the time when the plateau voltage is reached. The first mark at t = 160 seconds corresponds to the time when the crystal size distributions in Figures 6.4 and 6.5 and the crystal densities in Fig. 6.7 were unattainable due to overlapping of the crystals. The second mark signifies the region

where the growth of the crystals in Fig. 6.9 began to slow due to the presence of other crystals on the surface. Finally, the third mark corresponds to the time when the film is fully coalesced.

6.4. Summary

This chapter examined the effects of an organic additive on $PbSO_4$ growth and analyzed the early growth mechanisms of $PbSO_4$. Addition of sodium lignosulfonate to the H_2SO_4 was shown to impede, on average, the growth of the $PbSO_4$ crystals, which resulted in a $PbSO_4$ film with smaller crystals and an increased crystal density. For experiments with and without lignin, an increase in the crystal nucleation rate was observed when the oxidation current was applied. This was attributed to an increase in the supersaturation of the electrolyte. In addition, the early growth of the large $PbSO_4$ crystals was examined with and without lignin. For both cases, there was an initial, rapid growth rate, which declined after 50 to 150 seconds. The decline in growth rate was attributed to an increase in the $PbSO_4$ coverage, which increased the number of precipitation sites competing for $PbSO_4$. Finally, the potential-time transient at the beginning of oxidation was suggested to result from the relaxation of a supersaturated solution and the development of a $PbSO_4$ film with increasing resistance.

6.5. References

1. H. S. Chen, T. N. Cong, W. Yang, C. Q. Tan, Y. L. Li and Y. L. Ding, *Prog. Nat. Sci.*, **19**, 291 (2009).
2. P. Ruetschi, *J. Power Sources*, **127**, 33 (2004).
3. D. U. Sauer, in *Encyclopedia of Electrochemical Power Sources*, J. Garche, Editor, p. 805, Elsevier, Amsterdam (2009).
4. E. J. Ritchie, *Trans. Electrochem. Soc.*, **92**, 229 (1947).
5. G. J. Szava, *J. Power Sources*, **23**, 119 (1988).
6. G. I. Aidman, *J. Power Sources*, **59**, 25 (1996).
7. D. Pavlov, P. Nikolov and T. Rogachev, *J. Power Sources*, **195**, 4435 (2010).
8. D. Pavlov and P. Nikolov, *J. Electrochem. Soc.*, **159**, A1215 (2012).
9. C. Francia, M. Maja, P. Spinelli, F. Saez, B. Martinez and D. Marin, *J. Power Sources*, **85**, 102 (2000).

10. D. Pavlov, B. O. Myrvold, T. Rogachev and M. Matrakova, *J. Power Sources*, **85**, 79 (2000).
11. F. Saez, B. Martinez, D. Marin, P. Spinelli and F. Trinidad, *J. Power Sources*, **95**, 174 (2001).
12. D. P. Boden, J. Arias and F. A. Fleming, *J. Power Sources*, **95**, 277 (2001).
13. J. Valenciano, F. Trinidad and M. Fernandez, *J. Power Sources*, **113**, 318 (2003).
14. P. T. Moseley, R. F. Nelson and A. F. Hollenkamp, *J. Power Sources*, **157**, 3 (2006).
15. M. Calabek, K. Micka, P. Krivik and P. Baca, *J. Power Sources*, **158**, 864 (2006).
16. D. P. Boden, D. V. Loosemore, M. A. Spence and T. D. Wojcinski, *J. Power Sources*, **195**, 4470 (2010).
17. Y. Yamaguchi, M. Shiota, Y. Nakayama, N. Hirai and S. Hara, *J. Power Sources*, **85**, 22 (2000).
18. Y. Yamaguchi, M. Shiota, M. Hosokawa, Y. Nakayama, N. Hirai and S. Hara, *J. Power Sources*, **102**, 155 (2001).
19. Y. Yamaguchi, M. Shiota, Y. Nakayama, N. Hirai and S. Hara, *J. Power Sources*, **93**, 104 (2001).
20. I. Ban, Y. Yamaguchi, Y. Nakayama, N. Hirai and S. Hara, *J. Power Sources*, **107**, 167 (2002).
21. H. Vermesan, N. Hirai, M. Shiota and T. Tanaka, *J. Power Sources*, **133**, 52 (2004).
22. N. Hirai, D. Tabayashi, M. Shiota and T. Tanaka, *J. Power Sources*, **133**, 32 (2004).
23. N. Hirai, S. Kubo and K. Magara, *J. Power Sources*, **191**, 97 (2009).
24. J. Wang, Y. C. K. Chen, Q. X. Yuan, A. Tkachuk, C. Erdonmez, B. Hornberger and M. Feser, *Appl. Phys. Lett.*, **100**, 143107 (2012).
25. T. Ferreira and W. S. Rasband, *ImageJ User Guide - IJ 1.46*, imagej.nih.gov/ij/docs/guide/ (2010-2012).
26. N. A. Hampson and J. B. Lakeman, *Surf. Technol.*, **9**, 97 (1979).
27. M. P. J. Brennan and N. A. Hampson, *J. Electroanal. Chem.*, **48**, 465 (1973).
28. A. C. Simon, S. M. Caulder, P. J. Gurlusky and J. R. Pierson, *J. Electrochem. Soc.*, **121**, 463 (1974).
29. B. K. Mahato, *J. Electrochem. Soc.*, **127**, 1679 (1980).
30. J. R. Pierson, P. Gurlusky, A. C. Simon and S. M. Caulder, *J. Electrochem. Soc.*, **117**, 1463 (1970).
31. A. C. Simon, S. M. Caulder, P. J. Gurlusky and J. R. Pierson, *Electrochim. Acta*, **19**, 739 (1974).
32. B. O. Myrvold, *J. Power Sources*, **117**, 187 (2003).
33. L. M. Baugh, K. L. Bladen and F. L. Tye, *J. Electroanal. Chem.*, **145**, 355 (1983).
34. A. Milchev and M. I. Montenegro, *J. Electroanal. Chem.*, **333**, 93 (1992).
35. G. J. Hills, L. M. Peter, B. R. Scharifker and M. I. D. Pereira, *J. Electroanal. Chem.*, **124**, 247 (1981).
36. B. Scharifker and G. Hills, *Electrochim. Acta*, **28**, 879 (1983).
37. M. Perrin and A. Delaille, in *Encyclopedia of Electrochemical Power Sources*, J. Garche, Editor, p. 779, Elsevier, Amsterdam (2009).
38. A. Delaille, M. Perrin, F. Huet and L. Hernout, *J. Power Sources*, **158**, 1019 (2006).
39. D. M. Bernardi, *J. Electrochem. Soc.*, **137**, 1670 (1990).

CHAPTER 7

THEORETICAL CONSIDERATIONS FOR IMPROVING THE PULSE POWER OF A BATTERY THROUGH THE ADDITION OF A SECOND ELECTROCHEMICALLY ACTIVE MATERIAL

In this chapter, porous electrode theory is used to conduct case studies for when the addition of a second electrochemically active material can improve the pulse-power performance of an electrode by mitigating the ohmic losses at high depths of discharge. Case studies are conducted for the positive electrode of a sodium metal-halide battery and the graphite negative electrode of a lithium "rocking chair" battery. The study focuses on the impact of ohmic-to-charge transfer resistances within the porous structure, the capacity fraction of the second electrochemically active material, and the kinetic and thermodynamic parameters of the two active materials.

7.1. Introduction

To accelerate an electric vehicle, an important requirement of a battery is the ability to deliver high power pulses at all depths of discharge [1-3]. Nevertheless, a high power pulse can be difficult to achieve, especially at high depths of discharge (DoD). In some cases, high power is difficult to achieve at high DoD because of an increase in the ohmic resistance during discharge. The ohmic resistance increases due to the movement of the reaction fronts within the electrodes from more favorable (less resistive) to less favorable (more resistive) locations [4, 5]. For instance, this behavior has been documented in the positive electrode of sodium metal-halide batteries, where the low resistivity of the electrode (nickel and/or iron) and the higher resistivity

of the electrolyte (sodium tetrachloroaluminate) cause the reaction front to move from the separator to the current collector during discharge [6, 7]. At high DoD, the reaction front is far from the separator and the ionic path length is increased, which increases the overall ohmic resistance in the electrode.

One way to improve the pulse-power performance of an electrode is through the addition of a second active material that only reacts at higher DoD [7, 8]. A schematic of this concept is shown in Figure 7.1. Part a) shows the discharge and pulse-power process of an electrode with one active material. In this case, the reaction front starts near the separator and moves deeper into the electrode as the cell is discharged. When the electrode is pulsed at the high DoD, the reaction occurs deep within the electrode and there are high ohmic losses due to the increased ionic path length. In contrast, part b) shows the discharge and pulse-power process for an electrode with two active materials. For this case, the same initial behavior is observed, whereby the reaction front moves from the separator to the current collector during discharge. However, during the initial discharge, the second active material does not react. Therefore, when the electrode is pulsed at a high DoD, the high ohmic losses are avoided by reacting the second material close to the separator instead of the first material deep within the electrode. In the figure, the reduction in ionic path length between the two cases (one and two active materials) during the pulse is shown as Δx_{ion}. Note that in the second case, the second active material only reacts if the ohmic losses associated with reacting the main active material are greater than the losses associated with the poorer electrochemical performance of the second material.

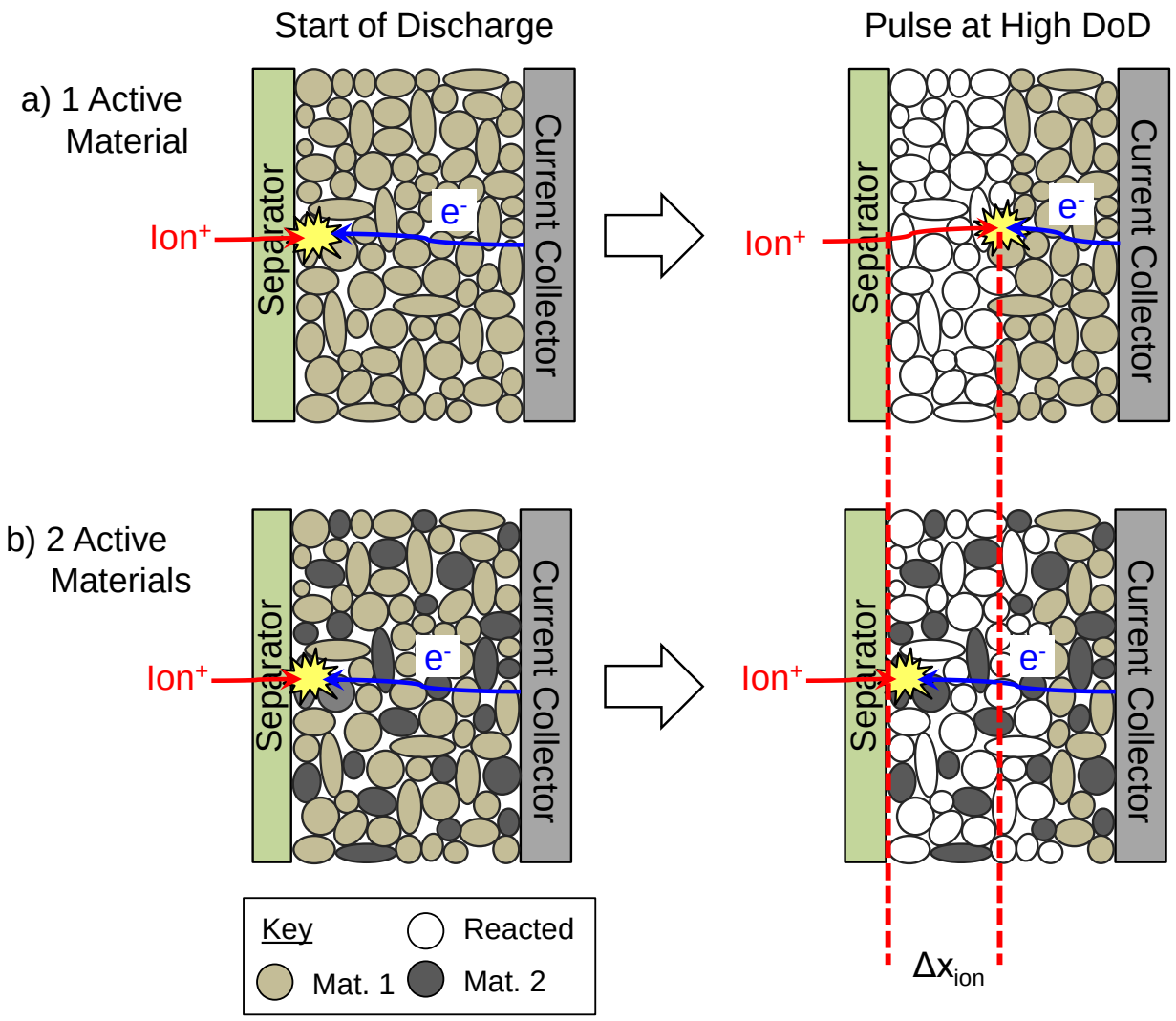

Figure 7.1. Schematic detailing how the addition of a second electrochemically active material can decrease the ionic resistance within an electrode during pulse-power operation at high depths of discharge. The schematic is valid for electrodes where the ionic resistance is much larger than the ohmic resistance.

Researchers have already used the concept outlined in Figure 7.1 to improve the pulse-power performance of the positive electrode of a sodium metal-halide battery [7, 8]. Galloway and Sudworth both provide descriptions of how the replacement of a small amount of nickel with

iron, which has a lower potential, can improve the pulse power at high DoD. However, these concepts have not been analyzed quantitatively, even though they are strongly supported by data from commercial cells. The aim of this paper is to explore conditions and designs when this concept is viable and if it may be applicable to other battery electrodes.

To accomplish this aim, a generic model was developed based on porous electrode theory, which can simulate the performance of an electrode with two active materials and can be applied to a variety of battery chemistries. Similar models have been developed by other researchers for the positive electrode of a lithium-ion battery [9-12]. These models were used to study the power and energy characteristics, stresses, and heat generation in electrodes with two active materials, but no analysis of the pulse-power performance was conducted. Furthermore, the concept outlined in Figure 1 is not applicable to the lithium-ion positive electrode because these electrodes discharge uniformly without reaction fronts (see Figure 7 in [12] for profiles during discharge at a 3C rate). Therefore, in order to test the viability of the concept outlined in Figure 7.1, different battery chemistries should be analyzed.

In this work, two case studies are conducted on two different electrode chemistries to analyze the viability and applicability of the concept outlined in Figure 7.1. First, the model is used to conduct an in depth case study on the positive electrode of a sodium metal-halide battery. Next, the analysis is applied to the graphite, negative electrode in a lithium-ion “rocking chair” battery, where it is shown that the addition of other carbonaceous materials to a graphite electrode has the potential to improve the pulse-power performance.

7.2. Model Formulation

7.2.1. Governing Equations

A schematic of the modeling domain, including the dependent variables, is shown in Figure 7.2. The model is transient, isothermal, and one-dimensional. It is formulated assuming the ohmic resistance in the solid electrode is negligible compared to the ohmic resistance in the electrolyte, *i.e.*:

$$\frac{\varepsilon^{1.5}\kappa}{(1-\varepsilon)^{1.5}\sigma} << 1 \tag{7.1}$$

where a Bruggeman-type correction is applied to both conductivities to account for the porous and tortuous nature of the electrode [13]. This assumption is valid for several commercial electrodes, including the positive electrode of a sodium metal-halide battery and the graphite negative electrode of a lithium-ion battery, which are considered in this work [5, 7]. The validity of Eq. 7.1 makes it possible to assign a constant value to the potential in the electrode. For numerical simplicity, the potential in the solid electrode is set equal to zero ($\phi_1 = 0$). Assuming minimal concentration variations, the potential in the liquid electrolyte is determined using Ohm's law. Conservation of charge, accounting for both Faradaic reactions, gives:

$$\varepsilon^{1.5}\kappa\frac{\partial^2\phi_2}{\partial x^2} = -a_I\varepsilon_{I,0}i_{rxn,I} - a_{II}\varepsilon_{II,0}i_{rxn,II} \tag{7.2}$$

In this model, the specific surface area, *a*, is an intrinsic property of the electrochemically active material. It is defined as the surface area of the active material per volume of the active material. This definition differs from that of Newman, where the specific surface area is defined as the surface area of the material per unit volume of the electrode [14]. In Eq. 7.2, ε is the volume fraction of the liquid electrolyte within the electrode and $\varepsilon_{I,0}$ and $\varepsilon_{II,0}$ are the initial volume

fractions of the 1st and 2nd electrochemically active materials in the electrode. All three values are assumed to be independent of DoD.

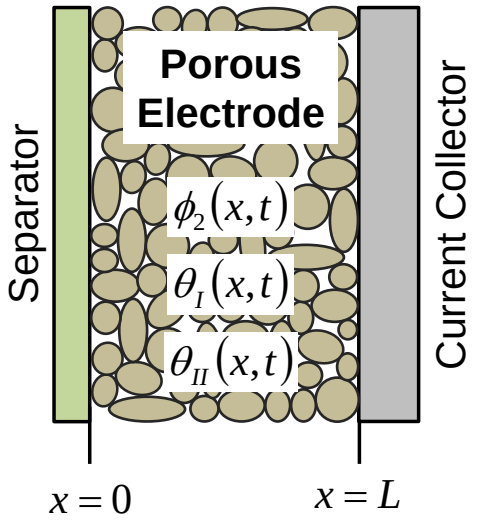

Figure 7.2. Schematic of the modeling domain and variables in the pulse-power simulations.

The reaction currents (i_{rxn}) are determined assuming the active materials undergo the following reaction:

$$A_k \leftrightarrow A_k^{n_k+} + \mathrm{n}_k \mathrm{e}^- \tag{7.3}$$

where the subscript k denotes active material *I* or *II*. This work is focused on simulating the maximum power of an electrode, which is obtained at high applied currents. At these high currents, the reaction kinetics are modeled by assuming the following Tafel equation:

$$i_{rxn,k} = i_0 \theta_k \gamma \exp\left[\frac{\gamma \alpha F}{RT}\left(-\phi_2 - U_k\right)\right] \tag{7.4}$$

where it is assumed the charge transfer coefficient, α, has the same value for both active materials. In Eq. 7.4, the open circuit potential (U_k) is set equal to the standard reference

potential due to the assumption of negligible concentration variations in the electrolyte. In addition, γ is defined as:

$$\gamma = \frac{i_{app}}{|i_{app}|} \tag{7.5}$$

The inclusion of γ generalizes the model formulation and makes it possible to simulate the cathodic and anodic discharge of an electrode.

The kinetic rate equation (Eq. 7.4) assumes that the reaction is directly proportional to θ_k, which is the ratio of the volumetric discharge capacity of the material to the initial volumetric discharge capacity of the material, where the volume is defined with respect to the electrode. θ_k is defined as:

$$\theta_k = \frac{\hat{Q}_k}{\hat{Q}_{k,0}}; \quad \hat{Q}_{k,0} = \frac{\varepsilon_{k,0} n_k F \rho_k}{M_k} \tag{7.6}$$

For an electrode undergoing a conversion reaction, the change in θ_k corresponds to a reduction in the volume of the active material. For an electrode undergoing an intercalation reaction, the change in θ_k corresponds to a reduction in the available sites for intercalation. The change in θ_k is simulated using the following:

$$\frac{\partial \theta_k}{\partial t} = -\frac{\gamma a_k \varepsilon_{k,0} i_{rxn,k}}{\hat{Q}_{k,0}} \tag{7.7}$$

7.2.2. Boundary and Initial Conditions

The simulations assume controlled-current operation of the electrode. The boundary conditions for the electrolyte potential (ϕ_2) are set using Ohm's law. At the separator, the current density is set equal to the applied current density, *i.e.*:

$$\varepsilon^{1.5}\kappa\left.\frac{\partial\phi_2}{\partial x}\right|_{x=0} = i_{app} \tag{7.8}$$

At the current collector, the ionic current density is set equal to zero, as follows:

$$\left.\frac{\partial\phi_2}{\partial x}\right|_{x=L} = 0 \tag{7.9}$$

At the start of the simulation, the potential difference between the electrode and electrolyte is set equal to the open circuit potential of the 1st active material, which results in the following:

$$\left(\phi_1 - \phi_2\right)\big|_{t=0} = U_I \text{ or } \phi_2\big|_{t=0} = -U_I \tag{7.10}$$

In addition, θ_k is set using the following initial conditions:

$$\theta_k\big|_{t=0} = 1 \tag{7.11}$$

7.2.3. Dimensionless Formulation

This section introduces a set of three scaled variables, which are used to reformulate the governing equations (Eqs. 7.2-4, 7.6-11), from which three dimensionless numbers emerge. The three scaled variables are defined as:

$$\bar{\phi}_2 = \frac{\varepsilon^{1.5}\kappa}{|i_{base}|L}\phi_2; \quad \bar{x} = \frac{x}{L}; \quad \tau = \frac{|i_{base}|}{\left(\hat{Q}_{I,0} + \hat{Q}_{II,0}\right)L}t \tag{7.12}$$

where i_{base} is the baseline current density applied before the high current pulse (see discussion of Figure 7.2 for more detail). These variables are used to reformulate Eqs. 7.2-6, which results in the following, dimensionless governing equations:

$$\frac{\partial^2\bar{\phi}_2}{\partial\bar{x}^2} = -\gamma\psi\left(\varepsilon_{I,0}\theta_I + \xi\varepsilon_{II,0}\theta_{II}\right)\exp\left(-\gamma w_T^{-1}\bar{\phi}_2\right) \tag{7.13}$$

$$\frac{\partial \theta_I}{\partial \tau} = -\psi \varepsilon_{I,0} \theta_I f_{I,0}^{-1} \exp\left(-\gamma w_T^{-1} \bar{\phi}_2\right) \tag{7.14}$$

$$\frac{\partial \theta_{II}}{\partial \tau} = -\xi \psi \varepsilon_{II,0} \theta_{II} f_{II,0}^{-1} \exp\left(-\gamma w_T^{-1} \bar{\phi}_2\right) \tag{7.15}$$

where $f_{k,0}$ is the initial capacity fraction of the active material in the electrode defined as follows:

$$f_{k,0} = \frac{\hat{Q}_{k,0}}{\hat{Q}_{I,0} + \hat{Q}_{II,0}} \tag{7.16}$$

In Eqs. 7.13-15, the dimensionless constants are defined as:

$$w_T = \frac{\varepsilon^{1.5} \kappa RT}{\alpha F |i_{base}| L} \tag{7.17}$$

$$\xi = \frac{a_{II} i_{0,II}}{a_I i_{0,I}} \exp\left(-\frac{\gamma \alpha F \left(U_{II} - U_I\right)}{RT}\right) \tag{7.18}$$

$$\psi = \frac{a_I i_{0,I} L}{|i_{base}|} \exp\left(-\frac{\gamma \alpha F U_I}{RT}\right) \tag{7.19}$$

w_T is the ratio of charge transfer to ohmic resistance [15], ξ is the ratio of kinetic and thermodynamic parameters between active materials I and II, and ψ is a dimensionless description of the kinetic and thermodynamic parameters of active material I. The value of ψ has an impact on the absolute power obtainable for a system, but it does not influence whether or not the addition of active material II will enhance the pulse-power performance.

As a result of the reformulation, the boundary conditions and initial conditions on the electrolyte potential (Eqs. 7.7-9) are redefined as:

$$\left.\frac{\partial \bar{\phi}_2}{\partial x}\right|_{x=0} = \frac{i_{app}}{|i_{base}|}; \quad \left.\frac{\partial \bar{\phi}_2}{\partial x}\right|_{x=L} = 0 \tag{7.20}$$

$$\bar{\phi}_2\big|_{t=0} = -\frac{U_I \varepsilon^{1.5} \kappa}{|i_{base}| L} \tag{7.21}$$

The initial conditions for the volume fractions of the active materials (Eq. 7.11) are unchanged by the introduction of the scaled variables.

7.2.4. Numerical Methods

Equations 7.13-21 were linearized and solved simultaneously in FORTRAN 95 using the subroutines BANDJ and MATINV [14]. Discretization of the equations was done using the forward time, central difference method. A mesh size of 201 points and a time step of 0.01 seconds were used. Computer experiments were performed for the mesh size and time step in order to test for convergence. The computing was performed on the Yeti Shared HPC Cluster at Columbia University.

7.2.5. Description of Model System

The positive electrode of a sodium-metal halide battery was selected as a test case for the pulse-power analysis. In a commercial sodium metal-halide battery, nickel and iron are used as the first and second electrochemically active materials, respectively. During discharge, the following half-cell reactions occur:

$$\mathrm{Ni}^{2+} + 2\mathrm{e}^- \rightarrow \mathrm{Ni} \qquad U_I = 2.58 \text{ V} \tag{7.22}$$

$$\mathrm{Fe}^{2+} + 2\mathrm{e}^- \rightarrow \mathrm{Fe} \qquad U_{II} = 2.34 \text{ V} \tag{7.23}$$

were the open circuit potentials are given with respect to the $\mathrm{Na}|\mathrm{Na}^+$ negative electrode of the sodium metal-halide battery. In the positive electrode, the iron and nickel ions exist as sparingly soluble metal chlorides with the remainder of the solid phase comprised of nickel metal as a

conductive backbone. The initial volume fractions of nickel chloride and iron chloride ($\varepsilon_{I,0}$ and $\varepsilon_{II,0}$, respectively) were determined assuming a constant volumetric capacity of 1777 C cm^{-3} for the electrode. In a commercial battery, the electrode is assembled in the discharged state as nickel and iron metal with sparingly soluble sodium chloride determining the total capacity. In this study, the constant volumetric capacity of 1777 C cm^{-3} corresponds to a fully discharged electrode with a composition of 61-65% (by weight) nickel and iron metal and 35-39% (by weight) sodium chloride, where the exact weight fractions depend on the initial capacity fractions of the two active materials ($f_{I,0}$ and $f_{II,0}$). These values agree well with the compositions studied by Zhu *et al.* [16].

Table 7.1 provides the values of all other parameters used in the simulations. The specific surface area was calculated using the following equation:

$$a_k = \frac{3}{r_{p,k}} \tag{7.24}$$

with an average particle radius ($r_{p,k}$) of 660 μm for both materials [16]. Note that this electrode satisfies the assumption outlined in Eq. 1 that the ohmic resistance in the solid electrode is negligible compared to the ohmic resistance in the electrolyte. For instance, evaluation of Eq. 7.1 with the parameters in Table 7.1 (and a conductivity of 3.92×10^4 S cm^{-1} for the solid nickel electrode) results in a value of $2.0 \times 10^{-5} << 1$ [17]. In addition, the assumption of minimal concentration variations in the electrolyte is valid for this electrode because the reactants exist as sparingly soluble chlorides, which are evenly dispersed throughout the electrode.

Table 7.1. List of parameters used in case study of the positive electrode in a sodium metal-halide battery.

Symbol	Description	Value
a_I , a_{II}	Specific surface area ($cm^2\ cm^{-3}$)	45.5
α	Charge transfer coefficient	0.5
ε	Porosity	0.5
i_{base}	Baseline discharge current density ($A\ cm^{-2}$)[16]	1.59×10^{-1}
$i_{0,I}$, $i_{0,II}$	Exchange current density ($A\ cm^{-2}$)	1.02×10^{-2}
κ	Electrolyte conductivity ($S\ cm^{-1}$) [18]	0.778
T	Temperature (K)	573

7.2.6. Simulation Procedure

This section contains a description of the simulation procedure that was employed to analyze the pulse-power performance of an electrode. Figure 7.3 shows an example of a simulated discharge curve for a sodium metal-halide electrode containing no iron (*i.e.*, $f_{II,0} = 0$). First, the electrode was discharged galvanostatically at a current (i_{base}) to a set depth of discharge (DoD). Once the DoD was reached, a high current pulse (i_{pulse}) was applied to the electrode for a time (t_{pulse}). For both case studies, t_{pulse} is equal to 10 seconds, which was chosen based on the discharge specifications set by the U. S. Advanced Battery Consortium (USABC) for plug-in hybrid electric vehicles [3]. The voltage at the end of the high current pulse is used to determine the pulse power of the electrode (P_{pulse}), which is the basis for the analysis below. To determine the voltage, the potential drop across the electrode was considered relative to the open circuit potential of a $Na|Na^+$ electrode as follows:

$$V_{cell} = \left(\phi_1\big|_{x=L} - \phi_2\big|_{x=0}\right) - U_{Na|Na^+} = -\phi_2\big|_{x=0} \tag{7.25}$$

where the open circuit potential is equal to zero ($U_{Na|Na^+} = 0$) because all open circuit potentials are taken with respect to the $Na|Na^+$ electrode in this case study.

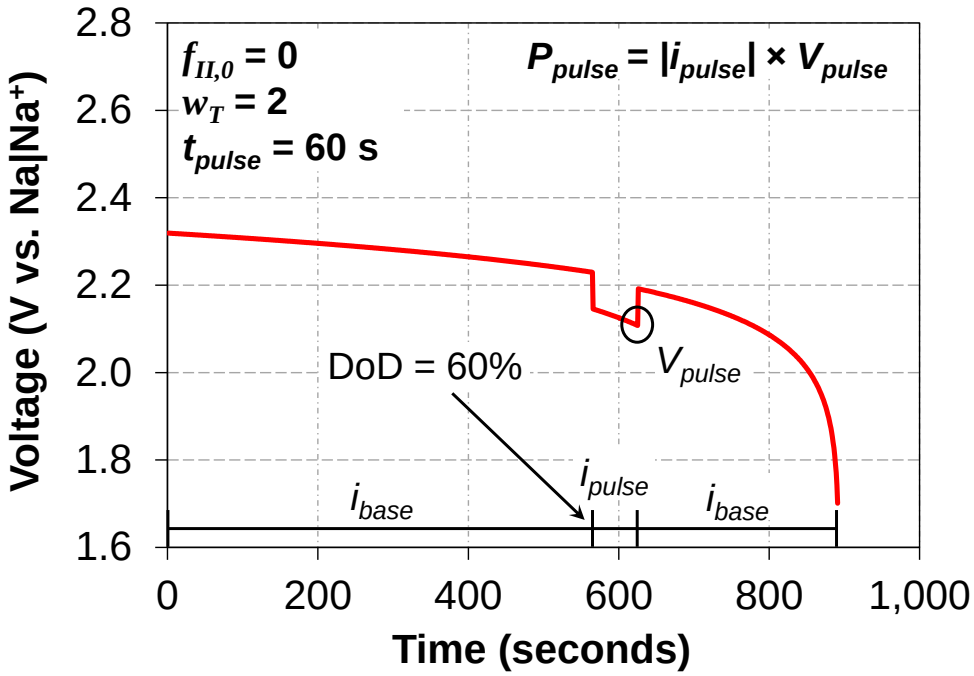

Figure 7.3. Simulated discharge curve exemplifying procedure used to analyze the pulse-power performance of the electrode.

7.3. Results and Discussion

7.3.1. Power Curves for the Metal-Halide Electrode

Figures 7.4-6 compare the P_{pulse} of electrodes containing one active material to the P_{pulse} of electrodes containing two active materials, where all electrodes have the same volumetric capacity (C cm^{-3}). In Figure 7.4, the second electrochemically active material (iron chloride) accounted for 1% of the total capacity. In Figure 7.5, the iron chloride accounted for 10% of the capacity. In Figure 7.6, it accounted for 50% of the capacity. For all active material fractions, simulations were run to DoDs of 60% (τ = 0.6) and 80% (τ = 0.8) for electrodes with three

different values of w_T (0.1, 0.25, and 0.75). The values of w_T in the simulations were adjusted by changing the length of the electrode. For each value of w_T, the electrodes with one and two active materials had the same total capacity. To put w_T into perspective, note that for the commercial sodium metal-halide cell published by Rijssenbeek *et al.*, a discharge at C/3 (10 amps) would correspond to $w_T \sim 0.64$ [6]. This value was determined using the parameters in Table 7.1 along with an average path length of 1 cm and an electrode area of 236 cm^2. The path length and electrode area were obtained through an ImageJ analysis of Figure 1 in [6].

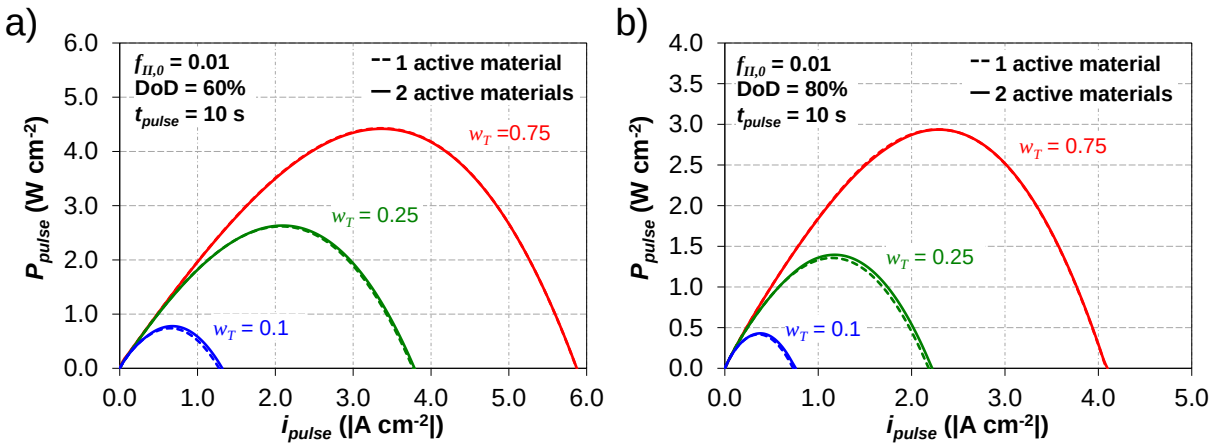

Figure 7.4. Comparison of simulated pulse-power (P_{pulse}) vs. pulse-current (i_{pulse}) for electrodes comprised of one and two active materials that were discharged to a DoD of a) 60% (τ = 0.6) and b) 80% (τ = 0.8). For the two-material simulations, the second material accounted for 1% of the total capacity. Definitions for P_{pulse} and i_{pulse} can be found on Figure 7.3.

Figure 7.4 shows that replacement of 1% of the capacity with the second electrochemically active material has a negligible impact on the pulse-power of the electrode. For both pulse-start times (*i.e.*, DoDs) and all three values of w_T, the P_{pulse} vs. i_{pulse} curves are almost identical for the simulations with 1 and 2 active materials. Replacement of 1% of the

capacity has no impact on the pulse-power because the second material does not have enough capacity to maintain the reaction front near the separator during the high current pulse. Instead, the electrode behaves like there is only one active material and large ohmic losses are still present.

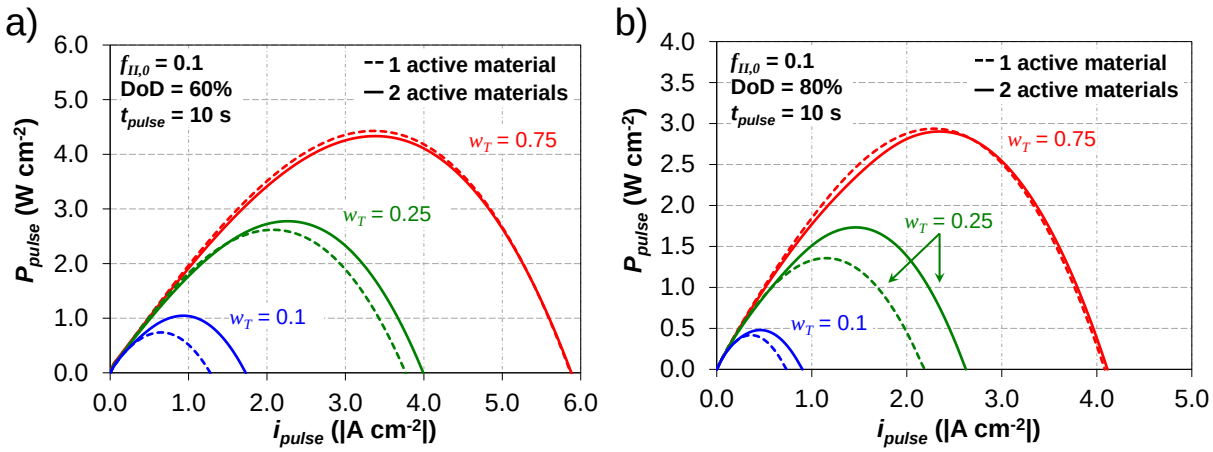

Figure 7.5. Comparison of simulated pulse-power (P_{pulse}) vs. pulse-current (i_{pulse}) for electrodes comprised of one and two active materials that were discharged to a DoD of a) 60% (τ = 0.6) and b) 80% (τ = 0.8). For the two-material simulations, the second material accounted for 10% of the total capacity. Definitions for P_{pulse} and i_{pulse} can be found on Figure 7.3.

In contrast, Figure 7.5 shows that the replacement of 10% of the capacity with a second active material can improve the pulse-power performance. For both DoDs and for w_T equal to 0.1 and 0.25, the electrodes with two active materials have a higher maximum pulse power than the electrodes with one active material. For $w_T = 0.1$, the second material increases the maximum power by 41% and 15% at DoDs of 60% (τ = 0.6) and 80% (τ = 0.8), respectively. For $w_T = 0.25$, the second material increases the maximum power by 6% and 28% at DoDs of 60%

and 80%, respectively. In contrast, the second material is shown to slightly *decrease* (~2%) the pulse power for $w_T = 0.75$. The higher w_T corresponds to a more uniform reaction distribution during the initial, baseline discharge [15]. This suggests that for higher values of w_T the first active material is still present close to the separator when the high current pulse is applied. Therefore, there is no benefit for adding the second active material.

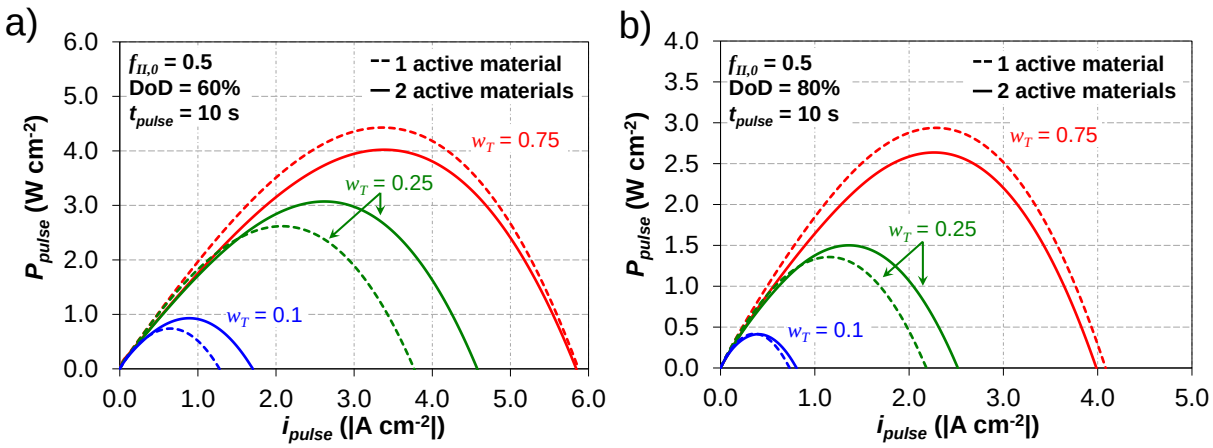

Figure 7.6. Comparison of simulated pulse-power (P_{pulse}) vs. pulse-current (i_{pulse}) for electrodes comprised of one and two active materials that were discharged to a DoD of a) 60% (τ = 0.6) and b) 80% (τ = 0.8). For the two-material simulations, the second material accounted for 50% of the total capacity. Definitions for P_{pulse} and i_{pulse} can be found on Figure 7.3.

Figure 7.6 shows that replacement of 50% of the capacity with the second active material has a similar trend to replacement of 10% of the capacity. For $w_T = 0.1$, the second material increases the maximum power by 26% and <1% at DoDs of 60% and 80%, respectively. For $w_T = 0.25$, the second material increases the maximum power by 17% and 11% at DoDs of 60% and 80%, respectively. In addition, for $w_T = 0.75$ the second material *decreases* the maximum

power by 10% and 11% at DoDs of 60% and 80%, respectively. The decrease in power is once again due to the uniform reaction distribution during the initial baseline discharge. For both electrodes with $w_T = 0.75$ (with and without the second active material), the reaction occurs close to the separator during the high current pulse. However, for the 50/50 composition of the active materials, almost all of the first active material has been consumed during the baseline discharge to 60% and 80% DoD. Therefore, the relatively poor pulse-power of this electrode is caused by the poor electrochemical performance of the second active material.

In summary, Figures 7.4 to 7.6 demonstrate that the addition of a second electrochemically active material to an electrode can significantly improve the pulse power. The level of improvement depends on the amount of second active material as well as the electrode depth of discharge. Additionally, significant improvements were only observed for electrodes with low w_T (< 0.75), due to the uneven reaction distributions during the baseline discharge, which deplete the active material near the separator.

While the addition of a second electrochemically active material can improve the pulse power of the electrode, it can also decrease the theoretical energy density. For instance, replacement of 1%, 10%, and 50% of the capacity with the second active material decreases the theoretical energy density of the electrode by 0.1%, 0.9%, and 4.7%, respectively. This decrease in energy is due to the lower voltage of the second material (iron chloride). Although the decrease in energy density is slight, the tradeoff between increasing power and energy remains an important consideration for designing an electrode with two active materials.

7.3.2. Active Material Distributions

The objective of this section is to show that the increase in pulse power for the electrodes with two active materials is due to the mechanism outlined in the introduction (see Figure 7.1). Figure 7.7 shows the simulated distributions of active material within a) an electrode comprised of only the first active material and b) an electrode where the second active material accounts for 10% of the capacity. The distributions are shown during a high current pulse at $i_{pulse} = 10 \times i_{base}$.

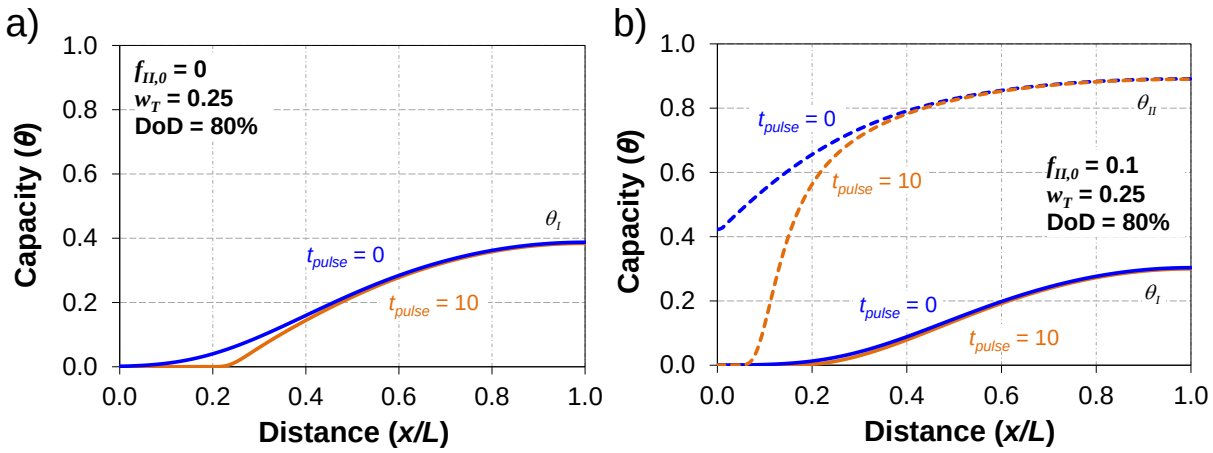

Figure 7.7. Simulated distributions of active materials during a high current pulse at $i_{pulse} = 10 \times i_{base}$ for a) an electrode with only the first active material and b) an electrode with 10% of the capacity replaced by the second active material. x/L=0 and x/L=1 correspond to the separator and current collector, respectively.

Fig 7.7a shows that when only one active material is present, the high current pulse results in the quick consumption of the active material near the separator, which forces the reaction front into the electrode. At the end of the pulse, all of the material within the first 20% of the electrode closest to the separator is consumed. In contrast, for the electrode with two active materials (Fig. 7.7b), the high current pulse has a minimal impact on the distribution of the

first active material. Instead, only the second active material is consumed. However, because there was a large amount of the second active material near the separator at the start of the pulse, the subsequent reactions only consumed the material within the first 10% of the electrode closest to the separator. Therefore, at the end of the pulse, the electrode with two active materials has only half as much ohmic resistance as the electrode with one active material (10% vs. 20% reaction penetration depth). This resulted in an overall improvement in the pulse-power performance (see Figure 7.5b).

7.3.3. Electrode Design Considerations

The results in Figures 7.4 to 7.6 indicate that the pulse-power performance of an electrode depends on the fractions of the first and second electrochemically active materials. This suggests that the model can be used as a design tool to determine what active material fractions maximize the pulse power of an electrode. The results of such an analysis for the sodium metal-halide electrode are shown in Figure 7.8 for an electrode with $w_T = 0.25$ that underwent high current pulses for 10 seconds. Two curves are shown for pulses after baseline discharges to 60% and 80% DoD. The curves show how the maximum pulse power of the electrode changes as a function of the capacity fraction of the second electrochemically active material. The power is plotted as the ratio of the maximum pulse power for an electrode with two active materials to the maximum pulse power of an electrode with one active material. Values greater than one indicate improvement in performance with the addition of the second material. The maximum pulse power was obtained from the peak of P_{pulse} vs. i_{pulse} curves (see Figures 7.4 to 7.6 for examples).

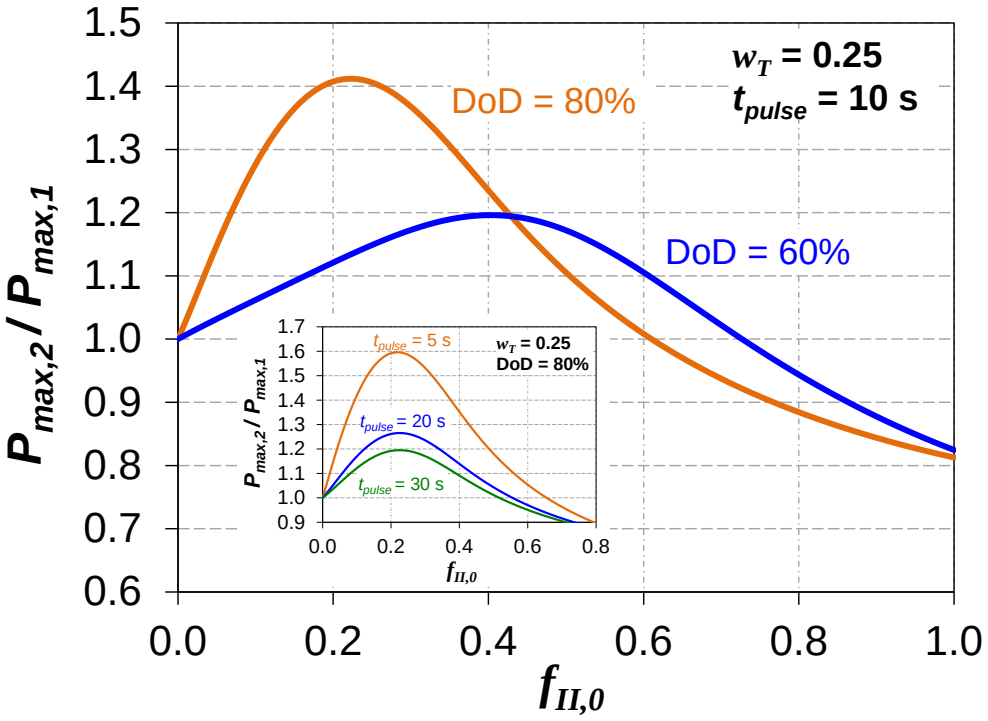

Figure 7.8. Simulated pulse-power as a function of the capacity fraction of the second active material (iron chloride) in the positive electrode of a sodium metal-halide battery. Pulse-power is plotted as the ratio of the maximum pulse-power of an electrode with two active materials (nickel + iron chloride) to the maximum pulse-power of an electrode with one active material (nickel chloride). Inset: pulse-power for pulse times of 5, 20, and 30 seconds.

The two, main curves in Figure 7.8 indicate that the optimal capacity fraction of the second material depends on the DoD of the electrode. Under the current operating conditions, the simulations suggest that electrodes with capacity fractions ($f_{II,0}$) of 0.2 to 0.5 can significantly improve the pulse power at both depths of discharge (up to 20% and 40% improvement for DoD equal to 60% and 80%, respectively). Note that electrodes with capacity fractions in this range will also have 1.9% to 4.7% lower theoretical energy densities than an electrode with only the first active material. For the positive electrode of a sodium metal-halide cell, this range

corresponds to a composition in the discharged state of ~3% to ~9% (by weight) iron, ~35% sodium chloride, and the remainder nickel.

The inset in Figure 7.8 shows results for pulses of 5, 20, and 30 seconds for pulses at 80% DoD. The results indicate that increases in the pulse time (t_{pulse}) slightly decrease both the range of beneficial capacity fractions and the net improvement in pulse power. This trend is expected since higher pulse times will consume more of the second active material and push the reaction front deeper into the electrode.

In addition to helping determine the best active material fractions for an electrode, the model can also be used to analyze which materials would be most beneficial as a second active material. The results of such an analysis are shown in Figure 7.9 for electrodes that underwent high current pulses for 10 seconds at 80% DoD. All simulations were conducted for electrodes with the same geometry and the same first active material, which corresponded to constant values of $w_T = 0.25$ and $\psi = 4.4 \times 10^{11}$ (Eqs. 7.17 and 7.19). The only difference between each curve is the value of ξ used in the simulations, which depends on the electrochemical properties of the second active material (Eq. 7.18). $\xi = 1$ corresponds to identical first and second electrochemically active materials. Note that $\xi = 0.088$ for the sodium metal-halide electrode used in the case study (Figures 7.4 to 7.8).

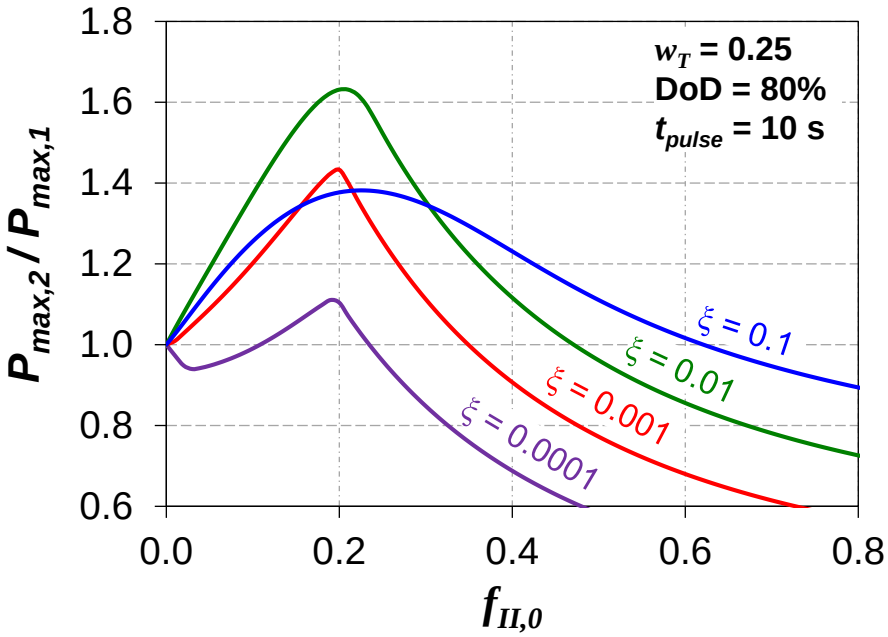

Figure 7.9. Comparison of the simulated pulse-power for electrodes with different values of ξ (Eq. 7.16), which corresponds to different electrochemical properties for the second active material. Pulse-power is plotted as the ratio of the maximum pulse-power of an electrode with two active materials to the maximum pulse-power of an electrode with one active material.

Figure 7.9 shows how the pulse power of the electrode changes with respect to changes in the capacity fraction of the second active material ($f_{II,0}$) and the value of ξ. The power ratios in Figure 7.9 have the same meaning as the power ratios in Figure 7.8. The results of the simulations predict that the improvement in pulse power will go through a maximum as the value of ξ increases. For instance, the peak pulse power ($P_{peak}(\xi)$) follows the trend $P_{peak}(0.01) > P_{peak}(0.001) > P_{peak}(0.1) > P_{peak}(0.0001)$. At low values of ξ, the electrochemical properties of the second material are too poor to provide any benefit during pulse power. This is exemplified for ξ = 0.0001, where simulations predict only a <12% increase in pulse power can be achieved

for a small range of capacity fractions (0.11 to 0.23). In contrast, at high values of ξ, the electrochemical properties of the second active material become too similar to the first, which causes the second material to react during the baseline discharge. This reaction will move the reaction front of the second material away from the separator, which increases the ohmic drop during a high current pulse and decreases the power. This is exemplified by the decrease in the maximum pulse power from ξ = 0.01 to ξ = 0.1.

7.3.4. Negative Electrode of a Li-ion Battery

In the previous sections, the sodium metal-halide electrode was used as a test case to analyze how the addition of a second electrochemically active material can improve the pulse power of an electrode. In this section, a second, brief case study is conducted to demonstrate how the addition of other carbonaceous materials (in particular, carbon black) to the graphite electrode of a commercial lithium-ion battery may also improve the pulse power.

To accomplish this, the model outlined in Equations 7.13-21 is utilized with adjustments made to the input parameters. The input parameters for the Li-ion case study are provided in Table 7.2. The geometric parameters for graphite (the first active material) were obtained from an analysis of a commercial 18500 graphite electrode using X-ray nano-tomography recently published by Ender [19]. The exchange current density ($i_{0,I}$) was calculated using Eq. 7 in [20] assuming a lithium salt concentration of 1 M and a 50/50 fraction of filled to unfilled intercalation sites. For carbon black (the second active material), the specific surface area was calculated using Eq. 7.24 assuming a particle diameter of 50 nm [21]. The exchange current density of carbon black reflects the most conservative estimate for a carbonaceous material (petroleum coke) that could be found in the literature [22].

Table 7.2. List of parameters used in case study of the negative graphite electrode in a lithium-ion battery.

Symbol	Description	Value
a_I	Specific surface area of graphite ($cm^2\ cm^{-3}$) [19]	3.6×10^3
a_{II}	Specific surface area of carbon black ($cm^2\ cm^{-3}$) [21]	1.2×10^6
α	Charge transfer coefficient	0.5
ε	Porosity [19]	0.182
κ	Electrolyte conductivity ($S\ cm^{-1}$) [20]	9.48×10^{-3}
$i_{0,I}$	Exchange current density of graphite ($A\ cm^{-2}$) (Eq. 7 in [20])	2.8×10^{-4}
$i_{0,II}$	Exchange current density of carbon black ($A\ cm^{-2}$) [22]	4.1×10^{-5}
L	Electrode thickness (cm) [19]	0.0076
T	Temperature (K)	298
τ_{tort}	Tortuosity [19]	11.2
U_I	Average open circuit potential of graphite (V)	0.1
U_{II}	Average open circuit potential of carbon black (V)	0.5

For both carbon materials, discharging of the electrode results in the oxidation of intercalated lithium, which can be expressed as follows:

$$\mathrm{Li} \rightarrow \mathrm{Li}^+ + \mathrm{e}^- \tag{7.26}$$

Both carbon materials undergo this reaction; however, each material has a different set of kinetic and thermodynamic parameters. It is assumed both materials contain a maximum of one lithium per six carbon (LiC_6) at the start of discharge [23]. The open circuit potentials for the reactions (U_I and U_{II} in Table 7.2) were determined from data in the literature [20, 21, 23, 24]. Both are given with respect to a $Li|Li^+$ electrode and correspond to the average open circuit potential of the reaction. This simplification to the open circuit potential is necessary for incorporation into the simple model. A full treatment, which is out of the scope of this work, would incorporate variations in the open circuit potential with degree of lithiation.

The only change in the model description for the Li-ion case study is the use of Eq. 7.16 in reference [20] to define the effective conductivity instead of a Bruggeman correction. This

corresponds to replacing $\varepsilon^{1.5}$ with ε/τ_{tort} everywhere in the model formulation (Equations 7.1, 7.16 and 7.20). Note that with or without this change, the electrode still satisfies the condition outlined in Eq. 7.1 that the ohmic resistance in the solid electrode is negligible. For instance, evaluation of Eq. 7.1 with and without this change using the parameters in Table 7.2 (and a value of $(1-\varepsilon)^{1.5}\sigma$ = 10 S cm^{-1} for the solid carbon electrode) results in values of 2.0 × 10^{-4} << 1 and 1.0 × 10^{-3} << 1, respectively [20]. To determine the battery voltage, the potential drop across the carbon electrode was considered relative to the open circuit potential of a $LiCoO_2|CoO_2$ electrode as follows:

$$V_{cell} = U_{LiCoO_2} - \left(\phi_1\big|_{x=L} - \phi_2\big|_{x=0}\right) = U_{LiCoO_2} + \phi_2\big|_{x=0} \tag{7.27}$$

where U_{LiCoO_2} is taken with respect to a Li|Li$^+$ electrode (3.8 V).

Figure 7.10 shows the results for simulations of a graphite electrode that underwent 10 second pulses after a baseline discharge at 1C and 2C to 80% DoD. All simulated electrodes have the same volumetric capacity. The figure plots the change in pulse power due to changes in the capacity fraction of carbon black. The pulse power is plotted as the ratio of the maximum pulse power of an electrode with two active materials (carbon black + graphite) to the maximum pulse power of an electrode with one active material (graphite). The results indicate that addition of carbon black to the negative electrode could improve the pulse-power performance of a Li-ion battery. For instance, the simulations in Figure 7.10 show that replacement of 0-60% of the graphite capacity with carbon black will increase the pulse power at both discharge rates. For the 1C rate, up to a 40% improvement in power is predicted for a capacity fraction of 22% carbon black. For the 2C rate, up to a 23% improvement in power is predicted for a capacity fraction of 24% carbon black. Note that replacement of 60% carbon black would result in a 6.5% decrease in the theoretical energy density of the electrode.

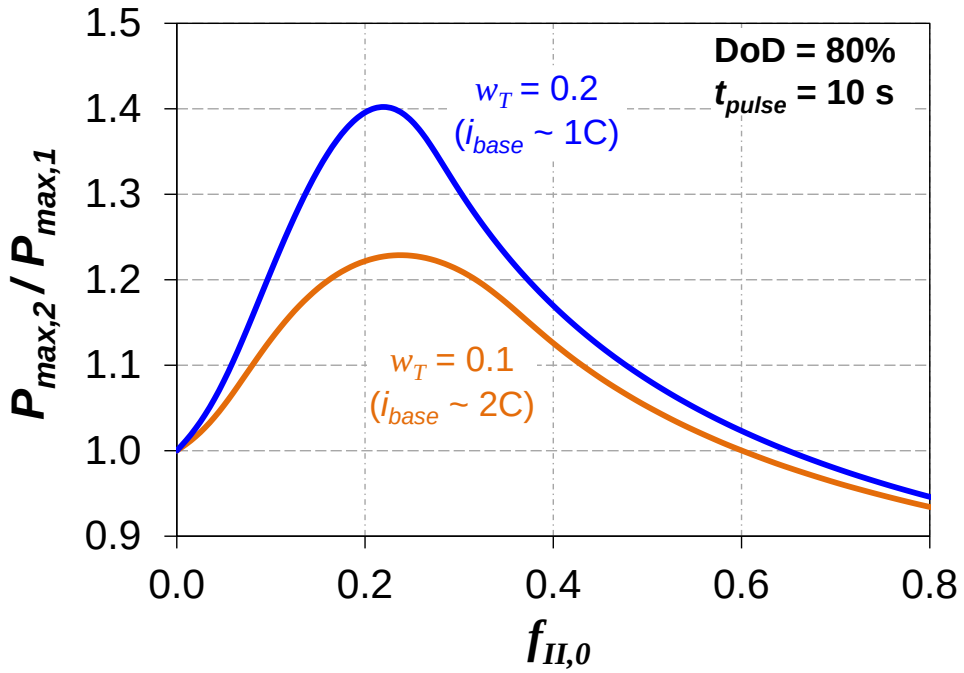

Figure 7.10. Simulated pulse-power as a function of the capacity fraction of the second active material (carbon black) in the negative electrode of a Li-ion battery. Pulse-power is plotted as the ratio of the maximum pulse-power of an electrode with two active materials (carbon black + graphite) to the maximum pulse-power of an electrode with one active material (graphite).

The simulated results in Figure 7.10 were obtained assuming minimal concentration variations within the electrolyte. However, at the high rates used in this study, it is likely that mass transport limitations could exist within this electrode, which may affect the simulated results. Despite this fact, the conclusion that carbon black will improve the pulse power is still valid because the presence of mass transport limitations would only provide another advantage for keeping the reaction front near the separator during the high current pulse. Therefore, the simulated results may slightly underestimate the improvements in pulse-power performance.

This case study was conducted using carbon black as the second electrochemically active material. Over the last twenty years, many different carbonaceous materials have been investigated for use in the lithium-ion negative electrodes (*e.g.*, carbon fibers, petroleum coke, and activated carbon) [22, 25-27]. It is likely that the pulse-power performance of the negative electrode can be optimized with the use of another carbon material (or blends of several carbons) as the second electrochemically active material.

7.4. Summary

The addition of a second electrochemically active material to a battery electrode is shown to improve the pulse-power performance at high DoD. For both the positive electrode of a sodium metal-halide battery and the negative electrode of a lithium-ion battery, improvements in performance are associated with a decrease in the ionic resistance due to movement of the reaction front towards the separator during pulse-power operation. Under simulated conditions, the maximum power of the sodium metal-halide electrode is predicted to improve by up to 40% when replacing a fraction of the nickel chloride capacity with iron chloride. Similar improvements in performance for the lithium-ion electrode were predicted when replacing a fraction of the graphite capacity with carbon black.

The impact of the second electrochemically active material on the pulse-power performance was shown to depend highly on the fraction of second active material, the relative importance of ohmic-to-charge transfer resistances (w_T), and the ratio of kinetic parameters between the first and second active materials (ξ). Improvements in the pulse power were predicted for low w_T, which corresponds to electrodes with high ionic resistance relative to charge transfer resistance. Additionally, simulations suggested there is an optimal value of ξ that will maximize the pulse-power of the electrode. Therefore, the electrochemical properties of the

second active material should be good enough relative to the first active material (high ξ) to maximize performance during the pulse discharge while poor enough (low ξ) to avoid reaction at low DoD.

7.5. List of Symbols

a	specific surface area ($cm^2\ cm^{-3}$)
f	initial capacity fraction of active material in the electrode
F	Faraday's constant (96,485 C mol^{-1})
i_{app}	applied current density (A cm^{-2})
i_{base}	baseline current density during discharge (A cm^{-2})
i_0	exchange current (A cm^{-2})
i_{pulse}	current density during high power pulse (A cm^{-2})
i_{rxn}	reaction rate (A cm^{-2})
L	electrode thickness (cm)
M	molar mass (g mol^{-1})
n	number of electron equivalents per mole
$\hat{Q}$	volumetric capacity (C cm^{-3})
R	ideal gas constant (8.314 J $mol^{-1}\ K^{-1}$)
t	time (s)
T	temperature (K)
U	open circuit potential (V)
x	distance from separator (cm)

Greek

α charge transfer coefficient

ε volume fraction in the electrode

θ ratio of specific discharge capacity of the material to initial specific discharge capacity of the material ($[C\ cm^{-3}]/[C\ cm^{-3}]_0$)

κ electrolyte conductivity ($S\ cm^{-1}$)

ρ density ($g\ cm^{-3}$)

σ electrode conductivity ($S\ cm^{-1}$)

ϕ_2 potential in the electrolyte (V)

Subscript

I denotes first active material

II denotes second active material

1 denotes solid electrode phase

2 denotes electrolyte phase

k denotes active material *I* or *II*

pulse denotes value during high current pulse

rxn denotes reaction

7.6. References

1. *U.S. Department of Energy Vehicle Technologies Program: Battery Test Manual for Electric Vehicles*, United States Department of Energy, Office of Energy Efficiency and Renewable Energy, Vehicle Technologies Office, INL/EXT-15-34184 (2015).
2. K. G. Gallagher, S.-H. Kang, S. U. Park and S. Y. Han, **196**, 9702 (2011).
3. *Battery Requirements for Plug-in Hybrid Electric Vehicles - Analysis and Rationale*, National Renewable Energy Laboratory, NREL/CP-540-42240 (2009).
4. M. Doyle, T. F. Fuller and J. Newman, *J. Electrochem. Soc.*, **140**, 1526 (1993).
5. M. Doyle, J. Newman, A. S. Gozdz, C. N. Schmutz and J. M. Tarascon, *J. Electrochem. Soc.*, **143**, 1890 (1996).
6. J. Rijssenbeek, Y. Gao, Z. Zhong, M. Croft, N. Jisrawi, A. Ignatov and T. Tsakalakos, *J. Power Sources*, **196**, 2332 (2011).

7. J. L. Sudworth, *J. Power Sources*, **100**, 149 (2001).
8. R. C. Galloway and S. Haslam, *J. Power Sources*, **80**, 164 (1999).
9. P. Albertus, J. Christensen and J. Newman, *J. Electrochem. Soc.*, **156**, A606 (2009).
10. Y. Dai, L. Cai and R. E. White, *J. Power Sources*, **247**, 365 (2014).
11. S. Basu, R. S. Patil, S. Ramachandran, K. S. Hariharan, S. M. Kolake, T. Song, D. Oh, T. Yeo and S. Doo, *J. Power Sources*, **283**, 132 (2015).
12. S. Jung, *J. Power Sources*, **264**, 184 (2014).
13. D. Kehrwald, P. R. Shearing, N. P. Brandon, P. K. Sinha and S. J. Harris, *J. Electrochem. Soc.*, **158**, A1393 (2011).
14. J. Newman and K. E. Thomas-Alyea, *Electrochemical Systems*, Wiley Interscience, Hoboken, New Jersey (2004).
15. A. C. West, *Electrochemistry and Electrochemical Engineering: An Introduction* (2012).
16. R. Zhu, M. Vallance, S. K. Rahimian and A. C. West, *J. Electrochem. Soc.*, **162**, A2051 (2015).
17. *ASM Ready Reference: Electrical and Magnetic Properties of Metals*, ASM International, United States of America (2000).
18. K. S. Mohandas, N. Sanil and P. Rodriguez, *Trans. Inst. Min. Metall., Sect. C*, **115**, 25 (2006).
19. M. Ender, J. Joos, A. Weber and E. Ivers-Tiffée, *J. Power Sources*, **269**, 912 (2014).
20. M. Ender, *J. Power Sources*, **282**, 572 (2015).
21. R. M. Gnanamuthu and C. W. Lee, *Mater. Chem. Phys.*, **130**, 831 (2011).
22. T. F. Fuller, M. Doyle and J. Newman, *J. Electrochem. Soc.*, **141**, 1 (1994).
23. M. Winter, P. Novák and A. Monnier, *J. Electrochem. Soc.*, **145**, 428 (1998).
24. C. Wang, A. J. Appleby and F. E. Little, *J. Electroanal. Chem.*, **497**, 33 (2001).
25. A. Mabuchi, K. Tokumitsu, H. Fujimoto and T. Kasuh, *J. Electrochem. Soc.*, **142**, 1041 (1995).
26. M. W. Verbrugge and B. J. Koch, *J. Electrochem. Soc.*, **143**, 600 (1996).
27. L. Zhang, M. Zhang, Y. Wang, Z. Zhang, G. Kan, C. Wang, Z. Zhong and F. Su, *J. Mater. Chem. A*, **2**, 10161 (2014).